DEVELOPMENT AND APPLICATION OF UV-VISIBLE AND MID-IR DIFFERENTIAL ABSORPTION SPECTROSCOPY TECHNIQUES FOR POLLUTANT TRACE GAS MONITORING

THÈSE N^{O} 2944 (2004)

PRÉSENTÉE À LA FACULTÉ ENVIRONNEMENT NATUREL, ARCHITECTURAL ET CONSTRUIT

Institut des sciences et technologies de l'environnement

SECTION DES SCIENCES ET INGÉNIERIE DE L'ENVIRONNEMENT

ÉCOLE POLYTECHNIQUE FÉDÉRALE DE LAUSANNE

POUR L'OBTENTION DU GRADE DE DOCTEUR ÈS SCIENCES

PAR

Rodrigo JIMÉNEZ PIZARRO

ingénieur chimiste diplômé, Universidad del Valle, Colombie
et de nationalité colombienne

acceptée sur proposition du jury:

Prof. B. Calpini, Prof. H. van den Bergh, directeurs de thèse
Prof. C. Comninellis, rapporteur
Dr A. Neftel, rapporteur
Prof. U. Platt, rapporteur
Dr V. Simeonov, rapporteur

Lausanne, EPFL
2004

Observing the dragon:

Classical analytical techniques vs. remote sensing

(Scientific Computing World, July/August 2001)

Summary

Spatial representativeness is an important quality criterion in trace gas monitoring, especially if measurements are intended for regulatory and model validation purposes. Open-path absorption spectroscopy techniques meet the representativeness requirement by providing concentrations averaged over atmospheric paths ranging from some hundred meters to some kilometers. This research concerns the characterization and application of a UV-visible differential optical absorption spectroscopy (DOAS) system, and the development and demonstration of a trace gas detection technique based on tunable, mid-infrared (mid-IR) quantum-cascade lasers (QCL).

The spectral accuracy, stability and resolution of the DOAS spectrometer, and the efficiency of its PMT[1]-based light detection system were characterized and tested in laboratory and field conditions. Additional laboratory experiments included exploratory test of a photodiode array (PDA) as multichannel analyzer, and spectral analysis of the arc of high-pressure Xe lamps. PDA measurements of NO_2 in the 360-530 nm range show an effective lower detectable fractional absorbance of $8 \cdot 10^{-4}$ (1-sigma) for a 3-s integration time, overpassing the detection capabilities of the scanner/PMT system.

DOAS measurements of SO_2, NO_2, and O_3 were extensively validated through laboratory calibration and intercalibration, and field intercomparison with conventional point monitors and EPA[2]-certified DOAS systems, showing good agreement among the different instruments. A nitrous acid (HONO) generator was developed and used for characterizing the DOAS detection capability. Laboratory measurements indicate a lower detection limit (LDL) of ~0.2 ppm·m HONO (2-sigma) for a 30-min integration time. Concerning formaldehyde (HCHO), a field intercomparison with HPLC[3]-analyzed DNPH[4] samples shows a non-aleatory, high degree of correlation (r^2 = 97%) between the two techniques, but unexplained, significant deviation from the 1:1 line (which is nevertheless within the 85% confidence interval of the correlation curve).

A mathematical method was developed for the estimation of detection limits through the analysis of sequential lamp spectra. LDL estimations with this method are in very good agreement with operational detection limits. Other data processing and concentration retrieval algorithms were developed and used for analyzing laboratory and field measurements (12 campaigns). The analysis and interpretation of observations in two of these field studies are reported in detail.

The first study concerns the dynamics and photochemical production regime of HCHO in the Grenoble region, France. DOAS measurements at a suburban location of Grenoble allowed estimating the sources of formaldehyde, and served at validating the results of a mesoscale photochemical grid model. Measurement-derived emission and photochemical production ratios are in good agreement with literature values, the emission inventory, and model calculations. A large fraction (>80%) of the HCHO observed at the measurement location is photochemically produced, and its production is VOC-limited / NOx-saturated. This

[1] PMT: PhotoMultiplier Tube

[2] EPA: US Environmental Protection Agency

[3] HPLC: High Performance Liquid Chromatography

[4] DNPH: 2,4-DiNitroPhenylHydrazine

investigation demonstrates also that DOAS is a well-suited technique for model validation purposes.

The second study concerns the emission of monocyclic aromatic hydrocarbons (MAH) from a wastewater treatment plant in Lausanne (Switzerland) using DOAS and GC[5]/FID[6]-analyzed grab samples. Combined analysis of the vertical wind speed and the MAH concentration time series suggest a quasi-diurnal cycle involving accumulation of fugitive emissions during the stagnant early morning hours followed by rapid upward convective dispersion from midday on. This study indicates that the wastewater treatment plant is a potentially significant source of MAH in the Lausanne area.

Measurements carried out in a high altitude (~2500 m ASL[7]) Andean valley (Sogamoso Valley, Colombia) are also presented and interpreted. A combined analysis of meteorological and O_3 measurements performed at ground level (including DOAS) and airborne (with a homemade tethered balloon), along with model calculations, provide evidence for mesoscale inflow to the Sogamoso Valley of clean air masses from the Colombian Eastern Savanna (~200 m ASL). This quasi-diurnal anabatic flow plays an important role in the ventilation of the Sogamoso valley, particularly during the dry season.

Despite of its high selectivity and sensitivity, and good temporal resolution, the UV-visible DOAS technique is restricted to a limited number species that display highly structured electronic bands. The advent of the quantum-cascade laser (QCL) in 1994, and its rapid development thereafter, offers to open-path absorption spectroscopy a promising doorway to the mid-IR. Quantitive detection of O_3 at ambient pressure with a 9.6 µm pulsed-operated, single-mode DFB[8] QCL was demonstrated in laboratory conditions. QCL transmission spectra in the 1044-1050 cm^{-1} range were obtained by tuning the laser temperature. O_3 column densities retrieved from the mid-IR spectra are in good agreement with simultaneous DOAS measurements but the detection limit attained (~25 ppm·m) is still too high for immediate test in open path conditions. Currently ongoing improvements on the QCL pulse acquisition system should allow achieving detection limits at the level of commercial DOAS systems (~2 ppm·m) in the very near future. These results demonstrate the applicability of the differential absorption method to QCL absorption spectroscopy at ambient pressure and encourage its use for open path detection.

Keywords: trace gas detection, differential absorption spectroscopy, DOAS, quantum-cascade laser, calibration, detection limit, field observation, ozone, nitrogen dioxide, formaldehyde, nitrous acid, monocyclic aromatic hydrocarbons, Andes, mesoscale, model validation

[5] GC: Gas Chromatography

[6] FID: Flame Ionization Detector

[7] ASL: Above the Sea Level

[8] DFB: Distributed FeedBack

Résumé

La représentativité spatiale est un critère de qualité important pour la mesure des gaz trace, particulièrement pour les mesures destinées au contrôle des normes de la qualité de l'air et pour la validation des modèles de qualité de l'air. Les techniques spectroscopiques à trajet optique ouvert remplissent pleinement ce critère. Elles permettent de mesurer des espèces chimiques sur la longueur d'un chemin optique allant d'une centaine de mètres à plusieurs kilomètres. Ce travail de recherche porte sur la caractérisation et l'utilisation d'un système de spectroscopie d'absorption optique différentiel (DOAS) fonctionnant dans l'ultraviolet-visible, ainsi que sur le développement et la démonstration d'une technique de détection des gaz trace par laser à cascade quantique (QCL) dans l'infrarouge moyen.

La précision, la stabilité et la résolution du spectromètre DOAS ainsi que l'efficience de son système de détection de lumière, basé sur un tube photomultiplicateur (PMT), ont été caractérisés et évalués dans le laboratoire et sur le terrain. Des études supplémentaires ont été réalisées en laboratoire. Ces études ont porté sur les tests d'un senseur à barrette de photodiodes (PDA) et sur l'analyse spectrale de l'arc des lampes de Xe à haute pression. Les mesures spectrales de NO_2 dans l'intervalle 360-530 nm avec le PDA ont montré une absorption résiduelle de $8 \cdot 10^{-4}$ (1-sigma) pour un temps d'intégration de 3 s. Cette performance dépasse les limites atteignables avec le système basé sur scanner et PMT.

Les mesures de SO_2, NO_2 et O_3 réalisées avec le DOAS ont été largement validées par calibration en laboratoire et inter-calibrations avec des moniteurs ponctuels et avec des systèmes DOAS approuvé par la EPA[9]. Un générateur d'acide nitreux (HONO) a été développé et utilisé pour évaluer la capacité de détection du DOAS. Les mesures de laboratoire indiquent une limite de détection (LD) de ~0.2 ppm·m pour le HONO (2-sigma) sur un temps d'intégration de 30 minutes. Concernant le formaldéhyde (HCHO), la comparaison sur le terrain avec des mesures réalisées par DNPH[10]/HPLC[11] montre une forte corrélation (r^2 = 97%), non aléatoire, entre les deux techniques. Cependant, il existe un écart significatif et inexpliqué de la ligne 1:1 (néanmoins, cette ligne se trouve dans l'intervalle de confiance de 85% de la courbe de corrélation).

Une methode mathematique basé sur l'analyse des spectres séquentiels a été développé pour l'estimation des limites de detection. Les estimations obtenues avec cette méthode montrent un très bon accord avec les LD opérationnelles obtenus sur le terrain. D'autres algorithmes de traitement de données et de calcul des concentrations ont été développés et utilisés pour l'analyse des mesures réalisées au laboratoire et sur le terrain (12 campagnes). L'analyse et l'interprétation des mesures obtenues au cours de deux de ces etudes de terrain sont discutées en détail dans ce travail.

La première étude a porté sur la compréhension des processus dynamiques et des régimes de production photochimique de HCHO sur la région de Grenoble, France. Des mesures DOAS effectuées sur un site dans la périphérie sud de Grenoble ont permis d'estimer les sources de formaldéhyde et de valider les résultats du modèle photochimique Eulérien de meso échelle. Les facteurs d'émission et de production photochimique obtenus à partir des mesures sont en très bon accord avec des valeurs de la littérature, avec le cadastre d'émissions, ainsi que avec

[9] EPA: US Environmental Protection Agency

[10] DNPH: 2,4-DiNitroPhenylHydrazine

[11] HPLC: High Performance Liquid Chromatography

les résultats du modèle. Les mesures et les simulations indiquent qu'une grande fraction de HCHO (>80%) mesuré est d'origine photochimique et que la production photochimique de HCHO est limitée par les COV[12] et en régime saturé par les NOx. Cette étude montre aussi que la technique DOAS est très adéquate pour la validation de modèles Eulériens.

La deuxième étude a porté sur l'émission des hydrocarbures aromatiques monocycliques (HAM) sur une station d'épuration des eaux usées à Lausanne, Suisse. L'émission des HAM a été mesurée par DOAS et par chromatographie en phase gazeuse (GC[13]/FID[14]). L'analyse des series temporelles de la vitesse verticale du vent et des concentrations de HAM a montré un cycle de variation quasi-journalier mettant en évidence l'accumulation des émissions fugitives au cours des premières heures de la journée, suivie de la dispersion convectif rapide à partir de midi. Cette étude de terrain a mis en évidence que la station d'épuration des eaux usées pourrait être une source importante d'émissions de HAM dans la région lausannoise.

Des mesures effectuées dans une haute vallée (~2500 m SNM[15]) de la région des Andes (vallée de Sogamoso, Colombie) sont aussi présentées et analysées. Une analyse combinée des mesures météorologiques et d'ozone effectuées a niveau du sol (y compris avec des systèmes DOAS) et en utilisant un ballon captif, ainsi que des calculs avec une modèle Eulérien ont permis de mettre en évidence le transport de masses d'air propre provenant des savanes (~200 m SNM) de l'est de la Colombie dans la vallée de Sogamoso. Ce flux anabatique quasi-journalière joue probablement un rôle important pour la ventilation de la vallée de Sogamoso, en particulier pendant la saison sèche.

La technique DOAS UV-visible, en dépit de sa haute sélectivité, sa sensibilité et sa bonne résolution temporelle est limitée à la mesure d'un nombre réduit d'espèces chimiques qui montrent des bandes d'absorption électronique très structuré. L'arrivée du laser à cascade quantique (QCL) en 1994 ainsi que son développement rapide offrent un futur prometteur dans l'infrarouge moyen à la spectroscopie à trajet optique ouvert. La faisabilité de la mesure de la concentration d'ozone en laboratoire à pression atmosphérique avec un laser à cascade quantique (9.6 µm mode pulse, DFB[16]) a été montrée au cours de ce travail de recherche. Des spectres d'absorption du QCL entre 1044 cm^{-1} et 1050 cm^{-1} ont été obtenus par réglage de la température du laser. Les densités de colonne d'ozone, déterminées à partir des spectres dans l'infrarouge moyen, montrent un excellent accord avec les mesures simultanées du DOAS. Cependant, la limite de détection obtenue (~25 ppm·m) est encore trop haute pour faire des mesures sur des trajets atmosphériques. Dans un futur proche, les améliorations du système d'acquisition de données du QCL devront permettre d'obtenir des limites de détection au niveau des systèmes DOAS commerciales (~2 ppm·m). Ces résultats montrent la validité d'application des méthodes d'absorption différentielle à la spectroscopie d'absorption du QCL à pression ambiante et encouragent leur utilisation pour la mesure sur des trajets optiques ouverts.

Mot Clés: gaz trace, spectroscopie d'absorption différentielle, DOAS, laser à cascade quantique, étalonnage, limite de détection, mesures du terrain, ozone, dioxyde d'azote formaldéhyde, acide nitreux, hydrocarbures aromatiques monocycliques, Andes, meso échelle, validation des modeles

---

[12] COV: Composés Organiques Volatils

[13] GC: Gas Chromatography

[14] FID: Flame Ionization Detector

[15] SNM: Sur le niveau de la mer

[16] DFB: Distributed FeedBack

Acknowledgements

Along these years of research, project development and teaching assistance at EPFL, I had the opportunity to count with the help and support of many people. I want to express my gratitude and appreciation to all of them, and in particular to the following persons and institutions:

Prof. Hubert van den Bergh for giving me the opportunity to work in his laboratory. His vision, interest, ideas and criticisms enriched very much my research.

Prof. Bertrand Calpini for his enthusiasm, vision, ideas, pragmatism, and intuition. I am also grateful with Bertrand for transmitting us his sense of teamwork, and for allowing me finding my place in his team.

Prof. Ulrich Platt, Albrecht Neftel, Prof. Christos Comninellis, Prof. Isabelle Bey and Valentin Simeonov for having participated as examiners of my thesis. I am also grateful with Isabelle and Bryan Duncan for their advice in many scientific and non-scientific issues.

Dieter Kita, Jeffrey Socha, Stelios Pezaris, and Dirk Appel at *Thermo Environmental Instruments Inc.* for their commitment and valuable technical support, particularly during the first years of research in DOAS. I gratefully acknowledge the financial support given by *Thermo Environmental Instruments Inc.* to this research work.

ICSC-World Laboratory for financially supporting the Sogamoso project and this research.

Bo Larsen at *Environment Institute / Joint Research Center* for introducing me to the carbonyl DNPH sampling and analysis trade, for analyzing a large number of DNPH samples, and for enriching scientific discussions and the friendly atmosphere that he sheds.

William Baehler and Michel Wanner at *SEHL / Ville de Lausanne* for their valuable contribution to the DOAS laboratory intercalibration and field intercomparison carried out at Lausanne during 1998-1999.

Daniel Hofstetter at *Université de Neuchâtel* for his help during the first stages of the quantum-cascade laser project and for valuable comments to the QCL manuscript.

Benoît Lazzarotto, a former colleague at EPFL now at *ROPAG*, for his contribution in the DOAS intercalibration measurements, for his friendship, team spirit, and cooking skills.

Jaime Diaz, Prof. Eugenio Giraldo, Juan E. Cetina, Prof. Diego Echeverry, Alirio Rodriguez, Adriana Cortazar, and Erika Zarate for their contribution, interest and commitment with the Sogamoso and Bogotá projects.

Valentin Simeonov for sharing with me the portion of his world made of optical components, electronics, and scientific enthusiasm.

Marian Taslakov for sharing his knowledge in optics and instrumentation.

Alain Clappier, Frank Kirchner, and Alberto Martelli for enriching discussions and criticisms. I also thank Alain for his support in the Sogamoso project.

Veronique Bauler, Flavio Comino, and Alfred Neunschwander for their fine work, kindness and patience.

Cesar Pulgarin for his deep commitment with the scientific cooperation between Switzerland and Colombia. His persistence made possible to Elizabeth and myself to come to EPFL and start our projects.

Francois Jeanneret, Benoît Lazzarotto, Dominik Stadler, Gilles Larchêveque, Olivier Couach, Ioan Balin, and Pablo Ristori, always supportive colleagues and comrades. I am particularly grateful to Pablo, Ioan, his wife Daniela, and Olivier for their friendship and support, especially during the last moths of my thesis.

Laszló Székely, Tiziana Ianonne, Fernando Jaramillo, Alfonso Martinez, Manuel Navarrete, Frederique Choffat, and Adriana Cortazar for their valuable work and assistance. I learnt from them at least as much as I could teach them.

My country, Colombia, for offering me education at a level that allowed me facing the demanding scientific environment of EPFL. I am thankful with my professors at *Universidad del Valle*. I invite those who disbelieve that I am still a chemical engineer to visit the laboratory and have a look at the HONO generator that I designed: it is ready to engage into industrial mass production!

Our many good friends all over the world, particularly Maria Beatriz, Diego, Claudia, Angela Guiovana, Mirtha, Rogelio, Francisco Javier, and Andrés Lema. Their sincere friendship helped us carrying on with this voluntary exile experience.

My parents, Hernando and Elvia Lucía, and brothers, Gustavo Hernando, Juan Fernando and Andres Felipe: Este logro es tambien de Ustedes! Es bueno saber que hay un punto fijo en horizonte sobretodo en aguas turbulentas.

Finally but most importantly my wife Elizabeth: sin ti no hubiera sido posible! Supiste tener confianza cuando yo dude. Gracias por tu compañia, confianza, apoyo incondicional y paciencia!

Table of Contents

"[London's] Inhabitants breathe nothing but an impure and thick Mist accompanied with a fuliginous and filthy vapour, which renders them obnoxious to a thousand inconveniences, corrupting the Lungs, and disordring the entire habits of their Bodies"
John Evelyn, 1661
(Fumifugium: or the inconveniencie of the aer and smoak of London dissipated)

Chapter 1
Introduction

Air pollution is not a modern problem. In contrast, our understanding and ability to measure, model, and predict the emission, transport, and fate of pollutants in the atmosphere is of recent acquisition. Besides the immediate impact of emissions on human and ecosystem health, pollutants perturb the radiative balance of the atmosphere. Understanding the global impact of human activities on the atmosphere is today an issue of paramount importance. The development of analytical methods that enable accurate detection of minute quantities of pollutants in the air has been the driving force behind the progress achieved in atmospheric chemistry during the last half a century. Open-path spectroscopic detection techniques have significantly contributed to this task.

The research here reported concerns the development and application of two spectroscopic detection techniques: Differential Optical Absorption Spectroscopy (DOAS) in the UV-visible, and mid-IR Quantum-Cascade Laser Absorption Spectroscopy (QCLAS). Laboratory and field measurements are presented. Measurements obtained in various field campaigns are analyzed and interpreted before their use for model validation. The structure of this research is schematically represented in **Figure 1-1**.

Chapter 2 outlines and integrates relevant concepts on atmospheric physics and chemistry, trace gas monitoring, and air pollution simulation. Open-path spectroscopic monitoring techniques are placed in context and their comparability to Eulerian model calculations is analyzed. Concepts developed in this chapter are extensively applied in Chapter 6.

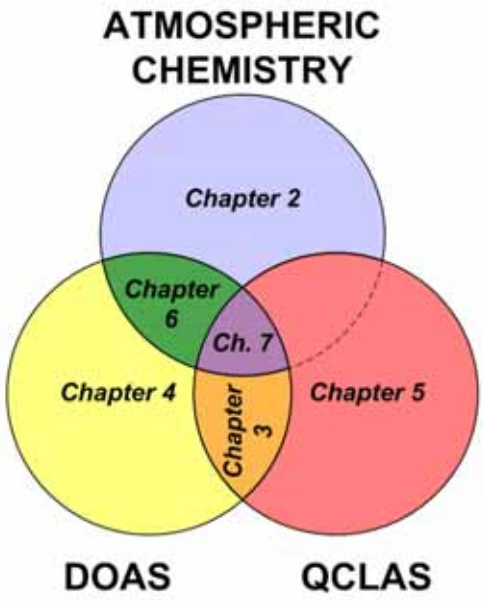

Figure 1-1. Research axes and structure of this Thesis.

Chapter 3 settles the theoretical basis for the differential absorption spectroscopy techniques developed (Chapters 4 and 5) and applied (Chapter 6) in this research, including an insightful discussion of the differential absorption concept and its practical application.

Chapter 4 deals with the characterization, test and development of a DOAS system, including the test of a photodiode array (PDA) for light detection, and the development and application of a calibration bench, including a HONO diluted gas mixture generator. This chapter present and analyzes laboratory intercalibrations and a 5-month intercomparison with other DOAS systems. Residual spectra derived and experimentally determined detection limits are presented. Algorithm and software developments are also briefly explained.

Chapter 5 presents the experimental development of a novel mid-IR QCL-based absorption spectroscopy system for the detection of ozone. The system uses differential absorption with successful results. This new technique has the potential of extending open-path detection to the mid-IR, where a large number of pollutants are potentially detectable.

Chapter 6 presents two field studies based on DOAS measurements. The first one concerns the dynamics and photochemical production of formaldehyde in the Grenoble air basin. The second one investigates the emission of monocyclic aromatic hydrocarbons from a wastewater treatment plant.

Chapter 7 concludes on the research and made a series of recommendations for future work.

This thesis is a combination of dedicated chapters and papers, whether published or submitted, as customary in EPFL/LPAS. Published papers are incorporated into this document in a very straightforward way, without major modification in format and appearance.

“Big whorls have little whorls that feed on their velocity, and little whorls have smaller whorls and so on to viscosity”
Lewis Fry Richardson, 1920
(The supply of energy from and to atmospheric eddies)

Chapter 2
Atmospheric Chemistry and Pollutant Monitoring

Trace-gas detection systems provide the basis for understanding the chemical evolution of the atmosphere at various spatial and temporal scales. This chapter outlines and integrates relevant concepts on atmospheric motion and chemistry, trace gas monitoring, air pollution simulation, and air quality management. It places in context open-path spectroscopic monitoring techniques, and analyzes their comparability to Eulerian model calculations.

Pollutant measurements and calculations presented in this research concern only the Planetary Boundary Layer (PBL), the lowermost layer of the troposphere (~0-3 km above the ground level - AGL). Field measurements were notwithstanding carried out in very different geographical settings: at low altitudes in central Europe and at high altitudes in the tropics (Colombia).

2.1 The troposphere: A complex, fast-mixing environmental compartment

In mass terms, the Earth's atmosphere ($5.14\ 10^{18}$ kg) is an insignificant geochemical reservoir since it contains less than 1 part in one million (ppm = 10^{-6}) of the total terrestrial mass ($5.98 \cdot 10^{24}$ kg). From the geochemical point of view, this minute mass fraction plays nonetheless a major role in the cycle of several elements, e.g. carbon and nitrogen.

Thermodynamic pseudo-equilibrium conditions confer to the atmosphere a vertical, compartmental stratification determined by abrupt changes in the temperature profile (temperature inversions). The lowermost of these layers, the troposphere, contains approximately 80-85% of the total mass of the atmosphere and is characterized by a monotonic temperature decrease with altitude, sustained by energy exchanges with the ocean and the land surfaces. The tropopause, i.e. the interface between the troposphere and the stratosphere, defined by a persistent temperature inversion, is located at ~18 km above the sea level (ASL) in the tropics and at ~10 km ASL at middle latitudes (McIntosh, 1983).

Along its elliptical translation orbit, the Earth intercepts a minute fraction of the energy radiated by the sun. The annual average solar radiation flux on the orbit's tangential plane, namely the solar constant, is 1368 W/m^2 [*] (Finlayson-Pitts, 2000). Approximately 23% of this radiation flux is absorbed in the atmosphere (Garstang, 1999). The photodissociation of oxygen and ozone in the stratosphere (Chapman cycle) accounts only for a small fraction of that absorption but serves at sustaining the vertical stratification (Finlayson-Pitts, 2000). Around 31% of the incident beam is returned to the space by scattering and reflection in the atmosphere and the surface. Finally ~46% of the solar beam is absorbed at the surface. Approximately 67% of this fraction is transferred back to the atmosphere as sensible and latent heat causing atmospheric motion. Therefore, due to the relative transparency of the atmosphere, the atmospheric motion is thus neither fueled from the space nor from within but from the surface (Garstang, 1999).

Moreover, the received radiation flux decreases with the latitude due to the Earth's sphericity. This uneven distribution of energy is at the base of the equatorial-to-poleward global temperature gradient. Because of Nature's trend to thermal equilibrium (obviously an unreachable condition for the Earth's atmosphere), heat is exchanged between the surface and the atmosphere leading to large-scale convective mixing of the upper layers of the oceans and the lower atmosphere (Dutton, 1995; Lockwood, 1979).

The atmosphere response to thermal exchange results in a complex spectrum of atmospheric motions (see **Figure 2-1**) ranging from frictional dissipation with wavelengths of some millimeters to planetary waves as long as the Earth's circumference (Barry, 2001; Dutton, 1995). As a consequence of these motions, the troposphere is the best stirred atmospheric layer with convective vertical mixing times on a scale of hours, zonal transport times along constant latitudes on the order of weeks, meridional transport times on a scale of months, and inter-hemispherical exchange times of ~1-2 years (Kley, 1997).

---

[*] Peak global radiation levels of up to 1070 W/m^2 were measured in the Sogamoso Valley, located in the Colombian Andes at ~2500 m ASL. Global radiation measurements include direct and diffuse radiation

In spite of this rapid turnover, large concentration gradients are observed in the troposphere, particularly of short-lived and moderately long-lived species (as defined in the next section), due to the irregular spatial distribution of emissions, and spatial and temporal variations of advective[1] and convective[2] transport. The spatial extension and position of a particular pollution phenomenon is thus a consequence of the lifetimes of the species emitted and their transformation products, and the meteorological conditions (Kley, 1997). Accordingly, the investigation of a pollution phenomenon, involving a number of species hence a span of lifetimes, entails the selection of appropriate spatial scales (Barry, 2001; Dutton, 1995) among the following (see **Figure 2-1**):

- Microscale (0.1-1 km): concerns phenomena that occur within *second to minutes*, such as the conversion NO into NO_2, whether by direct oxidation with O_2 or by titration of O_3, early after its release to the atmosphere.
- Convective or small scale (1-20 km): this spatial scale covers phenomena occurring on the scale of *minutes to hours*, as for instance the dilution of a pollutant plume from a road traffic tunnel portal. Some authors refer to this scale whether as “local” or “urban”.
- Mesoscale or regional scale (20-500 km): this spatial scale is required to describe phenomena that develop within *hours to days*, such as photochemical pollution. It is probably the scale of most concern in tropospheric air pollution research.
- Synoptic scale (500-5000 km): addresses phenomena that occur on the scale of *days to weeks*, such as the long-range (transboundary) transport of pollutants in the upper troposphere over continental or hemispherical scales.
- Planetary scale (> 5000 km): allows describing phenomena at the global scale with time spans ranging from *weeks to months*.

The mathematical description of the atmospheric motion at the scales above is founded in the application of the mass, momentum and energy conservation equations to a moving air parcel (Lagrangian description). Changing the coordinate reference system from moving parcels to fixed points (Eulerian description) allows easier comparison to standard measurements and makes the resulting equation set applicable to all scales of atmospheric motion. The Eulerian set of partial differential equations is however non-linear, and non-linearity is probably the most serious mathematical and computational difficulty in meteorological modeling (Dutton, 1995).

The conservation equations are in practice applied to phenomena belonging to a single scale of atmospheric motion, assuming that the interaction with widely different scales can be neglected. For instance, large-scale (synoptic) phenomena are generally treated without detailed consideration of atmospheric turbulence (Dutton, 1995). Such a simplification would render poor results in the mesoscale, a scale that is halfway between entirely turbulent and entirely advective motion. The simulation of mesoscale processes is a major challenge to dynamic meteorology with important implications in the investigation of regional-scale pollution phenomena. Nearly all the investigations presented in this research address regional air quality problems. As discussed below, open-path monitoring techniques provide valuable information in this context.

---

[1] Bulk movement

[2] Vertical turbulent movement

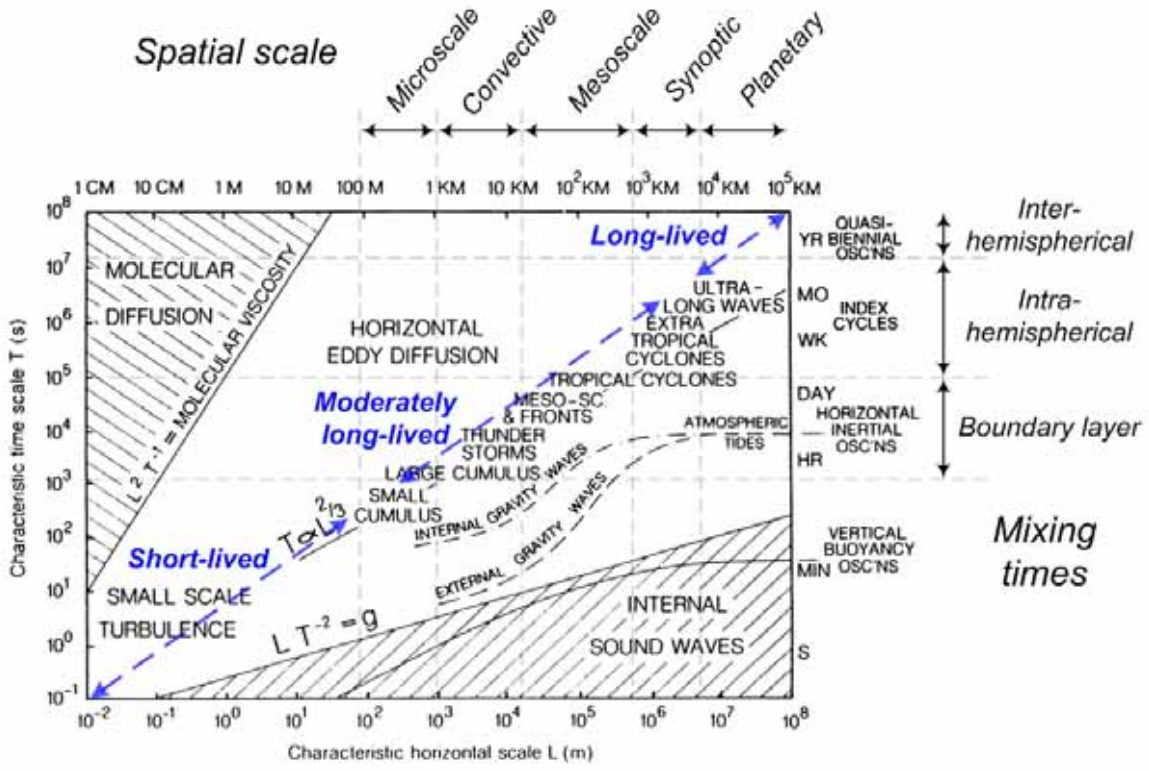

Figure 2-1. Spatial and temporal scales of atmospheric phenomena. Overlapping of trace gas lifetime ranges provides an indication of the spatial extension of pollution phenomena. Adapted from Barry (2001).

2.2 Air pollutants and atmospheric chemistry

Air pollutant emissions are usually classified according to their origin (anthropogenic, biogenic, volcanic, radiogenic), and based on the geometry of their sources (point, linear, area). Combustion is by far the main anthropogenic air pollutant emission source. Combustion releases traces gases as reaction co-products (CO_2, H_2O) and by-products (CO, NMHC[3], carbonylic compounds[4], NO, NO_2, SO_2), or simply by fugitive emission or uncontrolled evaporation of fuels (VOC[5]). Nitric oxide (NO), a particularly active compound in photochemical pollution, is generated by dissociation of molecular nitrogen at high temperatures, especially in internal combustion engines. Other anthropogenic emissions sources are associated to the manufacture and use of chemicals, and to farming activities, such as livestock raising, fertilizer use, and biomass burning for agricultural and grazing purposes.

[3] NMHC: non-methane hydrocarbons

[4] Compounds containing the carbonylic functional group, C=O (aldehydes and ketones)

[5] VOC: volatile organic compounds

Natural emissions can play important roles at several spatial and temporal scales, particularly in photochemical pollution. For instance, biogenic VOC, such as isoprene, enhance photochemical pollution at the regional scale, and NO produced by lightning in the upper troposphere is partially responsible for the elevated oxidant levels observed over the southern Atlantic Ocean.

Atmospheric trace gases (see **Table 2-1**) can be classified as primary or secondary, depending whether they are directly emitted (e.g. CO, SO_2 and benzene) or produced in the atmosphere by chemical transformation (e.g. O_3 and peroxyacetyl nitrate – PAN).

Some photochemically produced compounds, such as formaldehyde (HCHO), are as well directly emitted by combustion or other sources. The relative contribution of emissions and secondary production in the observed concentration of formaldehyde can be estimated by correlation of their time series to the time series of compounds known to be purely primary (e.g. CO) or secondary (e.g. O_3). See e.g. Friedfeld (2002). This approach[6] has nevertheless a limited validity since it neglects differences in sources and sink terms between the suspected dual source compounds (e.g. HCHO) and the source-representative compounds (e.g. CO and O_3). For instance, the fact that O_3 generally accumulates for longer periods in the atmosphere than formaldehyde would bias the direct correlation analysis (see **Section 6.1**).

About 21% of the Earth's present atmosphere consists of molecular oxygen (O_2), thus any molecules entering the atmosphere tend to be chemically driven toward increased oxidation states. Despite of its large abundance, molecular oxygen is a poor oxidizer. Most of the oxidation processes are sequence-initiated by more active species, most of them arisen from photochemical processes driven by solar radiation (Graedel, 1985).

The most important of these oxidants is the hydroxyl radical (HO – see **Table 2-1**), the existence of which was first suggested by Levy in 1971 (Graedel, 1985). Other important oxidizers are the hydroperoxyl (HO_2) and nitrate (NO_3) radicals, and ozone (O_3). Most of HO in clean atmospheres is produced via the photolysis of O_3 to electronically excited oxygen (O^1D), a small fraction of which (~10-20%) effectively reacts with water vapor,

$$O_3 + h\nu\left(\lambda \le 336\,\text{nm}\right) \rightarrow O\left(^1D\right) + O_2 \qquad \text{(Reaction 2-1)}$$

$$O\left(^1D\right) + H_2O \rightarrow 2\,HO \qquad \text{(Reaction 2-2)}$$

$$O\left(^1D\right) + M \rightarrow O\left(^3P\right) \qquad \text{(Reaction 2-3)}$$

Other important sources of HO in polluted atmospheres are the photolysis of nitrous acid (HONO)[7] and hydrogen peroxide (H_2O_2),

[6] This approach was employed to investigate the origin of HCHO in the Milan metropolitan area and in the Grenoble region (see Chapters 4 and 6, respectively)

[7] Laboratory measurements of HONO are presented in Chapter 4

	Species	Units [1]	Mixing ratio [2]	Sources [3]	Sinks [3-4]	Residence time	Trend	Ref. [8]
Long-lived	N_2	%	78.085%	V, B	----	~10^6 yr	Stable	g, j
	O_2	%	20.946%	B	B, A	~10^4 yr	Decreasing	g, j
	H_2O	g/kg	0.01-30	W, V	W	~9 days	Unknown	n
	Ar	%	0.934%	R	No cycle	---	Stable	j
	CO_2	ppm	367	V, B, A	B, C	~100 yr [5]	Increasing	a
	Ne	ppm	18.18	V	No cycle	---	Stable	j
	He	ppm	5.24	R	No cycle	10^{10} yr [6]	Stable	j
	CH_4	ppm	1.714	B, A	HO	~7-9 yr	Increasing	a, j, l
	Kr	ppm	1.14	R	No cycle	---	Stable	j
	H_2	ppm	0.5	P, B	HO	~10 yr	Stable	j
	N_2O	ppb	312	B, A	P	~10 yr	Increasing	a
	Xe	ppb	87	R	No cycle	---	Stable	j
	Rn	ppt	0.06	R	----	---	Stable	j
Moderately long-lived	CO	ppm	0.05 - 50	A, B, P	HO	~2-3 mo	---	a, e
	NMHC	ppb	1 - 2000	A, B	HO	~ 1 h - 2 mo [7]	---	a, d, e, m
	SO_2	ppb	0.2 - 2000	V, A, P	HO	~ 1-40 days	---	a
	NO	ppb	0.01 - 2000	A, B, L, P	O_3	~1-2 days	---	a, d
	NO_2	ppb	0.1 - 1000	P	HO, P	~1-2 days	---	a, d
	O_3	ppb	10 - 700	P	P, D	~ 2 days - 1 yr	Increasing	c, f, o
	HCHO	ppb	0.1 - 120	P, A, B	P, HO	~ 4 h - 15 days [7]	---	a, b, e
	NH_3	ppb	< 0.02 - 100	A, B	HO	~20 days	---	a
	HNO_3	ppb	0.02 - 50	P	HO, D	~1 day	---	a, d
	H_2O_2	ppb	< 0.1 - 40	P	HO, P, D	~1 day	Unknown	d
Short-lived	HONO	ppb	0.001 - 15	H, A, C	P, C	10-60 min	---	a, d, h
	NO_3	ppt	< 5 - 430	C	P, C	5 s - 10 min	---	a, i
	HO_2	ppt	< 1 - 40	P, C	---	< 1 - 200 s	---	a, d, k
	HO	ppt	0.004 - 0.5	P, C	---	< 1 s	---	a, k

[1] [mole / mole dry air] or [v/v]; water vapor in [g / kg dry air]

[2] Long-lived species: mixing ratios in the free/background troposphere
Moderately long- and short-lived species: from mixing ratios in the marine boundary layer to pollution episode peak values

[3] A: Antropogenic
B: Biogenic
C: Non-photochemical reactions
D: Deposition (dry/wet uptake)
H: Heterogeneous reaction
P: Photochemical and/or photolysis
L: Lightning
R: Radiogenic
V: Volcanic
W: Physical

[4] Main oxidant if a species is indicated

[5] Response time (Finlayson-Pitts, 2000)

[6] Calculated planetary halflife due to exospheric loss of disociated species (McIntosh, 1983)

[7] Calculated lifetime taken into account sinks only

[8] (a) Finlayson-Pitts, 2000
(b) Lowe, 1981
(c) NRC/CGER, 1991
(d) Seinfeld, 1998
(e) Wagner, 2002
(f) Thielmann, 2000
(g) McIntosh, 1983
(h) Stutz, 1996
(i) Geyer, 2000
(j) Warneck, 1988
(k) Platt, 1999
(l) Brasseur, 2000
(m) Atkinson, 2000
(n) Garstang, 1999
(o) Kley, 1997

Table 2-1. Troposphere composition: Mixing ratios, sources, sinks and residence times. Noble gases and DOAS-detectable species are denoted by light (yellow) and dark (aqua) shadowing, respectively. (Atkinson, 2000; Brasseur, 2000; Finlayson-Pitts, 2000; Garstang, 1999; Geyer, 2000; Kley, 1997; Lowe, 1981; McIntosh, 1983; NRC/CGER, 1991; Platt, 1999; Seinfeld, 1998; Stutz, 1996; Thielmann, 2000; Wagner, 2002; Wang, 1998; Warneck, 1988)

$$HONO + h\nu\left(\lambda < 400\,nm\right) \rightarrow HO + NO \quad \text{(Reaction 2-4)}$$

$$H_2O_2 + h\nu\left(\lambda < 370\,nm\right) \rightarrow 2\,HO \quad \text{(Reaction 2-5)}$$

and the conversion of hydroperoxyl radical (HO_2) at NO mixing ratios above ~10 parts-per-trillion (ppt = 10^{-12}) (Finlayson-Pitts, 2000),

$$HO_2 + NO \rightarrow HO + NO_2 \quad \text{(Reaction 2-6)}$$

HO_2, HO, and atomic hydrogen (H) are linked trough a series of fast reactions and constitute the hydrogen oxides (HO_X) group,

$$\left[HO_X\right] = \left[H\right] + \left[HO\right] + \left[HO_2\right] \quad \text{(Equation 2-1)}$$

In the polluted boundary layer, the photolysis of HONO is probably the most important source of HO radicals in the early morning hours. The formation of HONO is a current research topic in atmospheric chemistry since the mechanisms proposed so far cannot explain the concentrations observed in ambient air. Laboratory and field measurements indicate that a large fraction of HONO is produced by heterogeneous conversion of NO_2 on aerosol or even building surfaces. There is experimental evidence showing that these reactions involve adsorbed water and/or reactive sites on the surface of soot, although the intermediary steps are not yet fully elucidated (Finlayson-Pitts, 2000). HONO is a primary pollutant as well with emission ratios ranging within 0.35-1% of the NO_X emissions (Stutz, 1996).

The photolysis of formaldehyde is another important source of hydroxyl radicals in polluted atmospheres. HCHO photolysis has two possible channels,

$$HCHO + h\nu \rightarrow H + HCO \quad \text{(Reaction 2-7)}$$

$$HCHO + h\nu \rightarrow H_2 + CO \quad \text{(Reaction 2-8)}$$

but only the first one (reaction 2-7) leads to the formation of HO, through fast reactions with molecular oxygen,

$$H + O_2 \rightarrow HO_2 \quad \text{(Reaction 2-9)}$$

$$HCO + O_2 \rightarrow HO_2 + CO \quad \text{(Reaction 2-10)}$$

followed by conversion of HO_2 into hydroxyl radical in the presence of NO (reaction 2-6).

The concentration of HO at the global scale has implications on the global climate since it determines the cleansing capacity of the atmosphere (Brasseur, 2000; Wang, 1998), and consequently, the residence time of various greenhouse gases. Calculations performed with

various global scale photochemical grid models indicate that HO concentrations peak over the tropics[8], as expected because of the combination of elevated radiation and water vapor levels at these latitudes (see **Figure 2-2**). These calculations indicate as well a dramatic decrease (of up to ~60% in the northern hemisphere) of the HO radical concentration levels since pre-industrial times due to anthropogenic emissions (Wang, 1998).

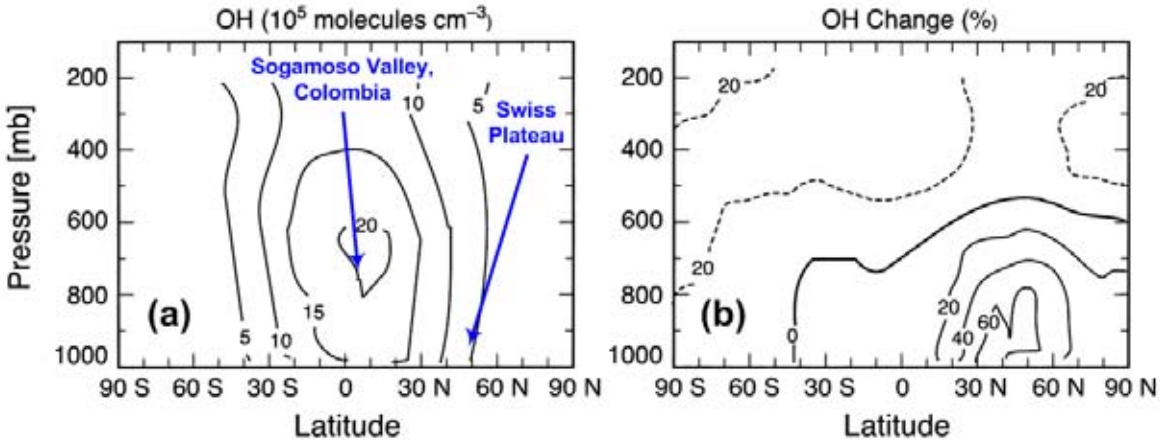

Figure 2-2. Global model-calculated (latitude-averaged) annual mean concentrations of hydroxyl radical for **(a)** the present atmosphere, and **(b)** percentage changes from pre-industrial times to present. Dashed and continuous lines indicate increase and decrease, respectively. The model estimates an overall, mass-weighted decrease of 9% of the mean HO concentrations since pre-industrial times (Wang, 1998).

The lifetime of an oxidizable compound is inversely proportional to the oxidant concentration and to its reactivity (reaction rate constant) with the oxidant species (see **Table 2-1**). In atmospheric chemistry, the lifetime ($t_{1/e}$) is usually calculated as the period of time required to oxidize 63% ♣ of the compound's initial concentration. Taking HO as the main oxidant as a matter of example[9], the lifetime is calculated as the inverse of the product of the reaction rate constant (k_{HO}) with the average hydroxyl radical concentration ($\overline{[HO]}$),

$$t_{1/e} = \frac{1}{k_{HO} \cdot \overline{[HO]}} \qquad \text{(Equation 2-2)}$$

[8] The HO peak concentration is model-predicted to take place at ~700 mbar, ~10 ºN, almost coinciding with the CAVASO 2002 campaign location (Colombian Andes – See **Section 6.3**)

♣ A trace gas is oxidized from initial concentration to 1/e of initial concentration

[9] The kinetic equation, $d[A]/dt = -k_{HO} \cdot [A] \cdot [HO]$, assumes that HO is the preponderant oxidizer of A. Other or additional terms must be included if oxidation by HO is not the predominant or the only sink

A more realistic value, the average lifetime, is obtained by including the main sources and sinks in the calculation. The lifetime of an oxidizable trace gas is at the same time indicative of its reactivity and of the spatial extension of the pollution phenomena in which is involved. For instance, a very stable species like methane displays a very low oxidation rate, leading to accumulation at the global scale. From another perspective, a species can be considered inert within a certain time span or spatial scale, e.g. carbon monoxide in urban photochemical pollution. The trace gas classification as short lived, moderately long-lived and long-lived species, as shown in **Table 2-1**, roughly corresponds to lifetimes on the scale of seconds to minutes, hours to months and years to geological times, respectively.

One of the best historically documented pollution phenomena is the so-called "London" Smog. This is mainly a primary pollutant type of phenomenon characterized by elevated concentrations of SO_2, soot (black carbon), and acidic aerosols enhanced by low ventilation conditions. It was only relatively recent recognized that the combustion of coal or other fuels with elevated contents of sulfur, or any other sources of SO_2, such as ore refining, unavoidable produce acid deposition. Since the atmospheric oxidation of SO_2 to sulfuric acid (H_2SO_4),

$$\begin{aligned} &SO_2 + HO \rightarrow HOSO_2 \\ &HOSO_2 + O_2 \rightarrow SO_3 + HO_2 \\ &SO_3 + H_2O \rightarrow H_2SO_4 \end{aligned} \qquad \text{(Reaction 2-11)}$$

is a relatively slow process, acid deposition is a problem that frequently concerns regional (mesoscale) or even continental (synoptic) scales. The oxidation of NO_2 into nitric acid (HNO_3), channeled mainly through the single-step reaction with hydroxyl radical,

$$NO_2 + HO + M \rightarrow HNO_3 \qquad \text{(Reaction 2-12)}$$

contributes as well to acid deposition.

The presence in the air of elevated concentrations of gas- and condensed-phase (particulate matter) primary pollutants is still a major environmental problem worldwide, particularly in transition and developing countries[10] (Emberson, 2001; Streit, 1996). Primary pollution is nevertheless a less complex scientific problem than photochemical pollution since the concentrations of primary pollutants (and their products in the case of acid rain) respond linearly to changes in emissions, as e.g. observed after redistributing the road traffic around a small town in central Switzerland (Jiménez, 1999).

An important stimulus to the research on atmospheric chemistry came in with the identification in the 1950s of "Los Angeles" Smog (photochemical pollution) as a new "type" of air pollution, as important in terms of public health and crop yield, as the historically documented "London" Smog. As shown below, photochemical pollution is a highly nonlinear process, since e.g. a reduction of emissions does not necessarily implies a decrease of the

[10] This is the case in the Valley of Sogamoso (Colombia). See Section 6.3

concentration of secondary pollutants (Finlayson-Pitts, 1997; Jiménez, 1999; Seinfeld, 1998). Moreover, the health and environmental impacts of secondary pollutants, such as ozone, peroxyacetyl nitrate (PAN), formaldehyde (HCHO) and secondary aerosols, can be more severe than those of their precursors (NO_X and VOC).

The increase of emissions associated with demographic and economic processes, such as the massive use of the automobile during the last ~50 years, and accelerated urbanization and industrial growth in transition and developing countries in more recent times, have boosted urban photochemical pollution at the global scale (NRC/CGER, 1991). Albeit a regional (mesoscale) process, photochemical pollution has also implications at the global scale, such as positive radiative forcing caused by increasing background levels of ozone, a potent greenhouse gas in the troposphere. The concentrations of ozone in the free troposphere have increased from 10-20 parts-per-billion (ppb = 10^{-9}) in preindustrial times to ~50 ppb and ~30 ppb currently in the northern and southern hemispheres, respectively (Marenco, 1994; Roscoe, 1997).

The only significant anthropogenic source of ozone in the troposphere is the photolysis of nitrogen dioxide (NO_2),

$$NO_2 + h\nu\left(\lambda < 420\,nm\right) \rightarrow NO + O\left(^3P\right) \qquad \text{(Reaction 2-13)}$$

followed by the very fast reaction of $O(^3P)$ ♦ with molecular oxygen,

$$O_2 + O\left(^3P\right) + M \rightarrow O_3 \qquad \text{(Reaction 2-14)}$$

Produced O_3 reacts readily with nitric oxide regenerating NO_2 formerly photolyzed,

$$NO + O_3 \rightarrow NO_2 + O_2 \qquad \text{(Reaction 2-15)}$$

In absence of reactive organic compounds (ROC), the combination of **Reactions 2-13** through **2-15** predicts the establishment of a pseudo-equilibrium condition among the irradiated mixture species. After reaching the photostationary state (PSS) condition, the chemical production rate of ozone,

$$P\left(O_3\right) = J_{NO_2}\left[NO_2\right] - k_{15}\left[NO\right]\left[O_3\right] \qquad \text{(Equation 2-3)}$$

becomes zero, $P\left(O_3\right) = 0$ (Kleinman, 2000). In the equation above, J_{NO_2} is the NO_2 photolysis rate (**Reaction 2-13**) and k_{15} is the rate constant of **Reaction 2-15**. In spite of its

♦ $O(^1D)$ and $O(^1S)$ are produced only at wavelengths shorter than 244 and 170 nm, respectively. Production by NO_2 photolysis is thus negligible in the troposphere

simplicity, the PSS model is instrumental in explaining observed daytime concentrations, particularly of NO_2, at low ROC levels,

$$\frac{[NO_2]}{[NO]} = \frac{k_{11}}{J_{NO_2}} \cdot [O_3] \qquad \text{(Equation 2-4)}$$

as for instance in a semi-rural region in Central Switzerland (Jiménez, 1997).

One interesting consequence of the PSS reaction scheme is the conservation of the NO_X lump,

$$[NO_X] = [NO] + [NO_2] \qquad \text{(Equation 2-5)}$$

independently of its initial split and the photochemical reaction path, i.e. $[NO_X] = [NO_X](0)$.

When ROCs are added to the irradiated mixture, the chemical system gains in complexity (see **Figure 2-3**) and deviates from simplest PSS condition expressed by **Equation 2-4** (see e.g. Neftel, 2002; Rohrer, 1998). In these conditions, NO_X can still be considered invariable in many cases and over limited spatial temporal scales, since NO_X sink reactions are in most cases relatively slow compared to the NO-NO_2 cycling reactions.

NO_X can thereby be perceived as a "catalyzer" of the ROC photo-oxidation, as shown in **Figure 2-3**. This schematic representation indicates as well that the addition of ROC to the chemical system enhances the production of ozone ($P(O_3) > 0$) with respect to the PSS condition (refer to equation 2-3), particularly because of the addition of two nitric oxide oxidation channels,

$$NO + XO_2 \rightarrow NO_2 + XO \qquad \text{(Reaction 2-16)}$$

involving whether the hydroperoxyl radical (X = H) or organic peroxides (X = R). Some observation-based models (Kleinman, 2000) and simplified chemical mechanisms use XO_2 as a lumped group.

The atmospheric photo-oxidation of ROC is a complex cascade-wise process (see **Figure 2-3**). For instance, the photo-oxidation of alkanes and alkenes (RH) starts with the attack by available oxidants (HO, NO_3, Cl) leading to the formation of alkyl radicals (R), which readily react with O_2 to produce alkylperoxy radicals (RO_2). The oxidation of nitric oxide (NO) produces alkoxy radicals (RO) that react with O_2 to produce carbonylic compounds ($R'CHO$) and hydroperoxyl radicals (HO_2). Carbonylic compounds ($R'CHO$) may undergo photolysis or react with HO, NO_3 or Cl. In any case HO_2 is produced. In polluted atmospheres, HO_2 is readily converted into HO (reaction 2-6).

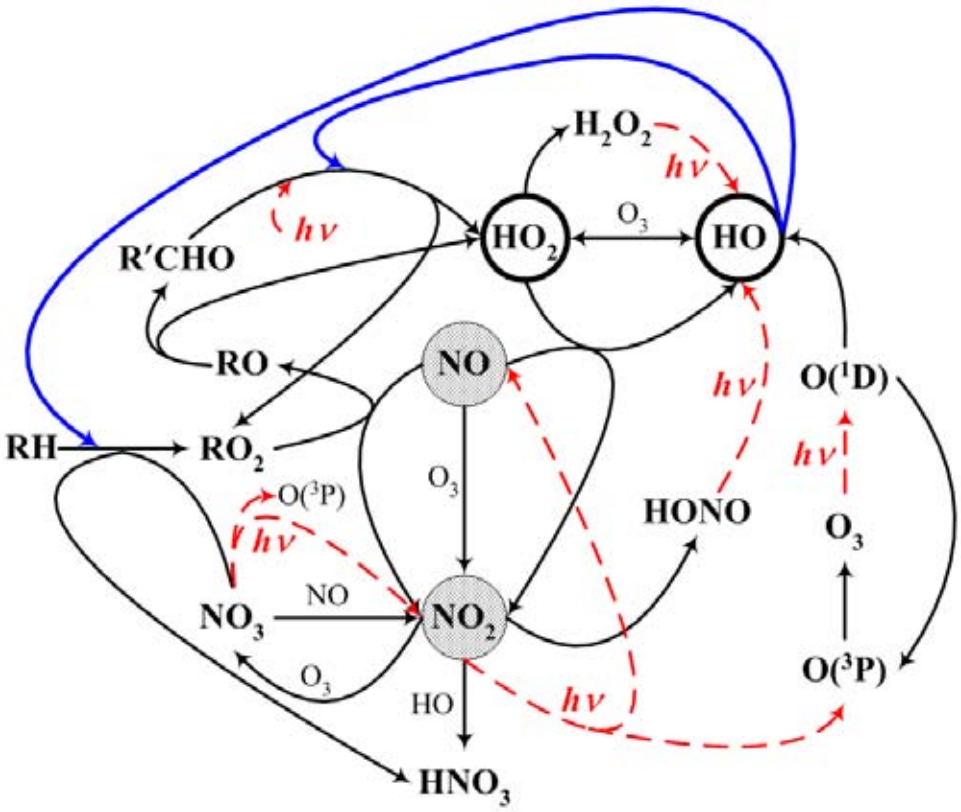

Figure 2-3. Simplified schematic representation of the photo-oxidation of ROC (particularly alkanes) in the troposphere. Ubiquitous species, such as molecular oxygen, water vapor or third bodies (M), e.g. nitrogen, are not included in the diagram. Nitrogen oxides (NO_X) and hydrogen oxides (HO_X) species are presented in dotted circles and bold circumferences, respectively. HO attack and photolysis reactions are displayed as thick solid lines (blue) and dotted lines (red), respectively. Besides nitric acid formation, no other sink reactions are shown.

As a result of the outstanding complexity of the ROC photo-oxidation process, which includes oxidant recycling, oxidation reaction branching (not explicitly shown in the diagram), and many feedback reactions, the concentration and production rate of secondary pollutants (such as O_3 and HCHO) are usually related to the concentration (or emission rate) of precursors (NO_X and ROC) in a highly non-linear way as shown in **Figure 2-4** for a suburban location of Grenoble (France) (Couach, 2003; Jiménez, 2004a)[11]. This figure presents model-calculated isopleths of ozone and formaldehyde as a function of the fractional emission of NO_X and ROC (VOC). Both ozone and formaldehyde respond non-linearly but in different ways to reductions of NO_X and ROC emissions. Within the VOC-limited regime (the current condition at the investigated location), the model predicts e.g. that a cut of emissions along the mixed path $\overline{AB}$ significantly reduces formaldehyde whereas causing no change on ozone.

[11] See Chapter 6

Conversely, within the NO_X-limited regime, a comparatively smaller reduction of the NO_X emissions along $\overline{CE}$ yields noticeable reductions on both, HCHO and O_3, while a considerable ROC cut ($\overline{CD}$) produces almost no change on either compound. The non-linearity is associated with the increasing production of nitric acid (HNO_3) and other NO_Z compounds at higher NO_X levels. In these conditions, the photo-oxidation process is slowed down since NO_X sink reactions compete in an efficient with the NO-NO_2 cycling reactions.

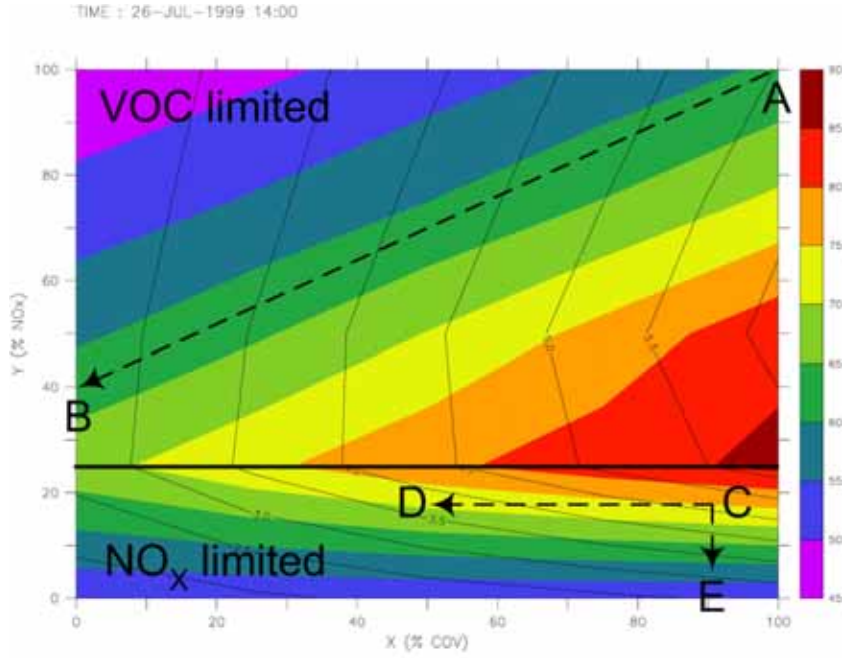

Figure 2-4. Calculated ozone and formaldehyde isopleths at Vif, a suburban location at 20 km south of Grenoble downtown (France), on 26th July 1999, 14:00 CET (Jiménez, 2004a). Concentrations are presented as a function of the factional emission of NO_X and VOC (ROC). Tonality scales and lines indicate ozone and formaldehyde concentrations in ppb, respectively (see **Section 6.1**).

2.3 The role of monitoring, field campaigns and simulation models in air pollution research and management

As discussed above, the spatial extension of air pollution phenomena results from a complex interplay between atmospheric motion and pollutant lifetime. Polluted air masses in deep valleys and other complex topography areas[12] are frequently quasi-constrained to their particular regions as a result of persistent local wind circulation patterns and topographic barrier effects. Such geographical areas can be treated as air basins (airshed), i.e. air volumes with well-defined boundaries and air mass exchange interfaces. Basin is for hydrologists a

[12] The Grenoble area (France) and the Sogamoso Valley fit into this characterization (see Chapter 6).

precise concept since the boundaries of a water catchment area are usually well defined. The complexity of the atmospheric motion does not allow for such a precise definition in atmospheric sciences due to e.g. the variability of the synoptic conditions and their influence on the regional circulation patterns. Air basin is nevertheless a very useful concept in air quality research and management. Air basins are usually defined on the basis of geographical, meteorological, and emission characteristics. Land use patterns and political boundaries are frequently taken into consideration as well. More scientifically-sound determination methodologies, based on statistical analysis of pollutant time series, have been also used (Yu, 2001).

Since an air basin is a sort of "control" volume, it allows for a clear definition of the background conditions. Concerning air pollution at the regional scale, the background concentration ($c_{background}$) can be defined as the contribution term to a measured concentration (c),

$$c = c_{regional} + c_{background} \qquad \text{(Equation 2-6)}$$

that is beyond the control of the region ($c_{regional}$), i.e. that cannot be modified by any changes in emissions within the region and does not depend on the regional-scale meteorology.

Air basins are usually managed as units for regulatory purposes. The improvement of air quality at the air basin scale requires deep understanding of the atmospheric physics and chemistry involved as much as consideration of economic and social constraints (see e.g. Streit, 1996). Air quality management aims at the attainment and maintenance of air quality at levels that grant protection to human health and welfare based on dose-response relationships. The protection of crops, ecosystems, materials, and visibility is usually regarded as a secondary goal (WHO, 2000). The achievement of these goals implies the establishment of governmental policies on environment, transport, land use, and energy that are implemented through an Air Quality Management System[13] (AQMS – see **Figure 2-5**). An AQMS comprises three major tasks: monitoring, information, and management (Noll, 1977).

The management task is aimed at implementing pollution abatement strategies through a series of regulation mechanisms (WHO, 2000). Devising technically feasible, cost-effective pollution abatement strategies requires the support of deterministic mathematical models along with consideration of economic and social constraints (Jiménez, 2000; Streit, 1996). Suitable computational models must be:

(1) Selected according to the type of pollution phenomena to abate (primary/secondary, gas-phase/aerosol) and to the topography and meteorology of the region.

(2) Validated by checking their capability to adequately simulate the dynamics of air pollution within the spatial domain (e.g. an air basin).

Physical numerical models are whether Lagrangian or Eulerian depending on the coordinate reference system used (see Section 2.1). Lagrangian models allow calculating the trajectory and composition of a moving air parcel within a measured or calculated wind field, by solving

[13] A project was undertook in parallel with this research to establish an appropriate AQMS in the Sogamoso Valley, Colombia

the kinematic equation coupled to a statistical description of the turbulence (Emeis, 1997). Lagrangian models are intrinsically appropriate for back trajectory analysis, and aerosol formation and dispersion calculations.

Eulerian models are based on the mass, momentum and energy conservation equations. These equations are numerically solved using a finite volume (grid-based) approximation (Emeis, 1997; Finlayson-Pitts, 2000). Grid models are widely used for the simulation of the air pollution dynamics, particularly in the gas-phase and at urban (convective) and regional (mesoscale) scales. One intrinsic advantage of the Eulerian models is that their results can be directly compared to ground-based (fixed coordinate system) and airborne measurements, which simplifies the validation task. The box model (Finlayson-Pitts, 2000) is the simplest Eulerian-like model. It is constituted by a single cell, usually of variable height (see **Figure 2-6**). Box models are useful for the analysis of chemical mechanisms, and for the simulation of the trace gas dynamics in remote areas (e.g. Wagner, 2002)[14]. From another perspective, grid models can be regarded as series of interconnected fixed-volume box models.

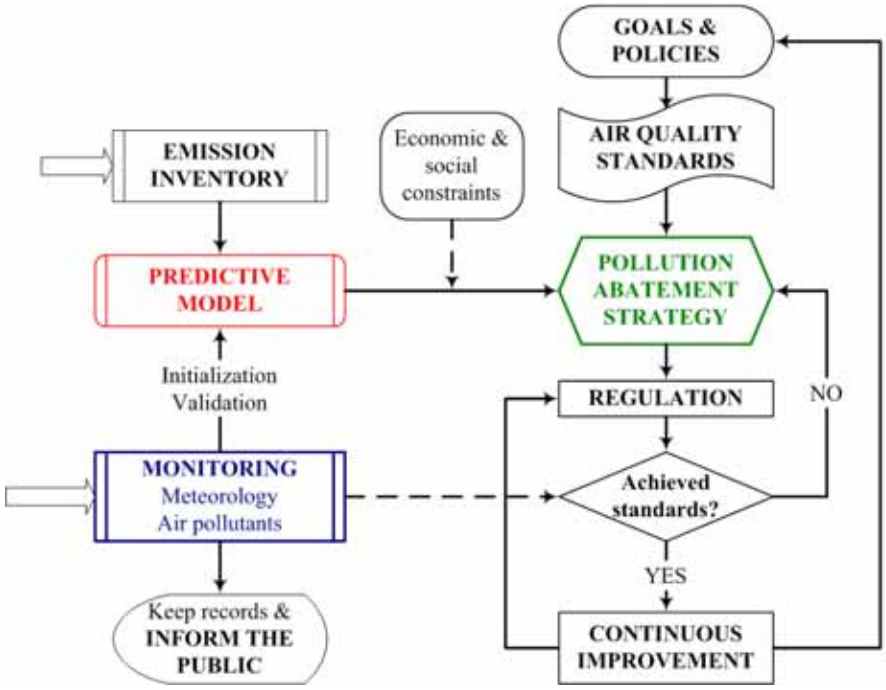

Figure 2-5. Air Quality Management System (AQMS): Task and information flow diagram.

There are two main approaches to the numerical modeling of air pollution: statistical and physical (Emeis, 1997). The most used statistical numerical model, the Gaussian plume model, is a restricted analytical solution of the diffusion equation. Statistical models are devised to provide a time-averaged (steady-state) description of the pollutant dispersion in the atmosphere. This characteristic made them useful for regulatory purposes (e.g. impact assessment) but intrinsically unsuited for describing the pollution dynamics.

[14] The mass conservation equation of a box model was used to determine mathematical validity conditions of formaldehyde emission and photochemical production ratios derived from measurements (see Section 6.1)

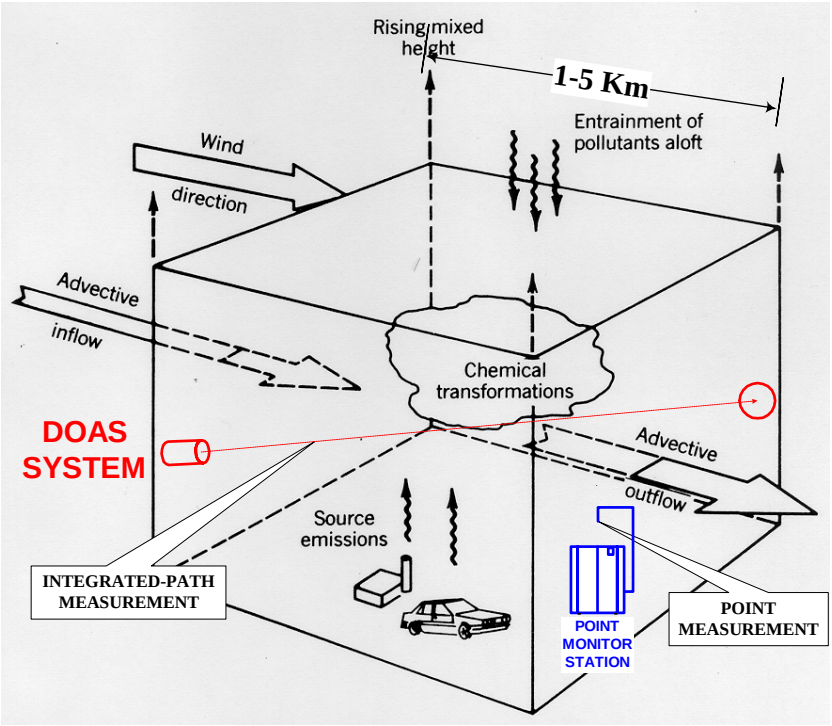

Figure 2-6. Schematic of a box model. This diagram represents as well a cell of a Eulerian (grid-based) model, its horizontal resolution, and the representativeness of point and path-integrated (e.g. DOAS) validation measurements. Adapted from Finlayson-Pitts (2000).

Model-predicted concentrations must be validated against field measurements. Meteorological calculations must be assessed as well, whenever meteorology is numerically simulated (prognostic models). Validated simulation models are important decision-making tools in air quality management. They allow testing and screening among different pollution abatement scenarios under various meteorological conditions (see **Figure 2-5**).

The monitoring task involves routine, long-term measurements of various meteorological parameters and ambient air pollutant concentrations, and the inventory of pollutant emissions. Inasmuch as the emission inventory is a critical input to simulation models, it must be revisited and updated on a periodic basis. Gas- and condensed-phase pollutants are regularly measured at various selected locations (monitoring network[15]) inside, and sometimes outside the air basin (background measurements). Most monitoring networks around the world perform regular ground-level measurements only of criteria pollutants, i.e. those regulated as primary standards. Although this definition depends on national regulations, criteria pollutants are usually among the following (WHO, 2000):

- Gas-phase: CO, SO_2, NO_2, O_3
- Aerosol: TSP, PM_{10}, $PM_{2.5}$, Pb

[15] A 4-station monitoring network was established in the Sogamoso Valley

Continuous progress in air pollution and toxicological research and advances in pollution control technology implies that standards of regulated pollutants are revisited and tighten on an almost periodic basis. Moreover, additional pollutants are included in regulatory lists over longer periods of time. For instance, benzene (carcinogenic compound) is since year 2000 a criterion pollutant in the European Union (EU), and formaldehyde (anticipated carcinogenic) is a potential candidate for the near future[16]. This has important implications in terms of monitoring device development (see next section).

The ability to detect with a high degree of accuracy minute quantities of pollutants in the air is thus not only at the basis of the development of the air pollution science, but as well fundamental for devising appropriate abatement strategies. In brief, the detection of trace gas in the atmosphere serves at the following purposes (Jiménez, 2000; Noll, 1977; Wert, 2003):

- Determining the atmospheric composition and its evolution for research purposes
- Determining long-term air quality trends
- Determining compliance with air quality standards (primary and secondary)
- Initializing and validating simulation models

Regarding the last purpose, it is frequent to find that photochemical grid models are granted validation because of their ability to reproduce observed concentrations of only one or two species, e.g. O_3 and NOx. Such a limited assessment must be call into question. In order to add robustness to the assessment, calculations of other photochemically-active species, e.g. peroxy radicals (Plummer, 1996) or formaldehyde (Jiménez, 2004a; Solberg, 2001) should be compared as well with measurements.

The spatial representativeness (see next section) and coverage of the measurements used for validating the model must be considered as well. Air quality information obtained from standard monitoring networks is usually insufficient for the characterization of the spatial distribution of pollutants, particularly in the vertical direction, therefore insufficient also for model validation purposes. The complementary information can be obtained through measurement campaigns, which usually involve sophisticated instrumentation for ground level and vertical profiling measurements (e.g. LIDAR[17], aircraft- and balloon-borne instrumentation), generally not available for routine monitoring. Model validation intended field campaigns involve the measurement of a large enough number of meteorological parameters and trace gases at suitable spatial and temporal resolutions. These measurements usually target a single air basin during short periods of time (~1 month). Due to cost and other operational limitations not all the measurements can be performed during all the campaign period. Some sophisticated measurements, e.g. LIDAR (Schoulepnikoff, 1998), are usually performed only during very special weather or other pollution episode[18] triggering conditions. These periods are known as Intensive Observation Periods (IOP) (see **Figure 2-7**). Previous analysis of the campaign results, measurements must undergo quality control and assessment (QC/QA). Measurement campaigns are performed also in remote areas. Data obtained in these campaigns allows obtaining information on the global "background" composition of the atmosphere and testing various atmospheric chemistry hypothesis (see e.g. Plummer, 1996;

[16] Formaldehyde and benzene are measurable with DOAS (see Chapters 4 and 6). Measurements with QCL-based systems have not been demonstrated yet but detection with comparable TDLAS systems has been reported

[17] LIDAR: LIght Detection And Ranging

[18] Episodes are defined whether by concentrations overpassing regulatory standards or by pollutant accumulation and circulation processes involving e.g. the residual layer

Wagner, 2002). Despite of their importance, the capability of simulation models should not be overestimated. In order to address the right questions to the models, campaign measurements should be analyzed and interpreted as much as possible before using them for model validation purposes.

2.4 Characteristics and representativeness of trace gas measurements

The advent of the electronic devices in the early 1940s furthered the development of instrumental techniques for trace gas analysis, e.g. with the application of the photomultiplier tube (PMT). There is nowadays available a spectrum of techniques for the detection of trace gases down to the ppt concentration level (see e.g. Parrish, 2000; Platt, 1999; Roscoe, 1997; Sigrist, 1993).

The performance of a detection technique must be assessed according to the following analytical requirements (Calvert, 1990; Platt, 1994; Platt, 1999; Sigrist, 1993):

- Sensitivity: Calvert (1990) defines sensitivity as the detection system gain (signal-to-concentration derivative). A technique of high sensitivity would be thus potentially able to measure species at their lowest concentration levels in ambient air. This can be a very demanding criterion since some key species are present at sub-ppb levels. Besides gain, sensitivity is quantified by the lower detection limit (LDL)[19], i.e. the lowest concentration that can be detected with a given statistical probability.
- Selectivity and multicompound detection: refers to the capability to detect and quantify one or various species in multicomponent mixtures or matrices without being interfered by species of comparable properties. The capacity to detect multiple compounds with the same instrument is also a desirable characteristic.
- Dynamic range and linearity: atmospheric mixing ratios range from fractions of parts-per trillion (ppt = 10^{-12}) to percentages (% = 10^{-2}). The dynamic range is defined (Calvert, 1990) as the ratio of the highest measurable concentration to the LDL. A large dynamic range allows e.g. sensing a species with the same instrument in remote and highly polluted atmospheres.
- Comparability and accuracy: a high degree of accuracy implies that measurements are free of bias and systematic errors. This characteristic is assessed through calibration and intercalibration in laboratory conditions, and "blind" intercomparison in open-air conditions[20].
- Temporal resolution: can be defined as the shortest "sampling" time required for achieving detection with a given level of precision. Requirements in temporal resolution vary within orders of magnitude depending on the type of phenomenon investigated. Provided that sample analysis is made on-line, a good temporal resolution allows for real-time operation (on-line monitoring).

[19] The relation between LDL and precision in relation to the methods presented here (DOAS and QCLAS) is discussed in chapters 4 and 5. Accuracy is also discussed

[20] Intercalibration and intercomparison of DOAS measurements are presented in Chapter 4. The calibration with DOAS of QCL measurements of O_3 is presented in Chapter 5

Further desirable characteristics are portability for *in situ* measurements, operational robustness, low operational costs and maintenance (which allows for unattended operation), and simplicity of design and operation.

Detection techniques can be classified according to several characteristics. One of them is the operational principle. A large number of techniques rely on spectroscopic phenomena, such as light scattering and absorption[21], fluorescence and chemiluminiscence. Non-spectroscopic techniques include chromatographic separation (e.g. GC and HPLC) coupled to various detection techniques (e.g. UV/VIS/IR absorption, FID, MS, ECD)[22], mass spectroscopy (MS), and various electrochemical and wet chemistry analytical methods. The sampling procedure is another important classification criterion since it determines the spatial and temporal resolution of the measurements. Air sampling can be performed by the following methods (Sigrist, 1993):

- Extractive sampling: samples are collected for subsequent analysis with highly sensitive and selective laboratory techniques, e.g. gas chromatography. Despite of their analytical performance, these techniques cannot be used for real-time monitoring. Due to cost and/or sampling rate limitations, the number of samples and/or the sampling period is usually restricted as well. This implies a poor temporal resolution and/or short time coverage. In addition, extractive measurements are representative only of the sampling site (point measurement). This can be an advantage or a disadvantage depending on the measurement purpose. Furthermore, the sample composition can be altered during manipulation and storage due to wall adsorption and surface reactions.
- *In situ* monitoring: point monitors offer the advantage of real-time operation although often with a lower analytical performance than extractive methods. These techniques operate by instantaneous or "grab" sampling. The sample is thus manipulated over shorter periods of time than classical extractive methods, which reduces the risk of sample alteration. Point analyzers are widely used for the monitoring of criteria pollutants.
- Remote sensing: all current remote sensing techniques are spectroscopic, i.e. rely on the measurement of light-matter interactions for the detection of trace gases. Notable examples are Differential Optical Absorption Spectroscopy (DOAS), open-path (OP) Tunable Diode Laser Absorption Spectroscopy (TDLAS), open-path Fourier Transform InfraRed spectroscopy (FTIR), and LIght Detection and Ranging (LIDAR). Remote sensing techniques are intrinsically contactless and generally provide good temporal resolution. Concentrations retrieved by remote detection are whether spatially resolved (e.g. LIDAR) or path integrated (e.g. DOAS, OP-TDLAS and OP-FTIR).

Besides technical considerations, a prime criterion for technique development and selection is the adequacy between analytical capability and the measuring purpose. Measurements intended for regulatory and model validation purposes are important examples.

Ambient air monitoring usually requires less stringent detection capabilities than atmospheric chemistry research but a more reliable and less expensive operation in the long term. The selection criteria for this application, besides sensitivity and selectivity, are thus operational robustness and cost.

---

[21] An outline of open-path absorption spectroscopy is presented in Chapter 3

[22] HCHO intercomparison measurements obtained by DNPH/HPLC are presented in Chapter 4 and 6

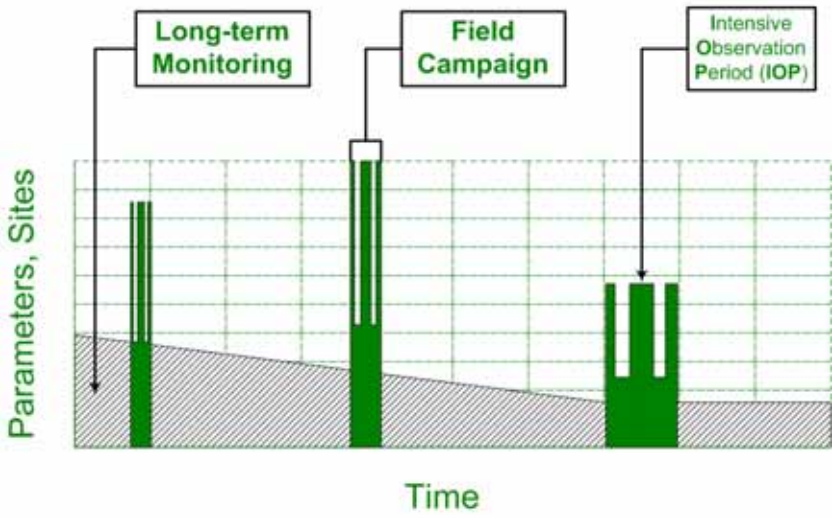

Figure 2-7. Air quality measurement: Long term monitoring and field campaigns. Continuous improvement in air quality implies that the number of monitored parameters and/or sites decreases with time (monitoring phase out). Field campaigns involve (continuous) measurements of a comparatively large number of parameters at various sites during a short period of time, and an even larger number of parameters/sites during one or various intensive observation periods (IOP).

The validation and initialization of urban and regional scale (photochemical) grid models require measurements matching their temporal and spatial resolution. This last one is typically within 0.1-5 km on the horizontal scale and of variable length on the vertical axis. Point measurements may lack of representativeness for the validation of model calculations at the ground level, particularly in poor atmospheric mixing conditions and for primary pollutants (see **Figure 2-6**). Open-path spectroscopic detection techniques (e.g. DOAS) provide instead path-averaged measurements of various trace gases. In the case of DOAS, the atmospheric absorption paths typically range from some hundred meters to some kilometers. DOAS measurements are thus particularly well suited for model validation and initialization purposes. The validation of calculations above the ground level requires measurements with whether range-resolved (e.g. LIDAR) or airborne systems.

DOAS fulfill to a high degree of achievement the analytical requirements mentioned above, providing as well a good compromise between analytical performance and operational cost. DOAS is thus appropriate for atmospheric chemistry research, grid model validation and routine monitoring alike (Jiménez, 2000; Plane, 1995; Platt, 1994).

DOAS systems are capable of multicompound detection, usually at the sub-ppb level, with a temporal resolution in the order of ~1-30 min (see Chapter 4). A non-exhaustive list of detectable trace gas species with high-pressure Xe lamp based systems includes NO, NO_2, NO_3, HONO, O_3, HCHO, SO_2, NH_3, BTEX[23] and other MAH[24] (see **Table 2-1**). HO can be

[23] Benzene, toluene ethylbenzene and xylenes

[24] Monocyclic aromatic hydrocarbons

detected with dedicated systems. DOAS is intrinsically a contactless technique, thus appropriate for the detection of highly reactive species, such as NO_3, and HONO (Platt, 1994; Platt, 1999). Besides their interest for model validation, path-integrated DOAS measurements provide a good indication of the average exposure to pollutants. Path-integrated measurements are as well suitable for fenceline (perimeter) monitoring. The operational costs of DOAS are comparatively low since no routine calibration is needed. Maintenance downtimes are short.

At the present time, DOAS measurements are limited to a reduced number of species that have relatively narrow, highly structured transition bands in the UV-visible (see Chapters 3 and 4). Long-open path detection techniques based on tunable laser sources in the infrared (IR), such as Quantum-Cascade Lasers (QCL - see Chapter 5), have the potential to extend the advantages of the DOAS technique to the measurement of a large number of species (Jiménez, 2004b).

2.5 References

Atkinson, R. Atmospheric chemistry of VOCs and NO_X. *Atmos. Environ.* 34: 2063-2101, 2000

Barry, R.G. and A.M. Carleton. Synoptic and dynamic climatology. Routledge, London, 2001

Brasseur, G. and R. Prinn. Is the "cleansing capacity" of the atmosphere changing? *Global Change Newsletter* (43): 12-13, 2000

Calvert, J.G. Glossary of atmospheric chemistry terms. *Pure Appl. Chem.* 62 (11): 2167-2219, 1990

Couach, O., F. Kirchner, R. Jiménez, I. Balin, S. Perego and H. van den Bergh. A development of ozone abatement strategies for the Grenoble area using modeling and indicators. *Atmospheric Environment*: accepted for publication, 2003

Dutton, J.A. Dynamics of atmospheric motion. Dover, New York, 1995

Emberson, L.D., M.R. Ashmore, F. Murray, J.C.I. Kuylenstierna, K.E. Percy, T. Izuta, Y. Zheng, H. Shimizu, B.H. Sheu, C.P. Liu, M. Agrawal, A. Wahid, N.M. Abdel-Latif, M. van Tienhoven, L.I. de Bauer and M. Domingos. Impacts of air pollutants on vegetation in developing countries. *Water Air Soil Pollut.* 130: 107-118, 2001

Emeis, S.M. Numerical dispersion models for emission monitoring by spectroscopic remote sensing methods. SPIE, *Spectroscopic Atmospheric Monitoring Techniques (LASER '97)*, Munich, Jun 19-20, 1997: 120-127

Finlayson-Pitts, B.J. and J.N. Pitts. Tropospheric air pollution: Ozone, airborne toxics, polycyclic aromatic hydrocarbons, and particles. *Science* 276: 1045-1052, 1997

Finlayson-Pitts, B.J. and J.N. Pitts. Chemistry of the upper and lower atmosphere. Academic Press, San Diego, 2000

Friedfeld, S., M. Fraser, K. Ensorb, S. Tribbleb, D. Rehlec, D. Leleux and F. Tittel. Statistical analysis of primary and secondary atmospheric formaldehyde. *Atmos. Environ.* 36: 4767–4775, 2002

Garstang, M. and D.R. Fitzjarrald. Observations of surface to atmosphere interactions in the tropics. Oxford University Press, New York, 1999

Geyer, A. The role of the nitrate radical in the boundary layer - Observations and modeling studies. Ph.D. Thesis, Ruprecht-Karls-Universität, Heidelberg, 2000

Graedel, T.E. The photochemistry of the troposphere. **In** J.S. Levine (ed), The photochemistry of atmospheres: Earth, the other planets, and comets, Academic Press, Orlando (FL), 1985: 39-76

Jiménez, R., C. Dubois, F. Jeanneret, G. Larchevêque, B. Lazzarotto, V. Simeonov and B. Calpini. Assessment of air quality in the Canton of Obwald. Field measurement campaign 1997 - Preliminary experimental report. EPFL/LPAS, Lausanne, 1997

Jiménez, R., H. van den Bergh and B. Calpini. Evidence of primary air pollutant reduction and photochemical pollution enhancement after opening a road tunnel to the public. *Analusis* 27 (4): 313-318, 1999

Jiménez, R., H. van den Bergh and B. Calpini. DOAS as an analytical tool for effective air pollution management. *3rd Specialty Conf. Environ. Progress Petroleum Petrochem. Industries*, Bahrain, May 1-3, 2000: Paper 006

Jiménez, R., O. Couach, F. Kirchner, S. Perego, B. Calpini and H. van den Bergh. Formaldehyde dynamics and photochemical production regime in the Grenoble region, France. *Atmos. Environ.*: submitted, 2004a

Jiménez, R., M. Taslakov, V. Simeonov, B. Calpini, F. Jeanneret, D. Hofstetter, M. Beck, J. Faist and H. van den Bergh. Ozone detection by differential absorption spectroscopy at ambient pressure with a 9.6 μm pulsed quantum-cascade laser. *Appl. Phys. B* 78: 249-256, 2004b

Kleinman, L.I. Ozone process insights from field experiments - Part II: Observation-based analysis for ozone production. *Atmos. Environ.* 34: 2023-2033, 2000

Kley, D. Tropospheric chemistry and transport. *Science* 276: 1043-1045, 1997

Lockwood, J.G. Causes of climate. Edward Arnold, London, 1979

Lowe, D.C., U. Schmidt and D.H. Ehhalt. The tropospheric distribution of formaldehyde. Kernforschungsanlage, Jülich, 1981

Marenco, A., H. Gouget, P. Nédélec and J.-P. Pagés. Evidence of a long-term increase in tropospheric ozone from Pic du Midi data series: Consequences: Positive radiative forcing. *J. Geophys. Res.* 99 (D8): 16617-16632, 1994

McIntosh, D.H. and A.S. Thom. Meteorología básica. Alhambra, Madrid, 1983

Neftel, A., C. Spirig, A.S.H. Prevot, M. Furger, J. Stutz, B. Vogel and J. Hjorth. Sensitivity of photooxidant production in the Milan Basin: An overview of results from a EUROTRAC-2 Limitation of Oxidant Production field experiment. *J. Geophys. Res.* 107 (D22): 2002

Noll, K.E. and T.L. Miller. Air monitoring survey design. Ann Arbor Science, Ann Arbor (MI), 1977

NRC/CGER. Rethinking the ozone problem in urban and regional air pollution. National Academy Press, Washington, 1991

Parrish, D.D. and F.C. Fehsenfeld. Methods for gas-phase measurements of ozone, ozone precursos and aerosol precursors. *Atmos. Environ.* 34: 1921-1957, 2000

Plane, J.M.C. and N. Smith. Atmospheric monitoring by differential optical absorption spectroscopy. **In** R.J.H. Clark and R.E. Hester (ed), Spectroscopy in environmental science, Wiley, Chichester (UK), 1995: 223-262

Platt, U. Differential optical absorption spectroscopy. **In** M.W. Sigrist (ed), Air monitoring by spectroscopic techniques, Wiley, New York, 1994: 27-84

Platt, U. Modern methods of the measurement of atmospheric trace gases. *Phys. Chem. Chem. Phys.* 1: 5409-5415, 1999

Plummer, D.A., J.C. McConnell, P.B. Shepson, D.R. Hastie and H. Niki. Modeling of ozone formation at a rural site in Southern Ontario. *Atmos. Environ.* 30 (12): 2195-2217, 1996
Rohrer, F., D. Brüning, E.S. Grobler, M. Weber and D.H. Ehhalt. Mixing ratios and photostationary state of NO and NO_2 observed during the POPCORN field campaign at a rural site in Germany. *J. Atm. Chem.* 31: 119–137, 1998
Roscoe, H.K. and K.C. Clemitshaw. Measurement techniques in gas-phase tropospheric chemistry: A selective view of the past, present, and future. *Science* 276: 1065-1072, 1997
Schoulepnikoff, L., H. van den Bergh, B. Calpini and V. Mitev. Tropospheric air pollution monitoring, LIDAR. **In** R.A. Meyers (ed), Encyclopedia of environmental analysis and remediation, Wiley, Chichester (UK), 1998:
Seinfeld, J.H. and S.N. Pandis. Atmospheric chemistry and physics: From air pollution to climate change. Wiley, New York, 1998
Sigrist, M.W. (ed). Air monitoring by spectrosocopic techniques. Wiley, New York, 1993
Solberg, S., C. Dye, S.-E. Walker and D. Simpson. Long-term measurements and model calculations of formaldehyde at rural European monitoring sites. *Atmos. Environ.* 35: 195-207, 2001
Streit, G.E. and F. Guzman. Mexico City air quality: Progress of an international collaborative project to define air quality management options. *Atmos. Environ.* 30 (5): 723-733, 1996
Stutz, J. Messung der Konzentration troposphärischer Spurensstoffe mittels Differentieller-Optischer-Absorptionsspektroskopie: Eine neue Generation von Geräten und Algorithmen. Ph.D. Thesis, Ruprecht-Karls-Universität, Heidelberg, 1996
Thielmann, A. Sensivity of ozone production derived from field mesurements in the Po basin. Ph.D. Thesis, ETHZ, Zurich, 2000
Wagner, V., R. von Glasow, H. Fischer and P.J. Crutzen. Are CH_2O measurements in the marine boundary layer suitable for testing the current understanding of CH_4 photooxidation?: A model study. *J. Geophys. Res.* 107 (D3): ACH 3 1-14, 2002
Wang, Y. and D.J. Jacob. Antropogenic forcing on tropospheric O_3 and OH since preindustrial times. *J. Geophys. Res.* 103 (31): 123-131, 1998
Warneck, P. Chemistry of the natural atmosphere. Academic Press, San Diego, 1988
Wert, B.P., M. Trainer, A. Fried, T.B. Ryerson, B. Henry, W. Potter, W.M. Angevine, E. Atlas, S.G. Donnelly, F.C. Fehsenfeld, G.J. Frost, P.D. Goldan, A. Hansel, J.S. Holloway, G. Hubler, W.C. Kuster, D.K. Nicks, J.A. Neuman, D.D. Parrish, S. Schauffler, J. Stutz, D.T. Sueper, C. Wiedinmyer and A. Wisthaler. Signatures of terminal alkene oxidation in airborne formaldehyde measurements during TexAQS 2000. *Journal of Geophysical Research* 108 (D3): ACH 8 1-14, 2003
WHO. Guidelines for air quality. World Health Organization, Geneva, 2000
Yu, T.Y. and L.F.W. Chang. Delineation of air-quality basins utilizing multivariate statistical methods in Taiwan. *Atmos. Environ.* 35: 3155-3166, 2001

"… use of the ratio of solar intensities at such wavelengths to determine the NO_2 abundance can present difficulties, since the ratio in absence of NO_2 must be known accurately. We have pursued the problem by making complete scans in the region 4350 to 4500 Å. With the full spectrum the identification of the absorber is unambiguous, and by making measurements under a variety of conditions it is possible to separately determine the tropospheric and stratospheric NO_2 abundances from ground-based measurements alone"
J.F. Noxon, 1975
*(Nitrogen dioxide in the stratosphere and troposphere measured by ground-based absorption spectroscopy, Science **189**:547-549)*

Chapter 3
Differential Absorption Spectroscopy Fundamentals

The trace gas detection techniques developed and applied in this research are based on the physical phenomenon of light absorption. This chapter provides a summary of the fundamentals of molecular absorption spectroscopy, including a derivation of the Beer-Lambert-Bouger (BLB) law from quantum mechanics principles. Important concepts for the practical application of spectroscopy to the detection of trace gases, such as lineshape, convolution, and instrument function are reviewed. Relevant atmospheric light scattering phenomena are briefly introduced. Finally, this chapter provides an insightful discussion of the differential absorption concept and its practical application. This chapter settles the theoretical foundations of the differential absorption spectroscopy techniques developed (Chapters 4 and 5) and applied (Chapter 6) in this research.

3.1 Absorption spectroscopy

The *Born-Oppenheimer approximation* states that electrons move so rapidly with respect to vibrating nuclei that their movement can be appropriately referred to nuclear coordinates only (Harris, 1989; Hollas, 1996). Applied to the Schrödinger equation, this approximation implies that the total energy of a molecule can be split into various energy terms related to the motion of nuclei (rotational, vibrational), and of electrons referred to nuclei,

$$E = E_R + E_V + E_{ES} \qquad \text{(Equation 3-1)}$$

The last term (subscript ES) accounts for electronic translational and rotational (spin) energies, and subscripts R, and V stand for rotational and vibrational motions, respectively[1]. An outstanding implication of this approximation is that light-matter (i.e. spectroscopic) interactions leading to each type of motions can be analyzed independently from each other. In practice, only rotational transitions can be treated in an isolated way. Molecular transitions of higher energy usually imply coupling of various types of motions: vibrational transitions are in general accompanied by changes of rotational levels (rovibrational transitions), and molecular electronic transitions are usually coupled to changes in rotational and vibrational levels (rovibronic transitions), as shown for instance in **Figure 3-1** for nitric oxide (NO).

Light absorption is an *inelastic* light-matter interaction in which the transition of an atom[2] or molecule from a lower (E_1) to an upper (E_2) energy level is *induced* by a photon[3]. Absorption occurs only if the photon frequency (ν) is close enough to the transition resonance frequency (ν_0) as defined by the Planck equation, $\nu \approx \nu_0 = (E_2 - E_1)/h$ (frequency distributions are described in **Section 3.3**).

The rate and fate of the transition between two atomic or molecular energy levels depends on the relative occupation of these energy levels as described by the Boltzmann distribution[4] under thermal equilibrium conditions (Saleh, 1991),

$$\frac{N_2}{N_1} = \frac{g_2}{g_1}\exp\left(-\frac{E_2 - E_1}{k_B T}\right) \qquad \text{(Equation 3-2)}$$

[1] The translational energy term has been intentionally omitted. This term is indicative of the motion of the molecule as a whole referred to an external observer

[2] In absence of bond, atoms cannot display rotational or vibrational transitions

[3] Stimulated emission is a photon-induced transition as well

[4] Thermal equilibrium state partitioning of semiconductors obeys the Fermi-Dirac distribution (Saleh, 1991)

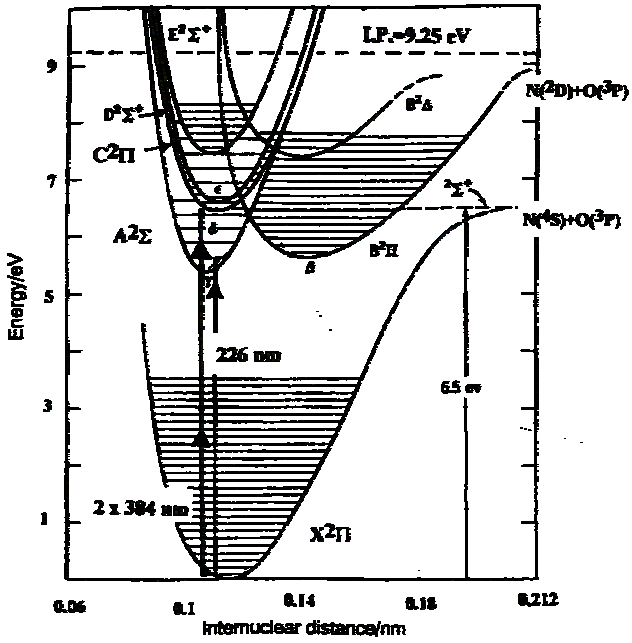

Figure 3-1. Potential energy diagram for nitric oxide (NO). The diagram shows the ground state ($X^2\Pi$) and several excited states along with the transitions $A^2\Sigma(\upsilon=0) \leftarrow X^2\Pi(\upsilon=0)$ and $C^2\Pi(\upsilon=0) \leftarrow X^2\Pi(\upsilon=0)$ obtained with frequency-doubled lasers. Note the photodissociation levels at 6.5 and 9.25 eV leading to nitrogen at ground and excited states, N(^{4}S) and N(^{2}D), respectively (Peng, 1995).

where N_1 and N_2 are the number densities (concentrations) of atoms or molecules at the lower (E_1) and upper (E_2) energy levels. The degeneracy terms, g_1 and g_2, are the number of states that have the same energy level, E_1 or E_2, respectively.

The Boltzmann distribution implies that high energy levels become increasingly populated as the temperature augments and the transition energy ($\Delta E = E_2 - E_1$) diminishes. Consequently, at ambient temperature, rotational levels are heavily populated but most atoms and molecules are at their ground electronic levels.

The classical electromagnetic theory establishes that only molecules with an uneven distribution of charges, i.e. an *electric dipole moment* ($\vec{\mu}$), whether permanent or transitory upon deformation, can absorb energy from an electromagnetic wave (light) upon resonant oscillation. In consequence, the strength of an atomic or molecular transition between the two stationary states, with wavefunctions ψ_1 and ψ_2, is determined by the *transition moment integral* ($\vec{R}_{21}$) over the wavefunction volume (dV),

$$\vec{R}_{12} = \int \psi_2^* \, \vec{\mu} \, \psi_1 \cdot dV \qquad \text{(Equation 3-3)}$$

During the transition period, the wavefunction is a linear combination of the two stationary state wavefunctions, i.e. $\psi = a_1\psi_1 + a_2\psi_2$. The $2 \leftarrow 1$ transition probability, as determined by the upper state wavefunction coefficient is $p_{21} = a_2^* a_2$. If the atom or molecule is irradiated with a broadband polychromatic source with frequencies near the resonance frequency, it can be demonstrated that p_{21} is proportional to the magnitude square of transition moment, $\left\|\vec{R}_{12}\right\|^2$, and to the amplitude square of the (electromagnetic radiation) oscillating electric field, $\boldsymbol{\varepsilon}_0^2$. This last variable is proportional to radiation intensity, I (energy per unit area and time), thus the initial rate at which the upper energy level is occupied upon irradiation,

$$\frac{d(p_{21})}{dt} \sim I\left\|\vec{R}_{12}\right\|^2 \qquad \text{(Equation 3-4)}$$

is proportional to the light intensity and to the magnitude square of transition moment integral (Harris, 1989). Therefore, a transition requires $\left\|\vec{R}_{12}\right\|^2 > 0$ to be allowed. The derivation of the Beer-Lambert-Bouger (BLB) law in **Section 3.2** from an equation homologous to **Equation 3-4** implies that the absorption cross section is proportional to the magnitude square of the transition moment integral.

3.1.1 Rotational and vibrational spectroscopy

Purely rotational transitions are induced by long wavelength radiation within ~0.5-300 mm (~1-600 GHz), i.e. ranging from the far infrared (IR) to the microwave and millimeter wave regions. This range correspond to photon energies from ~4 μeV to ~2 meV.

The solution of the Schrödinger equation for a *rigid rotor*[5] leads to rotational energy (E_R) quantized according to the *rotational quantum number*, $J = 0,1,2,\ldots$,

$$\tilde{E}_R(J) = \frac{E_{R,J}(J)}{h \cdot \boldsymbol{c}} = B \cdot J(J+1) \qquad \text{(Equation 3-5)}$$

where $\tilde{E}_R$ are the rotational term values (expressed as wavenumbers), $\boldsymbol{c}$ is the speed of light in the medium, and $B = h/\left(8\pi^2 \cdot \boldsymbol{c} \cdot I_R\right)$ is the rotational constant. $I_R = m_{AB} \cdot r^2$ is the molecule's moment of inertia, $m_{AB} = m_A \cdot m_B/(m_A + m_B)$ is the reduced mass of the molecule (composed of atoms A and B), and r is the internuclear distance. Space quantization of the rotational angular momentum implies that the rotational levels are (2J+1)-fold

[5] The molecular bond of a diatomic molecule is fairly well represented as a rigid, weightless rod (rigid rotor approximation). This representation is suitable too for linear polyatomic molecules, for which the rigid rotor is the axis between the end point nuclei

degenerate in absence of an external electric[6] or magnetic field. The relevant *rotational selection rules* derived from the transition moment integral are: (1) $\vec{\mu} \neq 0$; (2) $\Delta J = \pm 1$. Rule 1 implies that homonuclear (e.g. O_2, N_2), and "symmetric" linear polyatomic molecules, such as $S = C = S$ and $H - C \equiv C - H$, do not display rotational transitions[7].

Introduction of Rule 2 $(\Delta J = 1)$ * into **Equation 3-5** gives the rotational transition wavenumbers,

$$\tilde{\nu}_{J+1 \leftarrow J} = \tilde{E}_R(J+1) - \tilde{E}_R(J) = 2B \cdot (J+1) \qquad \text{(Equation 3-6)}$$

where J is used conventionally instead of J″ ♣. This equation indicates that rotational transitions are equally spaced $(\Delta\tilde{\nu} = 2B)$, and entails that *isotopomers*, i.e. molecules differentiable only by their isotopic composition, display slightly different rotational spectra, due to the dependence of the rotational constant on the molecular weight. Equation 3-6 entails as well. According the Boltzmann equation, the combined effect of the (2J+1)-degeneracy and the dependence on J of the transition energy (Equation 3-6) makes that the maximum population, and in consequence the strongest transitions to appear at $J'' > 0$.

The transition spacing decreases slightly with J, i.e. with increasing rotational speeds, due to centrifugal stretching of the molecular bond. Rotational transition wavenumbers are thus better represented by $\tilde{\nu}_{J+1 \leftarrow J} = 2B \cdot (J+1) - 4D \cdot (J+1)^3$, where $D \approx 4B^3/\omega^2$ is the centrifugal distortion constant, a parameter that depends on the stiffness of the bond, thus negatively on the (harmonic approximation) vibration wavenumber (ω) (Harris, 1989; Hollas, 1996).

The rotational spectra of *asymmetric rotor* molecules, e.g. ozone (described below), is of increasing complexity, and may require up to two additional quantum numbers, associated with the moment of inertia on the perpendicular axes, for appropriate description.

Vibrational transitions are induced by electromagnetic radiation ranging from the near to the far infrared (~0.77-500 μm). Photon energies in this range vary from ~2 meV to ~2 eV.

The potential energy (***V***) of a classical *harmonic oscillator*[8] is a parabolic function of the oscillator length, r, with a minimum at the equilibrium length, r_e, i.e. $\boldsymbol{V}(r) = \frac{1}{2} k_V \cdot (r - r_e)^2$. The solution of the Schrödinger equation for a vibrating diatomic molecule treated as a harmonic oscillator leads to vibrational energy levels (E_V) quantized according to the vibrational quantum number, $\upsilon = 0, 1, 2, \ldots$,

---

[6] The splitting of the rotational levels into (J+1) components in the presence of an electric field is known as the Stark effect

[7] Homonuclear and "symmetric" linear molecules still can display dipole-induced (Raman) rotational transitions.

* ΔJ = - 1 has no physical meaning

♣ Rotational transitions are conventionally notated as J′←J″, where J″ and J′ are the lower and upper rotational states, respectively

[8] A ball-and-spring oscillating system that obeys Hooke's law

$$\tilde{E}_V(\upsilon) = \frac{E_V(\upsilon)}{h \cdot \boldsymbol{c}} = \omega \cdot \left(\upsilon + \tfrac{1}{2}\right) \qquad \text{(Equation 3-7)}$$

Where $\tilde{E}_V$ are the vibrational term values (expressed in terms of wavenumbers), and ω is the harmonic oscillator *fundamental vibration* wavenumber, $\omega = 1/(2\pi \boldsymbol{c})\sqrt{k_V/m_{AB}}$. The force constant, k_V, is indicative of the stiffness of the molecular bond. Despite k_V insensitiveness to isotopic substitution (Hollas, 1996), the negative dependence of ω on the reduced mass, m_{AB}, implies that isotopomers display distinctive fundamental vibration frequencies.

As for the rotational case, vibrational transitions are allowed only if the permanent electric dipole moment is non-zero ($\vec{\mu} \neq 0$), which implies that homonuclear diatomic molecules are inactive regarding infrared absorption[9]. Heteronuclear diatomic molecules have a bond length (r) dependent, non-zero $\vec{\mu}$. This variation can be expressed through a two-term truncated Taylor series, $\vec{\mu} \approx \vec{\mu}_e + (d\vec{\mu}/dr)_e \cdot (r - r_e)$, which leads to a simplified expression of the transition moment integral,

$$\vec{R}_{12} \approx \left(\frac{d\vec{\mu}}{dr}\right)_e \cdot \int \psi_2^* \cdot r \cdot \psi_1 \cdot dr \qquad \text{(Equation 3-8)}$$

The resulting selection rule is $\Delta\upsilon = \pm 1$. The *vibrational selection rules* for absorption are thus: (1) $\vec{\mu} \neq 0$; (2) $\Delta\upsilon = 1$; (3) $(d\vec{\mu}/dr)_e \neq 0$, i.e. the maximum of the electric dipole moment must not occur at the bond equilibrium length.

According to the harmonic oscillator approximation (**Equation 3-7**), Rule 2 implies that all allowed vibrational transitions would be induced by radiation of the same wavenumber, ω. Anharmonicity effects impede this spectral indetermination to happen. The electric dipole moment is a linear function of the bond length only in the vicinity of the equilibrium length (electrical anharmonicity) thus allowed transitions are $\Delta\upsilon = \pm 1, \pm 2, \pm 3, \ldots$. This non-linearity is usually small, therefore the vibrational *overtones*, i.e. $|\Delta\upsilon| > 1$, are usually weak. In addition, the potential energy of real molecules increases in a sharper-than-parabolic fashion as $r \to 0$, and flattens asymptotically until reaching the dissociation energy as $r \to \infty$ (mechanical anharmonicity). A real-world potential well is shown in **Figure 3-1**. Anharmonic behavior is expressed through a power series of $\upsilon + \frac{1}{2}$ (here truncated to 3 terms),

$$\tilde{E}_V(\upsilon) \cong \omega_e \cdot \left(\upsilon + \tfrac{1}{2}\right) - \omega_e x_e \cdot \left(\upsilon + \tfrac{1}{2}\right)^2 + \omega_e y_e \cdot \left(\upsilon + \tfrac{1}{2}\right)^3 \qquad \text{(Equation 3-9)}$$

[9] Homonuclear molecules can still display dipole-induced (Raman) vibrational transitions

where ω_e is the harmonic oscillator vibration wavenumber, and $\omega_e x_e > 0$ and $\omega_e y_e$ are the second and third order anharmonic constants, respectively (Hollas, 1996). Since $\omega_e x_e$ is always positive, the energy levels close up, and the frequency of fundamental ($\Delta\upsilon = \pm 1$) vibrational transitions, $\tilde{\nu}_{\upsilon+1\leftarrow\upsilon} \approx \omega_e - 2\omega_e x_e \cdot (\upsilon + 1)$, diminish with increasing υ.

As mentioned at the beginning of this section, there is a stack of rotational transitions associated to each vibrational level, thus vibrational transitions are in general accompanied by changes in rotational levels (*rovibrational transitions*). According to the Born-Oppenheimer approximation, vibrational and rotational term values add up to form rovibrational term values, $\tilde{E}_{VR}$,

$$\begin{aligned}\tilde{E}_{VR}(\upsilon, J) &= \tilde{E}_V(\upsilon) + \tilde{E}_R(J, \upsilon) \\ &\cong \omega_e \cdot \left(\upsilon + \tfrac{1}{2}\right) - \omega_e x_e \cdot \left(\upsilon + \tfrac{1}{2}\right)^2 + B_\upsilon \cdot J(J+1) - D_\upsilon \cdot J^2 (J+1)^2\end{aligned} \qquad \text{(Equation 3-10)}$$

The rotational constants, B_υ and D_υ, are both slightly vibrational dependent (Hollas, 1996). The rovibrational selection rules result from the combination of the basic rules for vibrational ($\Delta\upsilon = \pm 1$) and rotational ($\Delta J = \pm 1$) transitions. Purely vibrational transitions ($\Delta J = 0$), although forbidden in principle, are observed in some cases[10]. In addition, anharmonicity implies that vibrational overtones are observed as well. A *rovibrational band* is thus composed by three branches: P, Q, and R corresponding to $\Delta J = -1, 0, 1$, respectively[11]. Assuming that $B_\upsilon \approx B$, and neglecting centrifugal distortion and the anharmonic terms, **Equation 3-10** implies, for instance, that P-branch transitions have wavenumbers $\tilde{\nu}_{P(J)} \approx \omega_0 - 2B \cdot J$, where ω_0 is vibration wavenumber of the pure vibrational transition and J is the lower state rotational quantum number. As for the purely rotational transitions, the Boltzmann distribution entails that the strongest transitions occur at J > 0 values.

The molecular vibrational behavior entangles as the number of bonded atoms (***N***) increases. The number of *normal vibrational modes*[12] of linear and non-linear polyatomic molecules are $3\boldsymbol{N} - 5$ and $3\boldsymbol{N} - 6$, respectively. The vibrational term values associated with each normal vibrational mode, $\tilde{E}_V(\upsilon_i) \approx \omega_i \cdot (\upsilon_i + d_i/2)$, take into account a possible degree of degeneracy (d_i). υ_i and ω_i are the vibrational mode quantum number and wavenumber, respectively (Harris, 1989; Hollas, 1996).

The vibrational selection rule as above apply ($\Delta\upsilon_i = \pm 1, \pm 2, \pm 3, \ldots$) with overtones allowed but generally weak. *Combination tones*[13] occur as well. Overtones and combination tone transitions are in general induced by photons of higher energy than single vibrational mode

[10] The electronic angular momentum in the ground electronic state must be non-zero as e.g. for NO

[11] Rovibrational transitions are labeled according to the branch and the lower vibrational state, e.g. P(20) indicating for J′ = 19 ← J″ = 20 between two vibrational levels

[12] In a normal mode of vibration, all nuclei move harmonically, in phase, and at the same frequency but generally with different amplitudes

[13] Transitions to vibrational excited states in which more than one normal vibration is excited

transitions. Most of these transitions are thus observed in the near-IR (0.77-2.5 μm) (Barton, 2002). Polyatomic vibrational transitions are notated whether by displaying all the vibrational quantum numbers, e.g. $(\upsilon_1'\upsilon_2'\ldots)\leftarrow(\upsilon_1''\upsilon_2''\ldots)$, or only those actually involved in the transition, e.g. 2_0^2 indicating for a $2\leftarrow 0$ transition of the second vibrational mode (υ_2). Changes in rotational quantum number are labeled according to their branch, as explained above[14].

Ozone provides a valuable example (see **Figure 3-2**). Quantitative detection of this trace gas was demonstrated in this research using a ~9.6 μm mid-IR quantum-cascade laser (QCL). Temperature tuning of this laser allowed scanning (~6 cm^{-1}) a significant part of the R-branch of the υ_3 rovibrational band of O_3 (see Chapter 5). Ozone is a non-linear molecule (***N*** = 3) with 3 normal vibrational modes: symmetric stretching (υ_1), bending, (υ_2), and asymmetric stretching (υ_3). As expected from its higher transition moment (see **Equation 3-8**), υ_3 is the strongest rovibrational band. The centers (i.e. the Q branch[15]) of the most intense absorption bands of the $^{16}O_3$ molecule are in decreasing intensity order: υ_3 1042 cm^{-1}, $\upsilon_1+\upsilon_3$ 2111 cm^{-1}, υ_2 701 cm^{-1}, υ_1 1103 cm^{-1}, and $\upsilon_2+\upsilon_3-\upsilon_2$[16] 1026 cm^{-1}. $^{16}O_3$ is a slightly asymmetric top rotor, $I_c \approx I_b > I_a$ (Ivanov, 1994). This implies that besides J, rovibrational transitions require the rotational number K_a and K_c to be appropriately defined (see **Figure 3-3**).
Symmetric vibrations in "symmetric" linear molecules, such as υ_1 in symmetric CO_2 isotopomers, are IR inactive since the dipole moment does not change upon this vibrational motion. On the other hand asymmetric stretching, bending and symmetric stretching in symmetric CO_2 isotopomers are IR active (Devi, 1996).

Polyatomic molecules with ***N*** > 3 display complex vibrational modes, including twisting, scissoring, and tunneling between e.g. cis- and trans- states (Harris, 1989; Hollas, 1996; Steinfeld, 1993).

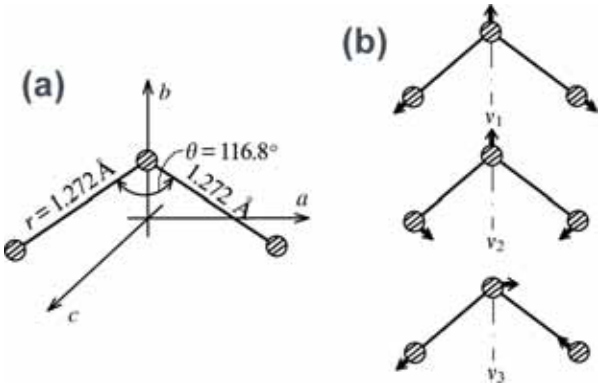

Figure 3-2. (a) Equilibrium geometry (electronic ground state) and **(b)** normal vibrational modes of the $^{16}O_3$ molecule (υ_1: symmetric stretching, υ_2: bending, υ_3: asymmetric stretching). $^{16}O_3$ is a slightly asymmetric top rotor, and the most abundant (99.29%) ozone isotopomer (Ivanov, 1994).

[14] An interesting example of overtone plus combination tone transitions is given in Chapter 5. Various $00^01\leftarrow 02^00$, 9P-branch transitions of the CO_2 molecule were used for calibrating the wavelength of a quantum-cascade laser (QCL)

[15] In the case of single vibrational modes, these vibrational wavenumbers are approximately the fundamental, ϖ_i.

[16] Alternative notation for the band (011)← (010).

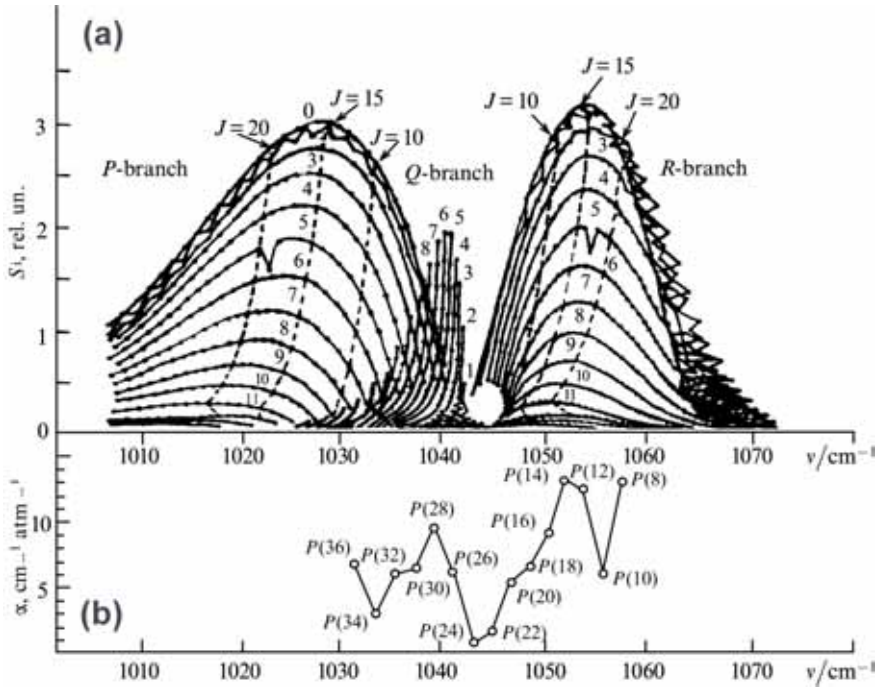

Figure 3-3. (a) Rotational structure of the υ_3 $(001 \leftarrow 000)$ rovibrational band of the $^{16}O_3$ molecule. The abscissa and ordinate are respectively the wavenumber and strength of the rovibrational transition. The P-, Q-, and R-branches (ΔJ = -1, 0, and 1, respectively) of the band are shown with J indicating the lower state rotational (total angular momentum) quantum number, i.e. J''. The numbers on the curves indicate the quantum number K_a, i.e. projection of J on the axis of I_a ($\Delta K_a = 0$). Note the systematic drift of the transitions to higher frequencies with decreasing K_a. **(b)** Ozone absorption coefficient as measured with a CO_2 laser (9P branch). As expected, the transition strength peaks within the R-branch (Barbe, 1977; Ivanov, 1994).

3.1.2 Electronic spectroscopy

Photons with energies of some eV are capable of inducing transitions between two electronic distribution states, i.e. between two electronic potential wells (see **Figure 3-1**). The detection of various traces gases was investigated in this research using absorption spectra from the near ultraviolet (UV) to the visible spectral regions, 200-770 nm (~2-6 eV). Photons in this range are energetic enough to produce extensive relocation of the electrons in a molecule, and eventually photodissociation. Electron relocation may cause vibrational and rotational motion as well. In consequence, *electronic bands* often include a large number of rovibrational transitions that in many cases cannot be resolved experimentally. This is particularly true in the liquid and solid states, in which electronic bands are usually featureless. The gas phase is thus better adapted for quantitative detection in the UV-visible.

The electronic state of a molecule is determined by scalar variables derived from the three following quantized vectorial variables: the total electronic orbital angular momentum, ***L***, the total spin quantum number (electron net spin), ***S***, and the total angular momentum (orbital plus electron spin), $\boldsymbol{J} = \boldsymbol{L} + \boldsymbol{S}$. The quantum numbers derived from these variables, Λ[17], Σ, and Ω, respectively, are the scalar components of the vectorial quantities along the internuclear axis (in the case of diatomic molecules). Allowed values of $\Lambda = 0,1,2,3,\ldots$ are designated in a homologous way to the atomic ***L*** number but with Greek characters, i.e. $\Lambda = \Sigma, \Pi, \Delta, \Phi, \ldots$. Allowed values of $\Sigma = \mathrm{S}, \mathrm{S}-1, \ldots -\mathrm{S}$ entail a *spin multiplicity* of $2\mathrm{S}+1$. The electron net spin quantum number (S) can take values $\mathrm{S} = 0, \frac{1}{2}, 1$, which translate into spin multiplicities of 1, 2, or 3, respectively. These values are referred as singlet[18], doublet and triplet, respectively. The quantum number that designates the component along the internuclear axis of the total angular momentum is calculated as $\Omega = |\Lambda + \Sigma|$. This quantum number determines for instance if the Q branch ($\Delta \mathrm{J} = 0$) is observed or not in rovibronic transitions (see below).

Electronic states of diatomic molecules are notated[19] as ${}^{2\mathrm{S}+1}\Lambda^{\{\pm\}}_{\{\Omega\}\{\mathrm{g,u}\}}$, where the subscripts "g" and "u", and the superscript ± indicate the symmetry of the electronic wavefunction[20] (Finlayson-Pitts, 2000; Harris, 1989; Hollas, 1996). The electronic states of polyatomic and most heteronuclear diatomic molecules are labeled in a similar way: the ground state is labeled X, and higher energy states of the same multiplicity are indicated with capitals $\mathrm{A, B, C}, \ldots$ in order of increasing energy. Lower case letters $\mathrm{a, b, c}, \ldots$ are used to indicate $\Delta \mathrm{S} \neq 0$ (relevant examples are given in **Table 3-1**).

Concerning the Λ, Σ, and Ω quantum numbers, the *electronic selection rules* for diatomic molecules are (1) $\Delta\Lambda = 0, \pm 1$, and (2) $\Delta \mathrm{S} = 0$. The second rule implies that $\Delta\Sigma = 0$, thus $\Delta\Omega = 0,1$. Concerning the symmetry, (3) $+ \leftarrow +$ or $- \leftarrow -$, and (4) parity changing ($\mathrm{g} \leftrightarrow \mathrm{u}$) are the only transitions allowed. Electronic transition rules are less tightly respected than the rotational or vibrational ones. For instance, the $\mathrm{A}\,{}^3\Sigma_\mathrm{u}^+ \leftarrow \mathrm{X}\,{}^3\Sigma_\mathrm{g}^-$ transition of the O_2 molecule, in principle forbidden because of the $+ \leftarrow -$ transition, does occur weakly. As a matter of fact, this transition band (Herzberg I) is readily observable over long atmospheric paths (> 50 m) due to the elevated concentration of O_2 in the atmosphere. The Herzberg I band is actually a strong spectral interference to the open-path spectroscopic detection of monocyclic aromatic compounds (MAH) (Jiménez, 2000; Volkamer, 1998). Field measurements are presented in **Section 6.2**.

A *rovibronic band* is constituted by a set of transitions between vibrational and rotational levels of two electronic potential wells. Vibronic transitions are not tied to the $\Delta\upsilon = \pm 1$

[17] All Λ>0 electronic states are doubly degenerate due to clockwise/anticlockwise electron orbiting.

[18] Most common ground state of stable molecules. An important exception is O_2, a triplet in the ground state.

[19] Parameters in brackets are not always necessary for a full description of the electronic state.

[20] The ± superscript denotes whether symmetry (+) or asymmetry (-) of the electronic wavefunction under reflection in a plane containing the nuclei. The "g" and "u" subscripts (parity) apply to homonuclear diatomic only and denote symmetry and asymmetry, respectively, to inversion through the center of the molecule.

selection rule[21] but are nevertheless strength-limited according to the *Franck-Condon principle*[22]. The strongest vibronic band is in general the one that lead to smallest change of the nuclei position and momentum, and the highest wavefunction overlapping. Since in most cases $\upsilon'' = 0$ thus $r'' \approx r_e''$ in the ground electronic state, the strongest transition is very likely the one for which $r' \approx r_e''$, which in many cases corresponds to the left endpoint ($r' < r_e'$) of the excited state potential energy well (see **Figure 3-1**). Vibronic bands that share a common lower or upper vibrational level are referred as *progressions*, and those with $\Delta\upsilon = 0$ as *sequences*. The frequency gap between subsequent vibronic bands in a progression is $\sim \omega_e'$ or $\sim \omega_e''$, depending whether the spectrum is one of absorption or emission. Sequences are more tightly packed, and the spacing is $\sim \left|\omega_e' - \omega_e''\right|$. **Figure 3-4** shows the vibronic bands (progressions) of the $A^1A'' \leftarrow X^1A'$ electronic transition of the trans- and cis-HONO, including the trans-HONO $2_0^{\upsilon'}4_0^1$ combination tone. In this case, according to the Franck-Condon principle, the maximum strength is observed for $\upsilon_2' = 2$ of the trans-HONO $2_0^{\upsilon'}$ vibronic band.

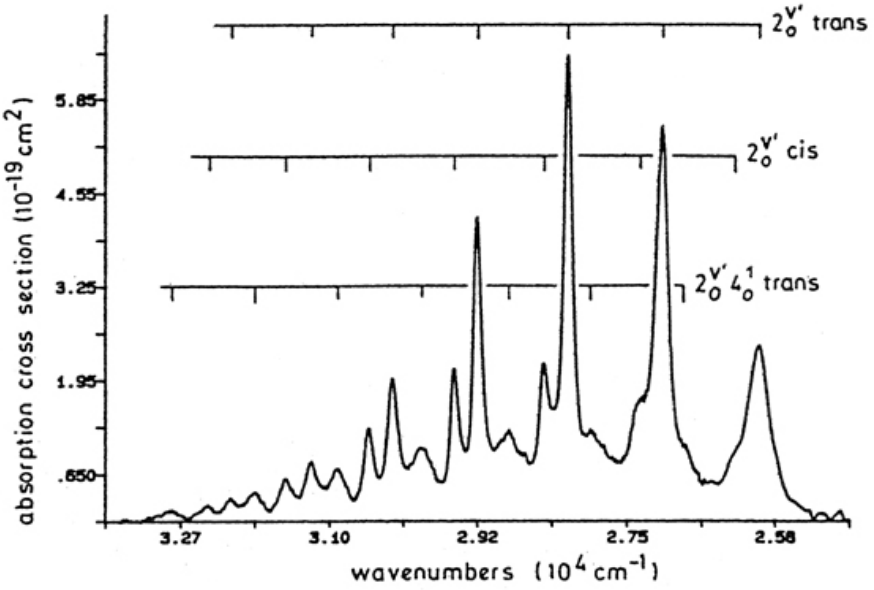

Figure 3-4. Experimentally measured cross section of nitrous acid (HONO) and spectral assignment of the $2_0^{\upsilon'}$ and $2_0^{\upsilon'}4_0^1$ vibronic bands (progressions) of the *trans*- and *cis*-HONO (Bongartz, 1991). Note that the rotational structure remains unresolved at the resolution of the spectrum (0.1 nm FWHM).

[21] On the contrary, the rovibrational selection rule still applies in most cases, thus in general P, Q and R branches take place within each vibronic band. Purely vibronic transitions ($\Delta J = 0$) are not observed in diatomics if $\Omega = 0$ in both electronic states.

[22] The Franck-Condon principle states that electronic transitions are so fast (~10^{-15} s) compared to nuclear motion (~10^{-13} s) that, during the vibronic transition, the nuclei nearly conserves their positions and momentum.

Despite of the growing complexity of the rovibronic transitions as the number of atoms increases, most polyatomic molecules still tie to the electron net spin conservation rule, $\Delta S = 0$. The overlapping of a large number of transitions has practical consequences. Vibronic progressions and sequences are in general discernible but the rotational structure remains in many cases unresolved, even when using high-resolution spectrometers. The spectrum in **Figure 3-4** is an example. In these conditions, individual rovibronic transitions cannot be fully assigned and characterized. In consequence, most UV-visible absorption cross sections are available in tabular form only. The lack of spectral information impedes the calculation of synthetic spectra on a line-per-line basis, as it is made in the IR using for instance the HITRAN database (see **Section 3.4**).

It is worth mentioning that is the structure that result from the vibronic transition what allows detection in the DOAS technique. Heavy polyatomic molecules display strong overlapping of a very large number of bands, which in general impedes their detection using differential absorption. This adds to the fact that heavy molecules have in general very short lifetimes in the atmosphere, thus their concentration is in general too small to allow for direct spectroscopic detection.

3.2 The Beer-Lambert-Bouger (BLB) law: Light absorption and scattering in the atmosphere

The *Beer-Lambert-Bouger (BLB) law*[23] states that as monochromatic light of wavelength λ traverses a *random,* attenuating medium, the radiant intensity decays exponentially with the optical path length, L, and the extinction or attenuation coefficient, ε (Swanson, 1999),

$$I(\lambda) = I_0(\lambda) \cdot \exp\left[-\varepsilon(\lambda) \cdot L\right] \qquad \text{(Equation 3-11)}$$

where I_0 and I are the radiant intensities at the beginning of the attenuation path (L = 0) and at pathlength L, respectively.

The BLB law can be derived from energy conservation considerations, and under certain simplifying assumptions, from the radiative transport equation (Swanson, 1999). The result is in both cases heuristic. A rigorous derivation that considers only (inelastic) attenuation due to absorption in an idealized 2-level atomic or molecular system is presented here below. Despite of its simplicity, the analysis allows withdrawing conclusions on the limits of the BLB law as applied for the retrieval of concentrations of atmospheric trace gases. Subsequently the BLB law is extended in order to make it accountable for inelastic interactions in an open atmospheric path.

[23] The BLB law was originally formulated by P. Bouger (1698-1758) and J.H. Lambert (1728-1777) as an empirical expression. A. Beer (1825-1863) was the first to use it for the determination of the concentration of an absorbing substance.

Figure 3-5 shows a collimated monochromatic light beam of frequency $\nu = \left(E_2 - E_1\right)/h$ and initial intensity I that undergoes attenuation as passing through a perpendicular slab of infinitesimal thickness $d\ell$ and unit perpendicular area. The slab contains N (number density – $N = N_1 + N_2$) absorbing atoms or molecules (at pressure P and temperature T) split between lower and upper energy levels, E_1 and E_2, respectively. A photon is absorbed per atom or molecule promoted from level 1 to level 2, thus $-dn = dN_2$. As a consequence the beam is attenuated by

$$-dI = \left[\left(dN_2/dt\right)\cdot h\nu\right]\cdot d\ell \qquad \text{(Equation 3-12)}$$

According to Einstein's formulation (Saleh, 1991), the probability rate of absorption (or stimulated emission), $w = \phi\cdot\sigma(\nu)$, is proportional to the photon flux ϕ, $\phi = I/(h\nu)$. $\sigma(\nu)$ is the absorption cross section at the resonance frequency[24]. A key concept for the derivation is the fact that *absorption events are mutually exclusive*, thus the probability rate of transition $2 \leftarrow 1$ is proportional to the number of atoms or molecules in the lower energy level, N_1,

$$\frac{dN_2}{dt} = w\cdot N_1 = \left[\phi\cdot\sigma(\nu)\right]\cdot N_1 \qquad \text{(Equation 3-13)}$$

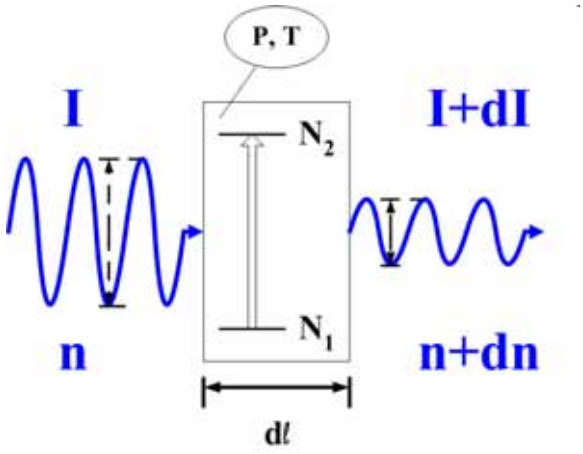

Figure 3-5. Schematic representation of the absorption monochromatic light in a 2-level atomic or molecular system of infinitesimal width $d\ell$. The induced absorption causes no change on the electromagnetic wave frequency but reduces its amplitude ($\varepsilon_0^2 \sim I$). The number of photons (dn < 0) and the radiation intensity (dI < 0) diminish upon absorption. The opposite process, i.e. light amplification, is achieved by inversion of the population followed by stimulated emission in a resonant cavity (laser).

[24] If light is polychromatic, the probability rate, $w = \boldsymbol{B}\cdot\rho_E(\nu)$, is proportional to the energy density per unit bandwidth, $\rho_E(\nu)$, and to Einstein's ***B*** coefficient

Combination of **Equations 3-12** and **3-13** produces $-dI/I = \sigma(\nu)\cdot N_1 \cdot d\ell$. This equation is equal to the BLB law,

$$-dI/I = \sigma(\nu)\cdot N \cdot d\ell \qquad \text{(Equation 3-14)}$$

only if the vast majority of atoms or molecules within the slab are in the lower energy state, i.e. $N_1 \gg N_2$ [♦]. In order to fulfill this condition, the transition $2 \leftarrow 1$ must have a very short lifetime. If this is not the case, the condition can still be fulfilled if the photon flux ϕ is low enough to avoid rapid population of level 2 [♥]. If level 2 depopulates only through spontaneous emission, the theory (Saleh, 1991) predicts longer lifetimes ($t_{1\leftarrow 2}$) for the less favored transitions at long wavelengths ($\lambda = c/\nu$) [♠], since $t_{1\leftarrow 2} = 1/A = \lambda^2/(8\pi\cdot S)$, where A is Einstein's spontaneous emission probability rate ($-dN_2/dt = A\cdot N_2$) and,

$$S = \int_0^\infty \sigma(\nu)\cdot d\nu \qquad \text{(Equation 3-15)}$$

is the strength of the transition $2 \leftarrow 1$ (see **Table 3-1**).

Two types of light sources were used in this investigation: high-pressure Xe lamps in the UV-visible-near IR (200-1200 nm) and a quantum-cascade laser (QCL) in the mid-IR (~9.6 μm). Collimated light beams from these sources have estimated maximum light intensities of ~20 and ~40 W/m^2, respectively[25]. These intensities correspond to photon fluxes of ~5·10^{15} photons/cm^2·s in the 400-600 nm[26] and ~2·10^{17} photons/cm^2·s at ~9.6 μm. These fluxes are too low to induce noticeable population of the excited states. In addition, the absorber concentrations investigated were very low, typically of some ppb, and only exceptionally of some hundred ppm (~3·10^{10}-2·10^{16} molecules/cm^3). In these conditions the populations of the various excited states are negligible ($N_1 \gg N_2$) and the BLB can be applied without restriction.

Integration of **Equation 3-14** for a multiple absorber mixture leads to the classical mathematical expression of the BLB law (see **Equation 3-11**),

---

♦ As assumed to be the case in thermal equilibrium conditions, i.e. before irradiation

♥ At very high photon fluxes, some materials (saturable absorbers) become transparent to radiation due to the depopulation of their ground level ($N_1 \rightarrow 0$)

♠ Excited states in the IR are in general longer lived than in the UV-visible. Excited states are as well several orders of magnitude more populated in the far-IR than in the UV according to Boltzmann's distribution

[25] The QCL used is pulsed operated. The intensity value is thus a time average. Measurements and calculations for the UV-visible and mid-IR are presented in Chapters 4 and 5, respectively

[26] Peak photon flux spectral region of high-pressure Xe lamps.

$$\tau(\nu) = \frac{I(\nu)}{I_0(\nu)} = \exp\left[-\sum_j \sigma_j(\nu) \cdot \int_0^L c_j(\ell)\, d\ell \right] \qquad \text{(Equation 3-16)}$$

where τ is transmittance, and $c_j(\ell)$ is the concentration (number density, $c_j = N_j \cong N_{j,1}$) of the j-th absorber at length ℓ along the absorption path, $0 \le \ell \le L$. The column density of the j-th absorber,

$$\int_0^L c_j(\ell)\, d\ell = \overline{c}_j \cdot L \qquad \text{(Equation 3-17)}$$

is customarily expressed in terms of its average over the path, $\overline{c}_j$, and the absorption pathlength (L). The linearity of the BLB law with respect to absorption by multiple compounds is a consequence of the principle of mutual independence of the absorption events, i.e. mathematically $dN_{j,2}/dt = \phi \cdot \sigma_j(\nu) \cdot N_{j,1}$, where $N_{j,1}$ and $N_{j,2}$ are the number densities of the j-th absorber in its lower and upper energy levels[27], respectively. The BLB law is then derived considering that the attenuation due to each individual absorbers pile up. Comparison with **Equation 3-11** gives the extinction or attenuation coefficient due to absorption[28], ε_A,

$$\varepsilon_A(\nu) = \sum_j \sigma_j(\nu) \cdot c_j \qquad \text{(Equation 3-18)}$$

In this equation and customarily hereafter, path-averaged concentrations, c_j, are written without a top bar (average) character. Introduction of the absorbance or optical density (due to absorption) term[29], $D = -\ln(\tau)$, allows linearizing the BLB law,

$$D(\nu) = -\ln\left[\tau(\nu)\right] = L \cdot \sum_j \sigma_j(\nu) \cdot c_j \qquad \text{(Equation 3-19)}$$

This equation has important implications:

- Concentrations can be derived from transmittance spectra provided that the absorbing compounds and their cross sections are known and the number of wavelengths (spectral channels) used is at least equal to the number of absorbers.

---

[27] The energy levels for absorbers included are separated by $E_{j,2} - E_{j,1} = h\nu$ although absorbers do not necessarily share the same lower level.

[28] Some authors (e.g. Quenzel, 1983) refer to the absorption extinction coefficient as optical density.

[29] D is referred as optical depth or optical thickness by some authors (e.g. Quenzel, 1983).

- When investigating a single absorber, the derivation of a cross section spectrum from transmitted intensity measurements, I(ν), requires accurate knowledge of the baseline intensity, $I_0(\nu)$, the concentration and the optical pathlength. The measurement of the baseline intensity (see Chapter 5) is by far the most common source of error in the cross section determination. The concentration is as well an important problem when dealing with unstable, very reactive, or surface active species.
- If the number of spectral channels used is higher that the number of absorbing compounds, (multiple) linear regression techniques provide a statistically more robust way of retrieving concentrations.

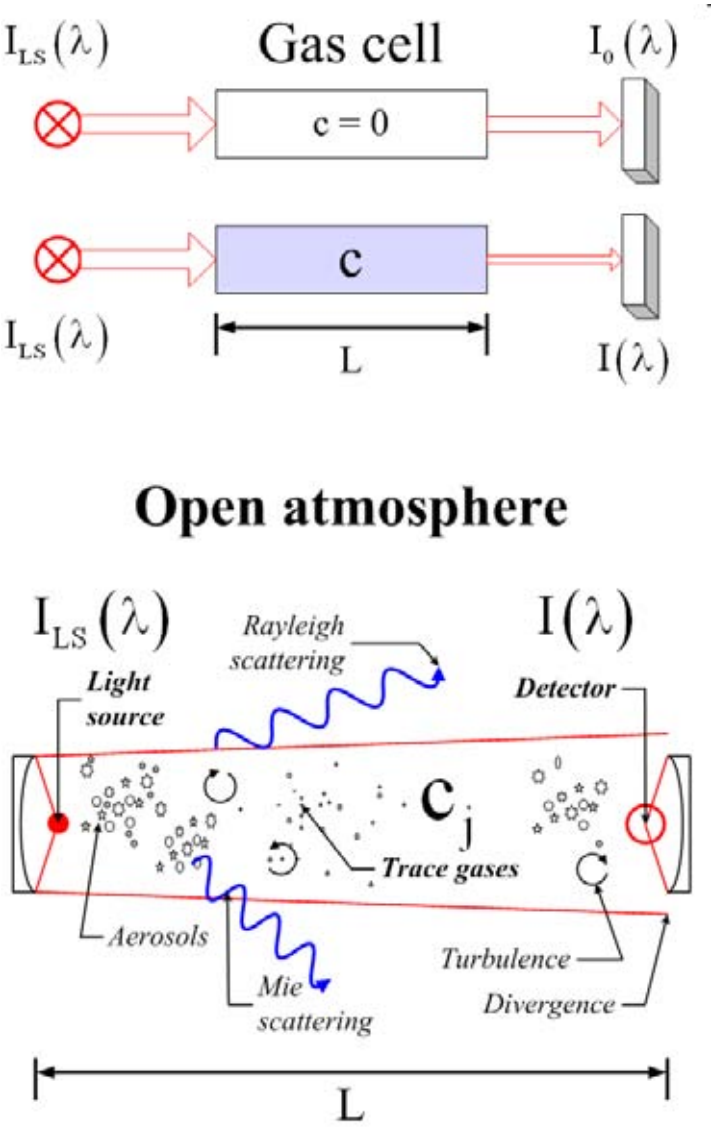

Figure 3-6. Light absorption in closed (**above**) and open (**below**) absorption paths. Light transmission in an open atmospheric path must take into consideration Rayleigh and Mie scattering effects, divergence and the transmission function of the spectroscopic system itself. Rapid variations of the atmospheric refraction index are associated with the turbulence, and require the light detection system to acquire spectra at frequencies above ~10 Hz.

As schematically shown in **Figure 3-6**, optical interfaces (as much as divergence) in a *closed path* system may contribute to the attenuation of the sensing beam (light source) of emitted intensity I_{LS}. Therefore, in practice, the baseline intensity I_0 is operationally defined and determined as the intensity measured in absence of absorption by the target species, the other attenuation terms considered time-invariable. For this reason e.g. the standard procedure in dual beam spectrometers requires "normalization" of the beam intensities, i.e. a previous comparative measurement of intensities between the "baseline" and "absorption" channels in absence of absorption. Single-beam spectroscopic measurements with a standard spectrometer were developed and used in this research for the validation of calibration gas tanks. Detailed information can be found elsewhere (Jiménez, 1998; Szekely, 2000).

Light attenuation in *open atmospheric paths* is a far more complicated phenomenon (see **Figure 3-6**). Besides absorption, a light beam is attenuated in the open atmosphere by elastic scattering phenomena. Neglecting the inelastic term due to atomic or molecular absorption by particles (Finlayson-Pitts, 2000), the extinction coefficient (Quenzel, 1983) in open atmospheric conditions is calculated as follows,

$$\varepsilon(\lambda) = \varepsilon_A(\lambda) + \varepsilon_R(\lambda) + \varepsilon_M(\lambda) \qquad \text{(Equation 3-20)}$$

where ε_R and ε_M are the extinction coefficients due to Rayleigh and Mie scattering, respectively. Rayleigh scattering is essentially due to scattering by N_2 and O_2 molecules, the main constituents of Earth's atmosphere. Rayleigh scattering dependence can be expressed in a simplified way by the following equation,

$$\varepsilon_R(\lambda) \approx \left(\frac{\boldsymbol{a}_R}{\lambda^4}\right) \cdot c_A \qquad \text{(Equation 3-21)}$$

where c_A is the concentration of air molecules ($2.46 \cdot 10^{19}$ molecules/cm^3 at 25 ºC, 1 atm – see **Table 2-1**). The Rayleigh specific "cross section" constant, $\boldsymbol{a}_R$, is ~$4.4 \cdot 10^{-16}$ cm^2·nm^4 for air of standard composition (Plane, 1995; Platt, 1994). As demonstrated below, a more rigorous treatment of the Rayleigh scattering (see e.g. Bodhaine, 1999; Young, 1981) is not required for the purposes of this research. Light scattering due to aerosols is far more complicated than the Rayleigh scattering. As a first approximation the extinction coefficient, ε_M, can be modeled according to Ansgtrom's power law (Iqbal, 1983),

$$\varepsilon_M(\lambda) \approx \beta \cdot \left(\frac{\lambda}{\lambda_0}\right)^{-\alpha} \qquad \text{(Equation 3-22)}$$

where λ_0 is a reference wavelength (usually 1 μm). Angstrom's parameters α and β are associated with the geometry, and number density of the aerosols, respectively. β typically ranges from ~0.1 to ~0.4 km^{-1}, corresponding to clean to highly polluted conditions. α is a

dimensionless power that varies within 0-4, being 1.3 an accepted value for the "average" atmosphere.

Typical extinctions at 300 nm due to Rayleigh and Mie scattering are typically ~0.13 km^{-1} and ~0.1-1 km^{-1}, respectively. **Figure 3-7** shows calculations of attenuation based on the simplified models above. The parametric transmittance curves show the strong dependence of the Rayleigh scattering on the wavelength, and indicate that at high aerosol loads, typical of polluted urban atmospheres, a collimated beam loses more than ~90% of its radiant power at 300 nm in a 1 km long path due to scattering, ~80% of this loss due to aerosol scattering. More important in the application of the differential approach is the fact that the scattering functions vary monotonically and slowly with the wavelength.

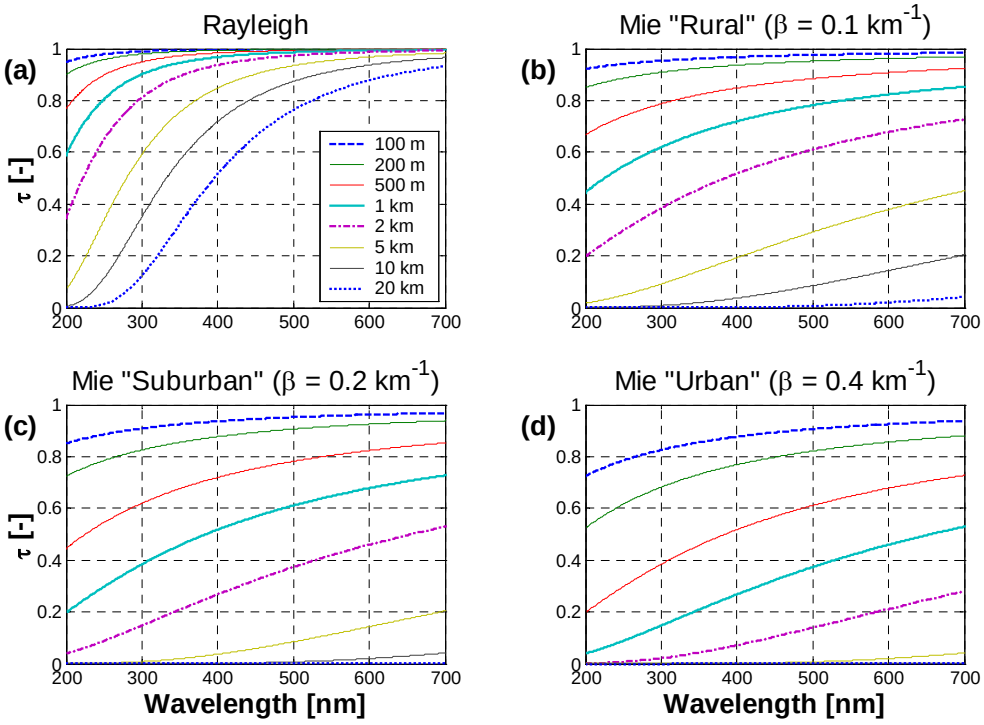

Figure 3-7. Estimated atmospheric transmission due to **(a)** Rayleigh scattering in the 200-700 nm range at various atmospheric path lengths (0.1-20 km). Mie extinction is estimated using a constant α = 1.3, and variable β values typical of **(b)** clean rural, **(c)** suburban, and **(d)** polluted urban atmospheres. The equivalent visibility ranges are 28, 11, and <5 km, respectively.

Besides physical attenuation phenomena, there are losses associated to the collimated beam divergence, the various optical interfaces, and the non-uniform spectral response of the detection systems. These non-physical losses are all grouped into the wavelength dependent transmission function of the system, $0 \le A(\lambda) \le 1$. The transmission equation for an open atmospheric path system is thus,

$$\tau(\lambda) = \frac{I(\lambda)}{I_{LS}(\lambda) \cdot A(\lambda)} = \exp\left\{-L \cdot \left[\varepsilon_M(\lambda) + \varepsilon_R(\lambda) + \sum_j \sigma_j(\lambda) \cdot c_j\right]\right\} \qquad \text{(Equation 3-23)}$$

This equation shows that the retrieval of concentrations from transmitted intensity spectra would require, in principle, a detailed knowledge of the emitted intensity spectra, of the transmission function of the system, and of the concentration and geometrical characteristics of the aerosols within the absorption path (attenuation due to Rayleigh scattering assumed to be a sufficiently well understood phenomenon). In simple terms, the baseline intensity as practice in closed path systems, i.e. the intensity in absence of absorption, is unknown and for practical effects impossible to determine. This would imply that the retrieval of concentrations from transmission measurements in open atmospheric path is in practice an almost impossible to accomplish task. The solution of this dilemma lies on the differential absorption approach, developed in **Section 3.5**.

A final characteristic of the atmosphere is the turbulence. It is commonly stated that atmospheric turbulence at ground level operates in the 1-10 Hz range (Platt, 1994). In order to avoid the perturbation caused by this effect, atmospheric spectra must be recorded (co-added) at frequencies higher than ~10 Hz, whether by using high-speed scanners or multichannel analyzers (MA, e.g. PDA or CCD – see Chapter 4) for the analysis of polychromatic light, or using monochannel detectors for the analysis of tunable pulsed lasers (continuous wave -CW- lasers can be used along with a chopping system) (Schiff, 1994; Zahniser, 2002).

3.3 Lineshape, instrument function and convolution

The absorption cross section σ, as introduced in **Equation 3-16**, is a proportionality term between the fractional transmittance ($-dI/I$) and the column density ($c \cdot L$), i.e. an indicator of the relative absorption per unit pathlength and concentration. As shown in the previous sections, the cross section is a fundamental variable, which is proportional to the transition moment integral thus to the strength of one or various transitions induced by radiation of a given wavelength.

Considering a single, isolated absorption event, one may think of the resulting transition line as an infinitely narrow Dirac-like function at the resonance frequency, ν_0. One may think that other mutually exclusive absorption events should occur at the same frequency, thus conserving the infinitely narrow transition shape. Various physical phenomena impede this to happen:

- Lifetime or natural broadening: the occupation of an excited energy level has a finite lifetime ($t_{1/e}$) that is equal to the inverse of the rate at which its population decays by radiative or non-radiative means[30]. According to Heisenberg's uncertainty principle, this time uncertainty on the occupation of the level implies an uncertainty on the transition energy, which translates into a finite line of halfwidth[31] $\Delta\nu_{min} \geq 1/\left(4\pi \cdot t_{1/e}\right)$ (Hollas, 1996; Saleh, 1991). It can be demonstrated that this frequency spread has a Lorentzian lineshape centered on the resonance frequency (Saleh, 1991). The natural linewidth stems from the quantum mechanics behavior and cannot be avoided. It is nevertheless so narrow that is in general not considered as a source of broadening.
- Collision broadening: inelastic collisions between atoms or molecules result in transitions between energy levels, thus contributing to the natural broadening. On the contrary, elastic collisions do not involve energy transfer but cause random phase shifts of the wavefunction associated with the energy level (Saleh, 1991). In this case, the result is Lorentzian broadening, the linewidth of which is proportional to the collision frequency, $\Delta\nu_L = \nu_{collision}/(2\pi)$, thus to the pressure of the system (Hollas, 1996).
- Doppler broadening: the broadening processes above are homogenous since they act evenly on all atoms or molecules of the system. On the contrary, the translational motion of each individual atom or molecule of the system results in a Doppler frequency shift. The distribution of speeds, described by Maxwell's equation, results in a temperature-dependent spreading of frequencies described by a Gaussian lineshape centered on the resonance frequency, ν_0. The Doppler line halfwidth (HWHM) is $\Delta\nu_D = \sqrt{2 \cdot \ln 2} \cdot \boldsymbol{\sigma}_D$, where $\boldsymbol{\sigma}_D = \tilde{\nu}_0 \cdot \sqrt{k_B \cdot T/MW}$ is the standard deviation of the Gaussian distribution ($\tilde{\nu}_0$ is the resonance wavenumber, and MW is the molecular weight of the atom or molecule concerned).

The various frequency broadening processes above result in a frequency spreading of the transition strength, S (see **Equation 3-17**), and consequently in a diminution of the effective cross section, thus of the transition probability, at the resonance frequency, ν_0. If a single transition is considered, the transition strength is a conservative, constant parameter, and the cross section can be expressed as the spreading of this strength according to a lineshape (Saleh, 1991),

$$\sigma(\nu) = S \cdot G(\nu) \qquad \text{(Equation 3-24)}$$

where G is the lineshape function, the area of which is normalized, i.e. $\int_0^\infty G(\nu)\,d\nu = 1$. Lineshapes that stem from homogeneous broadening processes (lifetime and collision) are properly described by the *Lorentzian profile*, G_L,

---

[30] If spontaneous emission is the only decay process, and the lifetime of the ground state is infinite, $t_{1/e} = 1/\boldsymbol{A}$, where $\boldsymbol{A}$ is Einstein's spontaneous emission constant.

[31] Half Width at Half-Maximum (HWHM).

$$G_L\left(\nu,\nu_0,\Delta\nu_L\right)=\frac{\Delta\nu_L/\pi}{\left(\nu-\nu_0\right)^2+\Delta\nu_L^2} \qquad \text{(Equation 3-25)}$$

The classical Gaussian distribution describes the inhomogeneous, thermal broadening, i.e. the *Doppler profile*, G_D,

$$G_D\left(\nu,\nu_0,\boldsymbol{\sigma}_D\right)=\frac{1}{\sqrt{2\pi}\cdot\boldsymbol{\sigma}_D}\cdot\exp\left[-\frac{\left(\nu-\nu_0\right)^2}{2\cdot\boldsymbol{\sigma}_D^2}\right] \qquad \text{(Equation 3-26)}$$

If both types of broadening take place, the lineshape is the convolution of Lorentzian and Gaussian profiles (Schreier, 1992). The resulting lineshape, known as the *Voigt profile*, G_V,

$$G_V\left(\nu,\nu_0,\Delta\nu_L,\boldsymbol{\sigma}_D\right)=G_L\otimes G_D=\int_{-\infty}^{\infty}G_L\left(\nu',\nu_0,\Delta\nu_L\right)\cdot G_D\left(\nu-\nu',\boldsymbol{\sigma}_D\right)\cdot d\nu' \qquad \text{(Equation 3-27)}$$

is a transcendental function that cannot be calculated analytically. In this research, the numerical method of Humlíček (1982) was implemented for its calculation (see **Chapter 4** and **Annex D**).

At near room temperatures, the lineshape depends only on pressure. It is established, as a rule of thumb (Schiff, 1994), that rovibrational transitions display Doppler and Lorentzian lineshapes at <10 torr and >100 torr, respectively. Between these two pressures, i.e. within the range 10-100 torr, neither Doppler nor collisional broadening dominate so the transition lines are better described by a convolution of both (Voigt lineshape).

Besides the physical broadening of transitions lines due to pressure and thermal effects, instrumental limitation cause degradation of the resolution of transmission spectra. This degradation is due whether to the finite resolving power of the spectrometer used for analyzing a transmitted broadband (polychromatic) light beam (e.g. a high-pressure Xe lamp), or due to the imperfect monochromaticity of the light source, e.g. a tunable semiconductor laser used along with a single channel detector (see **Figure 3-8**). In these conditions, the observed transmission spectrum, τ_H, appears broaden due to whether the spectrometer instrument function or the laser linewidth, H,

$$\tau_H\left(\nu\right)=\tau\left(\nu\right)\otimes H\left(\nu\right)=\exp\left[-\sigma\left(\nu\right)\cdot c\cdot L\right]\otimes H\left(\nu\right) \qquad \text{(Equation 3-28)}$$

As a result of the convolution, the optical density is a slightly non-linear function of the column density,

$$D_H(\nu) = -\ln\left[\tau_H(\nu)\right] \qquad \text{(Equation 3-29)}$$

The linearity between optical density and column density is still valid provided that the theoretical (true) optical density is small enough to be expressed by the first two terms of the Taylor's series[32], i.e. $\exp(-\sigma cL) \cong 1-\sigma cL$ thus leading to $\tau_H \cong 1-\sigma_H cL$, where

$$\sigma_H(\nu) = \sigma(\nu) \otimes H(\nu) \qquad \text{(Equation 3-30)}$$

is the convolved cross section. Applying the appropriate Taylor's series[33] to **Equation 3-29**, and then extending it for multiple absorbers,

$$D_H(\nu) \cong L \cdot \sum_j \sigma_{H,j}(\nu) \cdot c_j \qquad \text{(Equation 3-31)}$$

Mathematical analysis of the truncation error shows that this linearization is numerically valid within ±1% for (relative) *absorptances*, i.e. $1-\tau_H$, below 17%, an inherently fulfilled condition in open path spectroscopy of trace gases. In these conditions the optical density and the absorptance are undistinguishable, $D_H \cong 1-\tau_H$.

There appears to be a considerable degree of confusion on this matter. Some authors (e.g. Hermans, 1999) claim that is the cross section what must be convolved. This is inaccurate. The cross section is a derived variable not a directly observed one. Spectroscopic systems detect transmitted intensity. In view of this, it is the transmittance what results convolved upon observation.

Another mathematically more sophisticated approach consists in deconvolving a measured transmission spectrum knowing the instrument function (Blass, 1981). These mathematical techniques use the maximum likelihood principle and show an acceptable degree of success when applied to spectra of very high signal-to-noise ratios (SNR). This is very frequently not the case in differential absorption in which absorptance levels are usually very low, typically in the range 10^{-2}-10^{-5}. When using the differential absorption approach it thus appears cleverer to use properly convolved cross sections as reference spectra to fit with that trying to deconvolve measured spectra.

---

[32] $e^x = 1 + x + x^2/2! + x^3/3! + \ldots$

[33] $\ln(1+x) = x - x^2/2 + x^3/3 - \ldots \; -1 < x \leq 1$

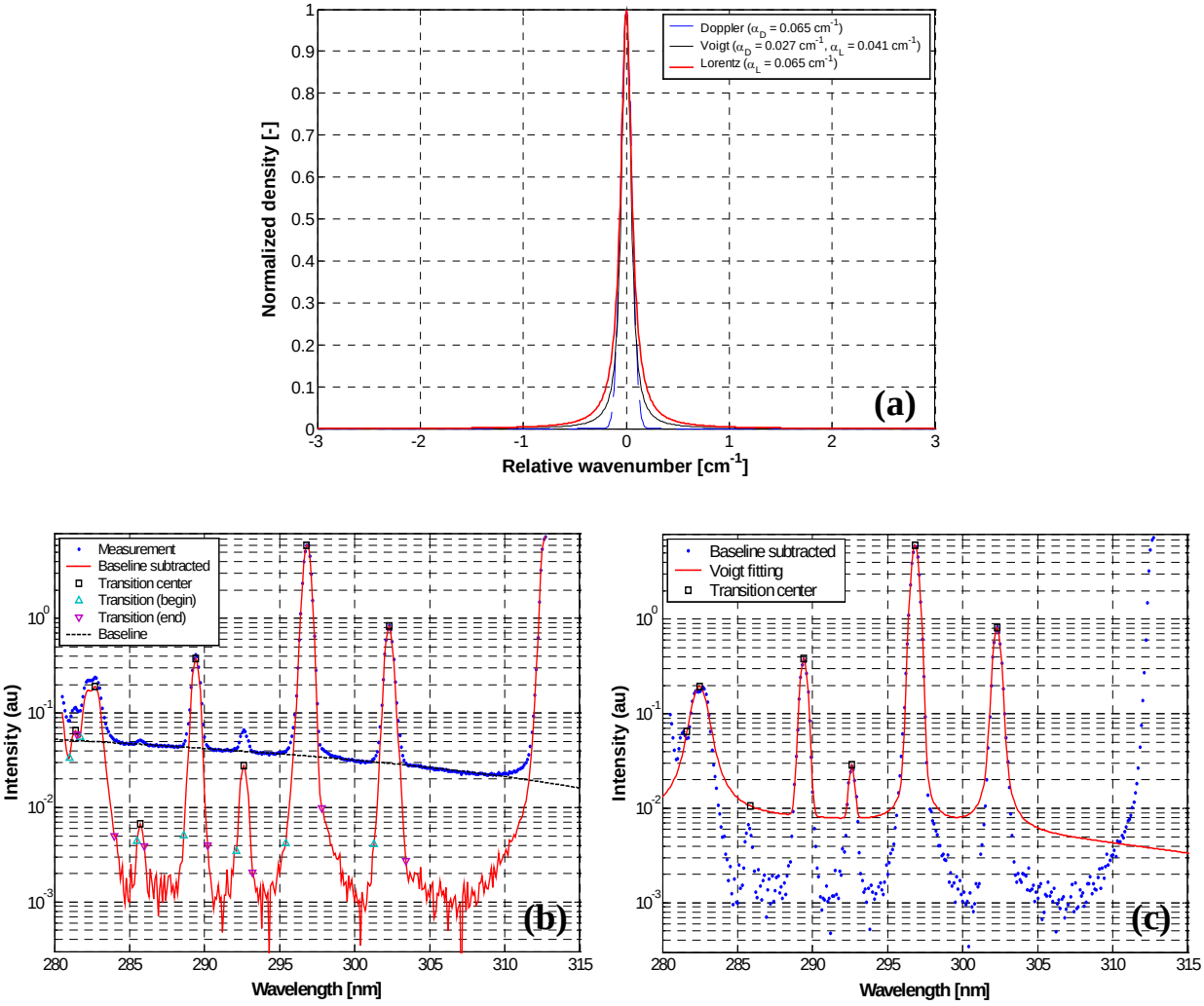

Figure 3-8. Laser linewidth and instrument function. **(a)** Lineshape of the quantum-cascade laser (QCL) used in this research (see **Chapter 5**) as calculated using three broadening functions of identical width at half-maximum. The QCL linewidth ~0.13 cm^{-1} FWHM was derived from CO_2 absorption measurements. The spectral range represents the typical QCL tuning range (~6 cm^{-1}). Panels **(b)** and **(c)** show the procedure used for derived the instrument function of the DOAS spectrometer near 300 nm. The Hg spectrum is (b) baseline subtracted, the atomic transition lines are identified, and subsequently (c) fitted to Voigt lineshapes. Cross sections in this spectral region are convolved with the fitted Voigt lineshape of the center transition only (296.7 nm), i.e. the one with the highest SNR.

3.4 Absorption cross section: Line-per-line calculation and databases

Absorption cross sections of various atmospheric trace gases in the UV-visible and in the mid-IR were required for the purposes of this research. Mid-IR cross sections were line-per-line calculated using the HITRAN database (Rothman, 1998). HITRAN contains all the information required for calculating mid-IR cross sections on a line-per-lie basis, i.e. by spectrally adding the cross section associated to each individual i-th rovibrational transition between lower and upper energy states $E'_i \leftarrow E''_i$. For this purpose, HITRAN internal calculation engine provides the transition strength of each transition S_i, given in [(cm^2/molecule)·cm^{-1}],

$$S_i = \left(\frac{h\tilde{\nu}_i}{\boldsymbol{c}}\right)\cdot\left(\frac{N''_i}{N}\right)\cdot\left(1-\frac{g''_i}{g'_i}\cdot\frac{N'_i}{N''_i}\right)\cdot \boldsymbol{B}_i \qquad \text{(Equation 3-32)}$$

by calculating the Einstein's coefficient for induced absorption of each transition, $\boldsymbol{B}_i$, on the basis of its transition moment integral, $\left\|\vec{R}_i\right\|^2$. The term $\left(g''_i N'_i\right)/\left(g'_i N''_i\right)$ is calculated using Boltzmann's equation. The ratio of the population in the i-th transition lower state to the total number density, N''_i/N, is calculated assuming local thermodynamic equilibrium (LTE). The collisional broadening of the i-th transition line is described by air- and self-broadening pressure coefficients (given in [cm^{-1}/atm]), $\gamma_{air,i}$ and $\gamma_{self,i}$, specific to the i-th transition, which describe the dependence of the linewidth on the partial pressures of air (buffer gas) and the molecule of interest, respectively. The line halfwidth of the i-th transition is calculated according to,

$$\Delta\tilde{\nu}_i = \left(\frac{T_{ref}}{T}\right)^{\boldsymbol{n}_i}\cdot\left[\gamma_{air,i}\cdot(P-p)+\gamma_{self,i}\cdot p\right] \qquad \text{(Equation 3-33)}$$

where $\boldsymbol{n}_i$ is the coefficient of temperature dependence of the linewidth (dimensionless - classically $\boldsymbol{n}$ = 0.5), P is the partial pressure of air, and p = y·P is the partial pressure of the molecule of interest (y is the mixing ratio of the molecule of interest and T_{ref} = 296 K is temperature of reference). Besides collisional broadening, pressure may cause shifting of the transition line. This dependence is incorporated in HITRAN through the air-broaden pressure shift coefficient, $\delta_{P,i}$, given in [cm^{-1}/atm]. The center wavenumber of the i-th transition upon shifting is $\tilde{\nu}_i = \tilde{\nu}_{0,i} + \delta_{P,i}\cdot P$. The cross section is then calculated according to Equation 3-26,

$$\sigma(\tilde{\nu}) = \sum_i S_i \cdot G(\tilde{\nu}, \tilde{\nu}_i, \Delta\tilde{\nu}_i) \qquad \text{(Equation 3-34)}$$

where S_i (in [(cm^2/molecule)·cm^{-1}]) and $G(\tilde{\nu}_i, \Delta\tilde{\nu}_i)$ (in [cm]) are the spectral strength and the lineshape of the i-th transition, respectively. As explained above, the transition lineshape must be selected according to the temperature and pressure conditions. At ambient temperature, this means Gaussian, Lorentzian, and Voigt profiles for pressures below 10 torr, above 100 torr, and within 10-100 torr, respectively. The sum must include of any transitions that upon broadening could significantly contribute to total cross section within the spectral range calculated. This calculation is to be repeated for all isotopomers of the molecule of interest included in the database. The species cross section is thus,

$$\sigma(\tilde{\nu}) \cong \frac{\sum_k z_k \cdot \sigma_k(\tilde{\nu})}{\sum_k z_k} \qquad \text{(Equation 3-35)}$$

where z_k is the fractional abundance of the k-th isotopomer. The denominator is intended at renormalizing the isotopomer weighting since it is frequent that minor isotopomer are missing in the database so the total abundance is sometimes less than 100%, i.e. $\sum_k z_k \leq 1$.

HITRAN-based line-per-line calculations of the ozone cross section in the ~9.6 μm region at 10 and 760 torr are shown in **Figure 3-9**. This was the mid-IR region used for quantitative detection of ozone demonstrated with a pulsed QCL tuned by temperature (see **Chapter 5**). This figure shows as well the degradation of the spectral resolution due to the finite linewidth of the QCL (~0.13 cm^{-1} FWHM). The convolved cross section was calculated according to **Equation 3-32**.

Line-per-line cross section calculations are at the present time in general restricted to the IR. Molecular cross sections in the UV-visible are in general available only as tabular data. The elevated number of rovibronic transitions associated with an electronic band impedes rigorous spectroscopic description and thus line-per-line calculations. Moreover, in many cases the rotational transitions within a vibronic band are so narrow and tightly packed that remain unresolved, even when using state-of-the-science spectrometers and tunable laser sources. The HONO vibronic bands shown in **Figure 3-4** provide a relevant example. For this reason, the current *modus operandi* is the use of high-resolution UV-visible cross sections instead of its calculation. Relevant cross sections used in this research are shown in **Figure 3-10**. The high-resolution literature data are shown along with the convolved cross section as calculated using **Equation 3-32**. The criteria for selection of literature cross-sections for differential analysis purposes were the following (see **Table 3-2**):

- Wavelength accuracy: discrepancies characterized by wavelength shifts of up to ±0.3 nm and wavelength stretching of up to ±1% were found in literature cross sections, particularly of monocyclic aromatic hydrocarbons (MAH). The largest acceptable inaccuracy was set equal to the digital resolution of the DOAS spectrometer, ±0.1 nm. The concentration retrieval developed in this research assumes that the wavelength of the reference spectra is fully accurate.
- Differential cross section: a high accuracy in the differential component of the cross section (see **Section 3.5**) was preferred over high accuracy of the absolute cross section only.
- Spectral resolution: cross section with the highest resolution was preferred. The resolution of the reference spectra must be higher than the DOAS spectrometer resolution (~0.55 nm FWHM, wavelength dependent).

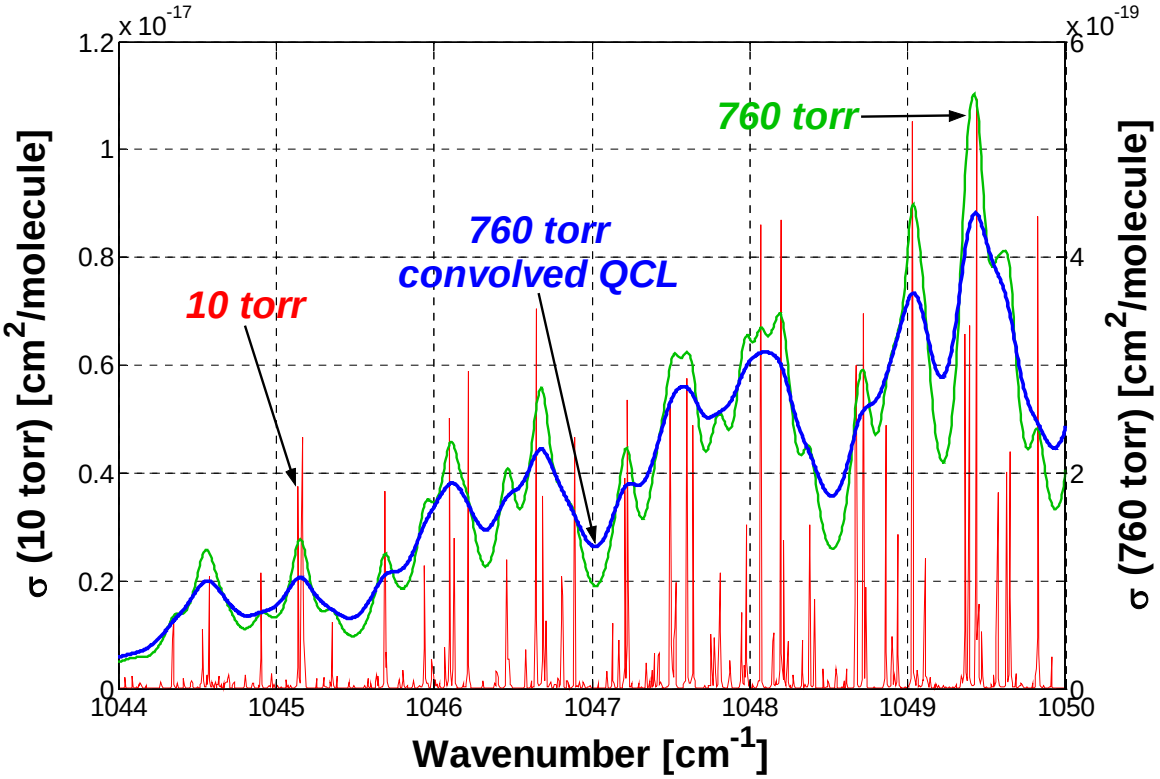

Figure 3-9. Cross section of ozone in the 9.6 μm spectral region at 10 and 760 torr. Transitions shown are essentially those of the Q-branch of the 3_1^0 rovibrational band. The pressure increase causes a ~20-fold decrease of the cross section. The linewidth of the probing QCL causes additional spectral degradation.

The spectral resolution of the available UV-visible literature cross sections of some compounds can be in some cases as large as ~0.1 nm (see **Table 3-2**), i.e. obtained with a resolving power only ~5 times higher than that of the DOAS spectrometer (~0.55 nm FWHM). In consequence, one may call into question the validity of **Equation 3-31** in these conditions. A simple analysis of the convolution function in the Fourier space allows shedding light on this matter.

An ideal spectrometer would have a Dirac-like instrument function. Referring to the cross derived from measurements with this idealized instrument as σ_∞, the literature cross section measured with a high resolution instrument (subscript R) would be $\sigma_R = \sigma_\infty \otimes R$, where $R(\nu)$ is the instrument function associated to the literature cross section. Then the cross section "observed" by the low resolution DOAS spectrometer (subscript H) would be $\sigma_H = \sigma_\infty \otimes H = \sigma_R \otimes T$, where $H(\nu)$ is the DOAS spectrometer instrument function, and $T(\nu)$ is a "transfer" function. If $R(\nu)$ and $H(\nu)$ are assumed to be Gaussian (see **Equation 3-26**), analysis of the equations above in the Fourier (frequency) space allows demonstrating that,

$$\Delta\nu_T = \sqrt{\Delta\nu_H^2 - \Delta\nu_R^2} \qquad \text{(Equation 3-36)}$$

where $\Delta\nu_R$, $\Delta\nu_H$, and $\Delta\nu_T$ are the instrument function (halfwidth) of the literature cross section, the cross section as observed by the low-resolution DOAS spectrometer, and the transfer function, respectively. This implies that a literature cross section with a spectral resolution, ~0.1 nm FWHM, should be convolved with an instrument function of ~0.54 nm FWHM instead of ~0.55 nm in order to assure full comparability between the convolved cross section and the DOAS measurements. This calculation shows that, for the purposes of this research, even literature cross sections resolved at ~0.1 nm FWHM can be convolved with a high degree of confidence directly using the measured instrument function of the low-resolution DOAS spectrometer. In addition, applying the correction in Equation 3-38 is risky since in most cases the instrument function of literature cross section is not reported, and almost never available in digital form.

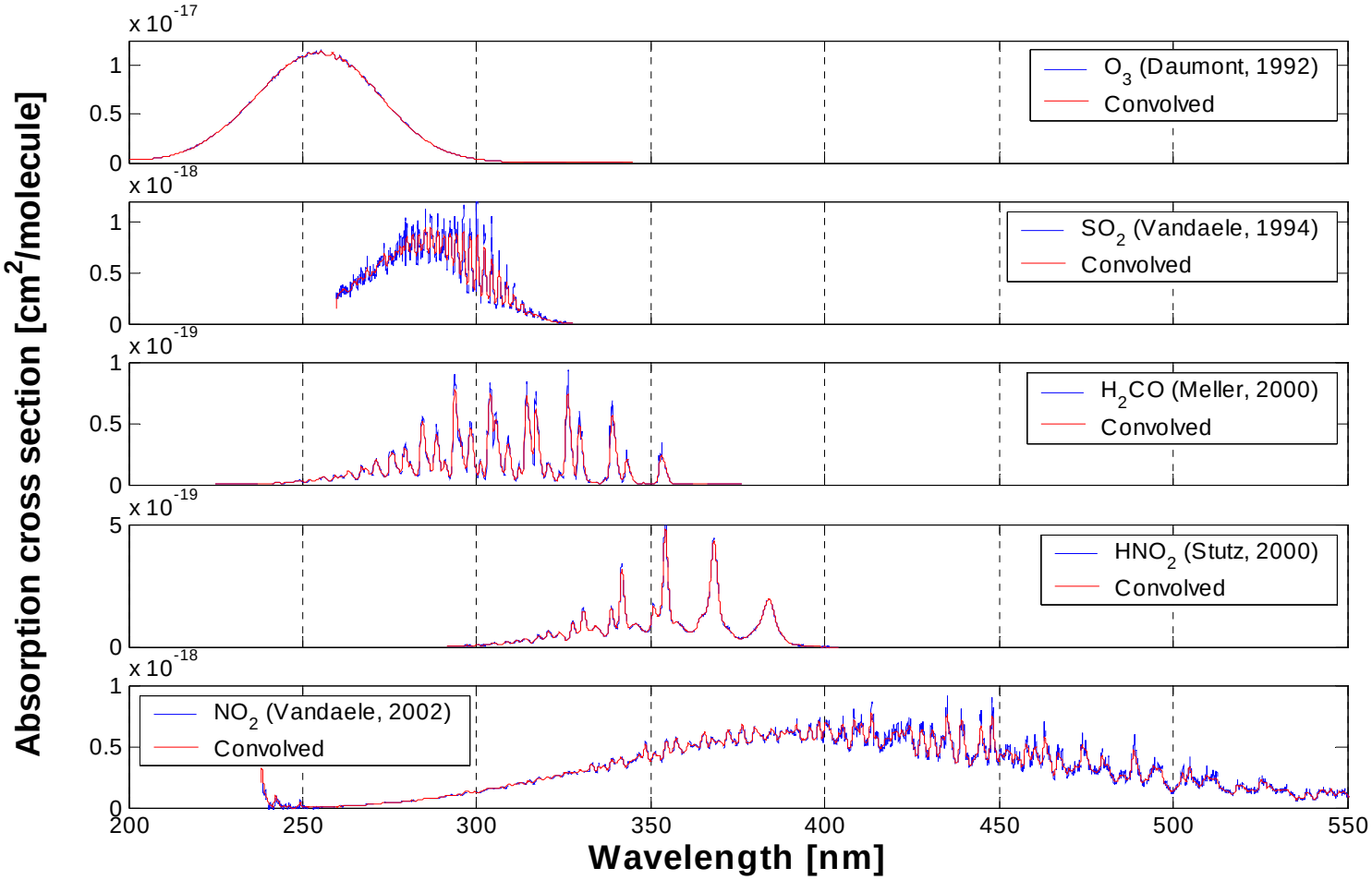

Figure 3-10. High resolution and DOAS instrument (~0.55 nm FWHM) convolved UV-visible absorption cross section of trace gases relevant to this research. Formaldehyde has the lowest absorption cross section among the species shown. In spite of its high absolute absorption cross section, ozone has a quite poor "differential" structure. This is due to the overlapping of a very large number of rovibronic transitions in the Hartley band.

(a)

Molecule	Spectral range (nm)	Electronic transition
O_2	190-300	$A\,^3\Sigma_u^+ \leftarrow X\,^3\Sigma_g^-$ (i)
O_3	250-350	$C \leftarrow X\,^1A_1$ (ii)
SO_2	270-317	$A\,^1B_1 \leftarrow X\,^1A_1$
H_2CO	300-360	$A\,^1A_2 \leftarrow X\,^1A_1$
NO_2	300-700	$A\,^2B_1 \leftarrow X\,^2A_1$
HNO_2	300-400	$A\,^1A'' \leftarrow X\,^1A'$
Benzene	220-270	$A\,^1B_{2u} \leftarrow X\,^1A_{1g}$

(b)

		Electronic band strength		RMS [cm^2/molecule]	
Molecule	**Range [nm]**	**S [cm/molecule]**	**f (oscillator) [-]**	**Absolute**	**Differential**
O3	250-350	7.93E-14	8.96E-02	5.25E-18	6.14E-20
SO2	270-317	3.74E-15	4.22E-03	5.37E-19	1.21E-19
H2CO	300-360	2.10E-16	2.37E-04	2.12E-20	1.40E-20
HNO2	300-400	6.44E-16	7.27E-04	1.09E-19	4.87E-20
NO2	300-700	6.26E-15	7.07E-03	3.43E-19	5.28E-20

Table 3-1. Electronic transition bands relevant to this research. **(a)** Spectroscopic notation (Stutz, 1996a), and **(b)** transition and oscillator strength, and average cross section. Notes: (i) Herzberg continuum (II and III bands); (ii) Hartley band.

		Wavelength [nm]		Uncertainty		
Molecule	**T [K]**	**Range**	**Resolution (FWHM)**	**Wavelength [nm]**	**Cross section**	**Source**
Ozone	298	195-345	0.01 **(e)**	0.005	2.50%	Daumont, 1992
Sulfur dioxide	294	260-328	2 cm^{-1}	0.05 cm^{-1} **(d)**	2.40%	Vandaele, 1994
Formaldehyde	297	225-375	0.08	0.003	~5%	Meller, 2000
Nitrous acid	300	292-404	0.08	0.02	1.45%	Stutz, 2000
Nitrogen dioxide	294	238-667	2 cm^{-1}	0.05 cm^{-1}	~3%	Vandaele, 1998
Oxygen **(c)**	295	250-290	0.15	0.004	~5%	Volkamer, 1998
Benzene	294	219-278	0.11	0.04 **(b)**	4.17%	Trost, 1997
Toluene	293	239-278	0.11	0.04 **(b)**	2.63%	Trost, 1997
Ethylbenzene	298	238-278	0.146	0.04 **(b)**	3.2% **(a)**	Etzkorn, 1999
o-Xylene	294	239-278	0.11	0.04 **(b)**	2.92%	Trost, 1997
m-Xylene	294	239-278	0.11	0.04 **(b)**	2.90%	Trost, 1997
p-Xylene	293	239-278	0.11	0.04 **(b)**	2.80%	Trost, 1997
Phenol	294	244-283	0.11	0.04 **(b)**	2.63%	Trost, 1997

(a) Uncertainty of the differential cross section

(b) Not reported; value shown is an estimation (1 pixel x dispersion)

(c) Reference spectra are given as relative transmittance (au)

(d) Not reported; assumed be equal to the value reported in a former investigation (Vandaele, 1998)

(e) Not reported; value shown is the wavelength step

Table 3-2. Selected literature UV-visible absorption cross sections used in this research (Daumont, 1992; Meller, 2000; Vandaele, 1998; Vandaele, 1994) (Etzkorn, 1999; Trost, 1997; Volkamer, 1998).

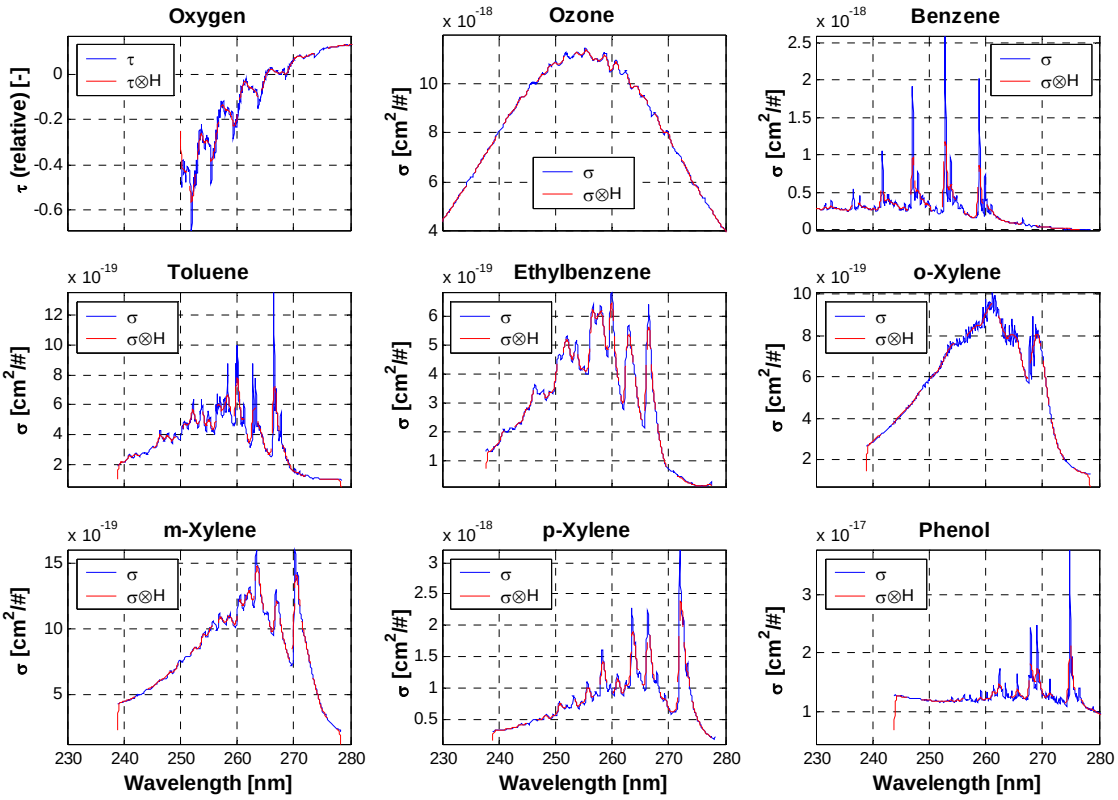

Figure 3-11. Absorption cross section of selected Monocyclic Aromatic Hydrocarbons (MAH) in the 230-280 nm spectral range. Phenol has a high, highly structured absorption cross section, which enables its detection at sub-ppb levels.

3.5 The differential absorption concept

As mentioned at the end of **Section 3.2**, the procedure used in closed absorption paths for the determination of the absorption baseline (I_0) cannot be applied in the open path. There are no means for selectively "removing" the absorbing compounds (within a wavelength range) from an open atmospheric path in order to measure I_0[34]. The solution to this dilemma lies in the splitting of the spectral variations in an absorption spectrum into "low" and "high" frequency terms, i.e. into slow and rapid variations with wavelength (Platt, 1994). The two-band system shown in **Figure 3-12** allows illustrating the differential absorption concept. The upper panel in this figure shows two slightly overlapped absorption bands "bounded" by λ_A and λ_B, and λ_B and λ_C, respectively, and with peak cross sections at λ_1 and λ_2. These bands overlie above a non-zero, slowly varying *cross section baseline*, σ_0. Introduction of this term allows splitting the cross section function as,

[34] The detection of NO_3 by differential absorption is a notable exception. Complete photolysis of NO_3 at daytime allows using daytime spectra as absorption baseline under certain conditions.

$$\sigma(\lambda) = \sigma_0(\lambda) + \Delta\sigma(\lambda) \qquad \text{(Equation 3-37)}$$

where $\Delta\sigma$ is the rapidly-varying component of the cross section or *differential cross section*. These two absorption bands produce two intensity dips, ΔI_1 and ΔI_2, in the atmospheric transmission spectrum (see **Figure 3-12**). These dips underlie below the "synthetic baseline", I_0', which in the case analyzed can be calculated by simple linear interpolation, as for instance for the band centered at λ_1 as $I'_{0,1} = I'_0(\lambda_1) = I(\lambda_A) + \left[I(\lambda_B) - I(\lambda_A)\right] \cdot (\lambda_1 - \lambda_A) / (\lambda_B - \lambda_A)$[35]. Since the synthetic baseline, I_0', accounts for all the slow-varying atmospheric attenuation terms, the intensity dips are ascribed exclusively to molecular absorption. According to the BLB law (**Equation 3-14**), the intensity dip is proportional to the differential cross section ($\Delta\sigma$) and the column density ($c \cdot L$). If the dip is small compared to the synthetic baseline ($\Delta I \ll I_0'$), the differential absorbance or optical density, ΔD, is essentially identical to the relative absorptance[36], $\Delta D \cong 1 - \tau' = \Delta I / I_0'$, thus the BLB law can be expressed in terms of the fractional absorption, $\Delta I / I_0'$ (Zahniser, 2002),

$$\Delta I / I_0' \cong \Delta D = \Delta\sigma \cdot c \cdot L \qquad \text{(Equation 3-38)}$$

This equation provides a solution to the open path spectroscopy dilemma as formulated above: an absolute concentration can be retrieved from the relative (differential) cross section and absorbance as defined by the transition (band) without any knowledge of the actual absorption baseline, I_0 (see **Figure 3-12**). **Equation 3-38** implies nevertheless that concentration retrieval is possible only for species that have at least one well-defined (well-shaped) transition (band) within the spectral range used for determination, otherwise a differential cross section[37] cannot be calculated. This requisite must be fulfilled but obviously does not guarantee detection, which is limited by instrumental factors. Laser-based differential absorption systems achieve to detect fractional absorptions as low as $\sim 10^{-6}$ (Zahniser, 2002). More common instruments operate typically in the $\sim 10^{-2}$-10^{-4} fractional absorption range (Plane, 1995; Platt, 1994; Stutz, 1996b).

The constancy of the column density[38] implies that the differential cross sections of the two bands are related according to $\Delta D_2 / \Delta D_1 = \Delta\sigma_2 / \Delta\sigma_1$. From a different perspective, this implies that the statistical robustness of the concentration retrieval can be largely enhanced by including as many as possible transition bands in the calculation.

---

[35] Tabularized peak differential cross sections are calculated in the same way and usually reported for comparison purposes only.

[36] $\tau' = 1 - \Delta I / I_0'$ (relative transmittance)

[37] The transmitted intensity must be measured at least at the 2 "boundary" wavelengths and at the peak cross section wavelength, e.g. at λ_A, λ_B, and λ_1 for the first band in **Figure 3-13**.

[38] The spectral effect of changes in the concentration is neglieagle if the transmission spectra are measured at the appropriate frequency. Average concentrations can then be derived from co-added spectra.

Introduction of **Equation 3-37** into **Equation 3-23** allows for a rigorous derivation of **Equation 3-38** for a multiple absorber mixture, $\Delta D(\lambda) = \ln\left[I_0'(\lambda)/I(\lambda)\right] = L \cdot \sum_j \Delta\sigma_j(\lambda) \cdot c_j$.

Since the synthetic baseline, I_0',

$$I_0'(\lambda) = I_{LS}(\lambda) \cdot A(\lambda) \cdot \exp\left\{-L \cdot \left[\varepsilon_M(\lambda) + \varepsilon_R(\lambda) + \sum_j \sigma_{0,j}(\lambda) \cdot c_j\right]\right\} \qquad \text{(Equation 3-39)}$$

carries all the atmospheric attenuation terms that vary slowly with wavelength, it can be defined as the intensity in "absence of differential absorption" (Platt, 1994).

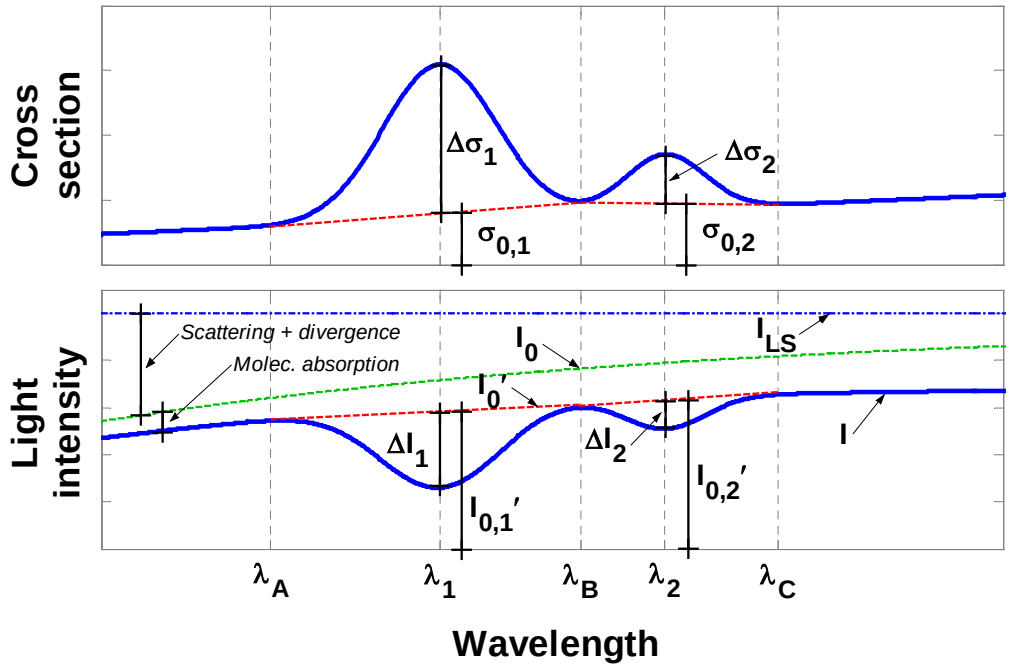

Figure 3-12. Schematic representation of the differential absorption spectroscopy principle.

In practice the spectral range for determination is chosen so to contain a series of transition bands. The differential cross section, i.e. the narrow component of the cross section, is thus calculated by subtraction of a synthetic, smooth trend curve or low-pass (LP) filter, f_{LP},

$$\Delta\sigma_H(\lambda) = \sigma_H(\lambda) - f_{LP}\left[\sigma_H(\lambda)\right] \qquad \text{(Equation 3-40)}$$

This equation makes explicit the fact that the cross section must be convolved previous subtraction of the broad LP-filter. This subtraction is mathematically equivalent to a high-pass (HP) filter operation. $\Delta\sigma$ is thus the HP-filtered cross section. The most commonly used LP-filter is the classical fitting polynomial, typically of 3rd-9th degree. The computationally more demanding Savitzky-Golay (SG) filter (Savitzky, 1964) appears to enhance the selectivity of the retrieval but operate successfully only over differential spectra with a high signal-to-noise ratio (SNR). Selectivity is obviously a critical retrieval quality criterion in wavelength ranges with a considerable number of species, e.g. the monocyclic aromatic hydrocarbons (MAH) region, 230-290 nm (Volkamer, 1998). Other local-polynomial regression filters have been tried (Lindström, 1996) yielding only very limited improvement with respect to the classical fitting polynomial filter.

Figure 3-13 shows the UV-visible differential cross section of atmospheric species relevant to this research. Differential cross sections were calculated by subtraction of a 2nd degree SG-filter (frame/range = 15% - refer to **Chapter 4** and **Annex D** for details). The case of ozone deserves further discussion. This compound has the highest absolute cross section among the selected species (see **Figure 3-10** and **Table 3-2**). On the contrary, its differential cross section (peak-to-peak) is the second lowest, exceeding only that one of formaldehyde. The Hugging band is constituted by a large number of rovibronic bands, which produces a high absolute cross section. These bands overlap to large extent, which leads to a weak differential structure.

The differential optical density is calculated in a homologous way,

$$\Delta D(\lambda) = \ln\left(\frac{I_{LS}(\lambda)}{I(\lambda)}\right) - f_{LP}\left[\ln\left(\frac{I_{LS}(\lambda)}{I(\lambda)}\right)\right] \qquad \text{(Equation 3-41)}$$

Rationing by the light source spectrum, I_{LS}, is intended at removing any "narrow" emission spectral features of the source. Whichever the type of type of LP-filter applied, the effective band-pass of the filter, in other terms the equivalent filter "averaging" length must be optimized: defective HP-filtering would in general cause a permanent concentration offset. Excessive HP-filtering may end up in some cases by stripping out all the differential features. In this case the differential cross section would be compared to noise not to signal!

The differential BLB is thus expressed as,

$$\Delta D(\lambda) \cong L \cdot \sum_j \Delta\sigma_{H,j}(\lambda) \cdot c_j \qquad \text{(Equation 3-42)}$$

thus in principle concentrations can be retrieved by multiple linear regression. An example of application is shown in **Figure 3-14**.

According to Calvert's definition (Calvert, 1990) (see **Section 2.4**) the sensitivity of the differential absorption method for the detection of species j, $\boldsymbol{S}_j$, is

$$\boldsymbol{S}_j = \frac{\partial \Delta D}{\partial c_j} \cong \Delta\sigma_{H,j} \cdot L \qquad \text{(Equation 3-43)}$$

This equation indicates 3 means for improving the sensitivity:

- Increasing the absorption pathlength, L.
- Properly selecting the spectral region for determination in order to maximize the differential cross section, $\Delta\sigma_H$.
- Increasing the spectral resolution, i.e. reducing the width of the instrument function $\Delta\lambda_H$ (see **Equation 3-30**). In most cases a higher spectral resolution, i.e. a narrower instrument function renders only a marginal increase of the differential cross section (see **Figure 3-13**). A special case is the detection of MAH. Spectral resolutions in the order of ~0.2 nm FWHM provided enhanced selectivity in this case.

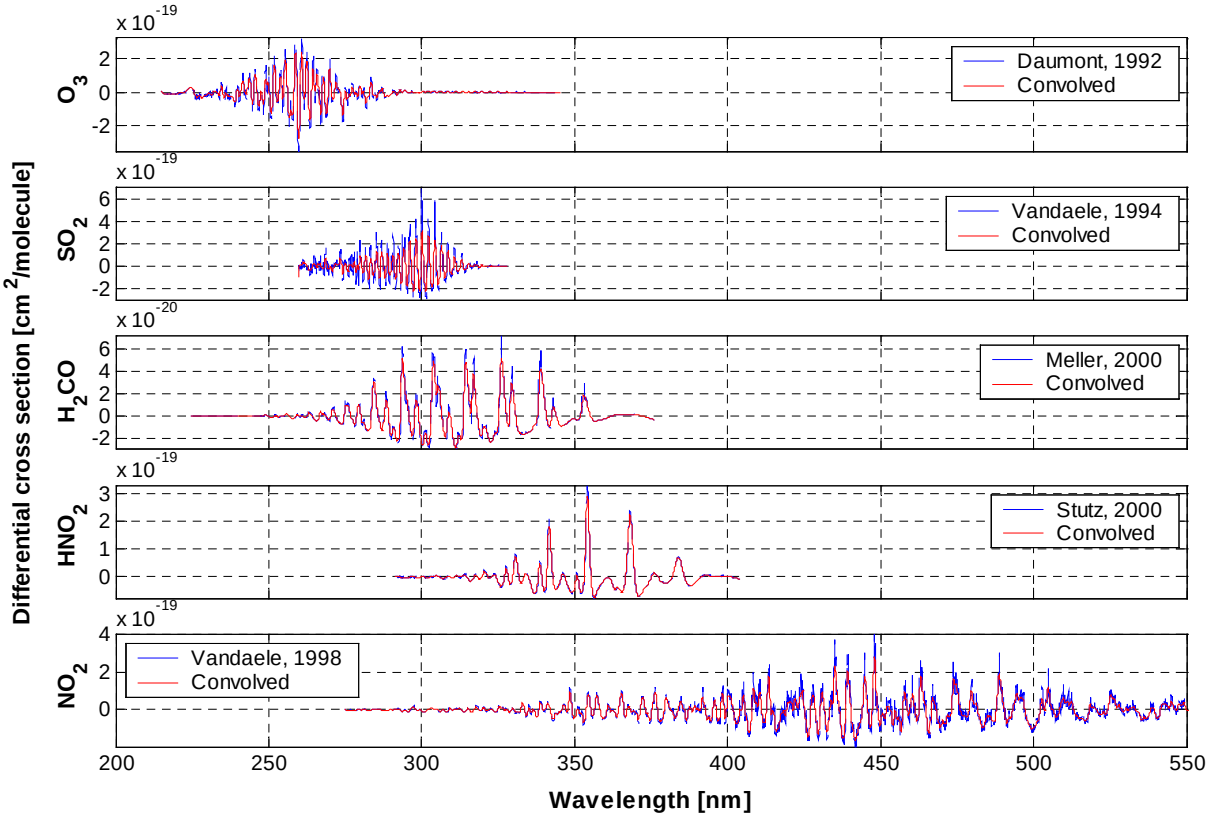

Figure 3-13. Differential absorption cross section of relevant atmospheric species at high resolution and at the resolution of the DOAS instrument used (~0.55 nm FWHM) in this research. Refer to Figure 3-10 for the corresponding absolute cross sections.

The next two chapters are devoted to the application of the differential absorption method in the UV-visible and in the mid-IR. **Chapter 4** presents laboratory and field results with a monostatic UV-visible DOAS system. This system uses polychromatic light from high-pressure Xe lamp that is after absorption analyzed using a Czerny-Turner wavelength-scanning monochromator. **Chapter 5** presents the demonstration of a QCL-based system. In this case the laser wavelength is tuned by temperature and the transmitted beam is analyzed using a monochannel detector (MTC). A recent application in astronomy tells of the universality of the differential absorption method. Charbonneau *et al* (2002) achieved to demonstrate the existence of sodium in the atmosphere of an extrasolar planet using differential absorption.

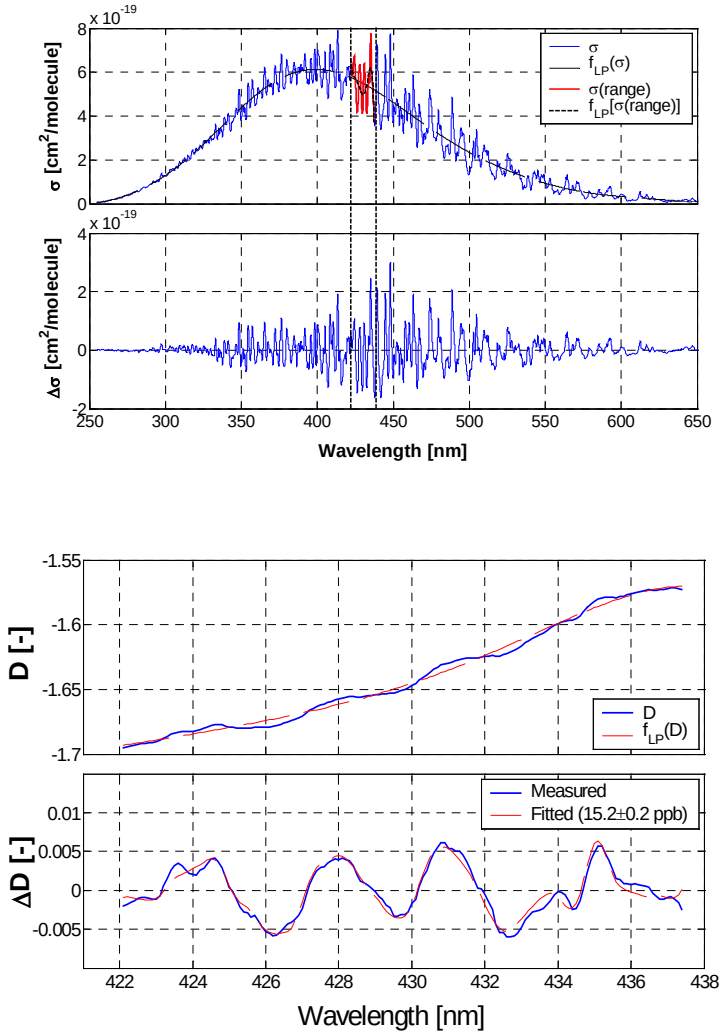

Figure 3-14. Example of application of the differential absorption concept for the retrieval of NO_2. The 2-min spectrum was recorded in Duitama, Colombia (2600 m AGL) on 26th January 2002. The absorption pathlength was 1080 m.

3.6 References

Barbe, A., C. Secroun, P. Jouve, N. Monnanteuil, J.C. Depannemaecker, B. Duterage and J. Bellet. Infrared and microwave high-resolution spectrum of the ν_3 band of ozone. *J. Molec. Spectrosc.* 64: 343-364, 1977

Barton, F.E. Theory and principles of near infrared spectroscopy. *Spectrosc. Europe* 14 (1): 12-18, 2002

Blass, W.E. and G.W. Halsey. Deconvolution of absorption spectra. Academic Press, New York, 1981

Bodhaine, B.A., N.B. Wood, E.G. Dutton and J.R. Slusser. On Rayleigh optical depth calculations. *J. Atm. Ocean. Tech.* 16: 1854-1861, 1999

Bongartz, A., J. Kames, F. Welter and U. Schurath. Near-UV absorption cross sections and trans/cis equilibrium of nitrous acid. *J. Phys. Chem.* 95 (3): 1076-1082, 1991

Calvert, J.G. Glossary of atmospheric chemistry terms. *Pure Appl. Chem.* 62 (11): 2167-2219, 1990

Charbonneau, D., T.M. Brown, R.W. Noyes and R.L. Gilliland. Detection of an extrasolar planet atmosphere. *Astrophys. J.* 568: 377-384, 2002

Daumont, D., J. Brion, J. Charbonnier and J. Malicet. Ozone UV spectroscopy I: Absorption cross-section at room temperature. *J. Atmos. Chem.* 15: 145-155, 1992

Devi, V.M., D.C. Benner, C.P. Rinsland, M.A.H. Smith and D.S. Parmar. Infrared spectroscopy of the CO_2 molecule. *Recent Res. Devel. Geophys. Res.* 1: 119-148, 1996

Etzkorn, T., B. Klotz, S. Sorensen, I.V. Patroescu, I. Barnes, K.H. Becker and U. Platt. Gas-phase absorption cross sections of 24 monocyclic aromatic hydrocarbons in the UV and IR spectral ranges. *Atmos. Environ.* 33 (4): 525-540, 1999

Finlayson-Pitts, B.J. and J.N. Pitts. Chemistry of the upper and lower atmosphere. Academic Press, San Diego, 2000

Harris, D.C. and M.D. Bertolucci. Symmetry and spectroscopy. Dover, New York, 1989

Hermans, C., A.C. Vandaele, M. Carleer, S. Fally, R. Colin, A. Jenouvrier, B. Coquart and M.-F. Mérienne. Absorption cross-sections of atmospheric constituents: NO_2, O_2, and H_2O. *Environ. Sci. Pollut. Res.* 6 (3): 151-158, 1999

Hollas, J.M. Modern spectroscopy. Wiley, Chichester, 1996

Humlícek, J. Optimized computation of the Voigt and complex probability functions. *JQSRT* 27 (4): 437-444, 1982

Iqbal, M. An introduction to solar radiation. Academic Press, Toronto, 1983

Ivanov, S.V. and V.Y. Panchenko. Infrared and microwave spectroscopy of ozone: Historical aspects. *Physics-Uspekhi* 37 (7): 677-695, 1994

Jiménez, R., I. Balin, H. van den Bergh and B. Calpini. DOAS 2000 characterization, calibration and development. Activity report. EPFL/LPAS, Lausanne, 1998

Jiménez, R., T. Iannone, H. van den Bergh, B. Calpini and D. Kita. Investigation of the emission of monocyclic aromatic hydrocarbons from a wastewater treatment plant at Lausanne (Switzerland) by differential optical absorption spectroscopy (DOAS). *A&WMA 93rd Annual Conf. & Exhib.*, Salt Lake City, June 18-22, 2000: Paper 830

Lindström, T., U. Holst and H. Edner. Robust local polynomial regression and statistical evaluation of DOAS measurements. M.Sc. Thesis, Lund University - Lund Institute of Technology, Lund (Sweden), 1996

Meller, R. and G.K. Moortgat. Temperature dependence of the absorption cross sections of formaldehyde between 223 and 323 K in the wavelength range 225-375 nm. *J. Geophys. Res.* 105 (D6): 7089-7101, 2000

Peng, W.X., K.W.D. Ledingham, A. Marshall and R.P. Singhal. Urban air pollution monitoring: Laser-based procedure for the detection of NO_X gases. *Analyst* 120: 2537-2542, 1995

Plane, J.M.C. and N. Smith. Atmospheric monitoring by differential optical absorption spectroscopy. **In** R.J.H. Clark and R.E. Hester (ed), Spectroscopy in environmental science, Wiley, Chichester (UK), 1995: 223-262

Platt, U. Differential optical absorption spectroscopy. **In** M.W. Sigrist (ed), Air monitoring by spectroscopic techniques, Wiley, New York, 1994: 27-84

Quenzel, H. Scattering, absorption, emission and radiative transfer in the atmosphere. **In** P. Camagni and S. Sandroni (ed), Optical remote sensing of air pollution, Elsevier, Ispra (Italy), 1983: 1-25

Rothman, L.S., C.P. Rinsland, A. Goldman, S.T. Massie, D.P. Edwards, J.-M. Flaud, A. Perrin, C. Camy-Peyret, V. Dana, J.-Y. Mandin, J. Schroeder, A. McCann, R.R. Gamache, R.B. Wattson, K. Yoshino, K.V. Chance, K.W. Jucks, L.R. Brown, V. Nemtchinov and P. Varanasi. The HITRAN molecular spectroscopic database and HAWKS (HITRAN atmospheric workstation): 1996 Edition. *JQSRT* 60: 665-710, 1998

Saleh, B.E.A. and M.C. Teich. Fundamentals of photonics. Wiley, New York, 1991

Savitzky, A. and J.E. Golay. Smoothing and differentiation of data by simplified least squares procedures. *Anal. Chem.* 36 (8): 1627-1639, 1964

Schiff, H.I., G.I. MacKay and J. Bechara. The use of tunable diode laser absorption spectroscopy for atmospheric measurements. **In** M.W. Sigrist (ed), Air monitoring by spectroscopic techniques, Wiley, New York, 1994: 239-333

Schreier, F. The Voigt and complex error function: A comparison of computational methods. *JQSRT* 48 (5/6): 743-762, 1992

Steinfeld, J.I. Molecules and radiation: An introduction to modern molecular spectroscopy. MIT Press, Cambridge (MA), 1993

Stutz, J. Messung der Konzentration troposphärischer Spurensstoffe mittels Differentieller-Optischer-Absorptionsspektroskopie: Eine neue Generation von Geräten und Algorithmen. Ph.D. Thesis, Ruprecht-Karls-Universität, Heidelberg, 1996a

Stutz, J. and U. Platt. Numerical analysis and estimation of the statistical error of differential optical absorption spectroscopy measurements with least-squares methods. *Appl. Opt.* 35 (30): 6041-6053, 1996b

Swanson, N.L., B.D. Billard and T.L. Gennaro. Limits of optical transmission measurements with application to particle sizing techniques. *Appl. Opt.* 38 (27): 5887-5893, 1999

Szekely, L. Contribution to the development of a calibration system for the measurement of nitrous acid (HONO) by differential optical absorption spectroscopy (DOAS). Diploma Work (Environmental Engineering), EPFL-University of Veszprém, Lausanne, 2000

Trost, B., J. Stutz and U. Platt. UV-absorption cross sections of a series of monocyclic aromatic compounds. *Atmos. Environ.* 31 (23): 3999-4008, 1997

Vandaele, A.C., P.C. Simon, J.M. Guilmot, M. Carleer and R. Colin. SO_2 absorption cross section measurement in the UV using a Fourier transform spectrometer. *J. Geophys. Res.* 99 (D12): 25599-25605, 1994

Vandaele, A.C., C. Hermans, P.C. Simon, M. Carleer, R. Colin, S. Fally, M.F. Mérienne, A. Jenouvrier and B. Coquart. Measurements of the NO_2 absorption cross-section from 42000 cm^{-1} to 10000 cm^{-1} (238-1000 nm) at 220 K and 294 K. *JQSRT* 59: 171-184, 1998

Volkamer, R., T. Etzkorn, A. Geyer and U. Platt. Correction of the oxygen interference with UV spectroscopic (DOAS) measurements of monocyclic aromatic hydrocarbons in the atmosphere. *Atmos. Environ.* 32 (21): 3731-3747, 1998

Young, A.T. On the Rayleigh-scattering optical depth on the atmosphere. *J. Appl. Meteor*. 20 (3): 328-330, 1981

Zahniser, M.S., D.D. Nelson and C.E. Kolb. Tunable Infrared Laser Differential Absorption Spectroscopy (TILDAS) sensors for combustion exhaust pollutant quantification. **In** K. Kohse-Hoinghaus and J. Jeffries (ed), Applied combustion diagnostics, Taylor & Francis, London, 2002: 648-668

Chapter 4

Differential Optical Absorption Spectroscopy (DOAS): Laboratory and Field Measurements

This chapter concerns the characterization, test and development of DOAS 2000, a monostatic DOAS system. After characterizing its current light detection system, based on a linear scanner system and a photomultiplier tube (PMT), the results of a test with a photodiode array (PDA) are analyzed and discussed in detail. This chapter reports the development and application of a calibration bench, including a nitrous acid (HONO) generator. Detection limits derived from sequential lamp spectra and laboratory measurements with calibration tanks and the HONO generator are presented and compared. A laboratory intercalibration and various blind intercomparisons with other DOAS systems, point monitors and analytical techniques are analyzed.

4.1 Instrument description, characterization and development

The Differential Optical Absorption Spectroscopy (DOAS) system characterized, improved and used in this research is a monostatic DOAS manufactured by Thermo Electron Air Quality Inc. (formerly Thermo Environmental Instruments Inc., Franklin – MA, USA) under the trade name of *DOAS 2000* (Kita, 2000; TEI, 1999). The system was originally prototyped and patented by Unisearch Associates Inc. (Concord – Ontario, Canada) under the name of *SENSAIR* (Schiff, 1997). DOAS research here reported was carried out within a joint project between Thermo Environmental Instruments Inc. and EPFL/LPAS. The project was aimed at characterizing and improving DOAS 2000.

A schematic representation of DOAS 2000 is shown in **Figure 4-1**. DOAS 2000 is a monostatic DOAS system that uses a coaxial Cassegrain telescope for light emission and collection, and a linear-scanner Czerny-Turner spectrometer for spectral analysis. The optical path is folded using a corner cube retroreflector. Details are given in the sections that follow, in **Table 4-1**, and in other reports (Jiménez, 1998).

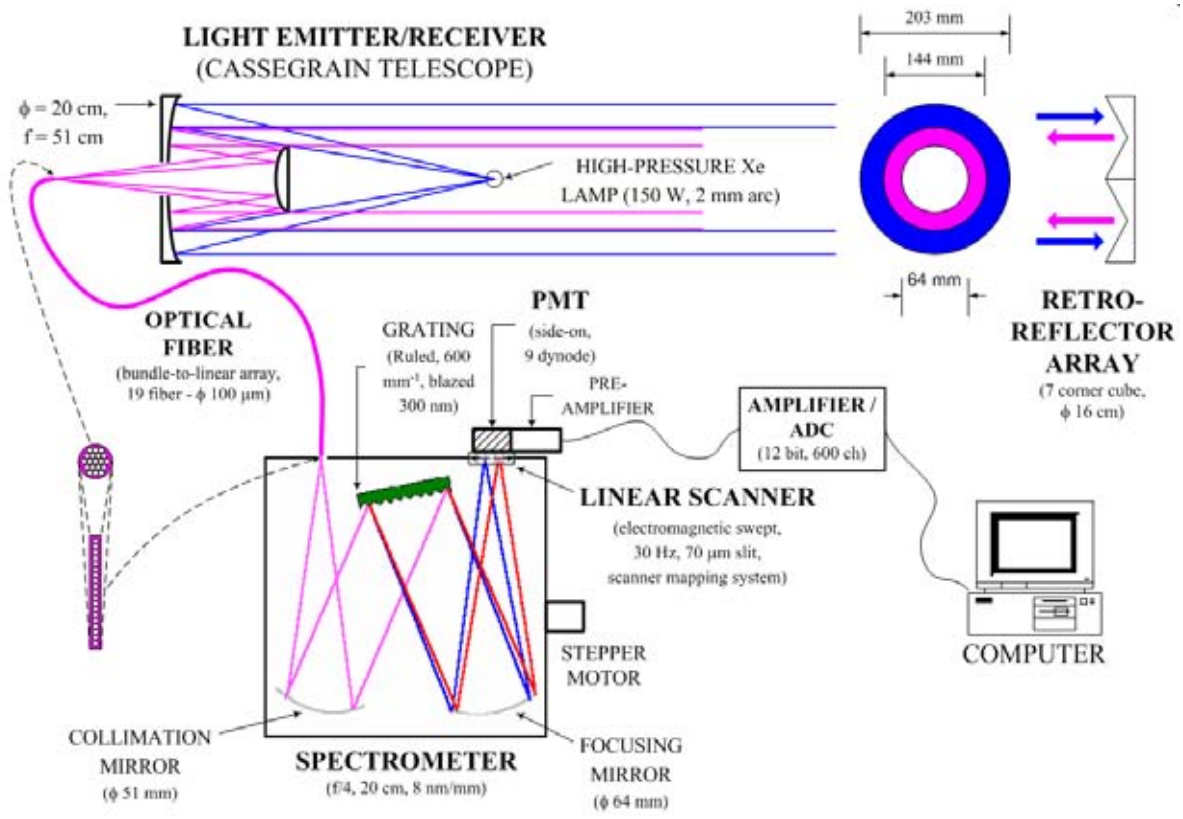

Figure 4-1. Schematic representation of the DOAS system used in this research (DOAS 2000, Thermo Electron Air Quality)

Telescope		
Type:	***Cassegrain***	
Main mirror:	f =	508.0 mm
	D =	203.2 mm
	f/D =	2.5
Convex mirror:	D =	63.5 mm
Light emission		
Ring radii =	72 - 102 mm	
Eff. f/D =	2.5	
Light collection		
Ring radii =	32 - 72 mm	
Eff. f/D =	3.5	

Optical fiber	
Type:	***Bundle to linear array***
Material:	Fused silica core / Doped silica cladding
# fibers =	19
NA =	0.12
L =	210 cm
Input:	*Circular aperture (bundle)*
Diameter: Fiber =	100 μm
Bundle =	620 μm
Output:	*Linear array (slit-like)*
W =	100 μm
H =	3.7 mm

Retroreflector	
Type:	***Corner cube***
Material:	MgF_2 / aluminum
Eff. D =	159 mm
# cubes =	7
Cube length =	35 mm

Spectrometer			
Type:	***Czerny-Turner***		
Focal length =	203.2 mm		
Fixed angle =			
Mirror	**f [mm]**	**D [mm]**	**f/D**
Collimating	203.2	50.8	4.0
Focusing	190.5	63.5	3.0
Grating			
Type:	*Ruled*		
Manufacturer:	ISA-Horiba		
Model:	510-11-110		
Groves =	600 mm^{-1}		
Blaze wavelength =	300 nm		
Dimensions =	58x58 mm		
Slit:	W =	70 μm	
	H =	3.5 mm	
Performance			
Dispersion =	8 nm/mm		
Resolution =	0.56 nm FWHM		

Light detection and spectral scanning	
Type:	***Linear scanner / PMT***
PMT	
Type:	*Side-on / Circular cage*
Manufacturer:	Hamamatsu
Model:	R2368
Positioning:	Horizontal
Active area =	16x18 mm
Spectral response =	185-850 nm
Peak response at =	420 nm
Cathode sensitivity =	150 μA/lm
Gain (max) =	$1.3x10^6$
Supply voltage (max) =	1250 V
Wavelength scanner	
Type:	*Linear (electromagnetically-swept slit)*
Scanning frequency =	30 Hz
Eff. amplitude =	4 mm
Analog-to-digital converter	
Resolution =	12 bit
Eff. sampling rate =	36 kHz
Scanner mapping system	
Type:	*Diode laser / masked photocell*
Mapping points =	17
Photocell pulse width =	1.7 ms

Table 4-1. Technical specifications of DOAS 2000.

4.1.1 A linear wavelength-scanning Czerny-Turner monochromator

The spectrometer was visually inspected and dismounted for accurate determination of its geometry. The optical fiber was inspected and metered under the microscope.

DOAS 2000 uses a compact f/4, 20 cm Czerny-Turner spectrometer for light analysis (see photograph in **Figure 4-2**). Light is delivered to the spectrometer via a 2.1-m long bundle-to-linear-image optical fiber composed of nineteen 100-μm fused silica fibers. Incoming light is collected by a ϕ 51 mm (2″), f/D = 4 spherical mirror, which collimates and images light onto a 600 mm^{-1} ruled grating (300 nm blazed equivalent-wavelength). Upon diffraction, the beam is focused onto a linear scanner using a ϕ 64 mm (2½″), f/D = 3 spherical mirror. Light is scanned with a 70 μm slit mounted on an electromagnetically driven coil that oscillates at 30 Hz. This spectral acquisition frequency is high enough to avoid the effects random light intensity variations due atmospheric turbulence, typically within the ~1-10 Hz range (Platt, 1994). The scanner position is quasi-real-time mapped using a diode laser/photocell system perpendicular to the detection plane.

Wavelength in the DOAS 2000 scanning monochromator is a function of the lead screw position, as determined by the stepper motor position (*mp*), and by the scanner position (*sp*). The center wavelength (λ_C), i.e. the wavelength at the geometric center of the scanner ($sp = 0$) depends only on the lead screw position. The wavelength calibration equation is thus expressed as,

$$\lambda(mp, sp) = \lambda_C(mp) + \Delta\lambda_C(mp, sp) \qquad \text{(Equation 4-1)}$$

where $\Delta\lambda_C$ is the difference to the center wavelength at a given stepper motor position as a function of the moving slit position. Accordingly the DOAS 2000 spectrometer is calibrated following a 2-step procedure, which differs slightly from procedures applied to single-channel detector spectrometers or to MA[1]-based spectrographs.

This first step aims at determining the dependence of center wavelength on motor position. For this purpose, the motor position is automatically tuned until observing the peak of selected standard atomic or laser transitions at scanner position the closest possible to its geometric center ($sp = 0$). Various Hg lines and a HeNe laser line (632.8 nm) are customarily used for calibration. The calibration is performed on a regular basis also in the field using a telescope in-built low-pressure Hg lamp / shutter system.

As expected for a cosinus mechanism, the center wavelength depends linearly on the number of turns of the lead screw, i.e. on stepper motor position (*mp*),

$$\lambda_C = a_0 + a_1 \cdot mp + a_2 \cdot mp^2 \qquad \text{(Equation 4-2)}$$

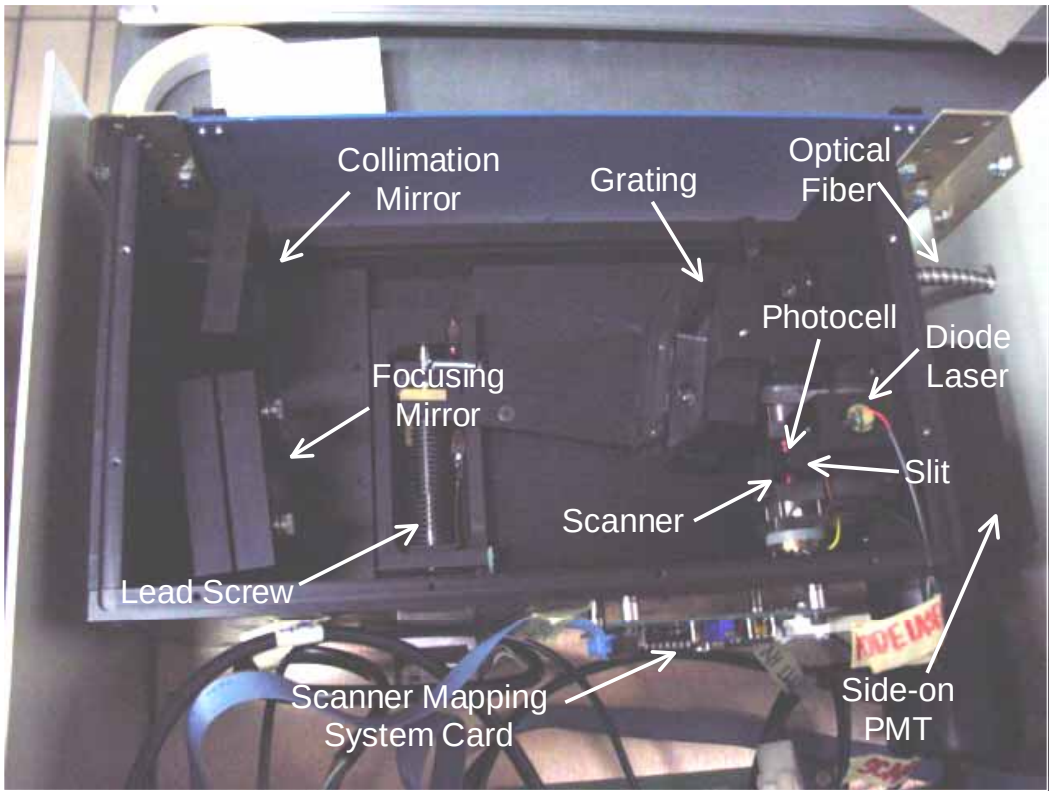

Figure 4-2. Anotated photograph of the DOAS 2000 spectrometer.

[1] Multichannel Analyzer (MA): this generic term applies for array detectors such as PDA (PhotoDiode Array) and CCD (Charge Coupled Device)

The second order constant (a_2) accounts for small non-linearity due to minute alignment errors. A typical center wavelength calibration curve is shown in **Figure 4-3**. The first constant, i.e. the center wavelength at $mp = 0$, a_0 = 216 nm, is the shortest wavelength that can be analyzed with the spectrometer. The linear term constant, a_1 = 0.9 Å/step, indicates that the center wavelength can be set at discrete steps of ±0.9 Å at a stepper motor accuracy of ±1 steps. Accurate control of the stepper motor leads to a statistically better overall accuracy of the center wavelength calibration curve, as indicated by polynomial fitting residuals of less than ±0.5 Å.

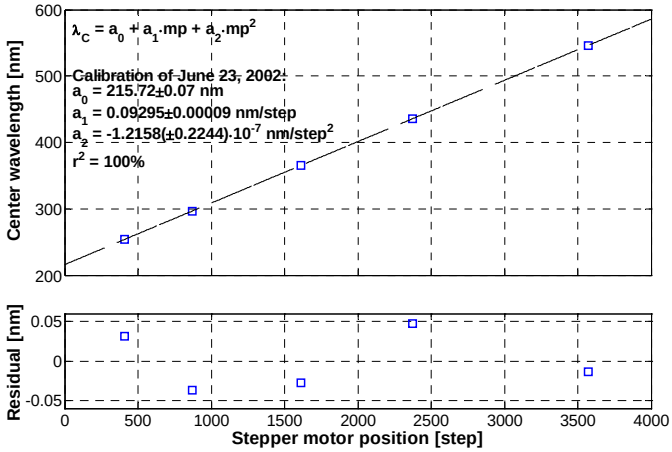

Figure 4-3. Center wavelength as a function of the lead screw position (calibration of 23rd June 2002). Residuals are within ±0.5 Å.

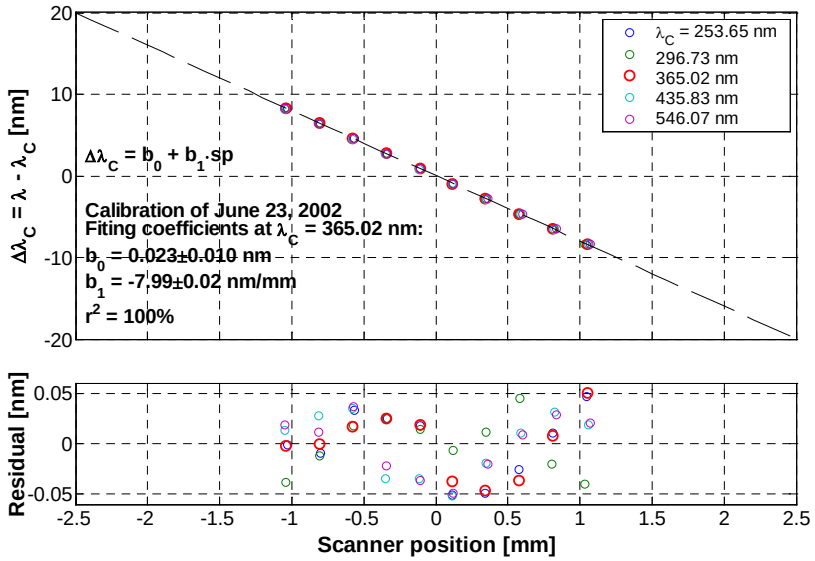

Figure 4-4. Wavelength difference dependance on the scanner position (calibration of 23rd June 2002). Residuals are within ±0.5 Å.

Following determination of the center wavelength calibration curve, the scanner calibration curve is determined by measuring the scanner position of each calibration lines at various motor positions, usually within ±90 steps (i.e. ± 8 nm), around their center wavelength positions ($sp = 0$). Wavelength differences to center wavelengths are calculated using the lead screw calibration curve and accurately known calibration wavelengths. As expected for a nearly flat field, the wavelength difference is a linear function of the scanner position as measured by the scanner mapping system,

$$\Delta\lambda_C = b_0 + b_1 \cdot sp \qquad \text{(Equation 4-3)}$$

The scanner calibration curve that accompanies the lead screw calibration curve above is shown in **Figure 4-4**. The linear regression constant (b_0) indicates a wavelength-equivalent scanner shift of 0.2 Å. This shift is statistically not different from zero, particularly when referred to the calibration curve residuals (±0.5 Å). The wavelength dispersion at the focal plane, i.e. the linear term constant, b_0 = 8 nm/mm, is on the contrary obtained with a high degree of precision (coefficient of variation, CV = 0.20%). The elevated precision is indicative of the flatness of the focal plane within the scanner range mapped. Spectra are reconstructed from time-dependent light intensity signal recorded only over the centralmost (quasi-linear) part of the scanner sinusoidal oscillation. The scanner amplitude effectively retained is ~4 mm, which results in ~32-nm wide spectra.

Periodic, automatic recording of Hg lines during a large number of field studies shows that the overall wavelength accuracy in field conditions is typically within ±1 Å, and in all cases better than ±3 Å.

4.1.2 Thermal management system

The DOAS system used in this research (DOAS 2000) was devised to operate at permanent monitoring sites. In contrast, the main application at EPFL/LPAS has been monitoring at temporary sites within field studies[2]. Temporary installation imply in general tougher operational conditions compared to permanent installation, particularly in terms of optical alignment stability. This is especially valid for DOAS 2000, which does not incorporate any active positioning system.

DOAS 2000 includes a 140×64×63 cm environmental enclosure (shelter) that houses the telescope, the spectrometer, and the Xe lamp power supply unit (PSU). See **Annex A**. The environmental enclosure, as originally designed, used a 410-W air conditioning unit (ACU – McLean Midwest, Proair CR23) and two radiators for temperature control. Thermal management with this type of system carries two intrinsic disadvantages:

[2] The system was applied also for laboratory measurements, as for instance for the calibration of a QCL-based O_3 detection system (refer to Chapter 5)

(1) Temperature control is limited to ON/OFF operation. Moreover, in order to prevent from ACU failure in the long term, a substantial gap has to be allowed between the ON/OFF temperature set points resulting in a fairly poor temperature control, ±5 K at the best.
(2) ACU was mounted directly on the environmental enclosure. Particularly in summer time, periodic compressor startups resulted in alignment loss in the long run. Partially due to this, alignment loss rates as high as ~1%/day were observed during some campaigns (see example in **Figure 4-5**).

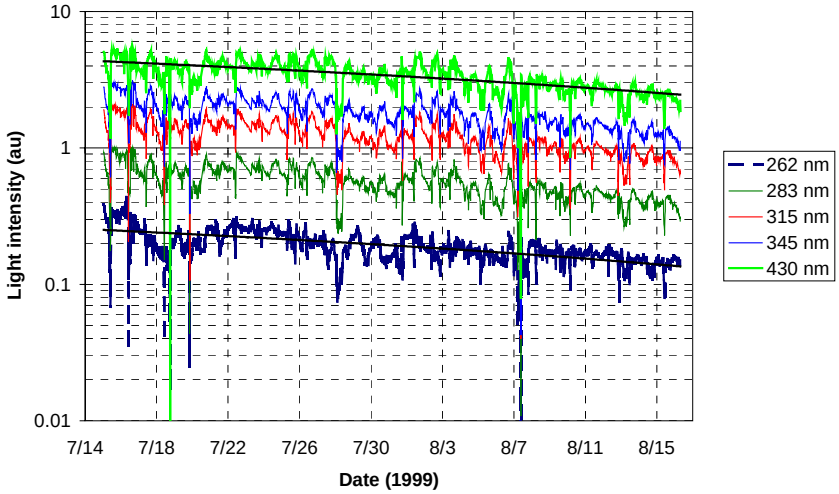

Figure 4-5. Time series of collected light intensity at 5 center wavelengths as recorded at Vif (suburban Grenoble, France) during GRENOPHOT 1999. Intensities are all referred to a photomultiplier supply voltage of 620 V. Note that the intensity at 262 nm is one order of magnitude lower compared to the intensity at 430 nm.

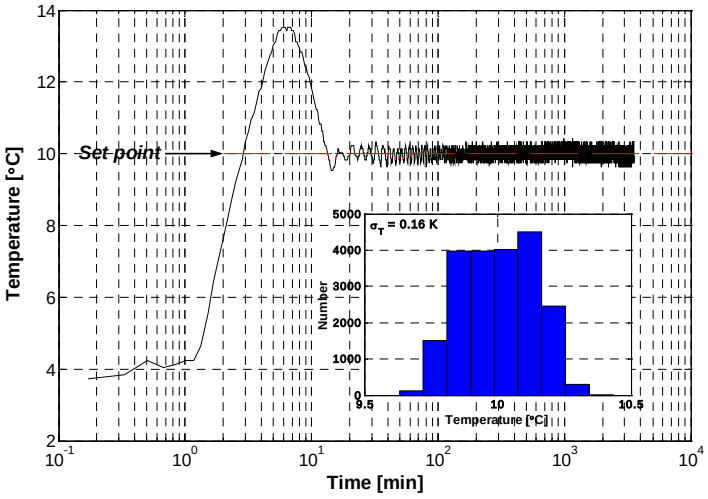

Figure 4-6. Temperature inside the DOAS 2000 environmental enclosure (spectrometer side) during January 9-12, 2003 (10-s resolved data). Ambient temperature at the start of the test was below 4 ºC. Temperature is controlled with a 6×80 W Peltier-based system.

The ACU/radiator system was replaced with a homebuilt Peltier-based thermal management system in order to overcome these problems. Peltier-based systems have the intrinsic advantage of providing cooling and heating upon simple polarity change, and have no moving parts. The system was devised to control the shelter temperature within ±0.5 K, and consists of six 72-W Peltier elements (Melcor, PT-8-12-40), a PID[3] temperature controller (RKC, CB100), an AC/DC transformer, and efficient fans and heat exchangers (see **Annex A**). A typical performance in winter conditions is shown in **Figure 4-6**. It is observed that starting from ~4 ºC (ambient temperature), the system damps until attaining stationary conditions (temperature setpoint = 10 ºC) after ~15 min of operation. Control achieved in these conditions was ±0.16 K (1-sigma). This very good performance is characteristic of "heating-only" conditions. It is obviously more difficult to control the shelter temperature when cooling is required. In harsh summer conditions, like for instance during the ESCOMPTE campaign (Marseilles area - France, 2001), the system was found capable of controlling the temperature within about ±2 K. This performance is weak compared to the design goal but far better than would be achieved with the original thermal management system. More importantly, mechanical vibration was essentially suppressed with the Peltier-based system.

4.1.3 Photomultiplier tube (PMT) response

DOAS 2000 utilizes a 9-dynode (circular cage) side-on PhotoMultiplier Tube (Hamamatsu, R2368) for light detection (refer to **Table 4-1**). Hamamatsu R2368 PMT technical data sheet is reproduced in **Annex B**. Two aspects of PMT response were investigated in laboratory conditions: dark current and gain.

The main sources of dark current[4] are ohmic leakage and thermionic emission from the photocathode (Jenkins, 1987; Moore, 2003). If thermionic emission dominates, the dark current increases exponentially with the square of the potential applied to the PMT,

$$j_D(HV) = j_D(0) \cdot \exp\left(\beta\sqrt{HV}\right) \qquad \text{(Equation 4-4)}$$

where *HV* is the PMT supply voltage (photocathode-to-anode potential), $j_D(0)$ is the dark current at zero voltage, and β is a temperature-dependent constant. The thermionic emission model explains accurately the Hamamatsu R2368 dark current data[5], which indicates that ohmic leakage is very low in this particular PMT (see **Figure 4-7**).

DOAS 2000 dark noise spectra[6] measured in the laboratory are shown in **Figure 4-8**. As expected, noise levels display random variation around center values that are essentially independent of the wavelength and are largely determined by the supply voltage. Wavelength independence, particularly at high supply voltages, is indicative of the good optical isolation

[3] PID: Proportional-Integral-Derivative

[4] PMT current output in absence of input light

[5] Data were kindly provided by Hamamatsu Photonics France, Swiss Office

[6] Spectra of signal in absence of input light

of the spectrometer. Nevertheless, the dark noise increases with the supply voltage less rapidly that it should do if thermionic emission were the main source of noise. Noise spectra measurements are thus in apparent contradiction with Hamamatsu data. Quite good agreement to the thermionic emission model (i.e. good linearity on the logarithmic scale) is notwithstanding observed upon subtraction of the dark noise at zero voltage (see **Figure 4-9**). The zero-voltage noise (~2.7 mV rms on average) is indeed the lowest noise level that can be obtained with the DOAS 2000 spectrometer in its current configuration. It originates from various sources, especially the PMT pre-amplifier and the analog-to-digital-converter (ADC). The zero-voltage noise is comparable or even higher than the thermionic dark noise at low voltages. The operational range of the 12-bit ADC converter of DOAS 2000 is 0-10 V. In order to ensure good digital conversion accuracy, the PMT supply voltage is adjusted so to obtain output signals on the order of ~5 V. The zero-voltage noise is about 0.06% of this output level at a typical PMT supply voltage of 700 V.

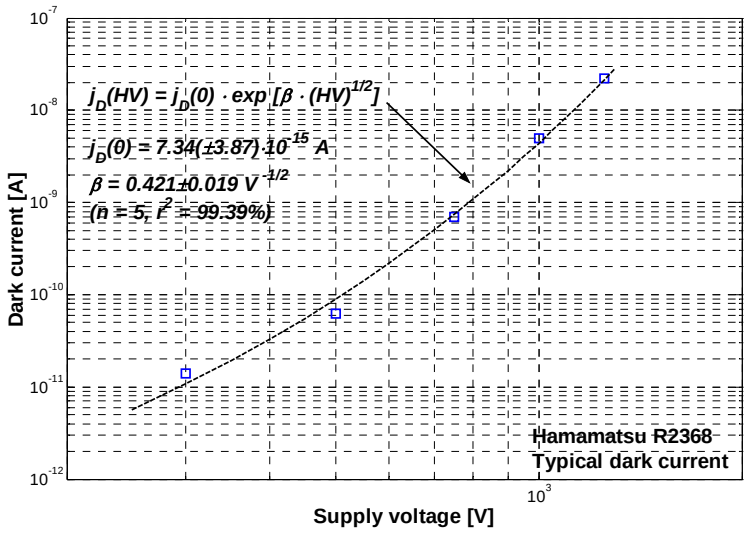

Figure 4-7. Typical dark current of the PMT (Hamamatsu, R2368) used by the DOAS 2000 spectrometer as a function of the supply voltage. Data was fitted of data to a thermionic emission model (Dark current data was kindly provided by Hamamatsu Photonics France – Swiss Office).

Far more relevant in terms of differential detection capability is the "differential" component of the dark noise. Splitting of the spectrometer noise into its slow- ($\delta_{I,0}$) and rapid-varying components ($\Delta\delta_I$) with wavelength[7],

$$\delta_I(\lambda) = \delta_{I,0}(\lambda) + \Delta\delta_I \qquad \text{(Equation 4-5)}$$

[7] As for the cross section and the absorbance in the previous chapter

leads to the following expression for the noise-baseline corrected, measured differential absorbance (ΔD^*),

$$\Delta D^*(\lambda) = \frac{\Delta I(\lambda) - \Delta\delta_I}{I_0'^*(\lambda) - \delta_{I,0}(\lambda)} \qquad \text{(Equation 4-6)}$$

where ΔI is the "true" intensity dip, and $I_0'^*$ is the synthetic baseline (refer to **Section 3.5** for details, particularly to **Equation 3-38**). Note that the rapid-varying component of the noise ($\Delta\delta_I$) is assumed to be random, thus wavelength-independent. This term appears only in the numerator of the **Equation 4-6** since the synthetic baseline is not a measured but a "statistically" calculated wavelength function. Moreover, the slow-varying component of the noise is in most cases small compared to the synthetic baseline ($\delta_{I,0} \ll I_0'$), therefore the resulting noise in the differential absorbance ($\delta_{\Delta D}$) is proportional to the rapid-varying noise term, i.e. $\delta_{\Delta D} \approx -\Delta\delta_I / I_0'$.

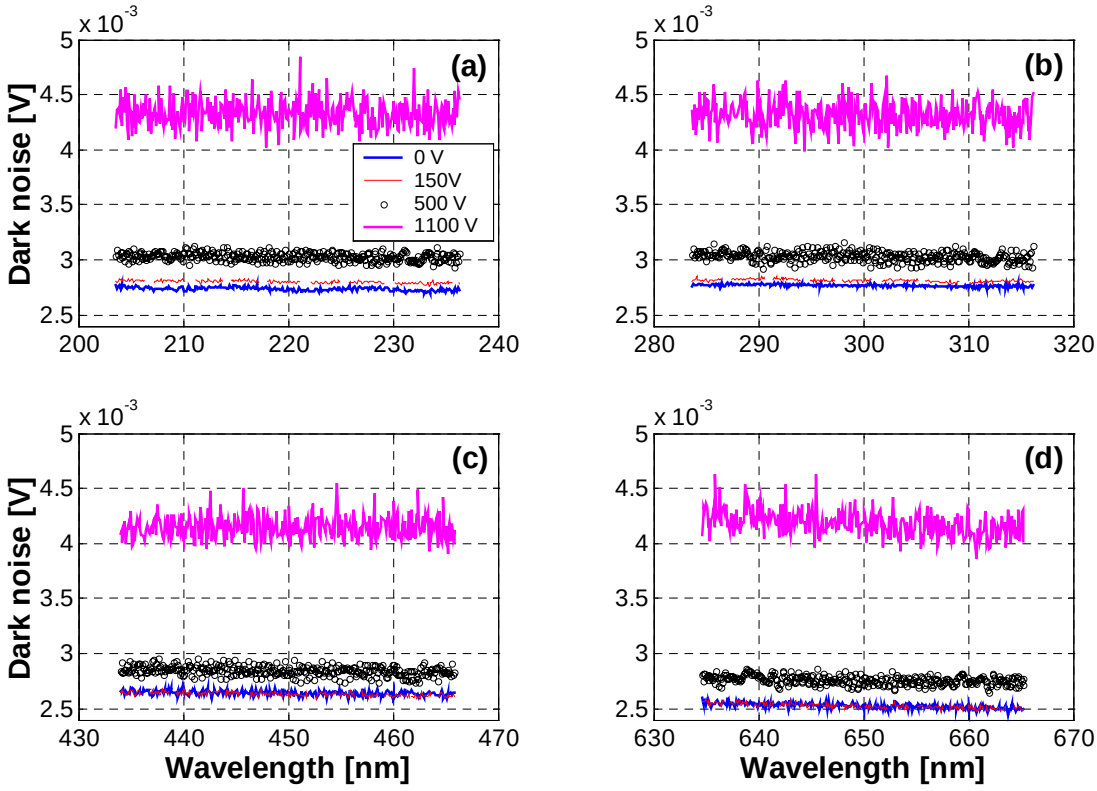

Figure 4-8. DOAS 2000 spectrometer dark noise spectra at various spectral ranges as a function of PMT supply voltage. Spectra were integrated over 1 min. Ordinate is the PMT pre-amplifier output in volts.

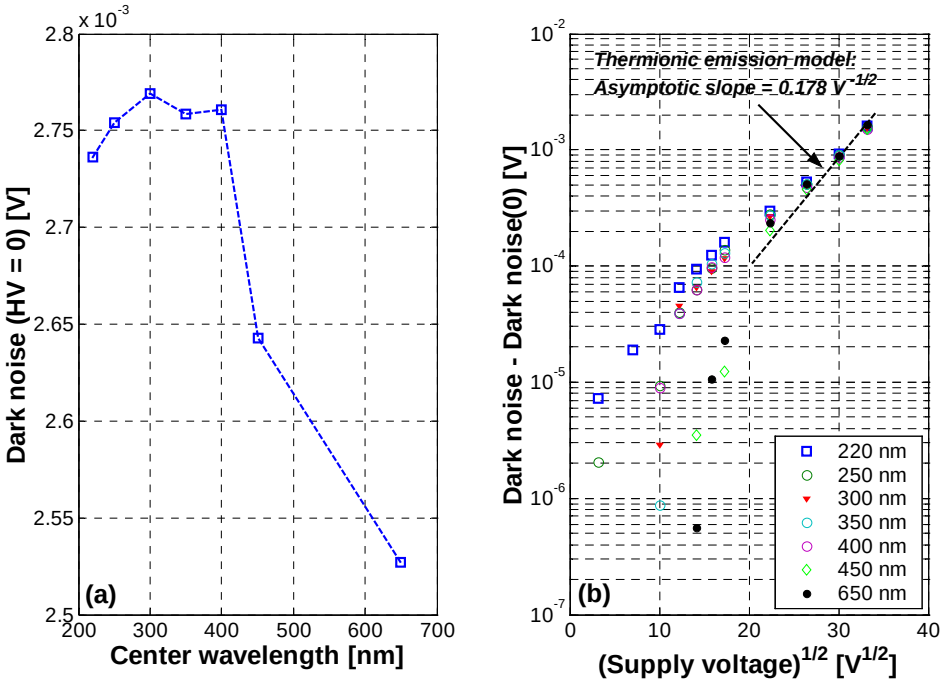

Figure 4-9. (a) Root-mean-square (rms) of the dark noise at zero supply voltage as a function of the center wavelength. **(b)** Dark noise diffrence referred to the noise at 0 V as a function of the square root of the supply voltage at various center wavelengths.

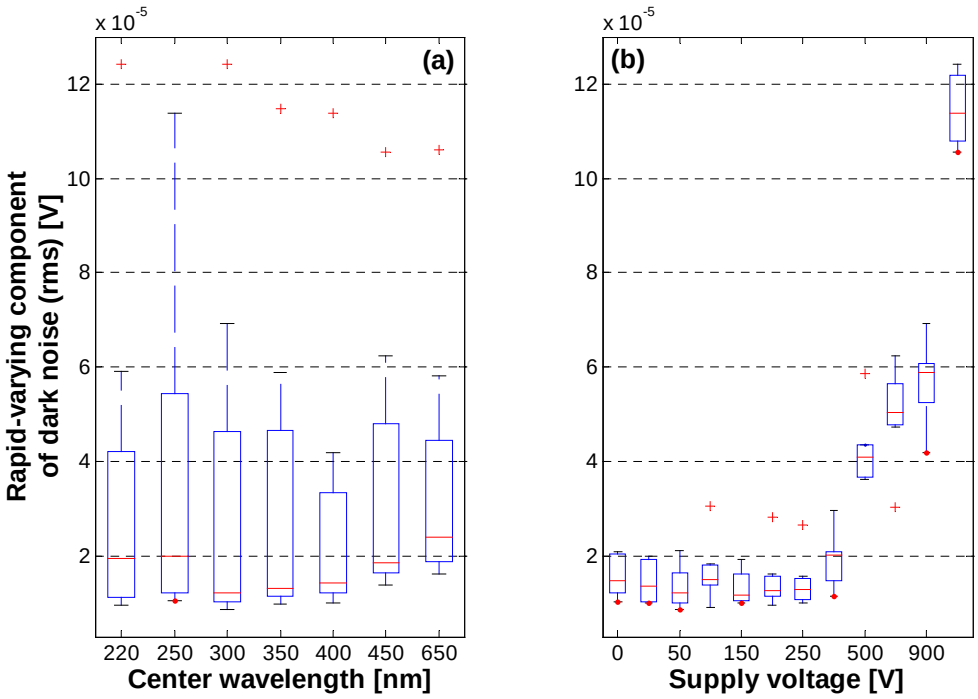

Figure 4-10. Root-mean-square (rms) of the rapid-varying component of the dark noise as a function of **(a)** the center wavelength and **(b)** the PMT supply voltage

The amplitude of the "differential" dark noise was estimated by subtraction of a 3rd degree fitting polynomial (low-pass filter) from the dark noise spectra, followed by root-mean-square (rms) averaging, $\Delta\delta_I = \mathrm{rms}\left[\delta_I - f_{LP}(\delta_I)\right]$. See box-and-whisker plots in **Figure 4-10**. As expected, the differential component of the dark noise is essentially independent of wavelength. In contrast, exponential increase with supply voltage is clearly observed from a "threshold voltage" of ~300 V. This is an expected result due to the random (pulsed) nature of thermionic emission, which implies exponential increase of both, average level and peak-to-peak variation (differential component), with supply voltage (Jenkins, 1987). More relevant for the purposes of this research is the fact that the differential component of the dark noise sets the theoretical lowest limit of detection (LDL). At ~700 V supply voltage with a light intensity of ~5 V, the lowest detectable fractional absorption with DOAS 2000 would be $\Delta D_{LDL} \approx 5 \cdot 10^{-5} / 5 \approx 10^{-5}$ at a signal-to-noise ratio (SNR) of 1 and for 1 min integration time. This calculation considers dark noise only. As discussed below, actual detection limits are up to two orders of magnitude higher.

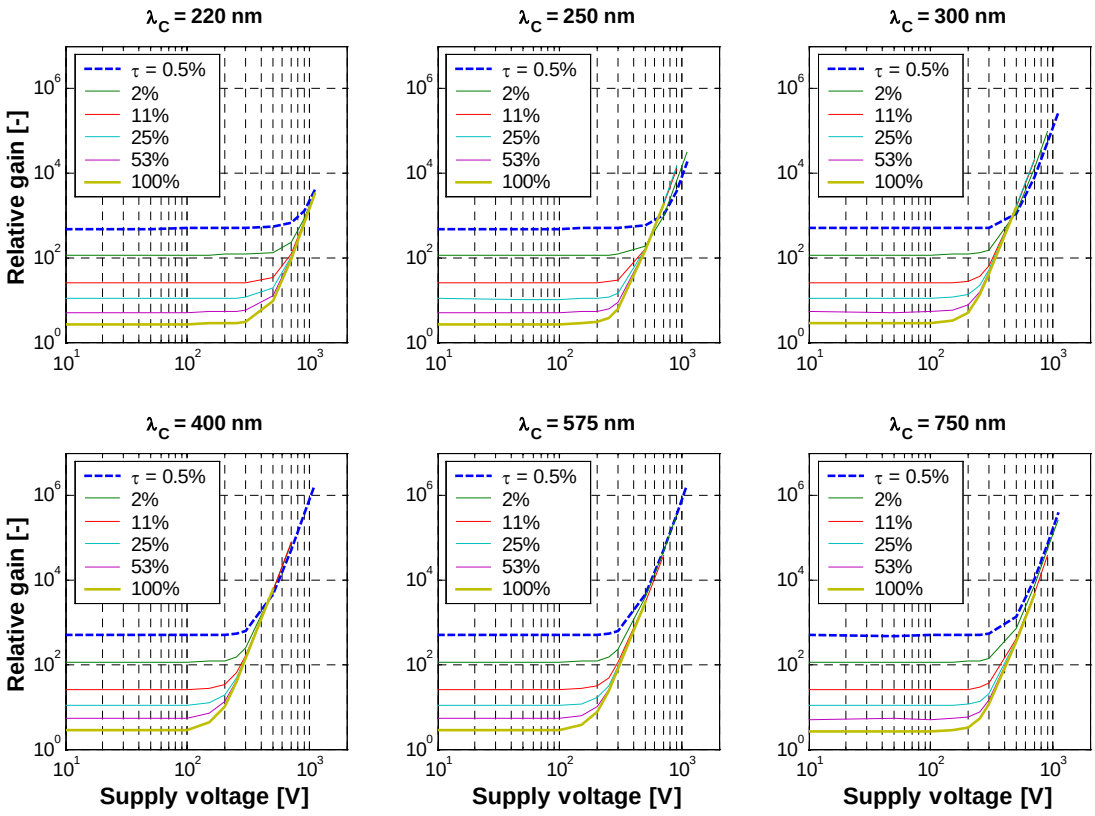

Figure 4-11. Gain curves of the PMT-based light detection system of DOAS 2000 at various center wavelengths.

The overall gain of a photomultiplier tube (G), i.e. the number of photoelectrons generated per photon, is proportional to the supply voltage powered to the number of dynodes (n_{dyn}),

$$G \sim HV^{\alpha_{dyn} n_{dyn}} \qquad \text{(Equation 4-7)}$$

The dynode coefficient, α_{dyn}, depends on the dynode material and usually varies between 0.7 and 0.8 (Jenkins, 1987).

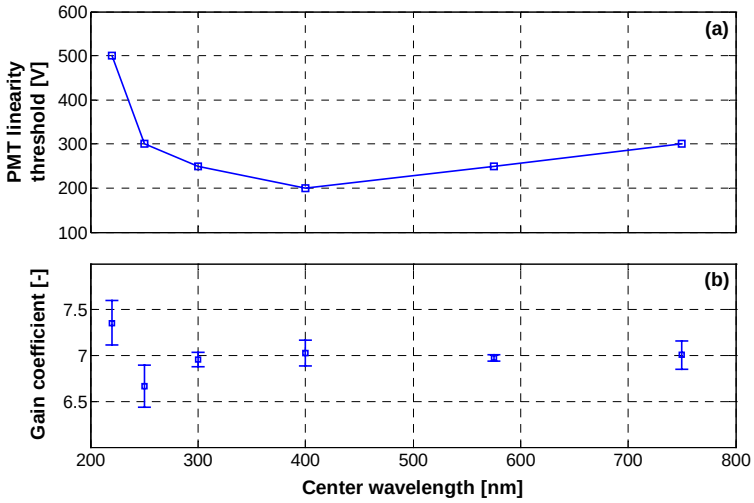

Figure 4-12. Hamamatsu R2368 PMT **(a)** linearity threshold voltages, and **(b)** gain coefficient derived from laboratory measurements.

Gain curves at various center wavelengths were determined by measuring the output signal at light intensities varied using neutral density filters (NDF) of 0.1%, 1%, 10%, 25%, and 50% nominal transmittance. The actual NDF transmittance was determined using a standard double beam spectrophotometer (Varian, Carry 500). For comparison purposes, an arbitrary, wavelength-independent value of 10^{-3} was used as "light intensity" before NDF. Results are shown in **Figure 4-11**. The "linearity threshold" voltage varies from 200 V at 400 nm to 500 V at 220 nm as shown in **Figure 4-12a**. This curve follows the PMT spectral response curves (cathode sensitivity and quantum efficiency) shown in **Annex B**. Below the wavelength-dependent linearity threshold voltages, the output signal is essentially constant, which explains the apparent (indeed illogical) gain increasing with decreasing input light intensity. Linearity threshold voltages ensue from a combination of wavelength-dependent factors, such as light source intensity[8], grating efficiency, and PMT cathode sensitivity and quantum efficiency (see **Table 4-1**). These factors combine to produce peak gain at about 400 nm. Maximum gain at this center wavelength ($1.8 \cdot 10^6$) is in agreement with manufacturer data (typical ~$1.3 \cdot 10^6$ – see **Annex B**).

[8] High-pressure, ozone-free Xe lamp (Hamamatsu, L2274)

Individual gain coefficients ($\alpha_{dyn} \cdot n_{dyn}$) for each center wavelengths were retrieved by linear fitting of log(*HV*) vs. log(G) data above linearity threshold. Correlation coefficients (r^2) were all higher than 99%. The average gain coefficient is 7.00±0.07. See **Figure 4-12b**. Hamamtsu R2368 is 9-stage PMT (n_{dyn} = 9). This gain coefficient implies thus a dynode coefficient of 0.777±0.007, in agreement with literature values (Jenkins, 1987).

PMT gain measurements allow appraising the light detection capability of DOAS 2000. Linearity threshold voltages determined in laboratory conditions (**Figure 4-12a**) provide a guideline for field measurements since they were performed using the same light source used in the field. Collected light levels in the field are nevertheless comparatively weaker towards the UV due to molecular (Rayleigh) and aerosol (Mie) scattering.

4.1.4 Light detection with a photodiode array (PDA)

Multichannel Analyzers (MA), particularly PhotoDiode Arrays (PDA), advantage scanner-based light detection systems (slotted disk and linear scanner) in terms of total number photons detected per unit time (Jenkins, 1987; Stutz, 1997). Provided good illumination conditions, PDA detectors are in principle a better alternative for low absorbance detection than CCD (Charge Coupled Device) detector due to their larger pixel capacity (~10^8 photoelectrons) compared to CCDs (~10^5 e^-). A higher SNR can be thus achieved with PDAs, despite their higher readout noise (~10^4 e^-) (PI, 1999). Notwithstanding this advantage, intrinsic characteristics of the PDA, such as its fairly high pixel-to-pixel variability (~1%) and the angular dependence of the detector response (Stutz, 1997), affect their performance in low absorbance applications (Platt, 1994). Solutions for these problems have been proposed and successfully demonstrated during the last years (Knoll, 1990; Stutz, 1997). Despite the proved reliability and performance of the slotted disk system, PDA detectors have grow increasingly popular for DOAS applications (Camy-Peyret, 1996; Evangelisti, 1995; Harder, 1997; Lanni, 1992; Plane, 1992; Stutz, 1996a; Stutz, 1997).

The use of a PDA for light detection in DOAS 2000 was tested in laboratory conditions. The PDA used in the test is a 1024-element NMOS[9] linear image sensor (Hamamatsu, S3903-1024Q♦) operating on a driver/amplifier electronics module (Hamamatsu, C4350)[10]. This head does not incorporate any thermoelectric (Peltier) cooling system. The detector was thus operated at ambient temperature. This supposes a quite high limitation in terms of integration time (Jenkins, 1987). Another limiting aspect of the detector is the photodiode height (25 μm × 0.5 mm sensitive area). Although this detector, particularly when operated at ambient temperature, is probably not the best choice for atmospheric measurements[11], it is still appropriate for an exploratory test in the laboratory. In fact, successful open path measurements using ambient-temperature operated PDA have been reported (Camy-Peyret,

[9] n-channel Metal Oxide Semiconductor (MOS) transistor (Jenkins, 1987)

♦ Quartz window

[10] The multichannel detection system used in this test (PDA, head, sofware) was kindly provided by Hamamatsu Photonics France – Swiss Office

[11] Hamamatsu S5931-1024S PDA (built-in Peltier cooler, 25 μm × 2.5 mm sensitive area) would be a better choice for eventual implementation in DOAS 2000

1996; Evangelisti, 1995). Even more, Evangelisti *et al* (1995) used the same head used in this investigation for atmospheric measurements in the Milan area.

The detection part (scanner + scanner mapping system + PMT) of the DOAS 2000 spectrometer was partially dismounted for the test (see **Figure 4-2**). The PDA was placed at the focal plane using a plate machined for this purpose. The head built-in kinematic mechanism allowed for final optical alignment of the PDA.

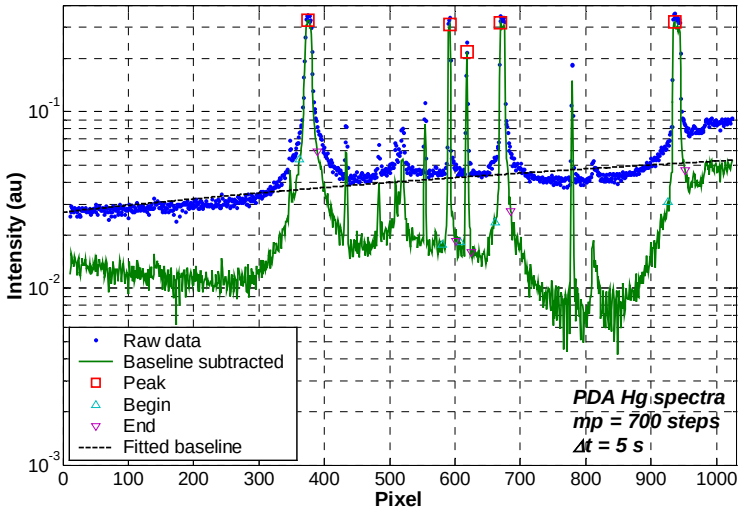

Figure 4-13. Initial fitting of a 5-s integrated Hg emission spectrum measured with a NMOS linear image sensor (Hamamatsu, S3903-1024Q). Fitting was obtained using the MATLAB-based *findPeakS.m* routine.

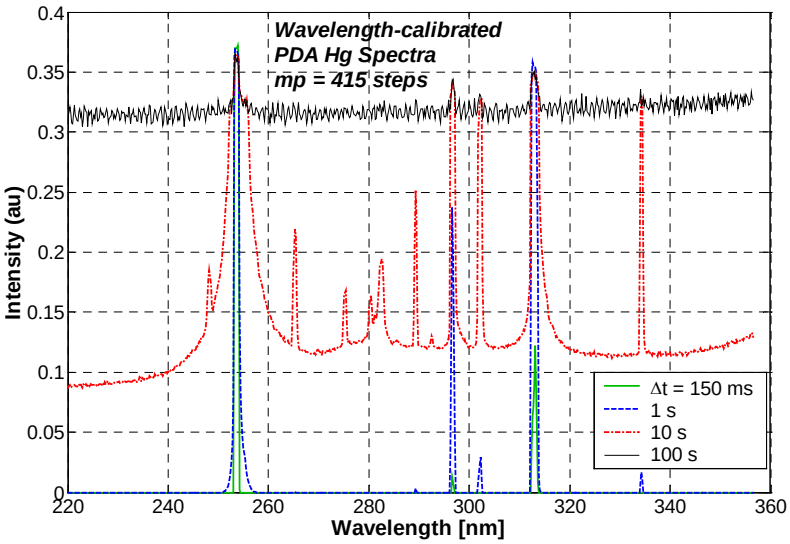

Figure 4-14. Low-pressure Hg lamp emission spectra as measured with an ambient-temperature operated PDA (Hamamatsu, S3903-1024Q) at various integration times.

Emission spectra of low-pressure Hg lamp integrated over 5 s at 23 motor positions were used for wavelength calibration (see example in **Figure 4-13**). Peak positions and transition characteristics where determined using *findPeakS.m* and *fitPeakS.m* algorithms and routines developed for the analysis of DOAS 2000 and QCL spectra (explanation in **Section 4.2**). Referring the pixel position (*i*) to a virtual center of (1024+1)/2 pixels, i.e. using $sp = i - 512.5$, fitting of the data to a composite of **Equations 4-1** through **4-3** yields the following wavelength calibration coefficients (r^2 = 100%):

a_0 = 216.478±0.067 nm

a_1 = 0.0922±0.0001 nm/step

b_1 = 0.1991±0.0001 nm/pixel

Coefficients a_2 and b_0 were assumed to be zero. Coefficients a_0 and a_1 agree well with the center wavelength calibration curve of the scanner-based system (see **Figure 4-3**), which shows that the PDA was appropriately positioned. Coefficient b_1 sets to ~2 Å the lowest achievable wavelength resolution of the DOAS 200 spectrometer using the S3903-1024Q PDA. The total sensitive width of the PDA is 25.6 mm (1024 photodiodes), thus the spectrometer dispersion at the focal plane as retrieved from the PDA calibration curve is 7.964±0.006 nm/mm. This figure perfectly matches (within the uncertainty limits) the scanner-based system dispersion (see **Figure 4-4**), indicating appropriate optical alignment of the PDA.

Ambient temperature operation implies elevated PDA dark currents that accumulate rapidly as shown in **Figure 4-14**. Noise level increases ~3 fold when passing from 10 to 100 s integration time. The highest SNR is thus obtained with an exposure time of 150 ms, the lowest allowed integration time for this particular PDA system.

NO_2 absorption spectra were obtained by co-addition of successive 150-ms spectra in order to test the detection capabilities of the system. NO_2 transmission spectra were measured while flowing 29.8(±2%) ppm NO_2 (calibration tank – SL Gas) through a 70 mm absorption cell. Baseline and transmitted light intensity spectra are shown in **Figure 4-15a**. A reasonable signal-to-noise ratio ($SNR = I/\sigma_I$) of ~250 is reached upon co-addition of twenty 150-ms spectra (see **Figure 4-15b**). The differential absorption was calculated by subtraction of a 6^{th} degree fitting polynomial.

Using a MA detector the spectral resolution is determined by the geometry of the spectrometer and in particular by the width of the entrance slit (Lerner, 1988). Hg transitions observed by the PDA at 150 ms integration time have linewidths that vary within 1.9-5.0 pixels FWHM. This variation is likely due to the high noise levels associated to ambient temperature operation (see **Figure 4-14**). In view of this uncertainty, the selected NO_2 cross section (Vandaele, 1998) was convolved with a Gaussian lineshape defined by the average linewidth (3 pixel – 0.60 nm FWHM). The measured spectrum was fitted to the convolved cross section using the non-linear least squares fitting routine developed for the analysis DOAS 2000 and QCL spectra (*fit2NLS3.m* – refer to **Section 4.2**). Very good agreement is observed overall the spectra range analyzed (350-530 nm), particularly when considering the very short integration time of the spectrum (2.85 s). Residual spectrum (R) values are very well described by a Gaussian distribution ($\sigma_R = 8 \cdot 10^{-4}$), which suggest that the residual is essentially featureless and stems mainly from random noise. Featured residual structures

(Stutz, 1996a; Stutz, 1997) are not observed. The retrieved concentration (34.6±0.99 ppm) is 16% higher than the stated tank concentration. The root-mean-square differential absorption to residual spectrum ratio (SNR = 1.5) provides a conservative estimate of the lower detection limit (LDL) of 1.6 ppm·m for a so defined SNR of 1. Assuming that noise decreases with the square root of the integration time ($SNR \sim \sqrt{\Delta t}$ - see **Section 4.3**), a LDL of 0.16 ppm·m would be attained after 5 min of spectral co-addition. This LDL is significantly smaller than the estimated detection limit of DOAS 2000 (0.25 ppm·m – see next section).

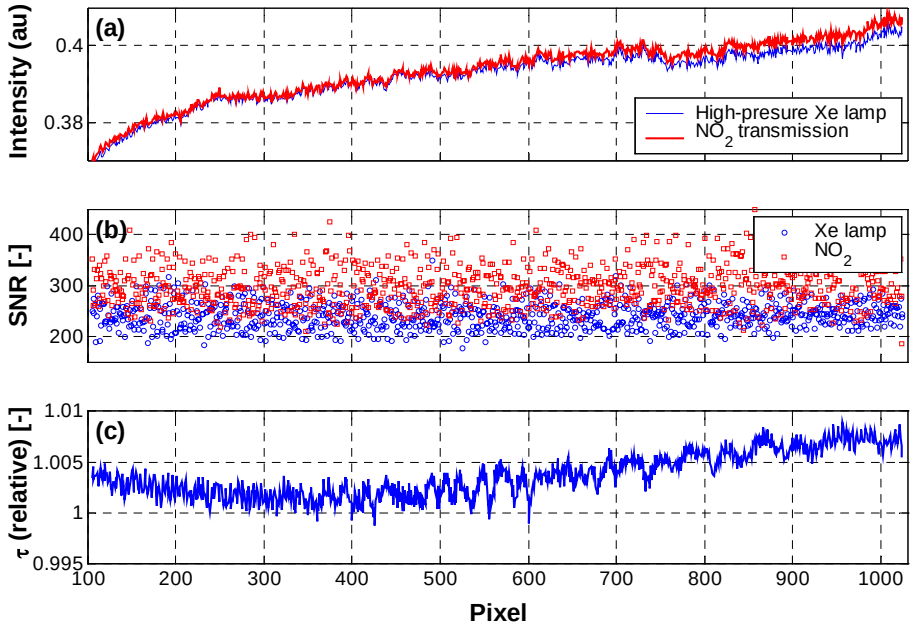

Figure 4-15. High-pressure Xe lamp emission and NO_2 transmission spectra measured with a PDA at *mp* = 2319 (center wavelength). Xe and NO_2 spectra in **(a)** are the average of twenty and nineteen 150-ms spectra, respectively. Panel **(b)** shows the averaged spectra signal-to-noise ratio (SNR). The lower panel shows NO_2 relative transmittance spectrum. NO_2 transmission spectrum in **(c)** was obtained by flowing 29.8 ppm NO_2 through a 70 mm long cell.

4.2 Algorithm and software development for concentration retrieval

DOAS 2000 uses a Windows®-based open-architecture software (developed in C++) for hardware control and data processing. Computer and spectrometer exchange information via a null modem RS-232 cable. The software allows full control of the spectrometer, and the Xe and Hg lamps (power supply units and Hg shutter) through operation algorithms written in a proprietary pseudo-language (similar to C++) and executed on a step-by-step basis (interpreter mode) (TEI, 1999). An example of interface screen in given in **Annex C**. In contrast to other commercial DOAS systems, DOAS 2000 offers the user a large degree of freedom concerning the operation of the system. User can choose wavelength ranges,

integration times, and developing her/his own data acquisition and processing routines. Notwithstanding this flexibility, currently available data processing functions in the DOAS 2000 interpreter show some limitations, particularly for the retrieval of important trace gases that are also minor light absorbers, e.g. CH_2O, HONO and MAH. DOAS 2000 software was devised for concentration retrieval based on reference spectra. Therefore, it does not incorporate functions for the extraction of the instrument function from (or by fitting of) atomic transitions nor for convolution of highly resolved cross sections. Another limitation is that only a single spectral subrange can be used when fitting spectra. In this investigation it was found that eliminating from evaluation short subranges that contain broaden Xe emission transitions improves the retrieval. Such a procedure was found particularly advantageous for the retrieval of formaldehyde in the 300-330 nm region (see **Section 6.1**). Finally, the software is limited to linear fitting. (Local) optimum spectral shift and stretch values can be determined but referred only to a single reference spectrum.

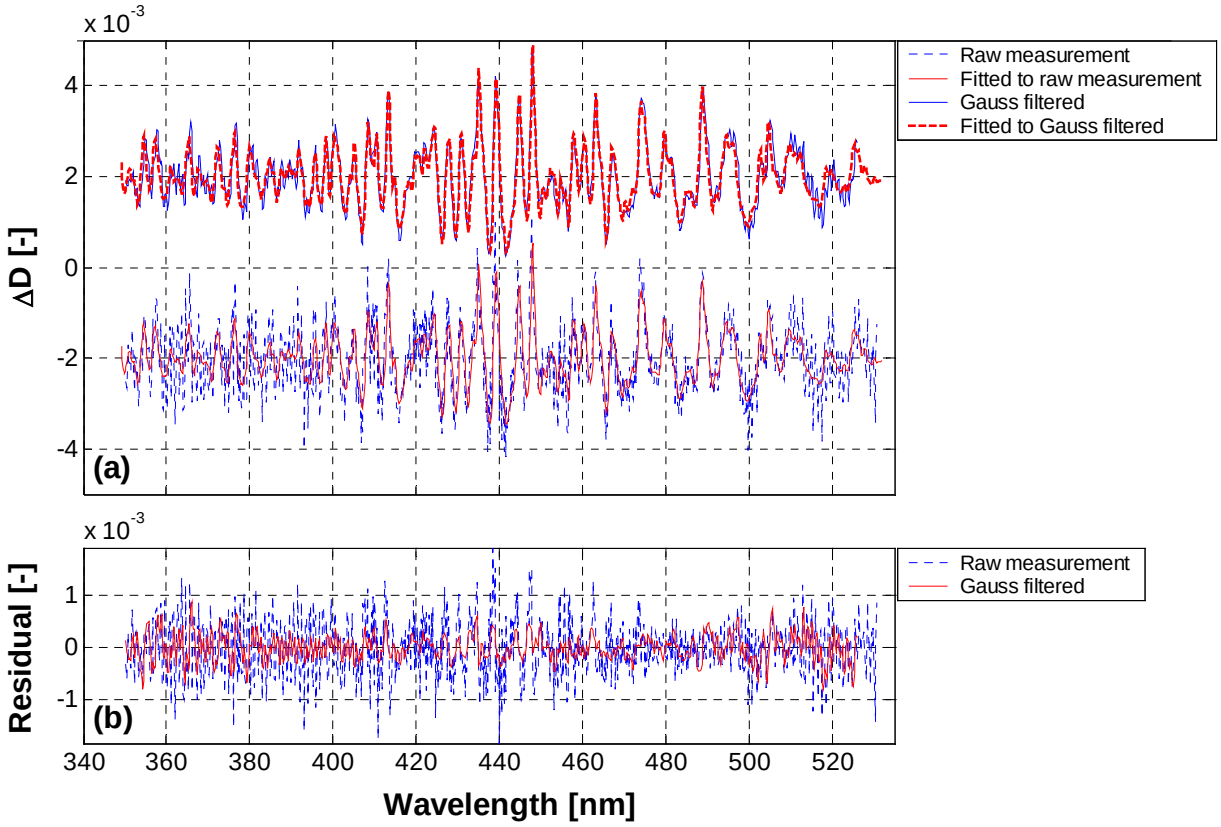

Figure 4-16. (a) NO_2 differential absorption spectrum, and **(b)** NO_2 fitting residual spectrum calculated from short-integration time (3 s) PDA spectra. Top spectrum in (a) was smoothed before non-linear fitting using a 3-pixel wide (FWHM) Gaussian convolution filter (re-normalized). Spectra in (a) were vertically displaced for visualization purposes.

Proved limitations of the DOAS 2000 software, and the need for tools for the analysis of disparate spectral data, such as the obtained by tuning a pulsed Quantum-Cascade Laser (QCL – see **Chapter 5**), and from a UV-visible photodiode array (see **Section 4.1.4**), made evident the need of developing flexible data structures and improved spectra processing routines. Eighty-two modular functions were implemented in MATLAB®. This comprises routines for spectra processing and other purposes (refer to **Annex D** for an abridged description).

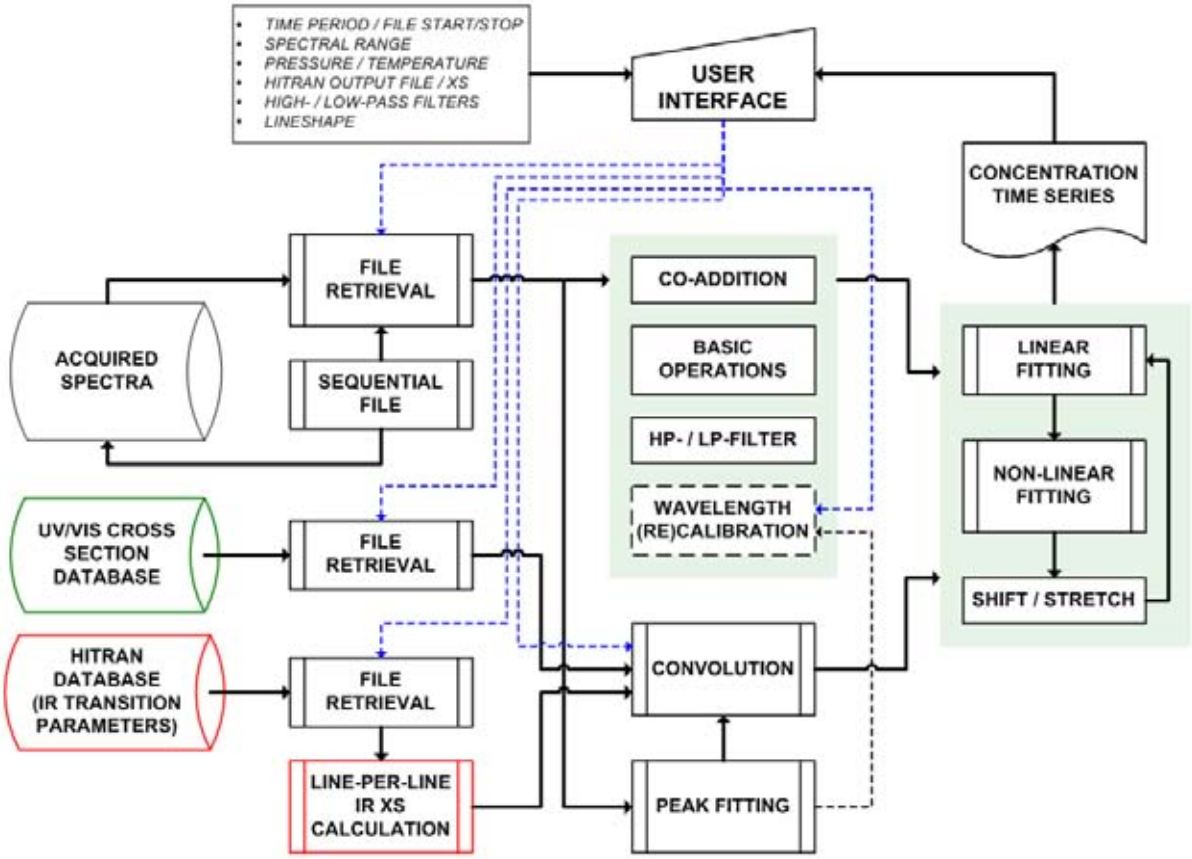

Figure 4-17. Schematic representation of the spectra-processing algorithm applied for concentration retrieval. In the case of DOAS 2000, a preliminary estimation of concentrations is obtained real-time using quasi-non-linear fitting routines implemented in the propietary sofware. Definitive concentrations were calculated using MATLAB®-implemented functions (refer to **Annex D** for details). Note the inclusion of the module for line-per-line calculation of mid-IR cross sections from HITRAN parameters (*HITRAN2XS.m*)

A schematic representation of the spectra-processing algorithm for concentration retrieval is shown **Figure 4-17**. Spectral analysis is based on the principles developed in **Chapter 3**, particularly from **Section 3.3** on. Briefly, the algorithm involves the following steps:

(1) Retrieval of sequential spectra files.
(2) Co-addition of sequential spectra[12] if required for SNR improvement.
(3) Background (noise) subtraction (in general not required for DOAS 2000 spectra).
(4) Rationing of the transmitted spectrum by lamp spectrum (not required for spectral regions of smooth variation), and relative absorbance calculation.
(5) Retrieval of selected absorption cross sections (see **Table 3-2**), or line-per-line calculation from HITRAN (Rothman, 1998) parameters when in the mid-IR (fundamentals in **Section 3.4** – calculation procedure implemented as *HITRAN2XS.m* – see **Annex D**).
(6) Determination of the instrument function (or estimation of the QC-laser linewidth in the mid-IR) by fitting of atomic transitions (or well-defined absorption transitions in the mid-IR, e.g. CO_2) to previously determined best-fitting lineshapes (Gaussian, Lorentzian or Voigt – refer to **Section 3.3**). A ~0.56 nm FWHM Voigt lineshape provides best fitting to Hg transitions as observed with DOAS 2000. Rapid calculation of Voigt profiles is achieved using Humlícek's algorithm (Humlícek, 1982). Refer to *findPeakS.m*, *fitPeakS.m*, *Humlicek.m* and other line*shape* functions in **Annex D**.
(7) Degradation of cross sections to the resolution of the spectrometer (or to the linewidth of the QC-laser) through convolution with the lineshape determined in step (6). Refer to *convParamXS.m* function.
(8) Calculation of differential absorbance and differential cross sections by subtraction of selected low-pass filters. Polynomials of 3^{rd}-9^{th} degree were most commonly used LP-filters in the research. The application of Savitzky-Golay filters (Savitzky, 1964) and orthogonal Forsythe polynomials (Himmelblau, 1970) was also investigated. See functions *lpfS2.m*, *sgS2.m*, and *diffS2.m*.
(9) Non-linear fitting of the measured spectrum to reference spectra (cross section) and concentration retrieval (refer to functions *sshiftS2.m*, *fitLS.m*, *wMLR.m*, and *fit2NLS3.m*).

The non-linear fitting routine (*fit2NLS3.m*) deserves further discussion. The procedure developed by Stutz and Platt (1996b) aligns cross sections to measured spectrum, i.e. in addition to cross section scaling coefficients, c_jL, their algorithm calculates as many wavelength shifts ($\delta\lambda_j$), and stretching/squeezing (m_j) coefficients as cross sections involved in the evaluation. Extensive field measurements show that DOAS 2000 spectra are accurate in wavelength within ±0.3 nm. Literature cross sections used in this research (see **Table 3.2**) are at least one order of magnitude more accurate. At the SNR levels of DOAS 2000 spectra, it seems thus more reasonable to align measured spectra to cross sections than the opposite. The non-linear model fitted by *fit2NLS3.m* is thus the following,

$$\Delta D^*(\lambda) = S\left(\Delta D(\lambda), \delta\lambda, m\right) = L\left[\sum_j \sigma_j(\lambda) c_j\right] + \delta_{\Delta D}(\lambda) \qquad \text{(Equation 4-8)}$$

[12] If co-addition is required, non-linear fitting is usually applied for optimum matching between sequential spectra provided noticeable Xe lamp emission transitions exist in the spectral range analized

where ΔD^* is the optimally aligned differential absorption spectrum, $\delta\lambda$ is the optimum wavelength shift, *m* is the optimum squeezing ($0 < m < 1$) or stretching ($m > 1$) coefficient, and $\delta_{\Delta D}$ is the residual spectrum. The algorithm implemented (*fit2NLS3.m*) uses the Levenberg-Marquardt-Ball method (Himmelblau, 1970) for the minimization of the sum of squared residuals (χ^2),

$$\chi^2 = \left[\mathbf{\Delta D}^* - \mathbf{\sigma c} \mathrm{L}\right]^{\mathrm{T}} \mathbf{W} \left[\mathbf{\Delta D}^* - \mathbf{\sigma c} \mathrm{L}\right] \qquad \text{(Equation 4-9)}$$

where W is a user-defined weighting function[13]. As in the algorithm of Stutz and Platt (1996b), *fit2NLS3.m* involves iterative linear fitting / non-linear fitting until convergence (see **Figure 4-17**). Tests with severely deformed simulated spectra showed a complex structure of the residual function including a considerable number of local optima. In view of this, a preliminary broad mapping of the residual function (χ^2), typically with 5^2 grid points, is performed in order to assure that the global optimum is attained. See **Figure 4-18**. Heuristically determined search limits of ±0.3 nm shift, ±2% stretching/squeezing were fixed for DOAS 2000 spectra. Wider search ranges in relative terms (±0.1 cm^{-1} shift, ±10% stretching/squeezing) were allowed to QC-laser spectra in view of their comparatively larger wavelength uncertainty (see **Chapter 5**).

Heuristically determined best-performing concentration retrieval parameters are summarized in **Table 4-1**. Routines developed in MATLAB have been so far used only for spectra post-processing due to the computational time limitation imposed by the interpreter mode execution (~1-3 s per spectrum depending on the PC). A MATLB toolbox allows for automatic conversion of routines into C++ code. Once compiled, the executable software should allow for real-time concentration retrieval.

4.3 Noise and detection limits

Statistics derived from short, sequential observations of the light source (high-pressure Xe lamp) provide information about the detection capability of the DOAS system. Noise (δ_I) is defined here as the discrepancy between a light spectrum integrated over a short period of time (I) and the average spectrum integrated over a long enough period of observation (I_∞), i.e. $\delta_I = I - I_\infty$. These rapid variations of intensity can be expressed in terms of fractional absorption as follows,

[13] Boldface characters indicate matrix operations

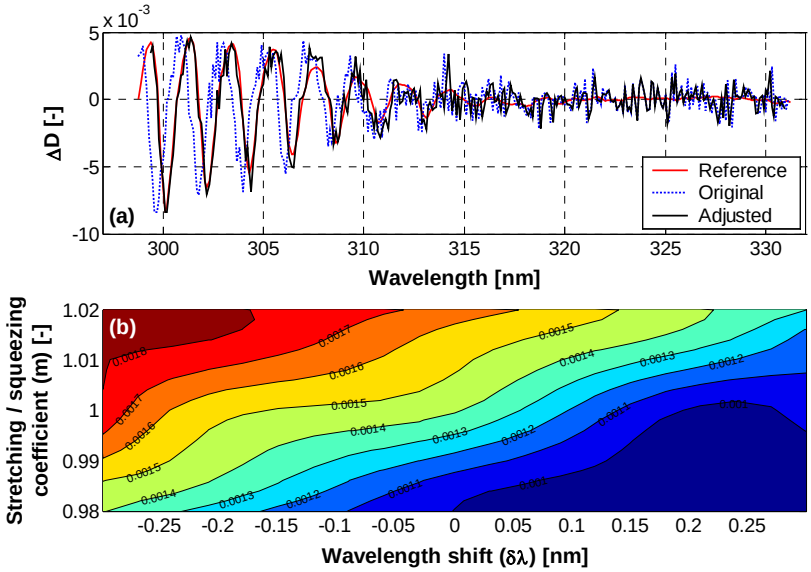

Figure 4-18. Performance of the spectra non-linear fitting routine (*fit2NLS3.m*). **(a)** The spectrum under analysis was obtained by deformation ($\delta\lambda$ = -0.25 nm, m = 1.015) of the reference spectrum (SO_2 - measured with DOAS 2000), followed by addition of Gaussin noise (10^{-3} fractional absorbance – 1-sigma). The adjusted spectrum fits optimally the refence spectrum. The scaling coefficient retrieved is 0.99±0.02. Panel **(b)** shows the countour map (initial iteration) of the sum of squres (χ^2) as a function of wavelength shift ($\delta\lambda$) and stretching/squeezing coefficient (m).

Center wavelength [nm]	Target species	Main intereferent species	Wavelength range [nm]	Low-pass filter [(c)]
262	BTEX	O_2, O_3	251.5 - 277.5	SG (f = 7%, P(2))
283	O_3	SO_2	273.5 - 290.2	P(9)
300	SO_2	O_3	292.0 - 312.0	P(6)
315 [(a)]	HCHO	SO_2, O_3, NO_2	299.5 - 313.0 313.8 - 321.5 323.5 - 327.5	P(5), P(4), P(3)
345 [(b)]	HCHO	NO_2	335.0 - 345.0	P(5)
354	HONO	NO_2	338.5 - 369.5	P(9)
430	NO_2	---	422.0 - 437.5	P(5)

(a) Three subranges are used for evaluation at 315 nm (center wavelength) in order to avoid two Xe lamp broaden emission lines. Polynomial filters are fitted independently over each subrange. Non-linear fitting considers the 3 subranges as whole for evaluation

(b) Obsolete

(c) SG: Savitzky-Golay (f: frame-to-range ratio); P(n): n-th degree fitting polynomial

Table 4-2. Heuristically determined best-performing wavelength ranges and low-pass filters for the retrieval of various trace gases from DOAS 2000 spectra.

$$\delta_{\Delta D} \approx \frac{\delta_I}{I_\infty} - f_{LP}\left(\frac{\delta_I}{I_\infty}\right) \qquad \text{(Equation 4-10)}$$

Subtraction of a low-pass filter assures those only the rapid-varying component is taken into consideration for the estimation of detection limits. Accumulation of subsequent spectra allows estimating the detection limit as a function of the integration time. Instead of determining the detection limit as a ratio of root-mean-square (rms) values, for instance for a SNR of 1 as $(cL)_{LDL} = \mathrm{rms}(\delta_{\Delta D})/\mathrm{rms}(\Delta\sigma)$, it seems better adapted to the multichannel nature of DOAS to estimate the detection limit as the retrieval error that results from adding differential noise ($\delta_{\Delta D}$) to a theoretical spectrum at a given column density. At a given noise level, the retrieval error in indeed insensitive to the magnitude of the column density according to statistical principles, and calculations at various column densities and noise levels retrieved from DOAS 2000 spectra.

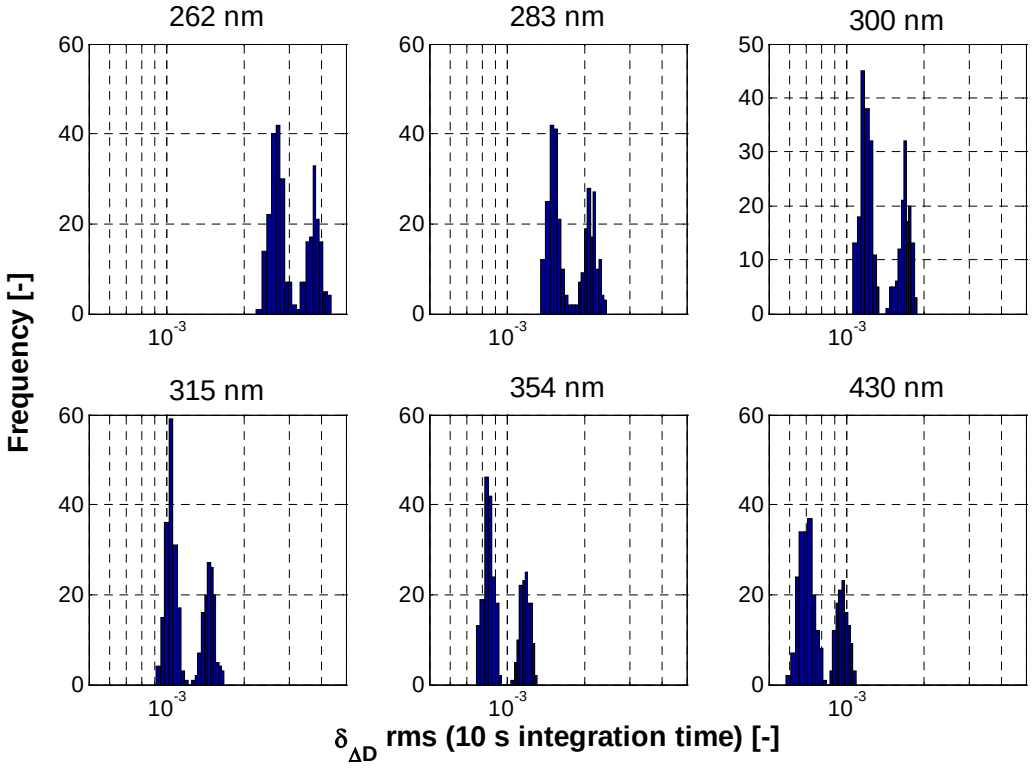

Figure 4-19. Frequency distribution of residual fractional absorbance at 10 s integration time and at various center wavelengths for DOAS 2000.

At conditions of constant illumination and constant PMT supply voltage, noise as defined above integrates random noise sources associated to the detection system and the variability of the lamp itself. Separation of these two terms is not very important for an estimation of the operational detection limits since the same type and model of lamp (Hamamatsu, L2274 – 150 W, 2.5 mm arc gap, ozone-free silica) were used for all DOAS measurements (laboratory and

field) here reported. Detection limits derived from lamp spectra statistics reflect thus the detection capability of the DOAS 2000 system as a whole.

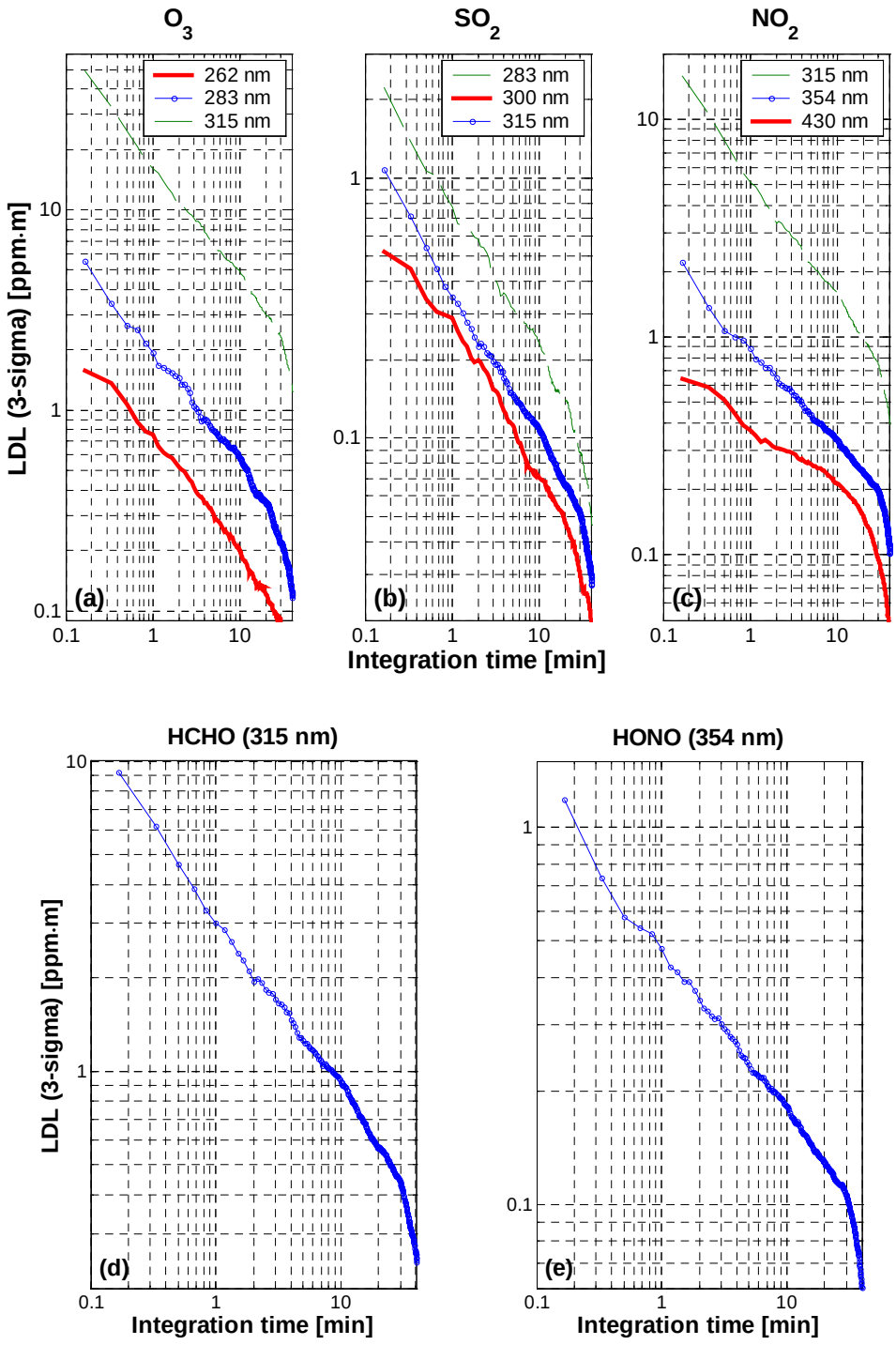

Figure 4-20. Estimated lower detectable column density (3-sigma) with DOAS 2000 for various traces gases and center wavelengths as a function of the integration time.

Noise and detection limits in this experiment were derived from 10-s Xe lamp spectra measured and co-added over a total effective integration time of 50 min (average spectrum). Measurements were repeated at the 6 center wavelengths shown in **Table 4-2**. The beam was collimated and then focalized onto the optical fiber using ϕ 5 cm spherical mirrors. A diaphragm was interposed between the lamp and the first spherical mirror in order to properly image the Xe lamp arc on the fiber.

Histograms of the residual fractional absorbance (differential noise – rms) at 10 s integration time are shown in **Figure 4-19**. Surprisingly distributions are bimodal. Fourier analysis of the corresponding time series show that low and high noise values are cyclic with a period of ~40 s on average, which points to the lamp as source of variability. There is no clear explanation to this observation at the present time.

Residual fractional absorbance spectra, calculated from subsequently stacked lamp spectra, were used to estimate the detection limit dependence on integration time. The detection limits were calculated as the retrieval error (3-sigma) Results for various trace gases and center wavelengths are shown in **Figure 4-20**. As expected, detection limits decrease approximately with the square root of the integration time ($\mathrm{LDL} \sim 1/\sqrt{\Delta t}$).

4.4 Laboratory calibration

DOAS is in principle an absolute detection technique that requires no calibration, at least no periodic calibration, as do require standard point monitors. In practice, the analytical performance of DOAS instruments must be verified in laboratory conditions and through field intercomparisons.

A calibration bench was built for measurement validation purposes as part of this research. The bench allowed for intercalibration of ozone and nitrogen oxide measurements with certified DOAS systems (OPSIS) and was used for investigating the detection of nitrous acid.

4.4.1 Calibration bench

The calibration bench is shown in **Figure 4-21** (see also picture in **Annex K**). The optical path is folded using three flat mirrors in order to accommodate the cells into the available breadboard. A dynamic (flow) system was preferred over a static one aiming at minimizing calibration bias due to e.g. photolysis and wall reaction.

A set of four calibration cells was designed and built. Cell lengths were calculated so to maximize the number of combinations, thus the number of column density calibration points when operating at constant concentration. Another criterium applied to the design was to achieve the best possible spacing in pathlength between subsequent combinations of cells. The cells designed are of 60, 200, 410, and 830 mm long (1.5 m maximum pathlength). Fifthteen independent combinations are possible with this set of cells. Each side of a cell is a

standard ϕ 55 mm KF head (port). Transmission windows (fused silica in the case of UV-visible measurements) are mounted within vacuum joints. This assures that the system is leak-free and allows for easy window exchange, as for instance for measurements in the mid-IR. Cells were internally coated with a Teflon®-like polymer in order to improve their inertness and surface quality. The entrance to the cells was designed so to allow for fast, tight connection using vacuum joints.

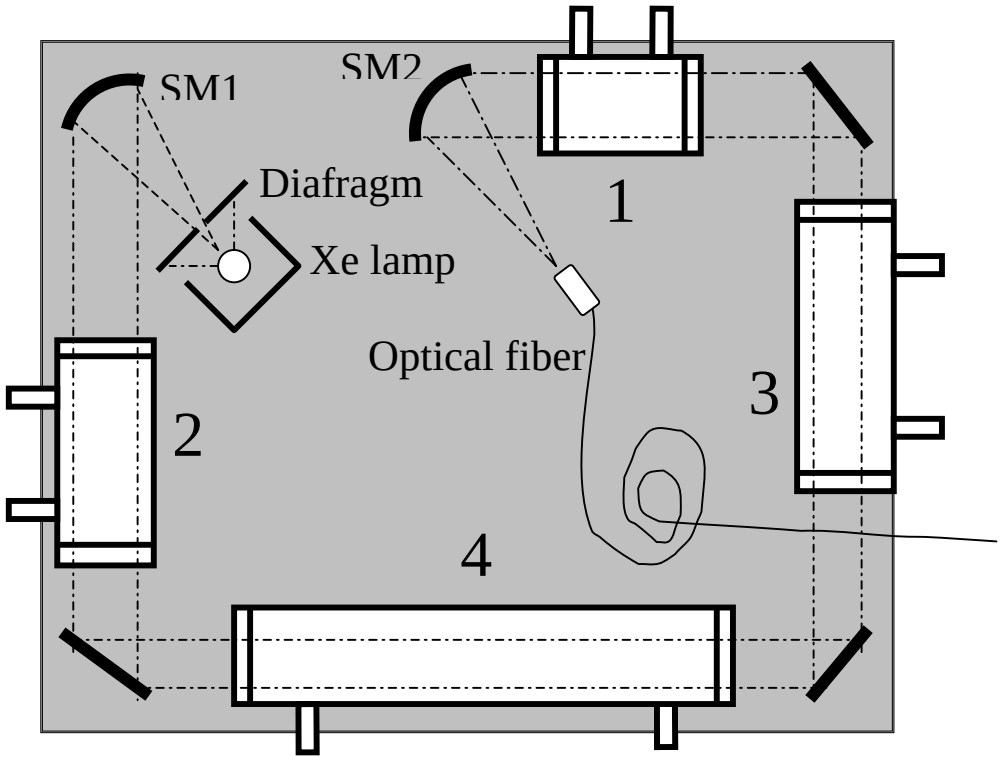

Figure 4-21. Schematic representation of the DOAS calibration bench. Cells are numbered according to increasing pathlength. SM: spherical mirror.

4.4.2 Intercalibration of criteria pollutants

Three DOAS spectrometers, two OPSIS and DOAS 2000, were intercalibrated for the measurement of NO_2 and O_3 using the calibration bench described above. OPSIS systems belong to Paul Schrer Institute (PSI) and the Air Quality Network of Geneva (ROPAG). The first one has been in operation for several years while the second one was recently purchased. All systems were set to provide concentrations on a 10-s basis over cycles of ~5 min (integration time per column density).

The calibration was made with a NO_2 certified calibration tank (SL Gas – 482 ppm ± 2%). Calibration NO_2 column densities were obtained by combination of cells 1, 2, and 3 and by diluting NO_2 with purified air to concentrations of 25%, 10% and 2% of its certified value. The dilution was made using mass flow controllers (MKS, 1179AX – 0.6% accuracy). Temperature and pressure were monitored using a Pt-100 and a pressure a transducer (Setra, 280E) linked to a 10-bit datalogger (Texas Electronics, Solus).

The calibration results are shown in **Figure 4-22**. A very good agreement is observed among the three systems within their uncertainty limits. Uncertainties of the linear regression coefficients would suggest that OPSIS systems are more precise than DOAS 2000. Nevertheless, care must be exercised when withdrawing such a conclusion since DOAS 2000 correlation includes additional points of low column density.

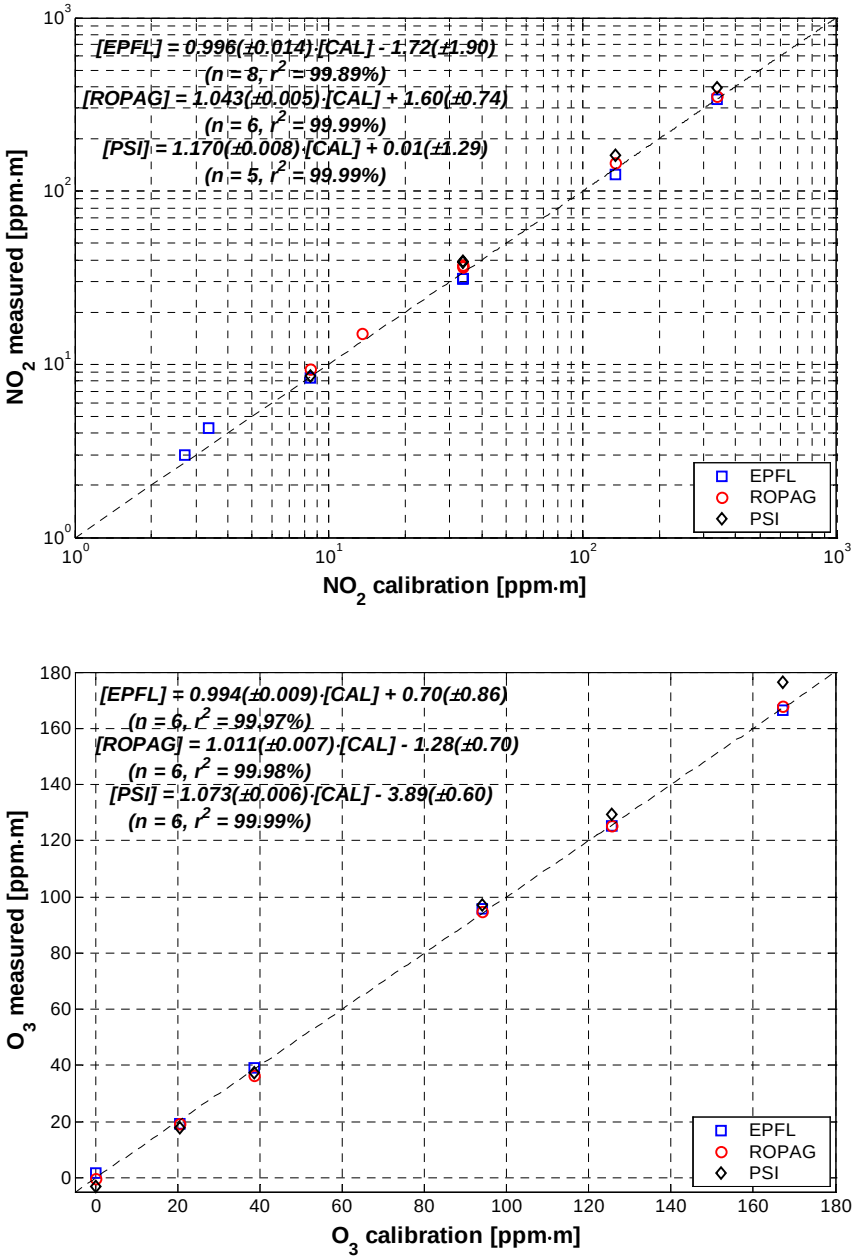

Figure 4-22. Laboratory intercalibration of three DOAS systems for the measurement of **(a)** NO_2, and **(b)** O_3. NO_2 calibration column densities were obtained by changing the absorption pathlength and by dilution of NO_2 from a certified calibration tank. Ozone was generated with a Sonimix generator feed with high quality synthetic air (SL Gas). ROPAG and PSI are OPSIS systems. Calibration curves are in ppm·m.

A similar procedure was followed with ozone. In this case, PSI showed significant span and offset of 7% and 4 ppm·m, respectively, compared to the calibration values obtained using a Sonimix generator. EPFL and ROPAG are fully comparable and their offsets are not significantly different from zero.

4.4.3 Development of a nitrous acid (HONO) diluted gas mixture generator

The ultimate purpose of this investigation was to estimate the lower detectable column density of HONO with DOAS 2000 on the basis of laboratory measurements. A fairly simple, inexpensive dynamic system was developed for this purpose (see **Figure 4-23** and **Annex K**).

HONO is produced by contacting aqueous solutions of sodium nitrite and sulfuric acid in a semi-continuous gas-bubble column reactor,

$$NaNO_2 + H_2SO_4 \rightarrow HONO + NaHSO_4 \qquad \text{(Reaction 4-1)}$$

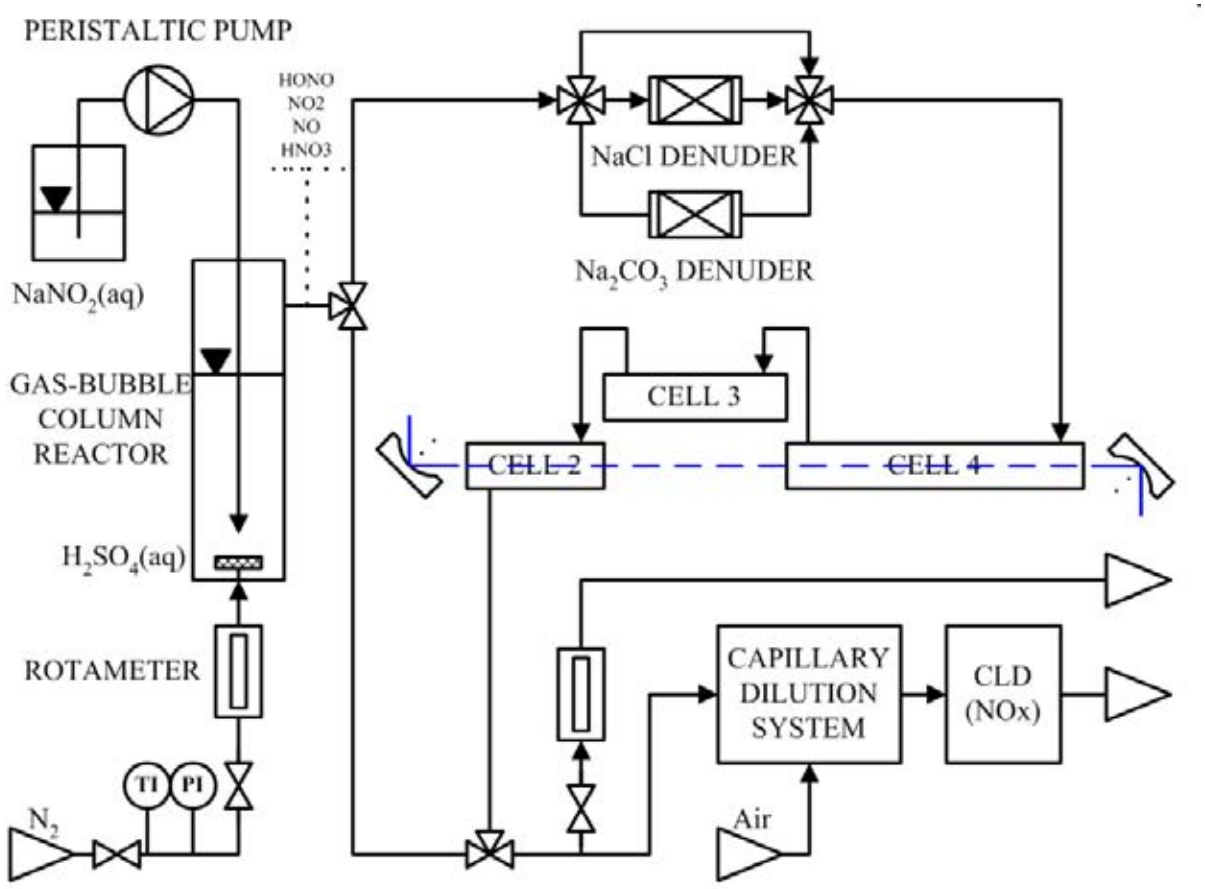

Figure 4-23. Schematic of the HONO generator and calibration bench.

The limiting reactant (usually $NaNO_2$) is delivered to the liquid pool at constant rate using a calibrated peristaltic pump (Masterflex, Easy-Load II – head 77201-60 / driver 7554-85 – see **Annex F**). The transfer of HONO from the aqueous to the gas phase is enhanced by circulation of the liquid pool induced by gas bubbles. This semi-continuous system is similar to the continuous generator developed by Taira and Kanda (1990). Their system requires nevertheless quite expensive peristaltic pumps to assure continuous, extremely stable delivery of reactants into the reaction vessel at very low flow rates (< 1 mL/min). Bongartz *et al* (1991) used also **Reaction 4-1** to produce HONO but in a batch reactor. A summary of other HONO generation methods is given elsewhere (Szekely, 2000).

A summary of the experimental runs carried out is given in **Table 4-3**. The results indicate that HONO-richer mixtures are obtained when using sulfuric acid as limiting reactant (continuously added). Upon production, the gas mixture is spectrally analyzed in the calibration bench. The bench allows for rapid checking of the optical absorption linearity (BLB law) by changing the optical pathlength. Following spectral analysis, the gas stream is sampled, and the sample is diluted using a capillary system. The diluted mixture is analyzed with a NOx chemiluminiscence detector (CLD – TECAN, CLD-502), which enables for real-time monitoring of NO and NO_2.

		Initial pool			Continuosly added			Gas phase			
	Variable	Compound	Inital Concentration [mM]	Volume [mL]	Compound	Concentration [mM]	Liquid Flow [mL/min]	Gas Flow [mL/min]	Max [NOy*] [ppm] [4]	Max [HONO] [ppm]	Max [HONO] / Max [Noy*]
Run #	1	H2SO4	75	300	NaNO2	15	8	996.4	[2]	18 [1]	[2]
	2	H2SO4	75	720	NaNO2	15	1.7-10	200 - 3300	[3]	[3]	[2]
	3	H2SO4	15	750	NaNO2	15	3.57	1022	280	30	10.71%
	4	H2SO4	15	1000	NaNO2	30	3.57	2073	255	32	12.55%
	5	NaNO2	30	500	H2SO4	15	3.57	2073	282	45	15.96%
	6	NaNO2	30	500	H2SO4	15	0.89	2073	335	70	20.90%
	7	H2SO4	25	1500	NaNO2	45.4	0.4	2073	186	10	5.38%
	8	H2SO4	15	750	NaNO2	15	3.57	1022	270	43	15.93%
	9	H2SO4	25	1500	NaNO2	45.4	0.89	2073	190	18	9.47%
	10 [5]	H2SO4	[2]	2200	NaNO2	---	0	2460	190	19	10.00%
	11	H2SO4	25	1500	NaNO2	45.4	2.63	2450	480	40	8.33%

[1] Estimated from raw spectra

[2] Missing data

[3] The response of the system was investigated by changing gas and liquid flow rates

[4] [NOy*] = [NOx] + [HONO]

[5] Reactor contained pool of previous run

Table 4-3. Summary of operational conditions and results of HONO generation runs.

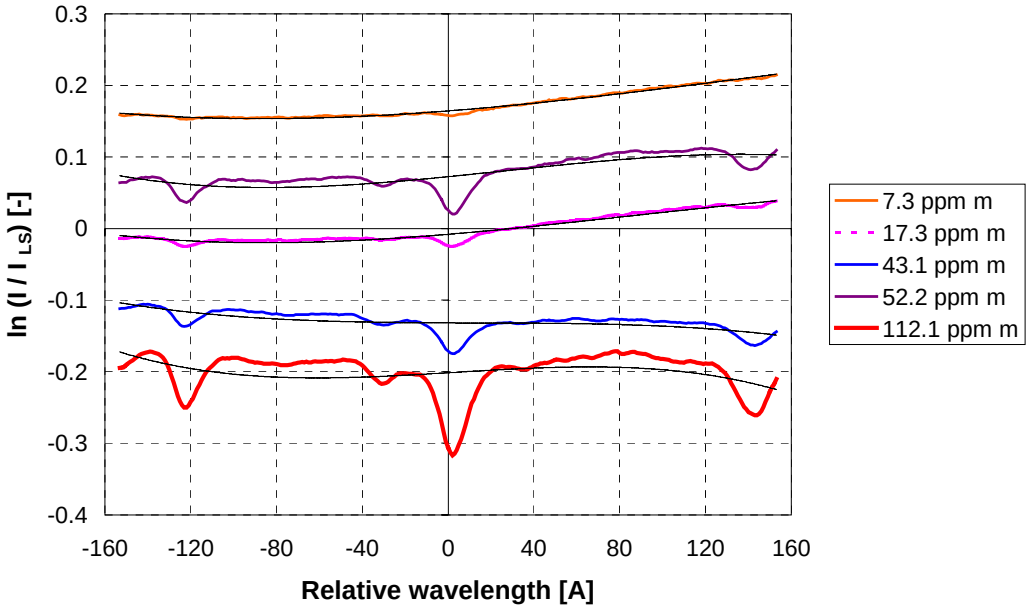

Figure 4-24. HONO spectra at various column densities as measured in the calibration bench. Integration times range from 1 to 50 min. Center wavelength is 354 nm.

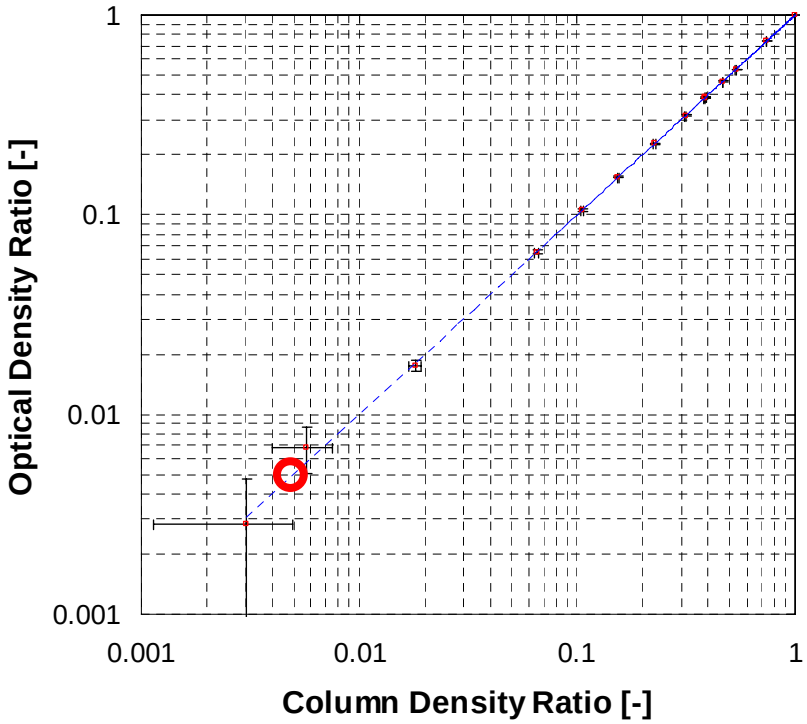

Figure 4-25. Normalized Beer-Lambert-Bouger (BLB) plot of HONO derived from measurements made in the calibration bench. The estimated detection limit ratio, $(\mathrm{cL})_{\mathrm{LDL}} / (\mathrm{cL})_{\mathrm{max}} \approx 0.5\%$, is denoted with a red circle.

HONO can be selectively removed from the gas mixture using a sodium chloride (NaCl) denuder,

$$NaCl + HONO \rightarrow NaNO_2 + HCl \qquad \text{(Reaction 4-2)}$$

The denuder is a bed a NaCl-glycerin-coated glass pearls (Szekely, 2000). The application of the denuder allows obtaining spectrally pure HONO spectra by subtraction of HONO-free spectra from gas mixture spectra. The concentration of the pure HONO spectra in the 339-369 nm range is derived by differential absorption analysis using the cross section of Stutz *et al* (Stutz, 2000). Confidence in the evaluation follows from the fact that the catalytic converter of the CLD detector reduces as well a significant fraction of HONO, which is reported by the CLD as NO_2.

A similarly-built Na_2CO_3 denuder allows removing HONO and large fraction of NO_2. As expected, upon application of this denuder the CLD was found to report very low values of NO_2. The concentration of NO in the generator mixture is determined in this way.

Figure 4-24 shows a set of spectrally pure HONO spectra spanning from 7 ppm·m to 112 ppm·m. The BLB plot shown in **Figure 4-25** was obtained using the spectrum at 112 ppm·m as reference. This plot allows estimating the HONO detection limit for an integration time of 5 min and a SNR of 2. The LDL is estimated at ~0.5% referred to the spectrum of highest column density, i.e. ~0.56 ppm·m. This detection limit (SNR = 2) is in good agreement with the estimation based on sequential spectra (SNR = 1 – refer to **Section 4.3**). Assuming monotonic decrease of the detection limit with the square root of the integration time allows expecting a reasonable detection limit of ~0.2 ppm·m (SNR = 2) for an integration time of 30 min.

Another system for the generation of controlled, diluted mixtures of VOC, particularly MAH, was also developed within this research. Results are shown in **Annex G**. This inexpensive system is based on the saturation principle, and allows producing diluted mixtures of MAH at very stable concentrations (random variation is typically within ~1%).

4.5 Field campaigns

DOAS 2000 was tested in an important number of field campaigns (see **Table 4-4**). Measurements were performed over absorption path lengths ranging from 220 m (wastewater treatment plant at Lausanne – see **Section 6.2**) to 1.5 km (Student Campaign 2001 in a rural/forested area in Valais, Switzerland). At 1.5 km the detection was severely limited by the collected light intensity. Based on the accumulated experience, it can be stated that the optimal absorption pathlength for DOAS 2000 in its current configuration is ~1 km.

The campaigns performed allowed testing DOAS 2000 over a fairly large span of concentrations, from quasi-background conditions in ASPA 2003 (but also episodic concentration levels) to the highly polluted conditions of Milan (PIPAPO 1998).

Results from two of the DOAS campaigns (GRENOPHOT 1999, STEP 1999) are analyzed in detail in **Chapter 6**. Formaldehyde measurements in Milan were reported in a paper (Jiménez, 2000) reproduced in **Annex H**. Results from a more recent campaign in the Colombia Andes (CAVASO 2002) are commented in some detail in **Annex I**. Time series of some campaigns are presented in **Annex J**.

DOAS Field Measurements

		Site			Time period		
Campaign	**Scale / Purpose**	**Country**	**Location**	**Type**	**Begin**	**End**	**L [m]**
PIPAPO (1998)	EUROTRAC-II	Italy	Seregno (Milan)	Urban	5/1/98	6/1/98	425
DICLA 1999	Intercomparison	Switzerland	Lausanne, VD	Urban	2/12/99	6/30/99	631 / 1230
GRENOPHOT 1999	Regional	France	Vif (Grenoble)	Rural / Surburban	7/15/99	8/16/99	968
STEP (1999)	Local / Intercomparison	Switzerland	Lausanne, VD	Industrial / Urban (a)	9/1/99	9/1/99	220
TUNNEL 2001	Local / Intercomparison	Switzerland	Sarnen, OW	Tunnel portal / Rural	4/29/01	5/22/01	610
ESCOMPTE (2001)	EUROTRAC-II	France	Marseilles	Rural / Surburban	6/11/01	7/12/01	762
CAVASO 2002	Regional	Colombia	Duitama (Sogamoso)	Urban	1/24/02	2/15/02	1080
BOP 2002	Regional	Colombia	PJD (Zipaquirá)	Rural / Surburban	2/26/02	4/18/02	872
ASPA 2003	Regional	France	(Strasbourg)	Rural	5/21/03	6/17/03	1096

Table 4-4. Summary of field campaigns involving DOAS measurements. Four campaigns for student training and carried out in Switzerland and France are not included.

4.6 DICLA 1999 (DOAS Intercomparison Campaign at LAusanne, Switzerland)

This campaign deserves particular attention for several reasons:

- Concerns the intercomparison of two DOAS system operating in an urban site.
- Measurements were carried over a quite long period of time (from mid-February until end of June 1999)
- Simultaneous measurements by the two systems were performed over fully comparable absorption paths during the second phase of the campaign.

The campaign was undertaken during the hazy, relatively harsh conditions of winter 1999 at Lausanne. The spectrometer and telescope of DOAS 2000 were installed in a tower of a historical building in downtown Lausanne (see **Figure 4-26**). Because of the particular conditions of this site, it was not possible to install the environmental enclosure. A simplified shelter had to be built on site in order to protect the system, particularly the spectrometer, against the chilly conditions at that particular time. The on-site constructed shelter was furnished with a heater to prevent against freezing. The simplicity of the system lead to a very poor temperature control, especially at the beginning of the campaign. This had a very negative impact on the performance of the spectrometer, particularly on the stability of the scanner. Measurements on the first path were carried out until beginning of June 1999. About 4 week of measurements were carried out over the second path, which covered an essentially identical area than the DOAS system operated by the environmental protection agency of Lausanne (SEHL). SEHL's DOAS is a bistatic OPSIS system, thus it covered the same distance that DOAS 2000 but operated at significantly higher light levels compared to DOAS 2000.

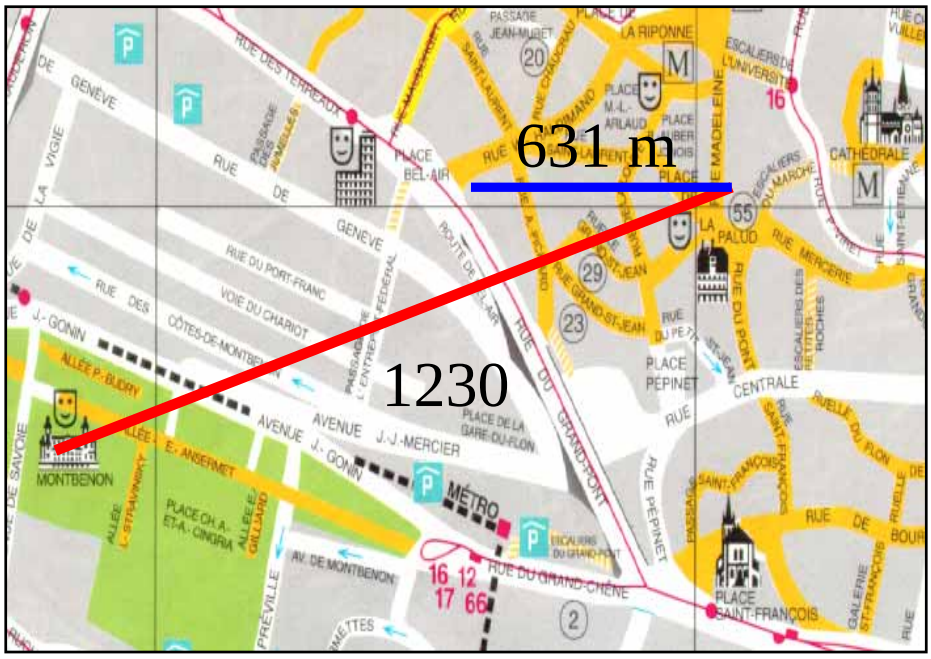

Figure 4-26. DICLA 1999 campaign location. The map indicates the beam location and total absorption pathlength of the folded paths of DOAS 2000 (Phase I = 631 m; Phase II = 1230 m). The OPSIS system operated by SEHL measured over the same distance than DOAS 2000 during Phase II but on a bistatic configuration (i.e. ~615 m absorption path).

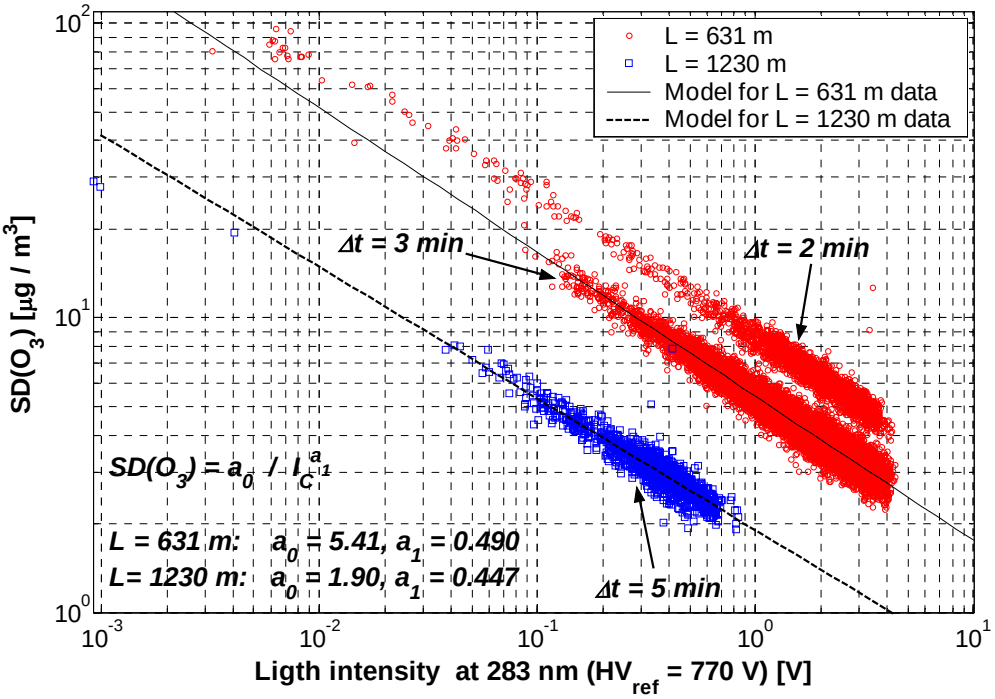

Figure 4-27. Standard deviation of the concentrations of ozone obtained with DOAS 2000 as a function of the collected light intensity, the pathlength and the integration time.

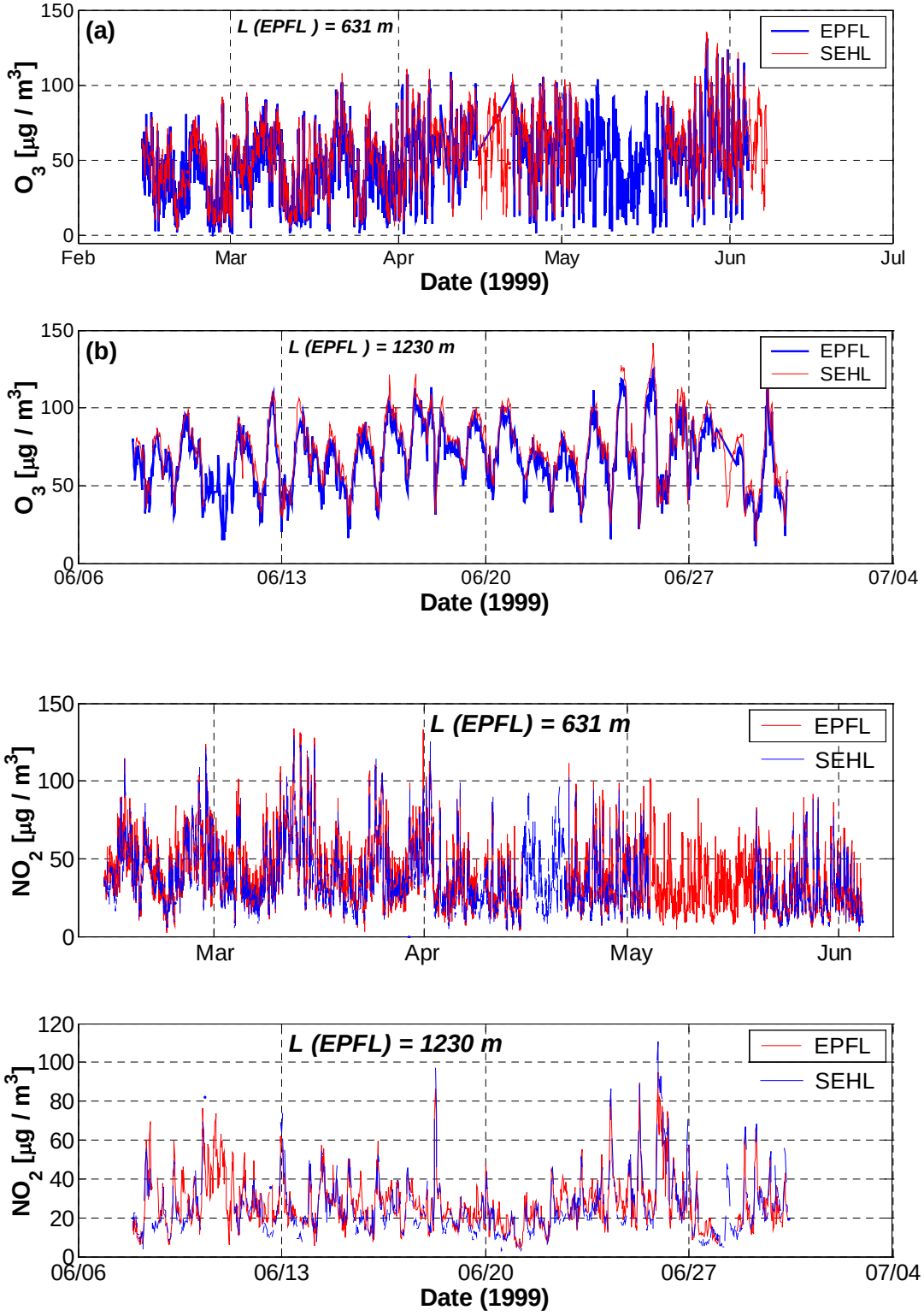

Figure 4-28. (a) Ozone and **(b)** nitrogen dioxide time series as measured by the two DOAS systems during DICLA 1999 Phase I and Phase II.

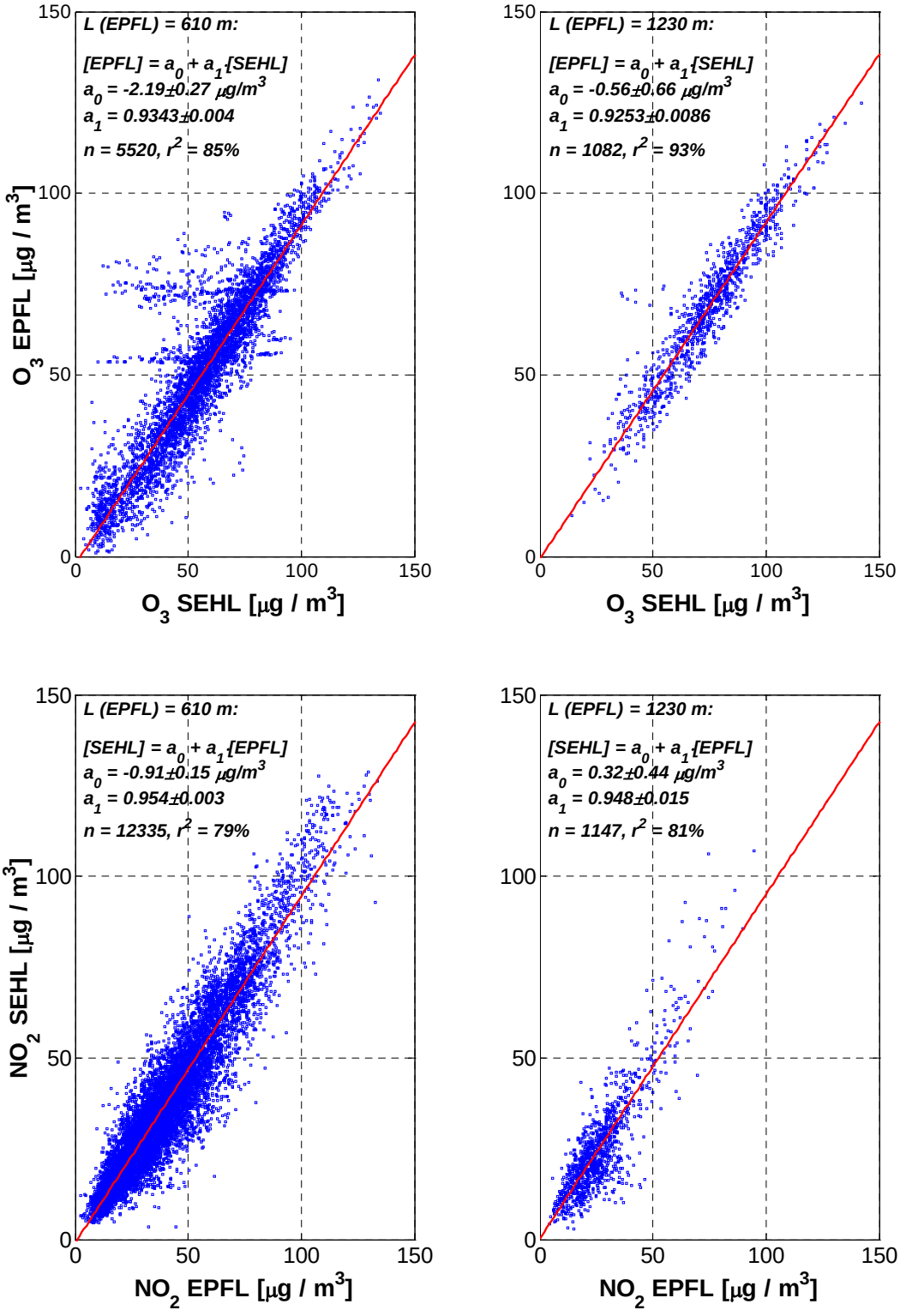

Figure 4-29. Intercomparison scatter plots of **(a)** Ozone and **(b)** nitrogen dioxide as measured by the two DOAS systems during DICLA 1999 Phase I and Phase II.

An interesting result is the dependence of the evaluation error of DOAS, i.e. the standard deviation of the retrieved concentration, on the light conditions (see **Figure 4-27**). This plot shows a dependence of the evaluation error (1-sigma) that is close to $\sigma_c \sim 1/\sqrt{I}$ (Stutz, 1996a), as expected from shot noise. The measurements show that when having the same number of photons for evaluation, the error decreases by a factor of ~3 after doubling the absorption path and increasing the integration time by ~40%. This information may be used for the establishment of quality control standards based on the light intensity referred to a constant PMT supply voltage.

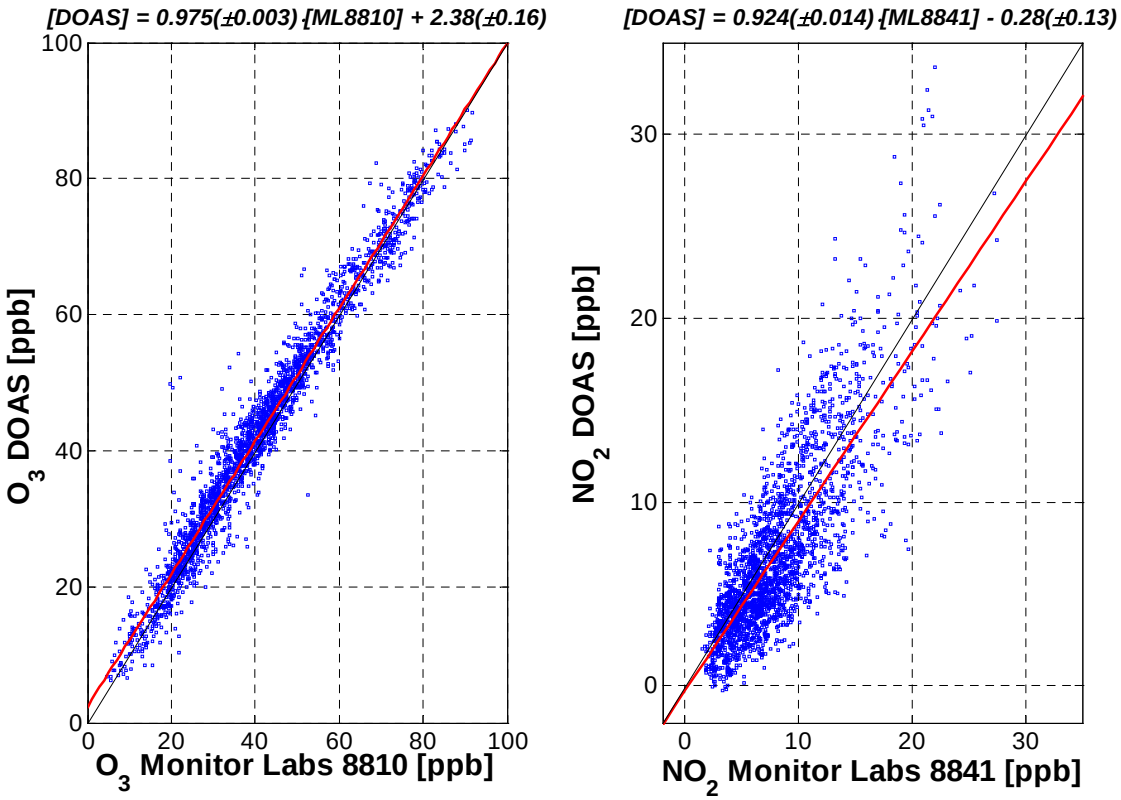

Figure 4-30. Intercomparison of DOAS and point monitor measurements of ozone and nitrogen dioxide at Vif (suburban Grenoble) during GRENOPHOT 1999.

Time series of ozone and nitrogen dioxide as measured with DOAS 2000 and OPSIS/SEHL are presented in **Figure 4-28**. Ozone concentrations retrieved with DOAS 2000 are smaller compared to OPSIS/SEHL. The opposite applies to nitrogen oxide, as confirmed by the scatter plots and correlations shown in **Figure 4-29**. Correlation coefficients are significantly higher for Phase II, which suggest that at least part of the discrepancy observed during Phase I can be ascribed to differences in the air masses observed by DOAS and OPSIS/SEHL. The significant reduction of the offset when passing from path I to path II corroborates this hypothesis. Offsets in Phase II are not statistically different from zero. The fact that Phase II corresponds to a period of better atmospheric mixing (summer) compared to Phase I (winter/spring) cannot be ruled out as cause of improvement in the correlation. Briefly, O_3

concentrations retrieved from DOAS 2000 spectra are ~7% smaller than values obtained by OPSIS/SEHL. On the other hand, NO_2 concentrations with DOAS 2000 are ~5% higher compared to OPSIS/SEHL. These levels of discrepancy have been observed between other DOAS systems (Camy-Peyret, 1996).

For sake of comparison, the scatter plots of O_3 and NO_2 measured with DOAS and point monitors at Vif (suburban Grenoble) are shown in **Figure 4-30**. A good correlation is observed between the O_3 values. In contrast, comparatively larger differences are observed in the NO_2 concentrations. These measurements are discussed in **Section 6.1**. Operational detection limits (1-sigma) at Vif are shown in **Figure 4-31**.

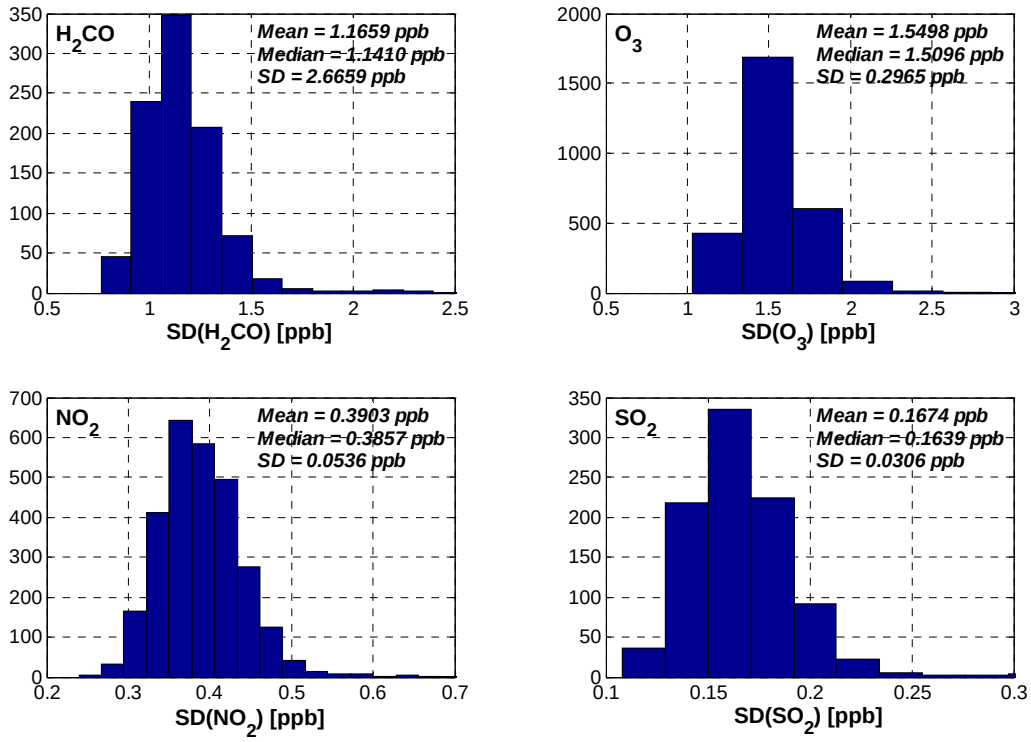

Figure 4-31. Histograms of DOAS operational detection limits (1-sigma) at Vif during the GRENOPHOT 1999 campaign (refer to Section 6.1 for details).

4.7 References

Bongartz, A., J. Kames, F. Welter and U. Schurath. Near-UV absorption cross sections and trans/cis equilibrium of nitrous acid. *J. Phys. Chem.* 95 (3): 1076-1082, 1991

Camy-Peyret, C., B. Bergqvist, B. Galle, M. Carleer, C. Clerbaux, R. Colin, C. Fayt, F. Goutail, M. Pinharanda-Nunes, J.P. Pommereau, M. Hausmann, U. Platt, I. Pundt, T. Rudolph, C. Hermans, P.C. Simon, A.C. Vandaele, J.M.C. Plane and N. Smith.

Intercomparison of instruments for tropospheric measurements using differential optical absorption spectroscopy. *J. Atmos. Chem.* 23: 51-80, 1996

Evangelisti, F., A. Baroncelli, G. Bonasoni, G. Giovanelli and F. Ravegnani. Differential optical absorption spectrometer for measurement of tropospheric pollutants. *Appl. Opt.* 34 (15): 2737-2744, 1995

Harder, J.W., R.O. Jakoubek and G.H. Mount. Measurement of tropospheric gases by long-path differential absorption spectroscopy during the 1993 OH Photochemistry Experiment. *J. Geophys. Res.* 102 (D5): 6215-6226, 1997

Himmelblau, D.M. Process analysis by statistical methods. Wiley, New York, 1970

Humlícek, J. Optimized computation of the Voigt and complex probability functions. *JQSRT* 27 (4): 437-444, 1982

Jenkins, T.E. Optical sensing techniques and signal processing. Prentice-Hall, London, 1987

Jiménez, R., I. Balin, H. van den Bergh and B. Calpini. DOAS 2000 characterization, calibration and development. Activity report. EPFL/LPAS, Lausanne, 1998

Jiménez, R., A. Martilli, I. Balin, H. van den Bergh, B. Calpini, B.R. Larsen, G. Favaro and D. Kita. Measurement of formaldehyde (HCHO) by DOAS: Intercomparison to DNPH measurements and interpretation from Eulerian model calculations. *A&WMA 93rd Annual Conf. & Exhib.*, Salt Lake City, June 18-22, 2000: Paper 829

Kita, D. Remote sensing by differential optical absorption spectroscopy. *A&WMA 93rd Annual Conf. & Exhib.*, Salt Lake City, 2000: Paper 278

Knoll, P., R. Singer and W. Kiefer. Improving spectroscopic techniques by a scanning multichannel method. *Appl.Spectr.* 44 (5): 776-782, 1990

Lanni, T.R. Developing a diode array spectrometer for tropospheric chemistry studies. Ph.D. Thesis, State University of New York at Albany, Albany (NY), 1992

Lerner, J.M. and A. Theveron. The optics of spectroscopy. Jobin-Yvon Instruments, Middlesex (UK), 1988

Moore, J.H., C.C. Davis, M.A. Coplan and S.C. Greer. Building scientific apparatus. Perseus, Cambridge (MA), 2003

PI. Systems for absorbance spectroscopy. Princeton Instruments, 1999

Plane, J.M.C. and C.-F. Nien. Differential absorption spectrometer for measuring atmospheric trace gases. *Rev. Sci. Instrum.* 63 (3): 1867-1876, 1992

Platt, U. Differential optical absorption spectroscopy. **In** M.W. Sigrist (ed), Air monitoring by spectroscopic techniques, Wiley, New York, 1994: 27-84

Rothman, L.S., C.P. Rinsland, A. Goldman, S.T. Massie, D.P. Edwards, J.-M. Flaud, A. Perrin, C. Camy-Peyret, V. Dana, J.-Y. Mandin, J. Schroeder, A. McCann, R.R. Gamache, R.B. Wattson, K. Yoshino, K.V. Chance, K.W. Jucks, L.R. Brown, V. Nemtchinov and P. Varanasi. The HITRAN molecular spectroscopic database and HAWKS (HITRAN atmospheric workstation): 1996 Edition. *JQSRT* 60: 665-710, 1998

Savitzky, A. and J.E. Golay. Smoothing and differentiation of data by simplified least squares procedures. *Anal. Chem.* 36 (8): 1627-1639, 1964

Schiff, H.I., J. Robbins, S.D. Nadler and G.I. MacKay. The Sensair - An improved DOAS system. *A&WMA 90th Annual Conf. & Exhib.*, 1997:

Stutz, J. Messung der Konzentration troposphärischer Spurensstoffe mittels Differentieller-Optischer-Absorptionsspektroskopie: Eine neue Generation von Geräten und Algorithmen. Ph.D. Thesis, Ruprecht-Karls-Universität, Heidelberg, 1996a

Stutz, J. and U. Platt. Numerical analysis and estimation of the statistical error of differential optical absorption spectroscopy measurements with least-squares methods. *Appl. Opt.* 35 (30): 6041-6053, 1996b

Stutz, J. and U. Platt. Improving long-path differential optical absorption spectroscopy with a quartz-fiber mode mixer. *Appl. Opt.* 36 (6): 1105-1115, 1997

Stutz, J., E.S. Kim, U. Platt, P. Bruno, C. Perrino and A. Febo. UV-visible absorption cross-section of nitrous acid. *J. Geophys. Res.* 105 (D11): 14585-14592, 2000

Szekely, L. Contribution to the development of a calibration system for the measurement of nitrous acid (HONO) by differential optical absorption spectroscopy (DOAS). Diploma Work (Environmental Engineering), EPFL-University of Veszprém, Lausanne, 2000

Taira, M. and Y. Kanda. Continuos generation system for low-concentration gaseous nitrous acid. *Anal. Chem.* 62: 630-633, 1990

TEI. DOAS 2000 - Differential Optical Absorption Spectrometer. Instruction manual. Thermo Environmental Instruments, Franklin (MA), 1999

Vandaele, A.C., C. Hermans, P.C. Simon, M. Carleer, R. Colin, S. Fally, M.F. Mérienne, A. Jenouvrier and B. Coquart. Measurements of the NO_2 absorption cross-section from 42000 cm^{-1} to 10000 cm^{-1} (238-1000 nm) at 220 K and 294 K. *JQSRT* 59: 171-184, 1998

"A semiconductor injection laser that differs in a fundamental way from diode lasers has been demonstrated. It is built out of quantum semiconductor structures … Electrons streaming down a potential staircase sequentially emit photons at the steps. The steps consist of coupled quantum wells in which population inversion between discrete conduction band excited states is achieved by control of tunneling"
J. Faist et al, *1994*
*(Quantum Cascade Laser, Science **264**: 553-556)*

Chapter 5
Quantum Cascade Laser Absorption Spectroscopy (QCLAS)

This chapter reproduces the paper *Ozone detection by differential absorption spectroscopy at ambient pressure with a 9.6 μm pulsed quantum-cascade laser* published in *Applied Physics B 78: 249-256, 2004.*

Quantum-cascade lasers offer to open-path trace gas detection techniques a promising doorway to the mid-IR. Limitations due to spectral broadening at atmospheric pressure can be overcame using long atmospheric paths, appropriate acquisition rates, fairly large spectral ranges for unambiguous identification of species, and differential absorption analysis.

Ozone detection by differential absorption spectroscopy at ambient pressure with a 9.6 μm pulsed quantum-cascade laser

R. Jiménez [1], M. Taslakov [1], V. Simeonov [1*], B. Calpini [1], F. Jeanneret [1], D. Hofstetter [2], M. Beck [2], J. Faist [2] and H. van den Bergh [1]**

[1]Air Pollution Laboratory (LPAS), Swiss Federal Institute of Technology (EPFL)
CH-1015 Lausanne, Switzerland

[2]Institute of Physics, University of Neuchâtel; Breguet 1; CH-2000 Neuchâtel, Switzerland

Abstract

We report direct absorption spectroscopic detection of ozone at ambient pressure with a pulsed, DFB quantum-cascade laser (QCL) tuned within 1044-1050 cm^{-1} by temperature scanning. Wavelength calibration curves were derived from FTIR and CO_2 spectra and interpreted with respect to the heat transfer from the heterostructure to the sink. The laser linewidth (~0.13 cm^{-1} FWHM) was found to decrease with temperature, probably as a result of operation at constant current. Spurious spectral features due to baseline inaccuracies were successfully filtered out from the QCL O_3 spectra using differential absorption. Reference O_3 concentrations were obtained by applying the same method to UV spectra, simultaneously measured with a differential optical absorption spectrometer (DOAS). Column densities retrieved from QCL spectra are in fairly good agreement (±20%) with the DOAS values above 28 ppm·m. The estimated QCL lowest detectable, absolute and differential absorptions, ($7 \cdot 10^{-3}$ and $2 \cdot 10^{-3}$, respectively), entail effective detection limits of 14 and 25 ppm·m, respectively. Ongoing improvements in the acquisition system should allow the achieving detection limits at the level of commercial open-path DOAS systems (~2 ppm·m) in the near future. Our results demonstrate the applicability of the differential absorption method to QCL spectroscopy at ambient pressure and encourage its use for open path detection.

PACS:

42.62.Fi	Laser spectroscopy
82.80.Gk	Analytical methods involving vibrational spectroscopy
92.60.Sz	Air quality and air pollution

[*] Corresponding author: Fax +41/21/693-5145, E-mail: valentin.simeonov@epfl.ch

[**] Present address: MeteoSwiss, CH-1530 Payerne, Switzerland

5.1 Introduction

The understanding and mitigation of complex air pollution phenomena requires the application of elaborated finite volume models, which are typically run with a horizontal resolution of ~1-5 km for urban areas (Couach, 2003; Perego, 1999; Thunis, 2000). This averaged description of the atmosphere entails validation measurements of similar spatial resolution. Ground level point measurements frequently lack of representativeness for this purpose, particularly in poorly mixed atmospheres (Jiménez, 2000). On the contrary, optical remote sensing techniques (Sigrist, 1993), such as DOAS (Platt, 1993; Stutz, 1996), open-path (OP) FTIR and TDLAS, provide directly space-averaged concentrations of various trace gases. These spectroscopic techniques have nevertheless intrinsic limitations: DOAS is restricted to the few species that have relatively narrow, highly structured transition bands in the UV-visible. Compactness required to OP-FTIR systems usually implies low spectral resolution, which limits its selectivity. Achievable absorption paths are usually short (< 200 m) as well, which may lead to low sensitivity. Mid-IR TDLAS systems operate at high spectral resolution but are hardly tunable and require cryogenic cooling.

The advent of the quantum-cascade laser (QCL) in 1994 (Faist, 1994), and its rapid development during the last years (Capasso, 2002), has opened up the possibility of using tunable, non-cryogenic, narrow linewidth sources for real-time spectroscopic monitoring of a large number of molecular species in the mid-IR, particularly in the 3-5 μm and 8-13 μm H_2O atmospheric windows. QCL-based point measurements of several trace gases have been successfully demonstrated during the last years (Beyer, 2003; Hofstetter, 2001; Kosterev, 2002a; Kosterev, 2002b; Nelson, 2002; Schilt, 2002; Webster, 2001). With few exceptions (Beyer, 2003; Hofstetter, 2001; Schilt, 2002), these measurements have been performed at low pressure and in closed, folded optical path systems (e.g. White or Herriott cells) for sensitivity improvement. Extractive ambient air measurements rest obviously local and have the disadvantage of requiring sample manipulation, which frequently leads to undesirable wall and reaction effects. The signal-to-noise ratio (SNR) reduction due to broadening of the rovibrational bands at ambient pressure can be however compensated by using long open paths. Regarding for example the detection of O_3 at ~9.6 μm, the absorption levels obtained with a 100-m multiple-reflection cell operated at 10 mbar could be achieved as well with a ~1.8 km atmospheric path arrangement.

Our research aims at exploiting the advantages of the QCL for the detection of relevant trace gases using long open atmospheric paths. One intrinsic advantage of measuring in the mid-IR is that the detection is not affected by the presence of aerosols, in contrast with UV-visible systems (DOAS). The rapid progress in the mid-IR detection technology is expected to allow field-deployable, fully non-cryogenic operation in the near future. Currently available pyroelectric detectors are limited in bandwidth (< 2 kHz) (Kosterev, 2002a), and as shown in the last section, appear not yet suitable for open-path applications.

In order to simulate open-air conditions in the laboratory, we performed direct absorption spectroscopic measurements of O_3 at ambient pressure using a flow system. In addition its relevance in tropospheric air pollution and global warming, we chose ozone as the test compound because: (1) the QCL available spectral range (1040-1050 cm^{-1}) is within the strong υ_3 vibrational band (Flaud, 1998); (2) accurate O_3 monitoring techniques (UV DOAS and photometric point analyzers) are available, which allows for reliable laboratory calibration and future intercomparison in open path conditions.

5.2 Experimental setup

A schematic of the experimental setup is shown in **Fig. 1**. The quantum-cascade laser (QCL) used is an InGaAs-AlInAs/InP distributed feedback (DFB) commercial prototype (Alpes Lasers, DFB-QCL) devised for pulsed operation (Alpes Lasers, TPG 128 and LDD 100- pulse timer and switcher, respectively) at near room temperature with a characteristic emission wavelength of ~1046.9 cm^{-1} (~9.55 μm) at 0 °C tunable at ~ $-7.5 \cdot 10^{-2}$ cm^{-1}/K from –40 to +80 °C (see next section for calibration details). A tap water-sink Peltier-based thermal management system allows controlling the QCL temperature within ±0.1 °C. Measured average power at –30 °C reaches 5.7 mW operating at 2.25% duty cycle (*dc*) with 6.9 A (peak current) pulses at 9.6 V (bias voltage). Slow temperature-scanning spectroscopic measurements were performed with the QCL emission driven by 50 ns electrical pulses (6 A / 8 V) repeated at 100 or 300 kHz (0.5 and 1.5% *dc*, respectively).

A 10.6 μm-optimized antireflection (AR)-coated, aspheric ZnSe lens (ϕ 28 mm, f = 25 mm) was employed to collimate the highly divergent, far field elliptical QCL beam (~60° vertical, ~40° horizontal). A 3 mm thick, AR-coated ZnSe beam splitter allowed making a 532 nm Nd:YAG beam coaxial to the mid-IR beam for alignment purposes. The QCL beam was directed into the absorption cell using a flat Al mirror (M1). The cell is a plain aluminum profile (100x9x4 cm) equipped with tight window frames, a 3 mm tick AR ZnSe window (ϕ 25 mm), and a Au-coated, path-folding mirror (FM) placed inside the cell. After a double pass along the cell (L = 192 cm - effective absorption pathlength), the QCL beam is directed (using the Al mirrors M1 and M2) to a spherical Al mirror (M3: ϕ 50 mm, f = 1 m), which finally focuses it onto a fast response (25 ns rise time), liquid nitrogen cooled HgCdTe (MCT) photovoltaic detector (Kolmar Technologies, KMPV11-1-J1/DC - 0.8 mm^2 active area, 60º angle of view, peak responsivity at 10.1 μm, 50 MHz built-in amplifier). The detector window was masked with a ϕ 2 mm pinhole in order to reduce the effect of background radiation sources. MCT signals were acquired with a 500 MHz, 8-bit digital oscilloscope (LeCroy, 9354 AL) triggered by the QCL electric driving pulse. For temperature scanning purposes, the QCL temperature controller (Alpes Lasers, TC-51) was externally driven with a 16-bit digital-to-analog converter (DAC) computer card (ADLink, PCI-6208V). The TC-51 actual temperature analog signal was digitized using a multimeter (Fluke, 8842A) and then gathered via GPIB by a LabView® data acquisition / scanning manager program. Temperature scans were performed bi-directionally, typically at 10-15 mK steps. This very slow scanning rate assures an almost perfectly monotonic, ripple-free linear temperature slope. A unidirectional 70 K scan takes typically ~20 min. The QCL signal amplitude is software-calculated by subtracting the MCT signal baseline (last ~100 data points) from the pulse peak average

intensity (~10 data point around the pulse maximum). Due to software and instrument communication limitations, only ~5 pulses per temperature step were actually acquired.

A closed circuit flow configuration was used for the ozone measurements. Previous every experimental run, high purity oxygen (SL Gas, O_2 > 99.9995%) was introduced into the circuit until achieving full purge of the system through the exhaust line. Baseline spectra were then recorded. Subsequently, a homemade oxygen photolyzer equipped with 3 low-pressure Hg lamps was used to build up and sustain at steady-state various ozone concentrations (1-700 ppm). Absorption spectra were then recorded. The concentration of ozone inside the cell was real-time monitored using a Differential Optical Absorption Spectrometer (Thermo Electron Air Quality, DOAS 2000) and a calibrated UV-photometric point monitor (Dasibi, 1008-RS - 1 ppb lower detection limit - LDL). The point analyzer was utilized for monitoring low ozone concentrations (< 2 ppm) only, in particular to check the attainment of full purging of the cell with O_2. In addition, its pump served to keep a constant flow (1.5 L/min) through the gas circuit. The flow conditions were real-time monitored using a Pt-100 thermometer and a pressure transducer (Setra, 280E) linked to a 10-bit datalogger (Texas Electronics, Solus).

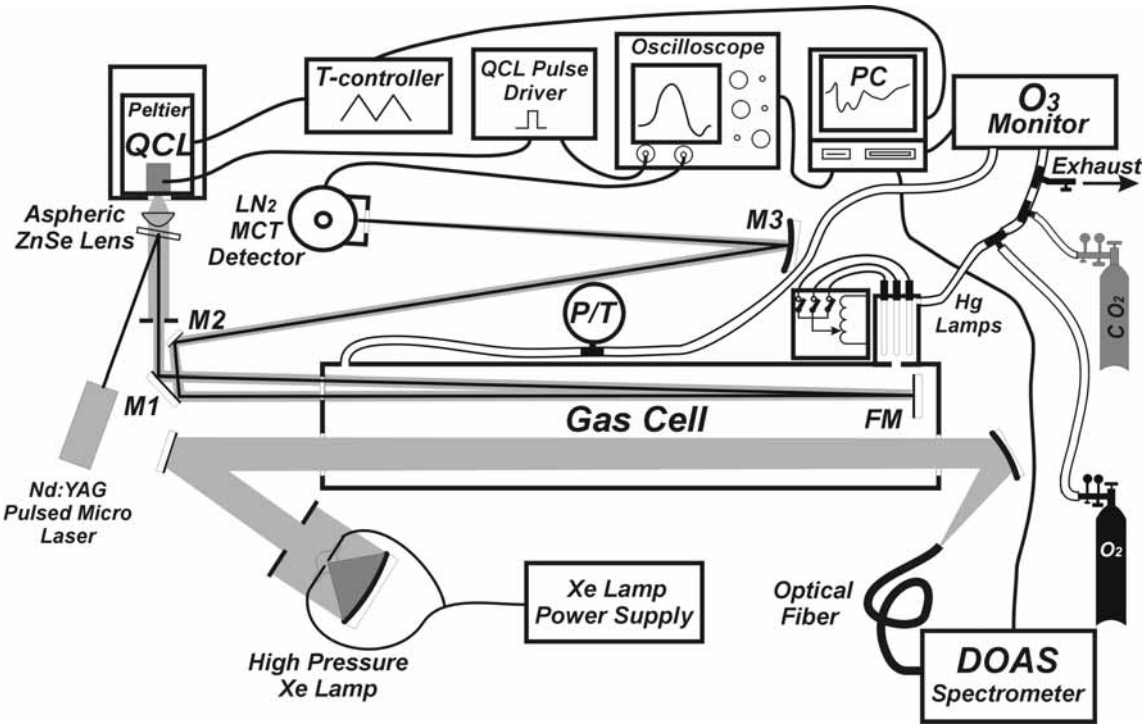

Figure 1. Schematic of the experimental setup. P/T, pressure transducer / temperature indicator.

The DOAS beam was obtained by collimation of light from a 150 W high-pressure Xe lamp (Hamamatsu, L2274). After a single pass through the cell (1 m absorption path length), the beam is focused onto a 19-optical-fiber bundle connected to a f/3.9 (0.2 m) Czerny-Turner spectrometer equipped with a 600 grooves/mm ruled grating. The diffracted beam is linearly scanned at 30 Hz by a miniature electromechanically-swept slit and detected by a side-on PMT. The scanner position is quasi-real-time mapped by a diode laser/etched photocell system perpendicular to detection plane. A transmitted intensity-controlled, automatic grating positioning routine was developed in order to measure O_3 over a large concentration span at optimum SNR conditions. In this way, the highest concentrations were measured in the 300-330 nm range and the lowest at 247-277 nm (Hartley band maximum). The first wavelength range assures that transmitted intensities are high enough to be properly detected, and the second one that the highest possible absorption is attained. The reference O_3 concentrations were retrieved by non-linear fitting of the DOAS spectra to a high resolution cross section (Daumont, 1992), previously convolved with the spectrometer function (0.56 nm FWHM). The implemented differential spectra fitting algorithm is similar to the one developed by Stutz and Platt (Stutz, 1996). Based on laboratory measurements, the DOAS LDL (3-sigma) in the 247-277 nm range at the minimum QCL spectra scanning/co-adding total time (≥ 1 h) is estimated to be lower than 0.74 ppm·m (the LDL at 2 min integration time is 2.7 ppm·m). The retrieved concentrations are precise within ±3% on average. Since both DOAS and QCL are based on optical absorption, full comparability between the two systems is assured, even if minor concentration gradients could develop along the cell.

5.3 Wavelength calibration and linewidth estimation

We obtained transmission spectra by slow temperature scanning. Appropriate spectral mapping of these scans requires accurate knowledge of the laser wavelength dependence on temperature at various operational conditions. We measured this dependence using a low resolution (0.5 cm^{-1} FWHM) FTIR spectrometer (Nicolet 800), and through CO_2 spectra measured at ambient pressure, displayed four well resolved $00^01 \leftarrow 02^00$, 9P-branch rovibrational transitions (P18, P20, P22, P24) (Devi, 1996) (see Fig. 2a). High purity carbon dioxide (SL Gas, CO_2 > 99.998%) spectra was acquired using bi-directional temperature scanning within –35 to +50 °C with the QCL excited with 50 ns electric pulses repeated at 100 or 300 kHz (0.5% or 1.5% *dc*, respectively).

The QCL heat sink temperatures (T_S) at the CO_2 broaden absorption transition maxima, $T_{S,k}$, were determined with a precision better than ±0.2 K (±0.015 cm^{-1} equivalent uncertainty). We observed statistically significant differences in $T_{S,k}$, of up to –0.6 K, between subsequent cooling-down and heating-up scanned CO_2 spectra. These small differences and the significant differences observed between CO_2 spectra measured at 0.5% and 1.5% *DC* ($\Delta T_{S,k}$ ≈ –4.4 K - see **Fig. 2a** are explained by the increase of the heterostructure-to-sink temperature gradient with an increase of the heat dissipated by the laser. The slight decreases with temperature of the overall heat transfer coefficient explains the wavelength calibration slope decrease with increasing power duties as observed in **Fig. 2b**. Calibration curves are

appropriately described by first-degree fitting polynomials. Before linear fitting of the $(T_{S,k}, \tilde{\nu}_k)$ data pairs, the temperature-scanned CO_2 spectra were co-added and averaged, baseline subtracted, low-pass filtered (Savitzky-Golay), and the peak absorption temperatures $(T_{S,k})$ determined as optical density local maxima. We took care of preserving separate calibration curves for heating-up and cooling-down scanned spectra in order to account for minute differences as explained above. The wavelength accuracy, estimated as the maximum calibration residual, is better than ±0.03 cm^{-1}.

Appropriate comparison of our experimental spectra with HITRAN-based (Rothman, 1998) calculations requires estimation of the QCL linewidth. For this purpose, the observed CO_2 transition lines were separately fitted to a model lineshape and analyzed. As expected at atmospheric pressure, the observed lines were found to best fit to a Lorentzian lineshape. Supported by convolution calculations that achieve reproducing the FTIR observations, we assume the QCL emission lineshape to be Lorentzian as well. This assumption allows estimating the QCL halfwidth $(\alpha_{L,QCL})$ by subtraction of the HITRAN-based calculated transitions halfwidths $(\alpha_{L,\sigma})$ from the observed halfwidths $(\alpha_{L,D} \cong \alpha_{L,\sigma} + \alpha_{L,QCL})$. This approach has been widely used for linewidth estimation (Claveau, 2002; Kosterev, 2002a; Schilt, 2002). The retrieved QCL halfwidths at 0.5 % *dc* range from 0.056 cm^{-1} for the P22 transition to 0.067 cm^{-1} for the P18 (1.7-2.0 GHz). These linewidths are narrower than expected for a 50 ns long pulse (Hofstetter, 2001; Schilt, 2002), and show negative dependence with the heat sink temperature. Retrieved linewidths at 1.5% *dc* and FTIR spectra show a similar behavior. Our findings are apparently in contradiction with recent theoretical calculations that state positive dependence of the QCL linewidth with temperature (Gorfinkel, 1996; Wacker, 2002). These calculations refer nevertheless to isothermal operation at a constant current (i) above the lasing threshold current (i_{th}). We obtained spectra by slow temperature scanning over a fairly large range, operating at fixed current thus at a variable i/i_{th} ratio. As a consequence, one can expect broader linewidths at lower temperatures for which the threshold current is smaller, thus the i/i_{th} ratio is higher. This may explain our experimental observations.

5.4 Absolute and differential analysis of ozone spectra

Ozone absorption spectra at seven steady-state concentration levels within 1-631 ppm were acquired by bi-directional scanning of the QCL at 0.5% *DC* from –35 to +35 °C (1044-1050 cm^{-1}). In this wavelength range, ozone displays the highly structured R-branch of its $001 \leftarrow 000$ vibrational band (Flaud, 1998) (O_3 is a greenhouse gas largely because of the infrared absorption in this band). Six to 45 absorption spectra were scanned per O_3 level. Baseline, $I_0(T_S)$, and absorption scans, $I(T_S)$, were logarithmically averaged. The average optical density, $\overline{D}$, was calculated as the average $\overline{\ln(I)}$ subtracted from the average $\overline{\ln(I_0)}$. Heating-up and cooling-down spectra were separately averaged and temperature-to-wavenumber transformed. The resulting absorption spectra are shown in the Fig. 3 along with their corresponding theoretical optical densities (D_H),

$$D_H(\tilde{\nu}) = -\ln\left[\tau_H(\tilde{\nu})\right] \qquad (1)$$

calculated using the DOAS-retrieved ozone concentrations (c). The theoretical transmittances, $\exp(-\sigma \cdot c \cdot L)$, were convolved with a Lorentzian QCL emission lineshape (H) of constant width, taken as the average halfwidth retrieved from the CO_2 spectra ($\overline{\alpha}_{L,QCL}$ = 0.063 cm^{-1}),

$$\tau_H(\tilde{\nu}) = \exp\left[-\sigma(\tilde{\nu}) \cdot c \cdot L\right] \otimes H(\tilde{\nu}') \qquad (2).$$

τ_H is the convolved theoretical transmittance, σ is the HITRAN-based calculated (pressure, temperature-dependent) absorption cross section (Rothman, 1998), and L is the absorption path length ($c \cdot L$ is the column density).

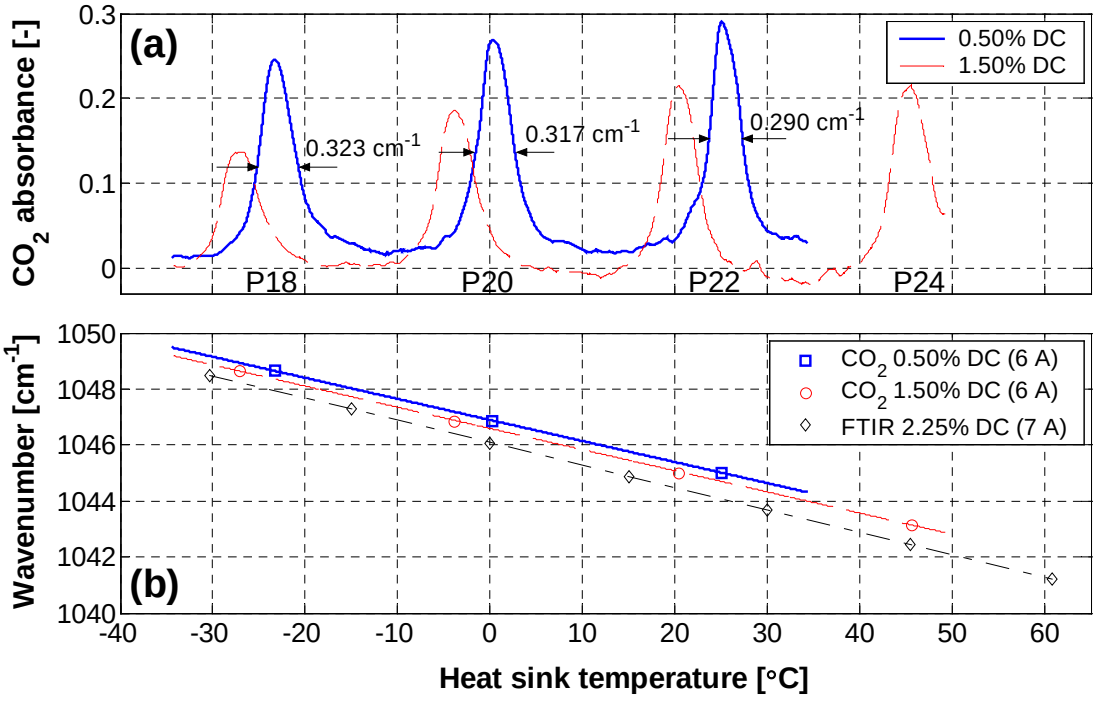

Figure 2. QCL wavelength and linewidth. **(a)** Temperature-scanned CO_2 absorption spectra at two duty cycles and at constant current (6 A). The observed $00^01 \leftarrow 02^00$, 9P-branch rovibrational transitions are indicated along with their linewidths. **(b)** CO_2- and FTIR-derived wavelength calibration curves at various duty cycles (*dc*) and peak currents.

The common-baseline absorption spectra displayed in **Fig. 3a** ($c \cdot L$ > 300 ppm·m) show consistently lower optical densities than the expected from the BLB law. This discrepancy stems from underestimation of the baseline level, probably due to optical misalignment. Calculated spectra in this panel show as well excessive spectral smoothing at the lower wavenumbers. This points out to a narrower-than-average QCL emission linewidth at the lower wavenumbers and provides additional evidence to the inverse linewidth-to-temperature dependence behavior.

At column densities below 80 ppm·m (see **Fig. 3b**), the relative difference between baseline and transmitted intensity, i.e. the absorptivity (1-τ_H), becomes smaller than ~5%. At these absorption levels, relatively small baseline deviations can cause spurious, broad features in the optical density spectra, particularly within the lower absorption range ($\tilde{\nu}$ < 1046 cm^{-1}).

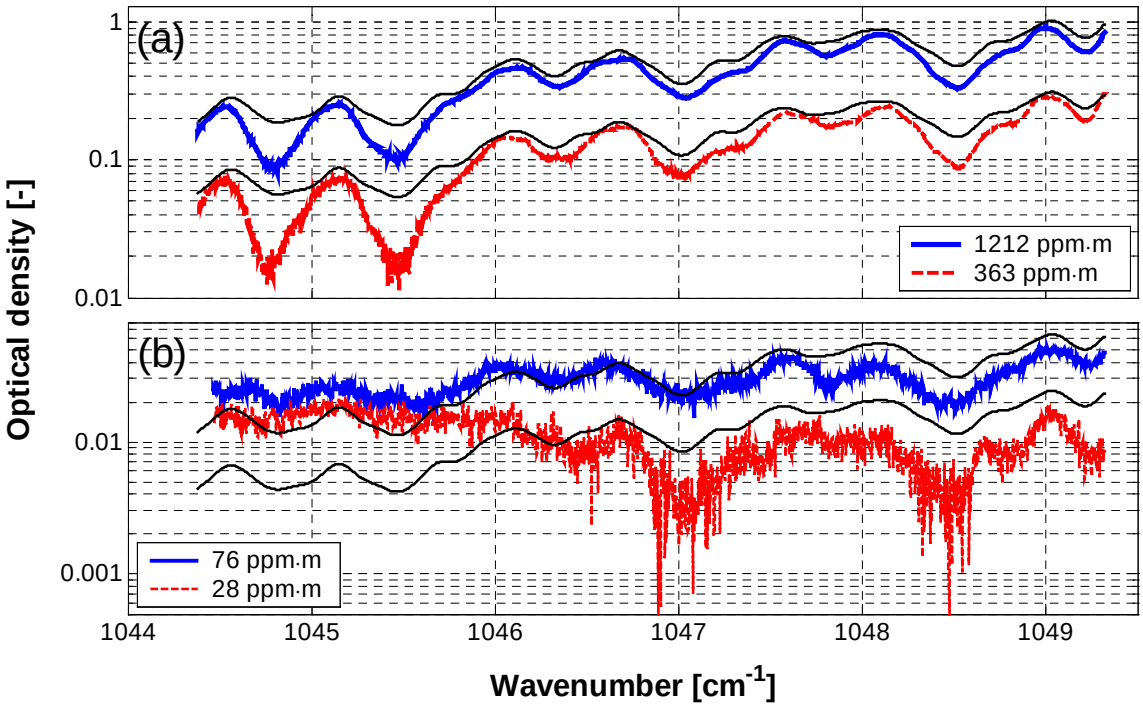

Figure 3. Measured (thick lines) and HITRAN-based calculated (thin lines) QCL absorption spectra at **(a)** high/moderate and **(b)** low O_3 column densities over a 192 cm long effective absorption path. Discrepancies mainly stem from baseline inaccuracies.

The effect of an inaccurately defined baseline on atmospheric pressure absorption spectra is particularly noticeable on the 28 ppm·m spectrum shown in **Fig. 4a**, which is apparently in poor agreement with the HITRAN-based calculated optical densities. The concentration retrieval in this situation can be largely improved using the differential absorption approach. In this approach, distinction is made between "*broad*" and "*narrow*" spectral variations (Platt, 1993; Stutz, 1996). The narrow variations are extracted from the absorption spectra by simple subtraction of a synthetic, smooth trend curve, $f(D)$. This low-pass (LP) filter represents the broadband spectral component and is defined by the absorption spectra itself so no assumption on the actual baseline is required. The differential optical density, ΔD, is calculated as the LP-filter subtracted optical density,

$$\Delta D(\tilde{\nu}) = D(\tilde{\nu}) - f\left(D(\tilde{\nu})\right) \qquad (3)$$

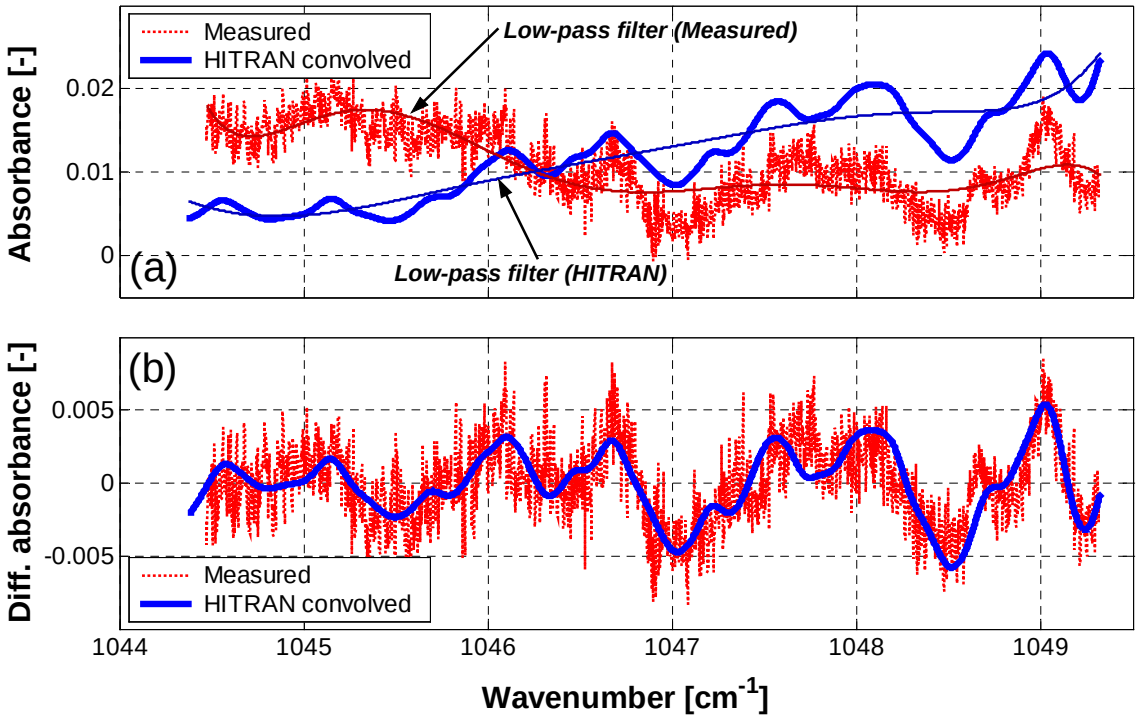

Figure 4. Application of the differential absorption method to the QCL spectra at 28 ppm·m O_3. **(a)** The measured and calculated absorption spectra are shown along with their corresponding polynomial low-pass filters (thin lines). **(b)** The measured differential absorption spectrum is in good agreement with the HITRAN-based calculation.

The LP-filters shown in Fig. 4a are plain 7th degree fitting polynomials. Subtraction of these trend curves leads to a highly improved agreement between measured and calculated absorbances (see **Fig. 4b**).

The procedure described above is the basis of the DOAS technique (Platt, 1993; Stutz, 1996), developed and successfully applied since the late seventies to the detection over long open paths of important trace gases in the UV-visible, frequently at the sub-ppb level. The differential absorption method makes possible the retrieval of concentrations in open path conditions, for which the light source spectra is known but the actual baseline spectra cannot be determined, particularly in the UV, where Mie attenuation is very important.

The resulting QCL differential absorption spectra along with their theoretical counterparts are shown in **Fig. 5**. Good agreement between measurements and calculations is observed for all the column densities above 28 ppm·m, which confirms that the discrepancies observed in Fig. 3 are due to baseline inaccuracies. A close look at Fig. 5 reveals that the differential spectra are slightly noisier at lower wavenumbers, i.e. at higher temperatures. This wavelength dependence of the SNR is explained by the significant decrease of the laser power (~70%) between –35 and +35 °C.

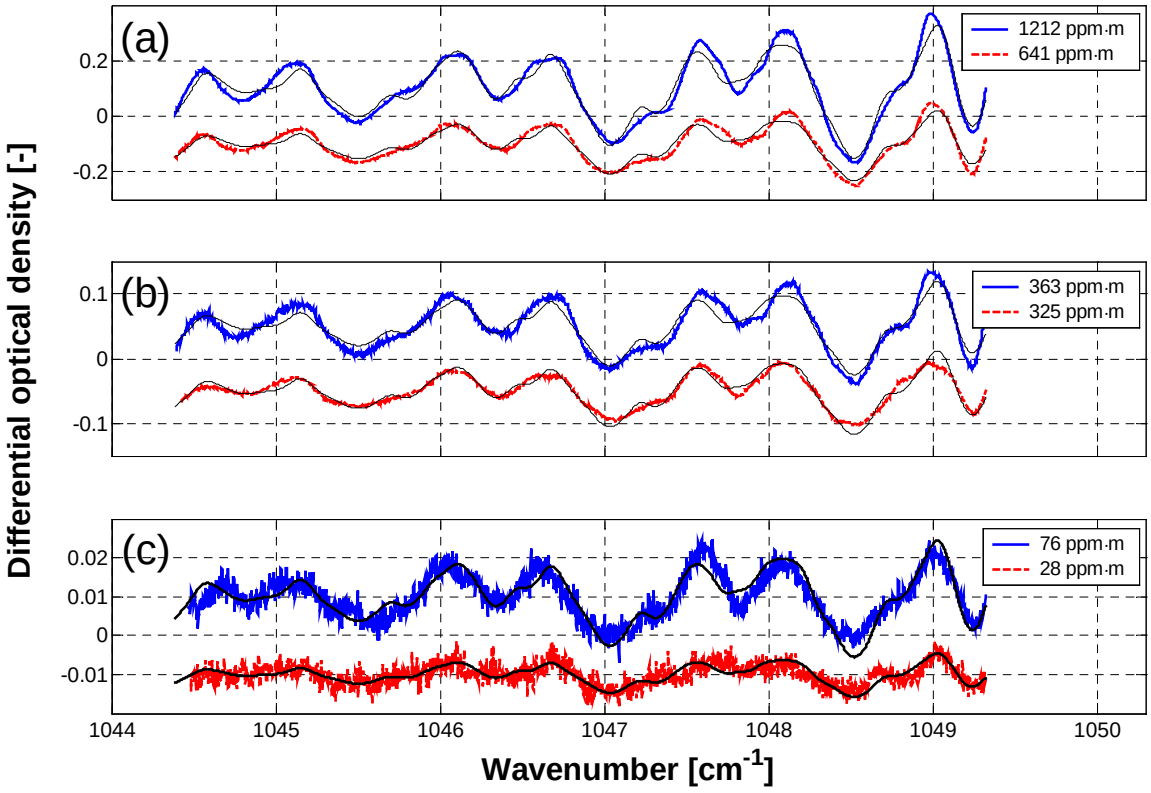

Figure 5. Measured (thick lines) and HITRAN-based calculated (thin lines) QCL differential absorption spectra at **(a)** high, **(b)** moderate, and **(c)** low ozone column densities. Measured and calculated spectra were vertically displaced for visualization purposes.

We investigated two approaches for concentration retrieval from both absolute and differential absorption spectra: comparison with a high SNR reference spectrum (D_0 and ΔD_0, for absolute and differential spectra, respectively) and linearization of the BLB law. The first approach assumes linear dependence of the absorbance, and consequently of the differential absorbance, with the column density. Due to the finite linewidth of the QCL, this assumption is rigorously valid only at column densities approaching that one of the reference spectrum, $(c \cdot L)_0$. The column density ratio, $a \cong (c \cdot L)/(c \cdot L)_0$, is retrieved by zero offset, least squares linear fitting of the measured spectra to the reference spectra, whether absolute, $D(\tilde{\nu}) \cong a \cdot D_0(\tilde{\nu})$, or differential, $\Delta D(\tilde{\nu}) \cong a \cdot \Delta D_0(\tilde{\nu})$. The concentrations shown in Fig. 6 were calculated using the highest column density (1212±34 ppm·m) spectrum as reference (a Savitzky-Golay low-pass filter was applied previous utilization).

The second concentration retrieval approach assumes that the optical density, D_H, is small enough ($D_H \cong 1-\tau_H$) to be appropriately expressed as,

$$D_H(\tilde{\nu}) \cong \sigma_H(\tilde{\nu}) \cdot c \cdot L \qquad (4)$$

where $\sigma_H = \sigma \otimes H$ is the convolution product of the cross section with the average QCL lineshape. The linearization above is numerically valid within ±1% for (relative) absorptances below 17%, an inherently fulfilled condition in open path spectroscopy of trace gases. Column densities are directly retrieved ($b \cong c \cdot L$) by least squares linear fitting of the convolved cross section, whether to the absolute, $D(\tilde{\nu}) \cong b \cdot \sigma_H(\tilde{\nu}) + b_0$, or to differential absorbance, $\Delta D(\tilde{\nu}) \cong b \cdot \Delta\sigma_H(\tilde{\nu})$ (the b_0 coefficient is intended at correcting a constant baseline offset). The differential convolved cross section, $\Delta\sigma_H$,

$$\Delta\sigma_H(\tilde{\nu}) = \sigma_H(\tilde{\nu}) - f(\sigma_H(\tilde{\nu})) \qquad (5)$$

is calculated by subtraction of an absorbance-homologous LP-filter (a 7th degree polynomial in our case). Results are shown in **Fig. 6**.

The most accurate column densities were retrieved from absolute spectra using the highest column density spectrum as reference. Discrepancies are typically lower than ±2% (above LDL), i.e. within the uncertainty of the DOAS measurements. On the other hand, retrieval from absolute absorption spectra with the convolved cross section yields rather accurate (~9% underestimation) column densities above ~300 ppm·m only. At lower column densities unmatched baseline features lead to very inaccurate (60% underestimation) or even negative column densities (see **Fig. 6a**). In contrast, the two approaches produce similar results when applied to differential spectra, typically with ±15% accuracy (above LDL). Moreover, fitting to the cross section yields more accurate results near the detection limit (see **Fig. 6b**). Below

~80 ppm·m, differential spectra were found to yield more precise (±1%) column densities than absolute spectra (±3% precision).

The detection limits of the absolute and differential methods were estimated using the root-mean-square (RMS) of the residuum (δ) between observed and calculated absorbances ($\delta_D = D - D_H$ or $\delta_{\Delta D} = \Delta D - \Delta D_H$) as a measure of the spectral noise. The LDLs are calculated as the column densities at which the expected spectral signal (RMS of D_H or ΔD_H) equals the discrepancy RMS, i.e. for a SNR of 1. The lowest detectable column densities with the absolute and differential methods are estimated at 14 ppm·m and 25 ppm·m, respectively (see **Fig. 7**). These values correspond to lowest detectable absolute and differential QCL absorptions (RMS) of $7 \cdot 10^{-3}$ and $2 \cdot 10^{-3}$, respectively. A close look at the 28 ppm·m O_3 differential spectrum (see Fig. 4b) indicates that the actual LDL of the differential method is probably better than the estimated from the RMS discrepancy analysis. This absorption spectrum is clearly above the LDL although it shows a peak-to-peak noise level of $\sim 5 \cdot 10^{-3}$ absorbance units. This fairly high noise level is due to the low pulse averaging rate achieved in the experiment (~20 Hz effective).

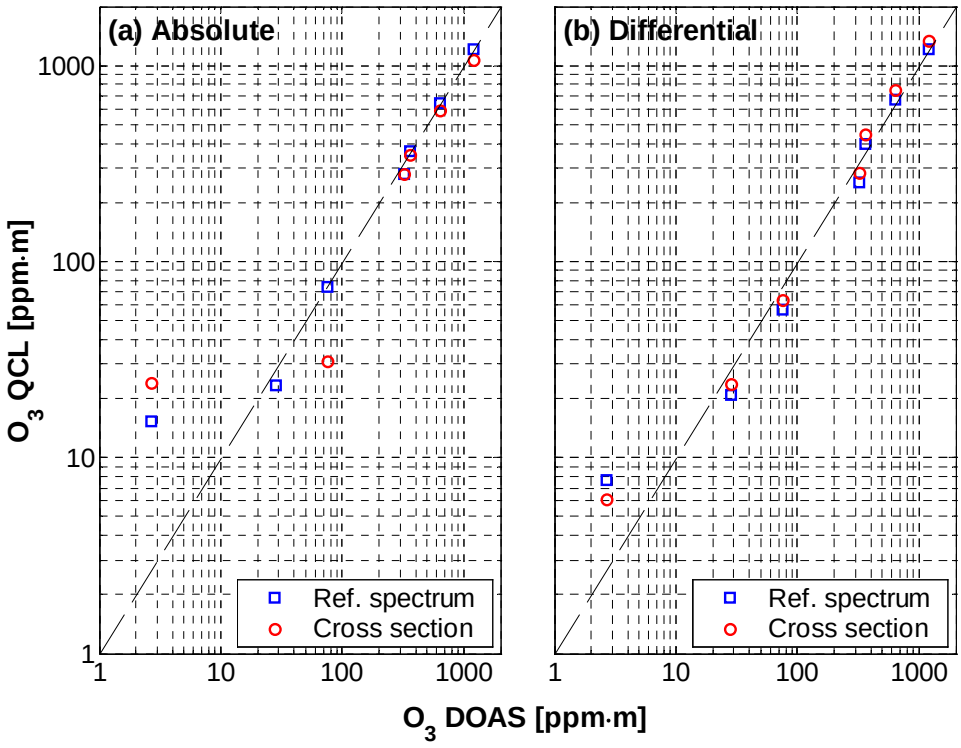

Figure 6. Comparison of ozone column densities retrieved from QCL **(a)** absolute and **(b)** differential absorption spectra to the QCL-equivalent reference values (DOAS). Retrievals using a high SNR spectrum as reference and with the convolved cross section are presented. The QCL and DOAS absorption pathlengths were 192 cm and 100 cm, respectively.

The resulting differential to absolute LDL ratio of 1.8 is well below the theoretical ratio of 5.8, estimated as the absolute to differential cross section ratio (RMS),

$$\frac{LDL_{DIFF}}{LDL_{ABS}} \approx \frac{RMS\left(\sigma_H\right)}{RMS\left(\Delta\sigma_H\right)} \qquad (6)$$

This implies that the LDL achieved with absolute absorption spectra is 3 times higher than expected. This reduced performance mainly stems from inaccuracy in the baseline determination.

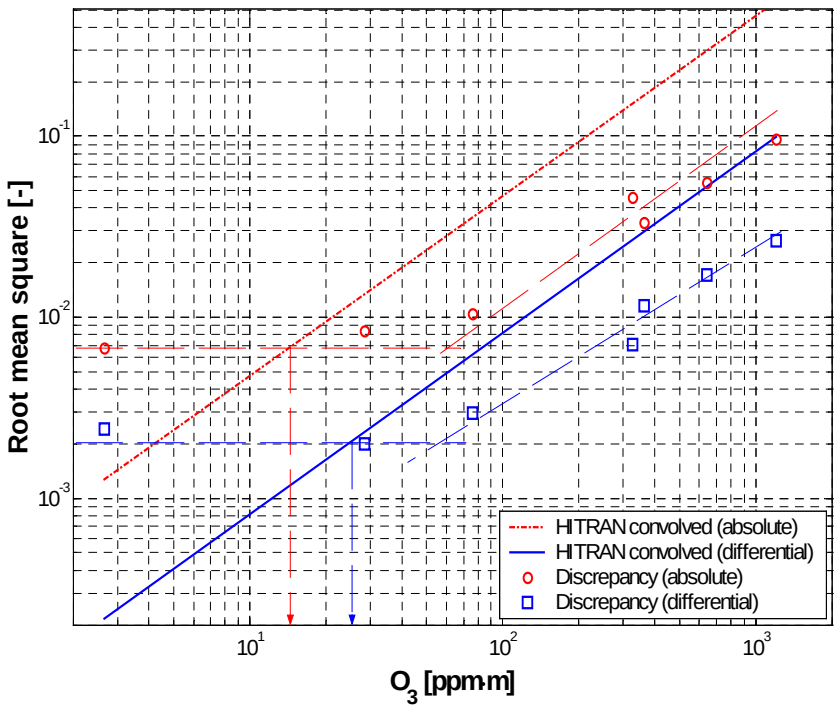

Figure 7. Root mean square of the theoretical spectral signal (HITRAN convolved) and of the discrepancy of measurements to the theoretical values as a function of the O_3 column density. Signal and discrepancy are given for QCL absolute and differential absorption spectra. The lowest detectable absorbances (RMS) and column densities are estimated for a SNR of 1.

5.5 Conclusions and perspectives

Our O_3 measurements covered a ~3-decade column density range (3-1212 ppm·m). Accurate concentrations (±2%) were retrieved from QCL absolute absorption spectra using a high SNR spectrum (1212±34 ppm·m) as reference. The differential method was found less accurate (±15%) but on average more reliable and precise at lower concentration levels (< 80 ppm·m).

For wavelength mapping purposes, we measured the heat sink temperature dependence on the duty conditions. This dependence can be satisfactorily explained considering the transfer of heat from the QCL heterostructure to the sink. A parametric extension of this analysis should allow representing a QCL calibration curve family with a single, parametric-dependent temperature-to-wavelength calibration curve.

A detailed mapping of the linewidth dependence on the duty conditions (*dc* and i/i_{th}) is important concerning the wavelength-dependent convolution of calculated cross sections. This procedure is particularly important for the retrieval of analytically difficult (adsorptive or reactive) species without requiring previous laboratory reference spectra measurements. We observed a negative dependence of the linewidth with temperature. This finding deserves further experimental investigation, preferably with a high-resolution FTIR spectrometer.

A fairly large spectral range is required for unambiguous identification of species at atmospheric pressure due to line broadening. We obtained spectra of up to 7 cm^{-1} by temperature tuning at ~0.3 cm^{-1}/min. This slow scanning speed is obviously unsuitable for open path measurements due to the dynamic nature of the atmosphere. We have recently attained scanning rates of ~2.5 cm^{-1}/min using a single, non-controlled temperature step with promising spectral results (fast scanning wavelength reproducibility have been extensively demonstrated – the work of Beyer *et al* (Beyer, 2003) is a remarkable example). Moreover, operation with shorter QCL pulses (~20 ns) should significantly improve the spectral resolution thus allowing for unambiguous identification of ozone using a narrower wavelength range (~3 cm^{-1}). Appropriate scanning times (~1-2 min) could be this way achieved.

Improving the current differential absorption LDL (25 ppm·m) to the level of commercial DOAS systems (~2 ppm·m) would require increasing ~160-fold the QCL pulse averaging rate. In addition, open-path detection would necessitate decreasing ~20-fold the current wavelength scanning time. This combination of requirements implies an effective pulse averaging rate of ~4 kHz for a ~300 effective data point averaged spectrum scanned in ~1-min. We are currently developing a synchronous (gated) sampling board that is expected to allow for pulse averaging at up to ~100 kHz. We intend to use two pairs of these boards for the simultaneous averaging of the signal peak and baseline of both, reference and transmitted pulses. Provided that the averaging rate is significantly improved, a reduction of the linewidth should render additional improvement of the SNR (~50% reduction of the linewidth yields ~30% increase of the $\Delta\sigma_H$ RMS.

Our results demonstrate the applicability of the differential method to QCL spectroscopy at atmospheric pressure and facilitate its application to open-path spectroscopic detection of trace gases. We have recently performed preliminary open-air QCL absorption measurements over a 460-m atmospheric path using a monostatic (emitter-retroreflector-receiver) configuration, and obtained return signals of good intensity and highly structured spectra.

Acknowledgements

We gratefully acknowledge Alpes Lasers for kindly providing us with the QCL used in this investigation, particularly to A. Müller for his cooperation and valuable discussions. EPFL/LPAS research was financially supported by EPFL/VPR, NCCR (Quantum Photonics Grant), ICSC-World Laboratory (Project LAND-14), and Thermo Electron Air Quality Inc.

5.6 References

Beyer, T., M. Braun and A. Lambrecht. Fast gas spectroscopy using pulsed quantum cascade lasers. *J. Appl. Phys.* 93 (6): 3158-3160, 2003

Capasso, F., C. Gmachl, D.L. Sivco and A.Y. Cho. Quantum cascade lasers. *Physics Today* 55 (5): 34-40, 2002

Claveau, C., M. Lepère, G. Dufour, A. Valentin, A. Henry, C. Camy-Peyret and D. Hurtmans. Diode laser emission linewidth determination. Application to H_2O line profile studies in the 5 and 1.4 μm regions. *Spectrochim. Acta A* 58: 2313-2321, 2002

Couach, O., I. Balin, R. Jiménez, P. Ristori, S. Perego, F. Kirchner, V. Simeonov, B. Calpini and H. van den Bergh. An investigation of ozone and planetary boundary layer dynamics over the complex topography of Grenoble combining measurements and modeling. *Atmos. Chem. Phys.* 3: 549–562, 2003

Daumont, D., J. Brion, J. Charbonnier and J. Malicet. Ozone UV spectroscopy I: Absorption cross-section at room temperature. *J. Atmos. Chem.* 15: 145-155, 1992

Devi, V.M., D.C. Benner, C.P. Rinsland, M.A.H. Smith and D.S. Parmar. Infrared spectroscopy of the CO_2 molecule. *Recent Res. Devel. Geophys. Res.* 1: 119-148, 1996

Faist, J., F. Capasso, D.L. Sivco, C. Sirtori, A.L. Hutchinson and A.Y. Cho. Quantum Cascade Laser. *Science* 264 (5158): 553-556, 1994

Flaud, J.M. and R. Bacis. The ozone molecule: infrared and microwave spectroscopy. *Spectrochim. Acta A* 54 (1): 3-16, 1998

Gorfinkel, V.B., S. Luryi and B. Gelmont. Theory of gain spectra for quantum cascade lasers and temperature dependence of their characteristics at low and moderate carrier concentrations. *IEEE J. Quantum Electron.* 32 (11): 1995-2003, 1996

Hofstetter, D., M. Beck, J. Faist, M. Nägele and M.W. Sigrist. Photoacustic spectroscopy with quantum-cascade distributed-feedback lasers. *Opt. Lett.* 26 (12): 887-889, 2001

Jiménez, R., T. Iannone, H. van den Bergh, B. Calpini and D. Kita. Investigation of the emission of monocyclic aromatic hydrocarbons from a wastewater treatment plant at Lausanne (Switzerland) by differential optical absorption spectroscopy (DOAS). *A&WMA 93rd Annual Conf. & Exhib.*, Salt Lake City, USA, 18-22 June, 2000: paper 830

Kosterev, A.A., R.F. Curl, F.K. Tittel, M. Rochat, M. Beck, D. Hofstetter and J. Faist. Chemical sensing with pulsed QC-DFB lasers operating at 15.6 μm. *Appl. Phys. B* 75 (2-3): 351-357, 2002a

Kosterev, A.A., F.K. Tittel, R. Köhler, C. Gmachl, F. Capasso, D.L. Sivco, A.Y. Cho, S. Wehe and M.G. Allen. Thermoelectrically cooled quantum-cascade-based sensor for the continuous monitoring of ambient atmospheric carbon dioxide. *Appl. Opt.* 41 (6): 1169-1173, 2002b

Nelson, D.D., J.H. Shorter, J.B. McManus and M.S. Zahniser. Sub-part-per-billion detection of nitric oxide in air using a thermoelectrically cooled mid-infrared quantum cascade laser spectrometer. *Appl. Phys. B* 75: 343-350, 2002

Perego, S. METPHOMOD - A numerical mesoscale model for simulation of regional photosmog in complex terrain: Model description and application during POLLUMET 1993 (Switzerland). *Meteor. Atmos. Phys.* 70: 43-69, 1999

Platt, U. Differential optical absorption spectroscopy. **In** M.W. Sigrist (ed), Air monitoring by spectroscopic techniques, Wiley, New York, 1993: 27-84

Rothman, L.S., C.P. Rinsland, A. Goldman, S.T. Massie, D.P. Edwards, J.-M. Flaud, A. Perrin, C. Camy-Peyret, V. Dana, J.-Y. Mandin, J. Schroeder, A. McCann, R.R. Gamache, R.B. Wattson, K. Yoshino, K.V. Chance, K.W. Jucks, L.R. Brown, V. Nemtchinov and P. Varanasi. The HITRAN Molecular Spectroscopic Database and HAWKS (HITRAN Atmospheric Workstation): 1996 Edition. *JQSRT* 60: 665-710, 1998

Schilt, S., L. Thévenaz, E. Courtois and P.A. Robert. Ethylene spectroscopy using a quasi-room-temperature quantum cascade laser. *Spectrochim. Acta A* 58: 2533-2539, 2002

Sigrist, M.W. (ed). Air monitoring by spectroscopic techniques. Wiley, New York, 1993

Stutz, J. and U. Platt. Numerical analysis and estimation of the statistical error of differential optical absorption spectroscopy measurements with least-squares methods. *Appl. Opt.* 35 (30): 6041-6053, 1996

Thunis, P. and A. Clappier. Formulation and evaluation of a non-hydrostatic mesoscale vorticity model (TVM). *Mon. Wea. Rev.* 128 (9): 3236-3251, 2000

Wacker, A. and S.C. Lee. Gain and loss in quantum cascade lasers. *Physica B* 314: 327-331, 2002

Webster, C.R., G.J. Flesch, D.C. Scott, J.E. Swanson, R.D. May, W.S. Woodward, C. Gmachl, F. Capasso, D.L. Sivco, J.N. Baillargeon, A.L. Hutchinson and A.Y. Cho. Quantum-cascade laser measurements of stratospheric methane and nitrous oxide. *Appl. Opt.* 40 (3): 321-326, 2001

Chapter 6
Field Studies

Two field studies are presented in this chapter. The first one analyzes the dynamics, emission, and photochemical production regime of formaldehyde in the Grenoble air basin based on DOAS measurements and photochemical grid model calculations.

The second one investigates the emission of monocyclic aromatic hydrocarbons (MAH) from a wastewater treatment and sludge incineration plant in Lausanne, Switzerland. This investigation is based on measurements with DOAS and GC/FID in the gas phase, and wastewater grab samples analyzed by SPME/GC/MS.

The first paper was recently submitted to *Atmospheric Environment*. The second one was published in *Proceedings of A&WMA 93rd Annual Conference and Exhibition* (Salt Lake City, June 18-22, 2000: Paper 830).

The results from another field study concerning formaldehyde in a suburban location of Milan, Italy, are presented in **Annex H** (*Measurement of formaldehyde (HCHO) by DOAS: Intercomparison to DNPH measurements and interpretation from Eulerian model calculations – Proc. A&WMA 93rd Annual Conf. Exhib., Salt Lake City, June 18-22, 2000: Paper 829*). Measurements and preliminary analysis of data obtained during the CAVASO 2002 campaign (Sogamoso Valley, Colombia) are presented in **Annex I**.

Formaldehyde dynamics and photochemical production regime in the Grenoble region, France

Rodrigo Jiménez [a,*], Olivier Couach [a], Frank Kirchner [a], Ioan Balin [a], Silvan Perego [b], Bertrand Calpini [a,c], and Hubert van den Bergh [a]

[a] *Air Pollution Laboratory (LPAS), Swiss Federal Institute of Technology (EPFL), CH-1015 Lausanne, Switzerland*
[b] *IBM Schweiz, Altstetterstrasse 124, CH-8010 Zurich, Switzerland*
[c] *MeteoSwiss, Aerological Station, CH-1530 Payerne, Switzerland*

Abstract

Measurements of formaldehyde by differential optical absorption spectroscopy (DOAS), conducted at a suburban location at 20 km south of Grenoble, and calculations with a photochemical grid model (METPHOMOD) were used to investigate the sources, dynamics, and photochemical production regime of CH_2O in the Grenoble region during GRENOPHOT 1999. A short intercomparison with DNPH/HPLC shows a high degree of correlation between the two CH_2O measurement techniques (r^2 = 97%) but also significant deviation from the 1:1 line (discrepancy is nevertheless below ±1 ppb). CH_2O displayed diurnal variation typical of photochemical pollutants with peak concentrations of up to 11 ppb during the observation period. METPHOMOD was applied for the simulation of a 3-day photochemical episode. Modeled concentrations of CH_2O, O_3, NO_2, and NO reproduce appropriately the field observations. Moreover, the model captures appropriately the morning, afternoon and night CH_2O peaks. The photochemical fraction of CH_2O was estimated from measurements by assuming proportionality of primary and secondary CH_2O respectively with NO_X and O_3, and using a differentiated labeling of primary, secondary, and boundary-advected formaldehyde in the chemical mechanism (RACM). Modeled and measurement-derived CH_2O photochemical fractions (~80% diurnal average) agree well, except during the sunrise period. The estimated CH_2O/NOx emission ratio (0.04±0.02 mole $mole^{-1}$) is in good agreement with the emission inventory and literature values (the validity of measurement-derived ratios is analyzed on the basis of the mass conservation equation). The model shows the development of primary CH_2O plumes of urban and industrial origin in the morning, and of secondary CH_2O plumes on the sunlit hours advected by mountain-valley winds. CH_2O production regime at the measurement site and at Grenoble downtown was found to be nearly linear with VOC emissions and weakly NOx saturated. Analysis of the photochemical production regime indicates that O_3 and CH_2O abatement strategies are compatible, despite the large differences in photochemistry and lifetime between these two pollutants.

Keywords: formaldehyde, emission ratio, photochemical production regime, DOAS, photochemical grid model

[*] Corresponding author. Phone +41-21-693-3189; Fax +41-21-693-5145; E-mail: rodrigo.jimenez@epfl.ch

1. Introduction

Elevated concentrations of ozone and other photochemical pollutants originate from the oxidation of volatile organic compounds (VOC) through a complex series of photochemical reactions "catalyzed" by nitrogen oxides (NO_X). The first moderately stable photo-oxidation products are the organic carbonylic compounds (Lelieveld, 2000; Trapp, 1995). Formaldehyde is the simplest, most important and usually the most abundant among them (Carlier, 1986; Larsen, 2001; Meller, 2000; Slemr, 1996; Solberg, 2000). Despite of its relatively short lifetime, particularly in sunlit conditions (~3 h - Slemr, 1996; Wert, 2003), CH_2O is an ubiquitous atmospheric component due to the photo-oxidation of CH_4 at the global scale (Wagner, 2002). The photolysis of CH_2O is a net source of hydroperoxyl radicals (HO_2) that in moderately and highly polluted atmospheres are readily converted into hydroxyl (OH) radicals,

$$HO_2 + NO \rightarrow OH + NO_2 \qquad \text{(A)}$$

The oxidation of CH_2O proceeds via photolysis,

$$CH_2O + h\nu \rightarrow H_2 + CO \qquad \text{(B1)}$$

$$CH_2O + h\nu \rightarrow H + HCO\left(+2O_2\right) \rightarrow 2HO_2 + CO \qquad \text{(B2)}$$

and by attack of OH and NO_3 (nitrate radical),

$$CH_2O + OH \rightarrow HCO + H_2O\left(+O_2\right) \rightarrow HO_2 + CO + H_2O \qquad \text{(C)}$$

$$CH_2O + NO_3 \rightarrow HCO + HNO_3\left(+O_2\right) \rightarrow HO_2 + CO + HNO_3 \qquad \text{(D)}$$

This sequence of reactions re-furnishes the photo-oxidation process with OH and enhances the NO_2/NO ratio, which ultimately increases the ozone production rate in sunlit conditions.

Formaldehyde is as well a combustion by-product (John, 1999; Klemp, 2002; Li, 1997; Staehelin, 1998), and an important product and by-product of the chemical industry (Carlier, 1986). CH_2O emissions may have a significant impact on photochemical pollution due to their elevated incremental reactivity (1.3-4.5 mole of O_3 per mole of CH_2O) (Finlayson-Pitts, 2000; Seinfeld, 1998).

This dual nature of primary (emitted) and secondary (photochemical) pollutant makes of CH_2O a well-suited species for model validation purposes (Solberg, 2000). The ability to reproduce CH_2O observations is indicative of the accuracy of both, emission inventories, and the atmospheric chemistry and physics description. Reported model calculations of CH_2O in

remote (Fried, 1997; Wagner, 2002) and rural atmospheres (Solberg, 2000) are in general in good agreement with observations. CH_2O levels in urban and suburban atmospheres appear more difficult to reproduce (see e.g. Baertsch-Ritter, 2003; Martilli, 2002; Sillman, 1995; Wert, 2003). This points to emission inventories of CH_2O and its precursors as the main source of error (Dodge, 1990; Solberg, 2000; Wert, 2003). In this context, CH_2O inventories should be verified against ambient air measurements. This requires splitting of the observed CH_2O concentrations into their primary and secondary components. In practice, this is performed by assuming proportionality with concurrent measurements of primary (e.g. CO, NOx, NOy, toluene) and secondary (e.g. ozone, PAN) pollutants (Anderson, 1996; Friedfeld, 2002; Possanzini, 2002; Slemr, 1996). Emission ratios are then obtained by linear regression or using principal component analysis (Li, 1994). In this paper we discuss the implications of the proportionality assumption as derived from the mass conservation equation.

Besides its central role in photochemical pollution, CH_2O is a toxic and an anticipated human carcinogen. Recommended workplace exposure limits are set as low as 16 ppb (8-h time weighted average - NIOSH, 2002). Being a public health issue, photochemical pollution abatement strategies should incorporate an assessment of changes in ambient air concentrations of formaldehyde due to reductions of VOC and/or NO_X emissions. Some investigations have explored the impact of the composition of the VOC mixture (see e.g. Dodge, 1990) but very little has been so far reported concerning the impact of NO_X emissions on the CH_2O production regime (see e.g. Solberg, 2000).

Our investigation concerns the Grenoble air basin (~470 thousand inhabitants), a complex topography region defined by the Y-shaped intersection of three narrow Alpine valleys surrounded by steep mountains of up to 2200 m above the sea level - ASL (see **Figure 1**). In recent years, this region has experienced strong photochemical pollution episodes with ozone peaks of up to 160 ppb. Due to its relative topographical isolation, air circulation in the Grenoble region is controlled mainly by local effects (Couach, 2002; Couach, 2003). Devising cost-effective O_3 abatement strategies for the Grenoble region requires thus a model capable of reproducing the complex airflow patterns along with the photo-oxidation process itself. CH_2O measurements reported and analyzed in this paper were carried out within the Grenoble photochemistry study (GRENOPHOT) 1999. This field study, conducted from mid-July to mid-August 1999, was devised to elucidate the dynamics of the photochemical pollution, and to build up a robust measurement database for model validation purposes (Couach, 2002; Couach, 2003).

In this paper we use DOAS measurements and photochemical grid model calculations to address the following questions: (1) What determines the diurnal variation of CH_2O in sunny and cloudy conditions? (2) What do they actually mean and what are the validity limits of the CH_2O emission and photochemical production ratios derived from ambient air measurements? (3) Are inventoried emissions in agreement with measurement-derived CH_2O emission ratios in Grenoble? (4) What are the sources of CH_2O at the measurement site and over the Grenoble region? (5) How sensitive is CH_2O in Grenoble to changes in emissions of VOC and NOx? (6) What would be the impact of various O_3 abatement strategies on the concentration of CH_2O in the Grenoble region?

2. Experimental

GRENOPHOT 1999 involved ground-level measurements at 11 sites, O_3 and wind profiling at two sites, and aircraft measurements during the two Intensive Observation Periods (IOP – July 24-27 and August 1-3, 1999). Measurements discussed in this paper were carried out at Vif (310 m ASL), a suburban location at 20 km south of Grenoble downtown (see **Figure 1**). Vif is located midway between the urban area of Grenoble and the maximum development of the O_3 plume (St. Barthélémy), as found in a preliminary field study (summer 1998). The campaign site was instrumented with an O_3 DIAL (differential absorption LIDAR) developed at EPFL validated through numerous field campaigns (Simeonov, 2002; Simeonov, 1999), a microwave wind profiler, a differential optical absorption spectroscopy (DOAS) system, O_3 and NO_X point monitors (Monitor Labs 8810 and 8841, respectively), and standard meteorological instruments.

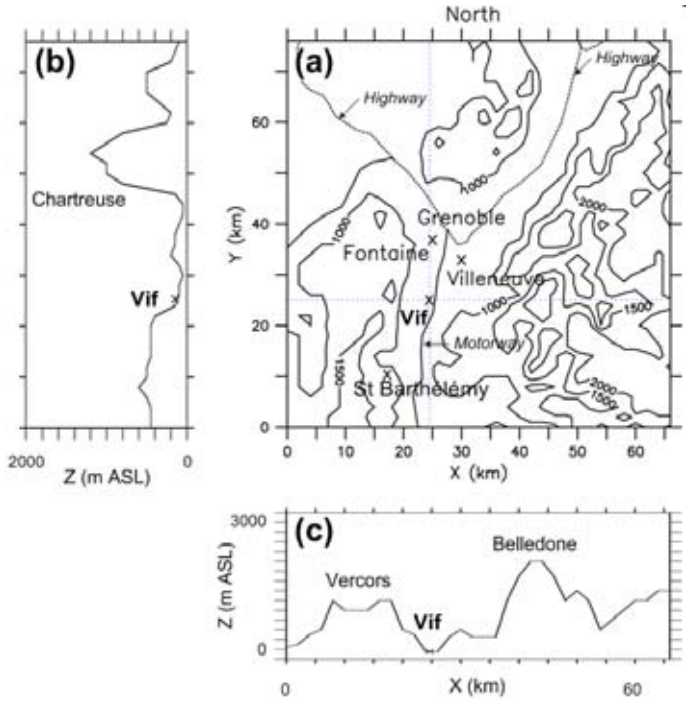

Figure 1. Grenoble region topography (nested simulation domain). **(a)** Contour map, **(b)** axial (North-South) and **(c)** transverse cross sections at Vif. The contour map shows relevant monitoring sites and highways (dashed lines).

The monostatic DOAS system deployed at Vif (Thermo Electron Air Quality, DOAS 2000) utilizes a f/3, ϕ 20 cm coaxial (emitter/receiver) Cassegrain telescope that collimates and directs through the atmosphere light from a 150 W high-pressure Xe lamp. The atmospheric path is folded using a 7-corner cube retroreflector (ϕ 16 cm). Back to the telescope, the beam is focused onto a 19-optical-fiber bundle (ϕ 0.62 mm) connected to a f/4 (20 cm) Czerny-Turner spectrometer (600 mm^{-1} ruled grating blazed at 300 nm). The diffracted beam is linearly scanned at ~30 Hz by a miniature electromechanically-swept slit, and detected by a

side-on photomultiplier tube. The scanner position is quasi-real-time mapped with a diode laser/photocell system perpendicular to the detection plane. A low-pressure Hg lamp is used for periodic, automatic wavelength check and recalibration. Further details are given elsewhere (Jiménez, 2003).

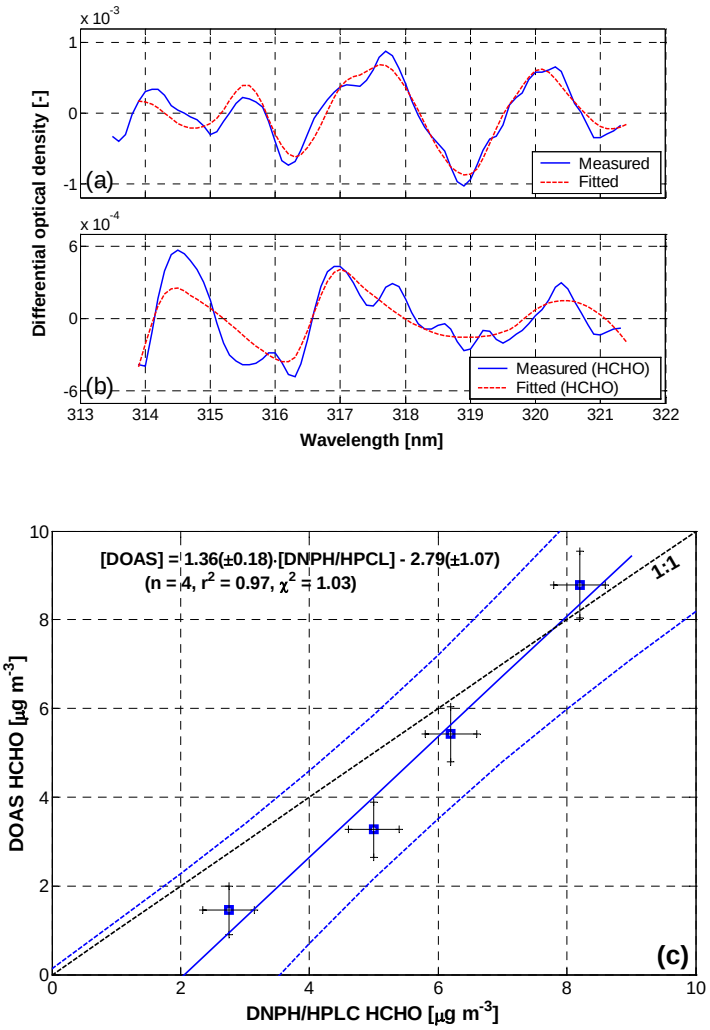

Figure 2. Formaldehyde measurement techniques at Vif. **(a)** Measured (27 July 1999 18:25 CET) and fitted differential absorption spectrum, and **(b)** calculated spectral contribution of CH_2O (8.8±0.8 μ m^{-3}). **(c)** Comparison between co-located, time-equivalent measurements of CH_2O by DOAS and DNPH/HPLC at Vif (July 26-27, 1999). Error bars are 1-sigma. The dashed boundary lines encompass the 85% confidence interval of the linear regression.

The DOAS sensing beam at Vif (2×484 m pathlength, ~3.5 m at above the ground level - AGL) crossed above a low traffic suburb motorway and a maize field. CH_2O, O_3, NO_2, and SO_2 concentrations were retrieved from 32-nm wide atmospheric spectra recorded at 5 sequential grating positions within 246-446 nm. The multicompound non-linear fitting algorithm used (Jiménez, 2003) involves convolution to the resolution of the spectrometer (~0.54 nm FWHM) of the absorption cross sections utilized. An example of spectral retrieval is shown in **Figure 2a-b**. The spectral intervals were chosen to optimize the differential

absorption signal-to-noise ratio (SNR) (Jiménez, 2003). Each spectrum was integrated over 2-3 min. Spectra centered at 315 nm were further co-added for the retrieval of CH_2O and SO_2. The co-addition of 3 subsequent spectra improves the CH_2O lower detection limit (LDL) by a $\sim\sqrt{3}$ factor, whereas maintains the temporal resolution at a reasonable level (~49 min) for the purposes of this study. At these conditions (968 m pathlength, 6-9 min integration time), the operational LDL (1-sigma) of CH_2O and SO_2 are ~1.1 ppb and ~0.2 ppb, respectively. The operational LDL of O_3 and NO_2 (~16 min time resolution) are ~1.5 ppb and ~0.4 ppb, respectively (see **Figure 3**).

Formaldehyde was measured as well with 2,4-dinitrophenylhydrazine (2,4-DNPH)-coated cartridges (Waters, Sep-Pak DNPH-Silica) for quality assurance purposes. Four *in situ* derivatization cartridges were sampled (6 h at 1 L min^{-1}) within the period July 25-26, 1999. One cartridge was left unused for blank analysis. A homemade KI O_3 scrubber (removal efficiency > 99%) was interposed before the cartridges to prevent from O_3 interference (Arnts, 1989). The cartridges were analyzed by HPLC at EMD (*École des Mines de Douaix*, France) following the European (EMEP) standard method (NILU, 2001; Solberg, 2000). Based on parallel sampling analysis, the DNPH/HPLC overall uncertainty is estimated as better than ±0.4 μg m^{-3} CH_2O (1-sigma). In order to achieve time resolution similarity, intercomparison DOAS concentrations were derived upon co-addition of the spectra recorded within each DNPH sampling periods. Direct averaging of the time series concentrations produces essentially identical results, which indicates fulfillment of the differential Beer-Lambert-Bouger (BLB) law (Platt, 1993).

The correlation coefficient (r^2 = 97%) and F-value ($F = 55.8 > F_{crit,95\%} = 18.5$) indicate a non-aleatory, high degree of comparability between the two techniques (see **Figure 2c)**. Former intercomparisons in urban and suburban atmospheres between DOAS and DNPH/HPLC (Jiménez, 2000; Lawson, 1990; Possanzini, 1999) report correlation coefficients within 10-68% (with shorter DNPH sampled volumes ~60-210 L), and similar levels of comparability between DOAS and other spectroscopic techniques (Lawson, 1990; Wert, 2003). The random error, i.e. the deviation from the correlation curve (< 0.5 μg m^{-3}), can be attributed to differences on spatial resolution and sampling time (DOAS:DNPH ~ 1:5). On the contrary, the significant deviation from the 1:1 line points to systematic errors. Possible sources of discrepancy are the uncertainty (±5%) of the CH_2O differential cross section (Meller, 2000), and non-representativeness of the blank cartridge associated with the elevated correlation curve offset (–2.8±1.1 μg m^{-3}). The limited number of DNPH samples impedes yet further analysis. Nevertheless, it is worth to note that the discrepancy to the 1:1 line decreases as the concentration increases. This may reflect better agreement at higher SNR and/or at conditions of intensive atmospheric mixing. The 1:1 line fits nevertheless into the 85% confidence interval of the correlation. The intercomparison results provide confidence on the CH_2O DOAS measurements.

Path-integrated (DOAS) and point (Monitor Labs 8810) measurements of O_3 are in very good agreement (r^2 = 96%, slope = 0.97±0.004, offset = 2.6±0.2 ppb), as expected for a secondary pollutant of relatively long lifetime. On the contrary, NO_2 measurements with the chemiluminiscence detector (CLD - Monitor Labs 8841) appear to be affected by local sources and/or instrumental artifacts (such as unselective catalytic reduction, i.e. NOz → NO), resulting in a correlation of lower quality (r^2 = 66%, slope = 0.92±0.01, offset =-0.3±0.1 ppb). Being less affected by local sources, the DOAS measurements represent better the average concentration in the area and matching closely the spatial resolution of the

photochemical grid model. By the exception of NO (measured by CLD), calculations presented hereafter are based on DOAS measurements only.

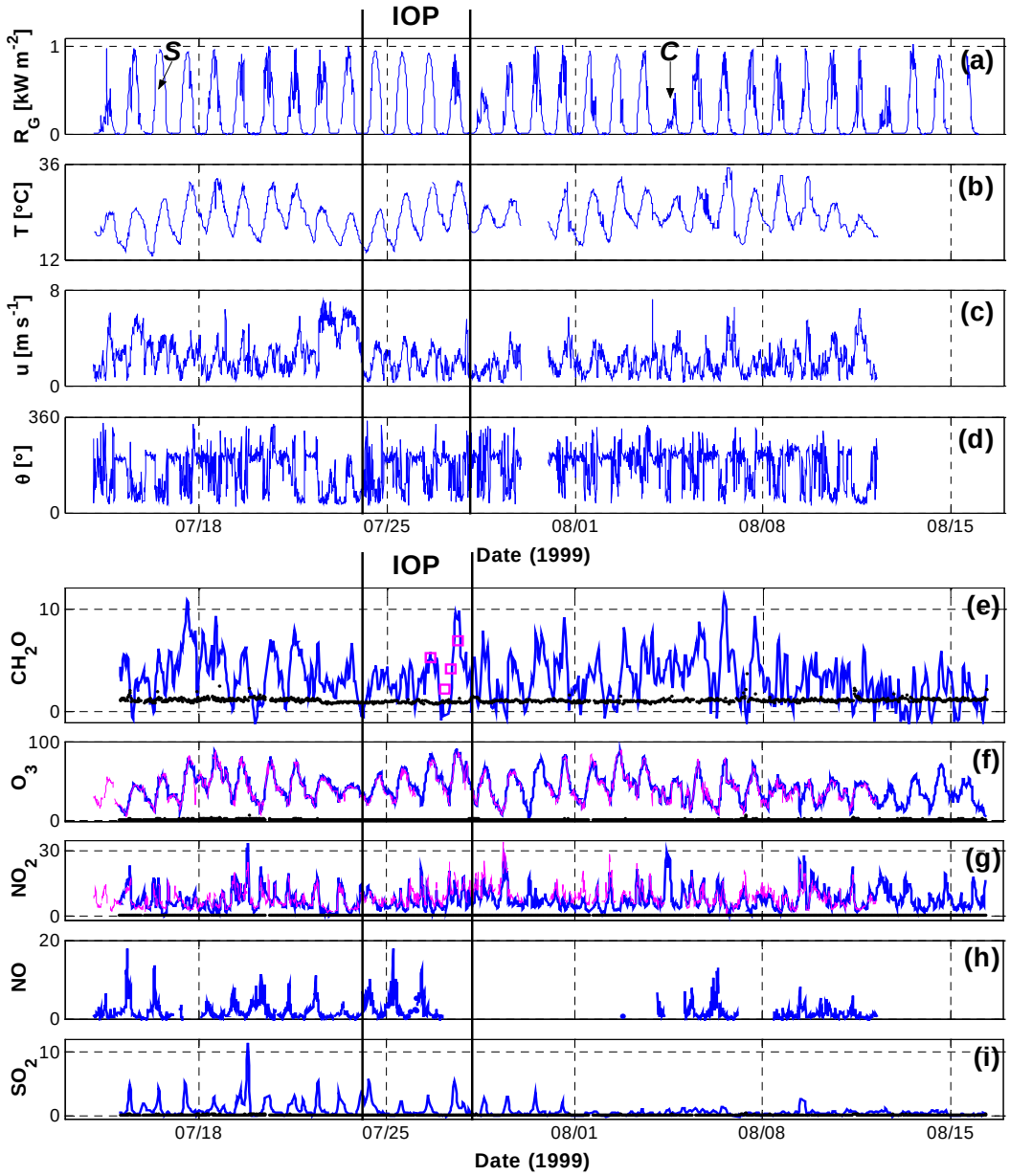

Figure 3. (a-d) Meteorological and **(e-i)** pollutant mixing ratio time series. All parameters were monitored at Vif, by the exception of (a) the global radiation, measured at Saint-Barthélémy (see **Figure 1**). Pollutant time series in (e-g) and (i) were measured by DOAS. Operational DOAS lower detection limits (1-sigma) are indicated with light color dotted lines. NO (h) was measured with a CLD monitor. CH_2O measurements by DNPH/HPLC in (e) are represented by squares. Simultaneous point measurements of O_3 and NO_2 are shown as light color dashed lines in panels (f) and (g), respectively.

3. Observations and average diurnal profiles

Meterorological time series are shown in **Figure 3a-d**. Sunny conditions prevailed during most of the observation period at Grenoble (July 14 – August 15, 1999), as indicated by the global (direct+diffuse) radiation (R_G) time series. The diurnal accumulated global radiation ($Q = \int_0^{24} R_G dt$), with a ~1:5 variation between the cloudiest (***C***) and sunniest (***S***) days (6.4 and 31.0 MJ m^{-2}, respectively), evidences normal decrease of the summer season (see **Figure 3a**).

Air circulation within the Y-shaped Grenoble region is controlled by valley-mountain winds and other local effects (e.g. channeling) to a large extent (Couach, 2002; Couach, 2003). The topography of the region shapes the wind circulation pattern, causing that e.g. winds within 330-30º are not observed at ground level (10 m AGL) at the monitoring site. Air circulation during the observation period displays a quasi-diurnal pattern with predominant wind directions (and peak wind speeds) of ~90º (~3 m s^{-1}) and ~200º (~1 m s^{-1}) at daytime and nighttime, respectively (see **Figure 3c-d**). Wind profiler measurements at Vif show that southward winds are predominant at daytime up to ~1200 m ASL. Monitoring stations upwind Vif towards Grenoble downtown report also southward winds at daytime. This demonstrates that the apparently westward winds at Vif are indeed locally channeled southward winds. Disruptions of the valley-mountain regime by strong synoptic winds are as well observed, as e.g. on July 22-23. The peak wind speed (~3 m s^{-1}) implies a transit time of ~2 h from Grenoble downtown to the measurement site. This transit time slightly shorter than the typical CH_2O lifetime, which suggests that a small fraction of CH_2O emitted in Grenoble downtown can still be observed at the Vif receptor.

CH_2O concentration levels at Vif are normally distributed with a median value of 3 ppb, and display a photochemical pollutant-like behavior with peak concentrations of up to 11 ppb. Ferrari et al. (1998) measured slightly higher CH_2O concentrations (2-18 ppb) at Grenoble downtown on late spring 1995. During the periods of lower solar radiation, particularly at the end of the campaign (from 8th August on), CH_2O displays a less clear diurnal variation, with concentrations close to LDL. Such a pattern is very likely the result of a reduced net photochemical production at the significantly lower radiation levels of this period. The relative strength of photochemically produced (secondary) over directly emitted formaldehyde (primary) is thus expected to be lower during this period compared to the sunnier periods.

Analysis of the scatter plots show that formaldehyde concentration is quite strongly correlated with ozone and odd oxygen, $[O_X] = [O_3] + [NO2]$. This indicates that photochemical sources determine CH_2O at Vif. Some correlation is observed as well for CH_2O with NOx and SO_2, particularly at daytime, but no correlation is observed between NOx and SO_2. Peak concentrations of SO_2 (of up to 11 ppb) are consistently observed at around midday. This points whether to heavy-duty (diesel-fueled) vehicles (HDV) or to industrial processes as sources of SO_2. In order to better understand the average behavior of CH_2O, we calculated average diurnal profiles that represent sunny and cloudy conditions. Instead of arbitrarily defining a boundary between sunniness and cloudiness, we applied (re-normalized) weighting coefficients to the diurnal profiles over the whole observation period, i.e.,

$$\bar{c}(t) = \frac{\sum_i w_i c_i(t)}{\sum_i w_i} \quad (1)$$

where $\bar{c}(t)$ is the diurnal average concentration profile, $c_i(t)$ is the concentration profile of the *i*-th day, and w_i is the radiation-dependent weighting coefficient for the *i*-th day. The accumulated global radiation values (Q) during the observation period are well described by a Gaussian (***G***) distribution with standard deviation σ_Q = 5.6 MJ m^{-2}. The diurnal weighting coefficients were calculated accordingly,

$$w_i = \boldsymbol{G}(Q_i, Q_{ref}, \sigma_Q) \quad (2)$$

where Q_i is the accumulated radiation on the *i*-th day, and Q_{ref} are the center values of accumulated global radiation associated to each weather conditions, i.e. max(Q) and min(Q) for *sunny* and *cloudy* conditions, respectively. Calculated diurnal profiles weighting coefficients (w_i) range within 0.08-12%. The average profiles were calculated taking into account missing values. The resulting profiles are shown in **Figure 4**.

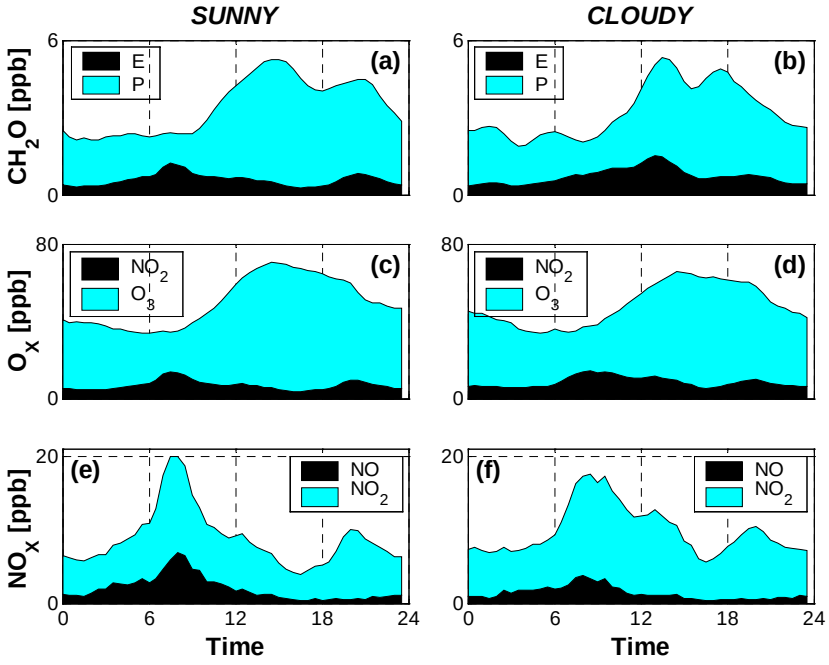

Figure 4. Weighted average diurnal profiles of **(a-b)** CH_2O, **(c-d)** Ox, and **(e-f)** NO_X at Vif for *sunny* (left) and *cloudy* (right) conditions. Panels (a-b) shows as well the distribution and evolution of primary (E) and secondary (P) CH_2O as estimated by multiple linear regression with NOx and O_3.

The NOx average profiles show emission peaks associated to road traffic at 8:00, 13:00 and 20:00 CET (Central European summer Time, CET ≅ SLT +2 – SLT: Sidereal Local Time). At midday NO_2/NO ratios are ~4 and ~9 for *sunny* and *cloudy* conditions, respectively. Assuming PSS and taking into account the ozone levels, this allows estimating that NO_2 photolysis rate on sunny conditions is as high as twice that of *cloudy* conditions. Ozone peaks at ~15:00 CET with average concentrations of 66 ppb and 58 ppb at *sunny* and *cloudy* conditions, respectively, indicating (as expected), a more intense photochemical activity in the first one. At *sunny* conditions, CH_2O peaks at about the same hour that ozone (~15:00 CET) and displays a secondary peak at ~21:00 CET. The time lag between the early afternoon peaks of CH_2O and O_3 calculated for the whole time series (66±60 min) is statistically not significantly different from zero. Friedfeld (2002) reports a similar result for the Houston area. On cloudy conditions, the two peaks appear earlier, at 13:30 and 17:30 CET, respectively. Strong correlation with O_3 on the sunlit hours indicates that the first peak is of photochemical origin in both sunlit conditions. The average concentrations of CH_2O in *sunny* and *cloudy* conditions (~3.3 ppb) are not significantly different, although the peaks have different duration and shape.

Interestingly, camel-shaped CH_2O profiles with concentration peaks spaced by some 4 h are observed in places as disparate as the Venezuelan Savanna (Trapp and de Serves, 1995), rural Germany (Slemr et al., 1996), central Japan (Satsumabayashi, 1995), suburban Milan (Baertsch-Ritter, 2003), and Rome (Possanzini et al., 2002). The nighttime peak is probably due to temporary diminution of the CH_2O sinks (photolysis and OH oxidation) compared to the sources still active at this time of the day (e.g. ozonolysis), along with the collapse of the mixing layer.

4. Source estimation and emission ratios

Formaldehyde observed at the measurement site (considered as a receptor) originates from emissions (E) and atmospheric photochemical reactions (P). Both components reflect local processes and advected air masses. It appears reasonable to add a constant background term (0) since the concentration would be expectedly non-zero even in the hypothetical absence of these two sources,

$$\left[CH_2O\right] = \left[CH_2O\right]_P + \left[CH_2O\right]_E + \left[CH_2O\right]_0 \qquad (3)$$

The primary CH_2O component (E) was assumed to be proportional to the concentrations of NOx and SO_2,

$$\left[CH_2O\right]_E \approx e_1\left[NO_X\right] + e_2\left[SO_2\right] \qquad (4)$$

As explained in the previous section, there is strong evidence showing that NOx and SO_2 come from different sources. It makes thus sense to use a linear combination of these compounds as surrogate of primary formaldehyde. The first term is associated to road traffic while the second reflect industrial emissions and heavy-duty traffic.

The secondary component (P) of CH_2O was assumed to be proportional to the concentration of O_3,

$$\left[CH_2O\right]_P \approx a\left[O_3\right] \quad (5)$$

Ox would be in principle a better surrogate of secondary CH_2O since it accounts also for titrated O_3. [Ox] is however partially co-linear with [NOx], thus an inappropriate variable in mathematical terms.

The assumptions above suffer from intrinsic limitations (see **Appendix**). The choice of NOx as surrogate of primary CH_2O neglects the transformation of NOx into NOz. The reactive odd nitrogen concentration ([NOy] = [NOx] + [NOz]) would be in principle a better surrogate. In practice, since emitted formaldehyde is rapidly oxidized in the atmosphere, the use of ambient [NOx] instead of [NOy] yield CH_2O/NOx ratios that are closer to the actual emission ratios. Concerning the secondary term, major differences exist between the photochemistry of ozone and formaldehyde. CH_2O is produced along with HO_2 mainly through the decomposition of alkoxy radicals (RO) following reduction of peroxides ($RO_2 + NO \rightarrow RO + NO_2$), whereas the photolysis of NO_2 is the only significant source of O_3 in polluted atmospheres. The sink reactions for CH_2O (**Reactions A-D**) are in relative terms faster than for O_3 resulting in a comparatively shorter lifetime for the first. Nevertheless, both field and modeling results indicate a strong correlation between secondary CH_2O and O_3, particularly in the morning hours.

The parameters in the model described by Eq. (3-5) were obtained by multiple linear regression. Deriving the ratios of emission and net photochemical production from average profiles enhances the statistical robustness of the retrieved coefficients (fitting coefficients are 91% and 92% for *sunny* and *cloudy* conditions, respectively, compared to a correlation coefficient of 25% using the whole time series).

Derived CH_2O/NOx emission ratios ($e_1 = E_{CH_2O} / E_{NOx}$) for *sunny* and *cloudy* conditions are 0.094±0.02 and 0.040±0.024 mol mol^{-1}. This last value is believed to be closer to the actual ratio since at conditions of lower irradiation (*cloudy*), the photochemical sinks of both primary formaldehyde and NOx are considerably smaller. The ratio in *sunny* conditions appears to be highly biased due to the more rapid conversion of NOx into NOz at conditions of higher radiation. Despite of the large gaps in the nitric oxide time series (48% missing), the measurement-derived CH_2O/NOx emission ratio on *cloudy* conditions is in very good agreement with likewise derived ratios for similar European (Klemp, 2002; Slemr, 1996) and North American locations (Li, 1994), ranging within 0.037-0.05 mol mol^{-1}, and in reasonable agreement with the ratio calculated from inventoried emissions in the Vif area, E_{CH_2O} / E_{NOx} = 0.0324±0.0002 mol mol^{-1} (retrieved from Bouscaren, 1999). See **Figure 5**. Significantly smaller ratios derived from tunnel measurements (John, 1999; Staehelin, 1998) (Kristensson,

2004) indicate that the actual emissions of CH_2O associated to road-traffic are about ~3 times higher that they might be in the stationary driving conditions inside tunnels. Tunnel measurements do not account for cold starts and non-steady driving conditions (Klemp, 2002). The CH_2O/SO_2 emission ratio for *cloudy* conditions (0.77±0.23 mol mol^{-1}) is similar to values derived from ambient air measurements in a Canadian rural site (0.98-2.14 mol mol^{-1}) (Li, 1997), and falls within the range calculated from tunnel measurements (0.4-3.2 mol mol^{-1}) (John, 1999; Staehelin, 1998).

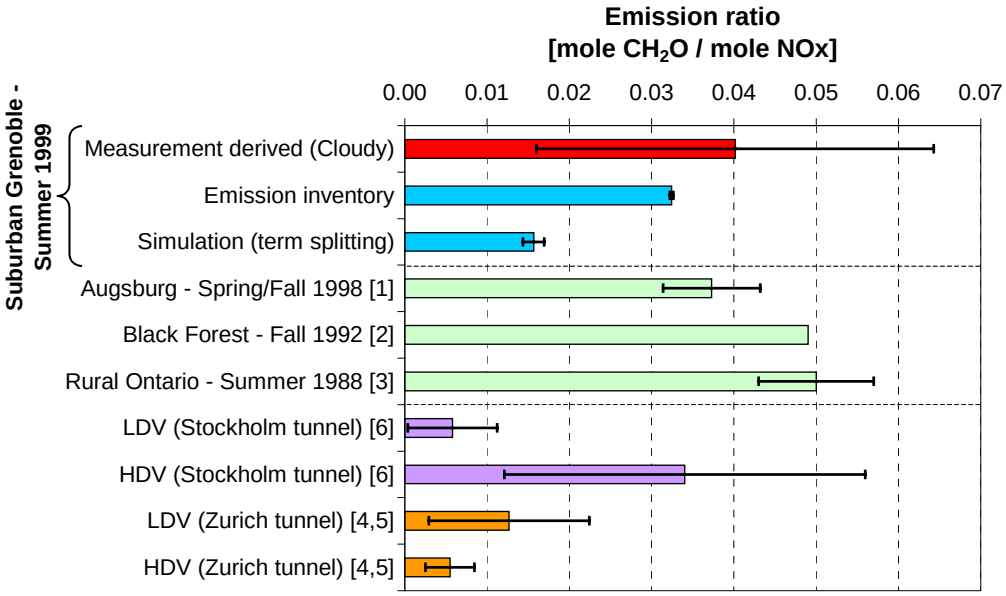

Figure 5. Measured- and simulation-derived CH_2O/NOx emission ratios at suburban Grenoble (Vif) and at various Northern Hemisphere locations. Ratios calculated from tunnel-measurement-derived emission factors are shown for comparison purposes. LDV and HDV, low- and heavy-duty vehicles. References: [1] Klemp et al., 2002; [2] Slemr et al., 1996; [3] Li et al., 1994; [4] Staehelin et al., 1998; [5] John et al., 1999; [6] Kristensson et al., 2004.

The CH_2O/O_3 net photochemical production ratios ($a = R_{CH_2O}/R_{O_3}$) retrieved for *sunny* and *cloudy* conditions at Vif are 0.088±0.006 and 0.079±0.007 mol mol^{-1}, respectively. This implies that the net photochemical production rate of O_3 at the measurement site is ~12-fold that of CH_2O. Photochemical ratios ranging within 0.095-0.15 mol mol^{-1} have been reported for the urban areas of Milan (Jiménez, 2000), Dallas (Wert, 2003), and Houston (Friedfeld, 2002). The CH_2O/O_3 photochemical ratios derived for suburban Grenoble are comparable to the CH_2O/O_3 asymptotic slope (~0.1 mol mol^{-1}) at the "low" O_3 values (< 70 ppb) derived from airborne measurements of the VOC-rich photochemical plume of the in the Houston-Galveston area (Wert, 2003).

The photochemical fraction diurnal profiles were calculated as,

$$f_{phot} = [CH_2O]_p / [CH_2O] \quad (6)$$

The estimated CH_2O photochemical fraction varies within 49-94% and 61-86% on average *sunny* and *cloudy* days, respectively (see **Figure 6b**). As expected, the lowest fractions are observed on the morning rush hours (~8:00 CET). The estimated peak photochemical fraction coincides with the first CH_2O peak. The mass-averaged CH_2O photochemical fraction for the average *sunny* day (83%) is significantly higher than for average *cloudy* day (78%). The fitting of the data to the statistical model described by **Eq. 3-5** indicates primary CH_2O accounts for ~1 ppb of the CH_2O concentration peak observed at ~21:00 CET on the average *sunny* day. The CH_2O peak at ~15:00 CET is on the contrary largely of photochemical origin. Concerning the average *cloudy* day, up to 25% of the peak at ~13:00 CET could be ascribed to emissions.

5. Photochemical grid model calculations

The dynamics of photochemical pollution in the Grenoble region was simulated with METPHOMOD (METeorology and PHOtochemistry MODel) (Perego, 1999), a prognostic, 3-D Cartesian photochemical grid model. The calculation domain is centered over Grenoble (68×78 km - see **Figure 1**), has a horizontal resolution of 2×2 km, and is vertically divided in 26 levels of increasing length (from 50 m at the ground level to 1 km at the top of the domain - 8 km ASL). The meteorological and trace gas boundary conditions were obtained by nesting this domain within a larger one (198×198 km - 6×6 km horizontal resolution) that covers Lyon and Geneva (Couach, 2002).

The simulated IOP (25-27 July 1999) was characterized by anticyclonic conditions dominated by relatively clean northerly synoptic winds from the Atlantic Ocean. Channeling of the synoptic wind along with katabatic (mountain-valley) winds during the sunlit hours resulted in southerly advection of air masses from Grenoble downtown towards the massifs of Oisan (southeast – behind the Belledone massif) and Vercors (southwest - see **Figure 1**). Reversing-flow katabatic winds are observed at nighttime. Temperature and wind fields calculated with METPHOMOD agree reasonably well to ground level and vertically resolved meteorological measurements, and achieve to capture the 3-layer atmospheric structure evidenced from wind profiler measurements (Couach, 2002; Couach, 2003).

The emission inventory of NOx, CO, CH_4, and 23 NMHC (non-methane hydrocarbon) species (Bouscaren, 1999) is resolved at 1 km^2 and 1 h, and gathers point, linear and surface sources within the Grenoble region (biogenic emissions are not considered). VOC (NMHC) emissions are lumped into 19 classes as required by RACM (Regional Atmospheric Chemistry Mechanism - Stockwell, 1997).

Modeled mixing ratios of O_3 and NOx correspond reasonably well to ground level and vertically resolved measurements, particularly at suburban and rural locations (Couach, 2002; Couach, 2003; Couach, 2004). Specifically regarding the monitoring site at Vif, modeled concentrations of O_3 and NO_2 appropriately reproduce the DOAS measurements at daytime but show systematic overestimation at nighttime (~18:00-6:00 CET), resulting in rather high root-mean-square (rms) errors of 13.7 and 7.9 ppb for simulated O_3 and NO_2, respectively (see **Figure 6d-e**). In a similar way, LIDAR-derived mixing heights at daytime are finely reproduced whereas the nighttime values are systematically underestimated (Couach, 2003). This points to underestimation of the turbulent kinetic energy at nighttime as a major source

of error in the modeling. Modeled mixing ratios of nitric oxide agree well with the CLD measurements in absolute terms but show a ~2 h time shift compared to the CLD measurements (see **Figure 6f**), which results in an elevated simulation error (4.8 ppb rms). This suggests that inventory emissions of NOx at Vif, and consequently of CH_2O, are quite accurate in absolute terms but to some extent inaccurate regarding the timing of emissions.

Modeled concentrations of CH_2O reproduce appropriately the field observations (1.0 ppb rms error) within their uncertainty limits (see **Figure 6a**). More importantly, the model captures the CH_2O concentration peaks at morning, afternoon and night, however of a lower intensity and overlying over a higher-than-observed baseline. In addition, the model predicts the photochemical peak at 15:00 CET about one hour earlier than observed. The good correspondence to observations indicates that the model captures appropriately the meteorology and basic photochemistry in the region.

In order to investigate the origin of formaldehyde in the Grenoble region, and for purposes of comparison with the measurement-derived estimations, emitted (E) and boundary-advected (B) formaldehyde were included as pseudo-species in the chemical mechanism (RACM). This differentiated labeling of CH_2O in RACM and the emission inventory allows distinguishing among primary (E), secondary (P), and boundary-advected (B) formaldehyde in the simulation domain,

$$\left[CH_2O\right] = \left[CH_2O\right]_P + \left[CH_2O\right]_E + \left[CH_2O\right]_B \qquad (7)$$

CH_2O sink reactions (**reactions A-D**) were copycatted for each pseudo-species added (P and B) in order to make them accountable for the CH_2O oxidation products. In simple terms, the modified mechanism ascribes formaldehyde resulting from emissions to $[CH_2O]_E$ (as per inclusion of this species in the emission inventory), and the initial concentration over the domain to $[CH2O]_B$. Having added these two terms, the formaldehyde variable as originally labeled in the mechanism (before inclusion of the two pseudo-species above) accounts only for photochemically produced formaldehyde, i.e. $[CH2O]_P$.

The time evolution of the boundary-advected CH_2O component indicates that the first ~18 h of simulation correspond to a transient period. Accordingly, only calculations from 25 July 1999 19:00 CET on were analyzed.

Maximum predicted concentrations of emitted and boundary-advected CH_2O are 0.6 ppb both. Simulated non-secondary (emitted + boundary-advected) CH_2O reaches 0.9 ppb at the maximum, somewhat smaller than estimated from measurements (up to 1.2 ppb on the average *sunny* day). The model results indicate that emissions and boundary advection have only a minor impact on CH_2O at Vif, except during the sunrise hours (see **Figure 6c**). During this period of time the modeled photochemical fraction (calculated according to Eq. (6)) reaches its lowest value (77%). Model-calculated CH_2O photochemical fractions (77-97%) agree fairly well with the measured-derived fractions for the average *sunny* day (49-94%) and for the simulated period (36-98% - calculated using the fitting parameters of the average *sunny* day). The largest disagreement between the two approaches is indeed observed at the sunrise hours (see **Figure 6b**). The fact that inventory emissions are time-shifted, as evidenced from NO calculations, suggests that modeled photochemical fractions are underestimated during this period of the day. Mass-averaged photochemical fractions over the

simulation period derived from field measurements and from the model calculations are 83% and 86%, respectively. This good agreement enables the extrapolation of the CH_2O component splitting analysis beyond the measurement site.

Figure 7 shows near-ground level mixing ratios of total and secondary CH_2O over the Grenoble region on 26 July 1999. A CH_2O plume with a maximum concentration of 8 ppb is observed in the morning (9:00 CET) over Grenoble downtown (**Figure 7a**). Comparison with the secondary CH_2O at that time (**Figure 7c**) shows that ~60% of CH_2O in this plume (5 ppb at the peak) is primary. Formaldehyde concentrations at Grenoble downtown reach 11 ppb at the beginning of the afternoon. Modeled CH_2O over Grenoble downtown agree well with the values reported by Ferrari et al (1998). Moreover, the model predicts CH_2O-CO correlation coefficients of 80% and 92% at Fontaine and Villenueve (see **Figure 1a**) respectively, indicating that road traffic emissions are main source of CH_2O at these urban locations.

Another formaldehyde plume with a peak concentration 6 ppb at 9:00 CET is observed at the northeast of Grenoble. This plume is mostly secondary, and results from a combination of emissions of CH_2O (~2 ppb) and fast-producing CH_2O precursors from a polymer and polymer precursors manufacturing facility at this location, and poor ventilation conditions at this time of the day.

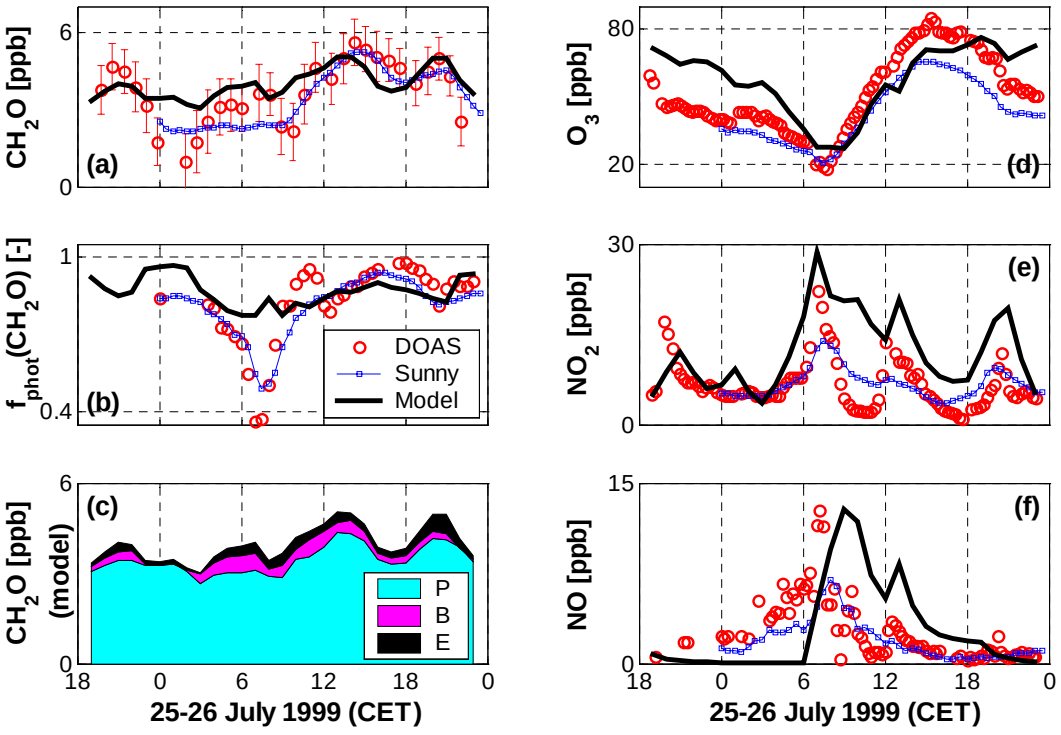

Figure 6. Measured and simulated mixing ratios of **(a)** CH_2O, **(d)** O_3, **(e)** NO_2, and **(f)** NO at Vif. Panel **(b)** shows the photochemical fraction of CH_2O calculated with the grid model or using measurement-derived ratios. Panel **(c)** shows the sources and evolution of CH_2O as calculated with the grid model. Measurements performed during the IOP are depicted with circles (○). Weighted average profiles at sunny conditions are shown with squares (□).

Morning Grenoble emissions are pushed southward and northeastwardly producing secondary formaldehyde. At 9:00 CET the southward plume with a peak CH_2O concentration of 6 ppb is midway between Grenoble downtown and Vif. The production of CH_2O from VOC emissions of Grenoble is favored by low speed and converging winds leading to long residence times in the area. About 80% of CH_2O in the plume is secondary. The plume peak reach Vif at 14:00 CET. At this time ~90% of CH_2O in the plume is secondary. On the northeast valley of Grenoble convergence winds limit the progress of the photochemical plume. As a consequence two plumes are observed. Formation of secondary CH_2O is observed also along the main highways.

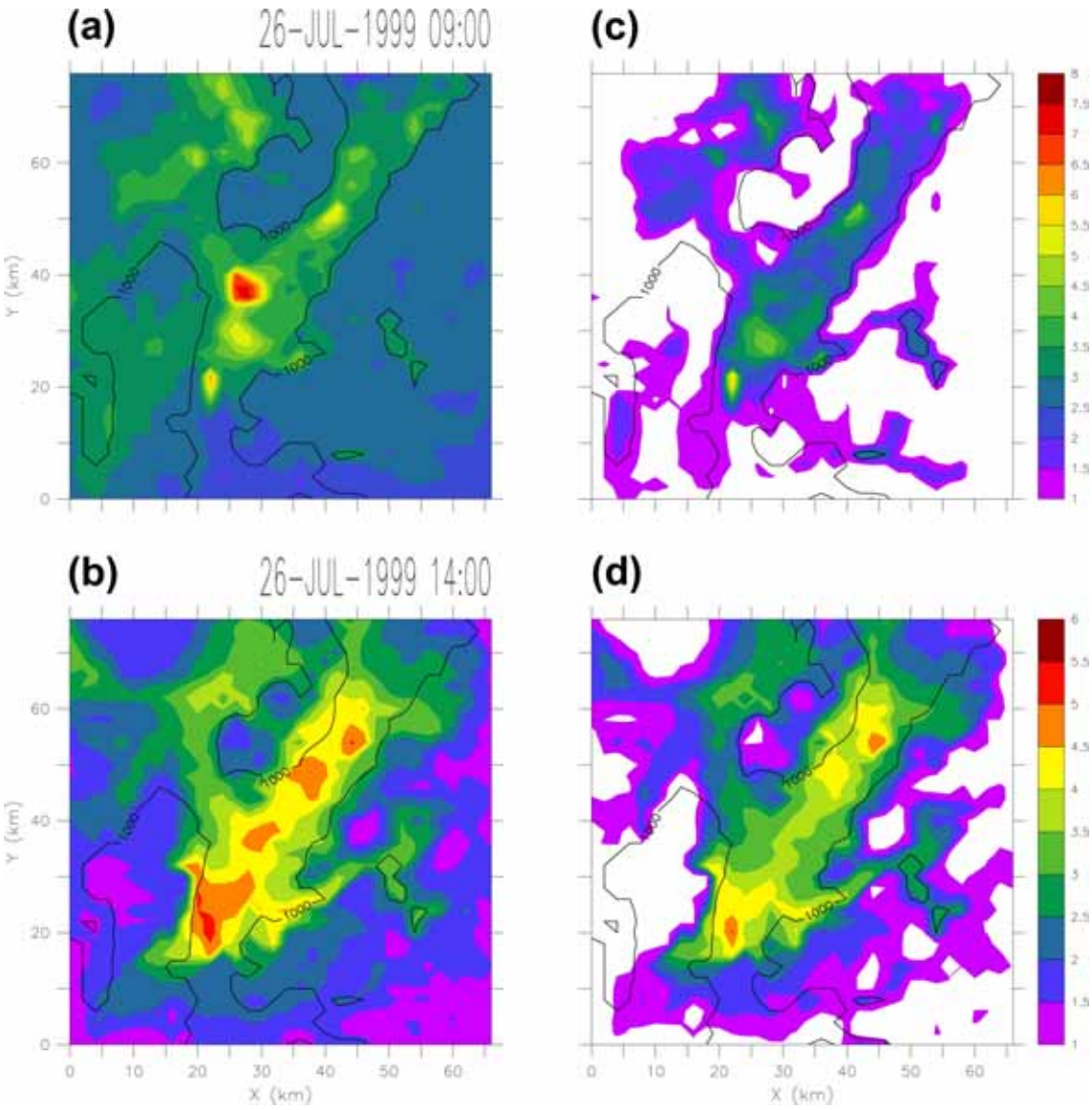

Figure 7. Simulated CH_2O mixing ratio at near-ground level on 26th July 1999. Left **(a-b)** and right **(c-d)** panels show total and secondary formaldehyde mixing ratios, respectively. Note that surface mixing ratios at 09:00 (a,c) and at 14:00 CET (b,d) have different tone scales.

Finally the model predicts the formation of a narrow secondary formaldehyde plume nearby Vif. This plume appears to stagnate due to convergent winds, and may be partially responsible for the elevated formaldehyde baseline levels at Vif.

6. Photochemical production regime

The main daytime source of formaldehyde and other carbonyls (R′CHO) at Vif is the photo-oxidation of VOCs in the presence of nitric oxide (via formation of peroxy radicals - RO_2) (Finlayson-Pitts, 2000; Seinfeld, 1998),

$$RO_2 + NO \rightarrow RO + NO_2 \left(+O_2\right) \rightarrow R'CHO + HO_2 + NO_2 \qquad (E)$$

This reaction implies positive dependence of the secondary CH_2O production rate with the VOC emission (provided CH_2O-forming compounds are present in the emission mix). Due to the feedback effect that CH_2O sinks exert on the OH concentration, as discussed in **Sect. 1**, CH_2O levels depends positively, but not necessarily in a linear way, on the VOC emissions, and weakly but non-linearly on the NOx emissions. Very little has been reported on this last aspect (see e.g. Dodge, 1990; Solberg, 2000).

We investigated the CH_2O photochemical production regime in the Grenoble region by calculating the CH_2O concentration at various hypothetical emission levels. **Figure 8** shows the isopleths of CH_2O, O_3, and OH at Vif as a function of the overall emissions of VOC and NOx in the Grenoble region (values are referred to the current emission levels). The isopleths are shown for 14:00 and 18:00 CET on 26th July 1999 (**Figure 8a-b** and **c-d**, respectively). The model predicts maximum concentrations of CH_2O and O_3 at Vif at these times, respectively (refer to **Figure 6**). The OH maximum concentration isopleths (0.45 and 0.22 ppt at 14:00 and 18:00 CET, respectively) clearly define the ozone production regime boundaries (see **Figure 8b** and **d**). The daytime production of O_3 at Vif is VOC-limited / NOx-saturated at the current emission levels (Couach, 2004). This condition prevails down to NOx emissions of 25% and 50% (referred to the current levels) at 14:00 and 18:00 CET, respectively. At lower emissions levels, O_3 is NOx-limited and insensitive to changes in VOC emissions.

The formaldehyde production regime at 14:00 CET is similar to that of ozone, nonetheless with a less pronounced NOx saturation. The transition between regimes occurs as well at the OH maximum, i.e. at 50% NOx emissions. The NOx saturation fades out during the afternoon hours resulting in a VOC- and NOx-limited regime at 18:00 CET.

The NOx saturation of the photochemical production of CH_2O is explained by removal of increasing amounts of OH radicals as the NOx concentration increases due to the production of nitric acid,

$$NO_2 + OH \rightarrow HNO_3 \qquad (F)$$

The HNO_3 sink reaction competes for OH with the peroxide formation reactions even at moderate levels of NOx. Thus, at constant total VOC levels, the NOx saturation effect is expected to be more pronounced for a VOC mix of low-reactivity (e.g. composed mainly of alkanes) than e.g. for alkene-rich mixtures.

Based on box model simulations, Dodge (1990) concludes that the dependence of the CH_2O production in the VOC emissions is nearly linear. Our calculations show a decrease of 38% of the peak CH_2O levels (14:00 CET) at Vif upon a 50% reduction of the VOC emissions at the current NOx levels. This percentage of reduction is calculated referred to the background concentration, i.e. the CH_2O concentration at zero emissions (~2 ppb). A 50% reduction would be observed if CH_2O were strictly linear with VOC. This quite good degree of approximation is a particularly interesting when considering the number of variables incorporated in the photochemical grid model (topography, meteorology, emissions) compared to the box model.

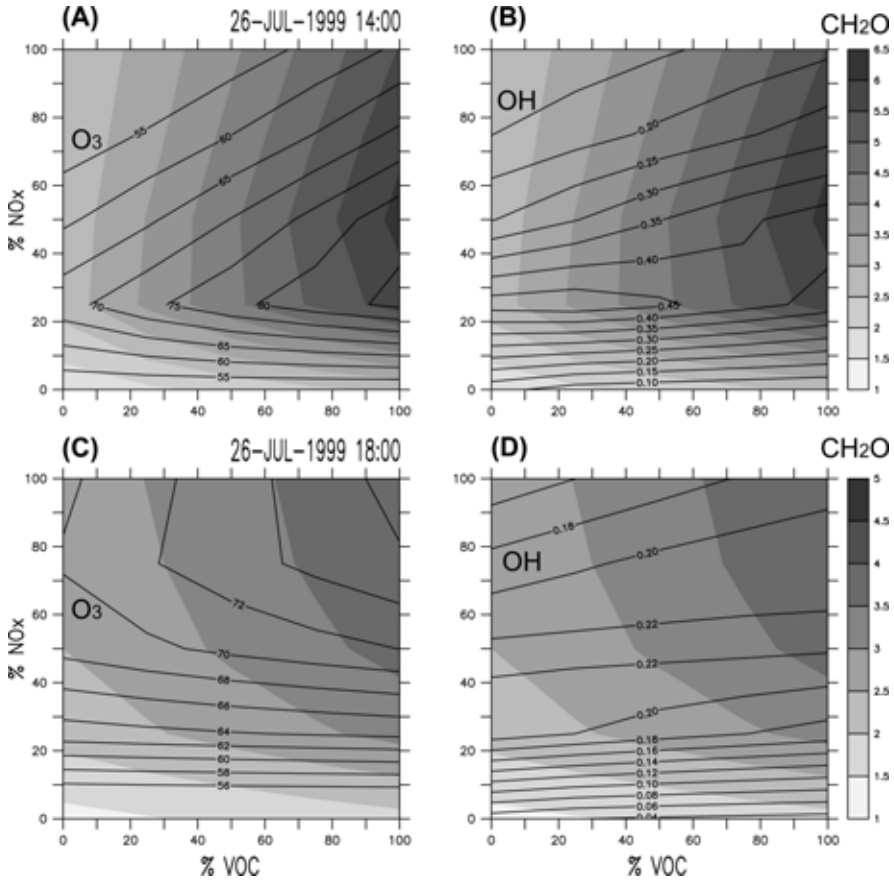

Figure 8. Isopleths of CH_2O, O_3, and OH at Vif on 26th July 1999. Emission control isopleths are shown for **(a-b)** 14:00 and **(c-d)** 18:00 CET, times at which the model predicts the current maximum mixing ratios of CH_2O and O_3, respectively. Controls on the current (100% level) emissions levels of VOC (abscissa) and NO_X (ordinate) are applied evenly over the nested domain for calculation purposes. Formaldehyde mixing ratios are displayed in grayscale. Mixing ratios of O_3 (left - in ppb) and OH (right - in ppt) are represented with contour lines.

A detailed analysis of the ozone formation regime in the Grenoble region (Couach, 2004) shows that the area of maximum ozone in the region is NOx limited. This analysis evidenced also that some areas, particularly Grenoble downtown, are NOx saturated. NOx and VOC must be simultaneously controlled in these areas in order to achieve O_3 reduction. Ozone production at Vif is weakly NOx saturated at the time of the O_3 maximum. The isopleths (**Figure 8a** and **c**) indicate that a combined reduction of VOC and NOx at this particular location would be more effective in reducing formaldehyde than ozone. Controlling NOx emissions only would lead to increasing the both CH_2O and O_3 at time of peak CH_2O (14:00 CET).

7. Conclusions

Quality-controlled DOAS measurements were used to investigate the temporal evolution and sources of formaldehyde in the photochemical plume of Grenoble. Photochemistry accounts for about 80% of CH_2O in the south of the Grenoble air basin. CH_2O emissions in this area are represented by a CH_2O/NOx emission ratio of about 0.04 mol mol^{-1}. A good level of confidence is given to this ratio as per good agreement between measurement-derived and emission inventory data. A photochemical grid model (METPHOMOD), previously validated on the basis of O_3 and NOx measurements, was used to describe the dynamics of formaldehyde over the Grenoble region. The model appropriately reproduces the CH_2O concentration at the measurement site. The introduction of a differentiated labeling for emitted, photochemically produced, and boundary-advected formaldehyde in the chemical mechanism (RACM) revealed a complex dynamics of formaldehyde in the Grenoble air basin. Primary CH_2O plumes of urban and industrial origin dominate the early morning hours. In the sunlit hours, secondary formaldehyde is produced and advected southwardly. More than 75% of formaldehyde over the region is of photochemical origin. In agreement with reported investigations (Dodge, 1990; Solberg, 2000), the photochemical production of CH_2O was found to be nearly proportional to the emissions of VOC. The CH_2O production regime is weakly NOx saturated at the CH_2O peak time. Our calculations indicate that O_3 abatement strategies based in Eulerian and Lagrangian indicators are compatible with the reduction of CH_2O in the Grenoble area. In the south of the Grenoble air basin, the control of NOx emissions must be with accompanied with a VOC reduction to achieve diminution of O_3 and CH_2O. Such a strategy would be more effective in reducing formaldehyde than ozone. The validation and analysis of formaldehyde calculations with grid models provides a valuable insight on the photochemistry at the regional scale, and allows highlighting VOC emissions not always easy to recognize from NOx and O_3 measurements and calculations only.

Acknowledgements

GRENOPHOT was funded by the *Association pour le Contrôle et la Préservation de l'Air dans la Région Grenobloise* (ASCOPARG). We thank the ASCOPARG staff, particularly M.B. Perssonaz, for their interest and committed logistic support. The DNPH samples were analyzed by N. Locoge and T. Léonardis at the *École des Mines de Douaix* (EMD), Douaix (France). We are grateful to P. Ristori and A. Clappier for valuable discussions and comments to the manuscript. Financial support from Thermo Electron Air Quality Inc. and ICSC-World Laboratory (Project LAND-14) is acknowledged.

References

Anderson, L.G., J.A. Lanning, R. Barrell, J. Miyagishima, R.H. Jones and P. Wolfe. Sources and sinks of formaldehyde and acetaldehyde: An analysis of Denver's ambient concentration data. *Atmospheric Environment* 30 (12): 2113-2123, 1996

Arnts, R.R. and S.B. Tejada. 2,4-Dinitrophenylhydrazine -coated silica gel cartridge method for determination of formaldehyde in air: Identification of an ozone interference. *Environmental Science & Technology* 23 (11): 1428-1430, 1989

Baertsch-Ritter, N., A.S.H. Prevot, J. Dommen, S. Andreani-Aksoyoglu and J. Keller. Model study with UAM-V in the Milan area (I) during PIPAPO: simulations with changed emissions compared to ground and airborne measurements. *Atmospheric Environment* 37 (29): 4133-4147, 2003

Bouscaren, R., E. Riviere and Y. Heymann. Réalisation d'un inventaire d'émissions simplifie pour la ville de Grenoble - 1 h, 1 km^2 - Convention 98338001 (Simplified emission inventory of Grenoble). CITEPA, Paris, 1999

Carlier, P., H. Hannachi and G. Mouvier. The chemistry of carbonyl compounds in the atmosphere - A review. *Atmospheric Environment* 20 (11): 2079-2099, 1986

Couach, O., I. Balin, R. Jiménez, S. Perego, F. Kirchner, P. Ristori, V. Simeonov, P. Quaglia, V. Vestri, A. Clappier, B. Calpini and H. van den Bergh. Study of a photochemical episode over the Grenoble area using a mesoscale model and intensive measurements. *Pollution Atmosphèrique* (174): 277-295, 2002

Couach, O., I. Balin, R. Jiménez, P. Ristori, S. Perego, F. Kirchner, V. Simeonov, B. Calpini and H. van den Bergh. An investigation of ozone and planetary boundary layer dynamics over the complex topography of Grenoble combining measurements and modeling. *Atmospheric Chemistry and Physics* 3: 549-562, 2003

Couach, O., F. Kirchner, R. Jiménez, I. Balin, S. Perego and H. van den Bergh. A development of ozone abatement strategies for the Grenoble area using modeling and indicators. *Atmospheric Environment* 38: 1425-1436, 2004

Dodge, M.C. Formaldehyde production in photochemical smog as predicted by three state-of-the-science chemical oxydant me chanisms. *Journal of Geophysical Research* (95): 3635-3648, 1990

Ferrari, C.P., P. Kaluzny, A. Roche, V. Jacob and P. Foster. Aromatic hydrocarbons and aldehydes in the atmosphere of Grenoble, France. *Chemosphere* 37 (8): 1587-1601, 1998

Finlayson-Pitts, B.J. and J.N. Pitts. Chemistry of the upper and lower atmosphere. Academic Press, San Diego, 2000

Fried, A., S. McKeen, S. Sewell, J. Harder, B. Henry, P. Goldan, W. Kuster, E. Williams, K. Baumann, R. Shetter and C. Cantrell. Photochemistry of formaldehyde during the 1993 Tropospheric OH Photochemistry Experiment. *Journal of Geophysical Research* 102 (D5): 6283-6296, 1997

Friedfeld, S., M. Fraser, K. Ensor, S. Tribble, D. Rehle, D. Leleux and F. Tittel. Statistical analysis of primary and secondary atmospheric formaldehyde. *Atmospheric Environment* 36 (30): 4767-4775, 2002

Jiménez, R., A. Martilli, I. Balin, H. van den Bergh, B. Calpini, B.R. Larsen, G. Favaro and D. Kita. Measurement of formaldehyde (HCHO) by DOAS: Intercomparison to DNPH measurements and interpretation from Eulerian model calculations. Air & Waste Management

Association, *A&WMA 93rd Annual Conference & Exhibition*, Salt Lake City (USA), June 18-22, 2000: Paper 829

Jiménez, R. Development and application of UV-visible and mid-IR differential absorption spectroscopy techniques for pollutant trace gas monitoring. Ph.D. Thesis, EPFL, Lausanne, 2003

John, C., R. Friedrich, J. Staehelin, K. Schlapfer and W.A. Stahel. Comparison of emission factors for road traffic from a tunnel study (Gubrist tunnel, Switzerland) and from emission modeling. *Atmospheric Environment* 33 (20): 3367-3376, 1999

Klemp, D., K. Mannschreck, H.W. Patz, M. Habram, P. Matuska and F. Slemr. Determination of anthropogenic emission ratios in the Augsburg area from concentration ratios: results from long-term measurements. *Atmospheric Environment* 36 (1): 61-80, 2002

Kristensson, A., C. Johansson, R. Westerholm, E. Swietlicki, L. Gidhagen, U. Wideqvist and V. Vesely. Real-world traffic emission factors of gases and particles measured in a road tunnel in Stockholm, Sweden. *Atmospheric Environment* 38 (5): 657-673, 2004

Larsen, B.R., A. Tudos, J. Slanina, K. Van der Borg and D. Kotzias. Quantification of airborne fossil and biomass carbonylic carbon by combined radiocarbon and liquid chromatography mass spectrometry. *Atmospheric Environment* 35 (33): 5695-5707, 2001

Lawson, D.R., H.W. Biermann, E.C. Tuazon, A.M. Winer, G.I. Mackay, H.I. Schiff, G.L. Kok, P.K. Dasgupta and K. Fung. Formaldehyde measurement methods evaluation and ambient concentration during the carbonaceous species methods comparison study. *Aerosol Science and Technology* 12: 64-76, 1990

Lelieveld, J. and F.J. Dentener. What controls tropospheric ozone? *Journal of Geophysical Research* 105 (D3): 3531-3551, 2000

Li, S.M., K.G. Anlauf, H.A. Wiebe and J.W. Bottenheim. Estimating primary and secondary production of HCHO in eastern North America based on gas phase measurements and principal component analysis. *Geophysical Research Letters* 21 (8): 669-672, 1994

Li, S.M., K.G. Anlauf, H.A. Wiebe and J.W. Bottenheim. Emission ratios and photochemical production efficiencies of nitrogen oxides, ketones, and aldehydes in the Lower Fraser Valley during the Summer Pacific 19993 Oxidant Study. *Atmospheric Environment* 31 (14): 2037-2048, 1997

Martilli, A., A. Neftel, G. Favaro, F. Kirchner, S. Sillman and A. Clappier. Simulation of the ozone formation in the northern part of the Po valley. *Journal of Geophysical Research* 107 (D22): 8195, 2002

Meller, R. and G.K. Moortgat. Temperature dependence of the absorption cross sections of formaldehyde between 223 and 323 K in the wavelength range 225-375 nm. *Journal of Geophysical Research* 105 (D6): 7089-7101, 2000

NILU. EMEP manual for sampling and chemical analysis (EMEP/CCC-Report 1/95, O-7726). Norwegian Institute for Air Research (NILU), Kjeller (Norway), 2001

NIOSH. The registry of toxic effects of chemical substances - Formaldehyde (RTECS #: LP8925000, CAS #: 50-00-0). National Institute for Occupational Safety and Health, 2002 (http://www.cdc.gov/niosh/rtecs - Accesed Aug 8, 2003)

Perego, S. Metphomod - A numerical mesoscale model for simulation of regional photosmog in complex terrain: Model description and application during POLLUMET 1993 (Switzerland). *Meteorology and Atmospheric Physics* 70 (1-2): 43-69, 1999

Platt, U. Differential optical absorption spectroscopy. **In** M.W. Sigrist (ed), Air monitoring by spectroscopic techniques, Wiley, New York, 1993: 27-84

Possanzini, M. and V. Di Palo. Performance of a 2,4-DNPH coated annular denuder/HPLC system for formaldehyde monitoring in air. *Chromatographia* 49 (3/4): 161-165, 1999

Possanzini, M., V.D. Palo and A. Cecinato. Sources and photodecomposition of formaldehyde and acetaldehyde in Rome ambient air. *Atmospheric Environment* 36 (19): 3195-3201, 2002

Satsumabayashi, H., H. Kurita, Y.-S. Chang, G.R. Carmichael and H. Ueda. Photochemical formations of lower aldehydes and lower fatty acids under long-range transport in central Japan. *Atmospheric Environment* 29 (2): 255-266, 1995

Seinfeld, J.H. and S.N. Pandis. Atmospheric chemistry and physics: From air pollution to climate change. Wiley, New York, 1998

Sillman, S., K.I. Alwali, F.J. Marsik, P. Nowacki, P.J. Samson, M.O. Rodgers, L.J. Garland, J.E. Martinez, C. Stoneking, R. Imhoff, J.H. Lee, L. Newman, J. Weinsteinlloyd and V.P. Aneja. Photochemistry of Ozone Formation in Atlanta, Ga - Models and Measurements. *Atmospheric Environment* 29 (21): 3055-3066, 1995

Simeonov, V., G. Larchevêque, P. Quaglia., H. van den Bergh and B. Calpini. Influence of the photomultiplier tube spatial uniformity on LIDAR signals. *Applied Optics* 38 (24): 5186-5190, 1999

Simeonov, V., B. Calpini, I. Balin, P. Ristori, R. Jiménez and H. van den Bergh. UV ozone DIAL based on a N_2 Raman converter - Design and results during ESCOMPTE field campaign. *21st ILRC*, Quebec, 2002: 403-406

Slemr, J., W. Junkermann and A. Volz-Thomas. Temporal variations in formaldehyde, acetaldehyde and acetone and budget of formaldehyde at a rural site in Southern Germany. *Atmospheric Environment* 30 (21): 3667-3676, 1996

Solberg, S., C. Dye, S.-E. Walker and D. Simpson. Long-term measurements and model calculations of formaldehyde at rural European monitoring sites. *Atmospheric Environment* 35 (2): 195-207, 2000

Staehelin, J., C. Keller, W. Stahel, K. Schlapfer and S. Wunderli. Emission factors from road traffic from a tunnel study (Gubrist tunnel, Switzerland). Part III: Results of organic compounds, SO_2 and speciation of organic exhaust emission. *Atmospheric Environment* 32 (6): 999-1009, 1998

Stockwell, W.R., F. Kirchner, M. Kuhn and S. Seefeld. A new mechanism for regional atmospheric chemistry modelling. *Journal of Geophysical Research* 102(D22): 25847-25879, 1997

Trapp, D. and C. de Serves. Intercomparison of formaldehyde measurements in the tropical atmosphere. *Atmospheric Environment* 29 (22): 3239-3243, 1995

von Kuhlmann, R. Tropospheric photochemistry of ozone, its precursors and the hydroxyl radical: A 3D-modeling study considering non-methane hydrocarbons. Ph.D. Thesis, Johannes Gutenberg-Universität, Mainz, 2001

Wagner, V., R. von Glasow, H. Fischer and P.J. Crutzen. Are CH_2O measurements in the marine boundary layer suitable for testing the current understanding of CH_4 photooxidation?: A model study. *Journal of Geophysical Research* 107 (D3): ACH 3 1-14, 2002

Wert, B.P., M. Trainer, A. Fried, T.B. Ryerson, B. Henry, W. Potter, W.M. Angevine, E. Atlas, S.G. Donnelly, F.C. Fehsenfeld, G.J. Frost, P.D. Goldan, A. Hansel, J.S. Holloway, G. Hubler, W.C. Kuster, D.K. Nicks, J.A. Neuman, D.D. Parrish, S. Schauffler, J. Stutz, D.T. Sueper, C. Wiedinmyer and A. Wisthaler. Signatures of terminal alkene oxidation in airborne formaldehyde measurements during TexAQS 2000. *Journal of Geophysical Research* 108 (D3): ACH 8 1-14, 2003

Appendix

The mass conservation equation dictates that the concentration (c) of a trace gas in a perfectly mixed box (0-D Eulerian model) of length Δx, and variable mixing height (h), evolves according to (Seinfeld, 1998),

$$dc/dt = (F + F_z) + D + E + R \qquad (A1)$$

where $F = u(c^0 - c)/\Delta x$ represents the net advective flux, $F_z = (c^\infty - c)(dh/dt)/h$ the entrainment flux, $D = -u_d c/h$ the deposition rate, $E = E''/h$ the emission rate, and $R = \sum \xi_j r_j$ the net photochemical production rate (u is the horizontal wind speed, u_d is the dry deposition velocity, E″ is the emission flux, ξ_j is the stoichiometric coefficient of the species of interest on the j-th reaction, r_j is the rate of the j-th reaction, and $c^0(t)$ and $c^\infty(t)$ are the background concentrations upwind and aloft the box, respectively).

CH_2O is emitted and photochemically produced in the atmosphere. Assuming respective proportionality between these terms and concurrently measured concentrations of purely primary (c_1) and secondary (c_2) species,

$$c(t) = e c_1(t) + a c_2(t) \qquad (A2)$$

allows splitting c into its primary (ec_1) and secondary (ac_2) components upon determination of the emission (*e*) and net photochemical production (*a*) linear combination constants. The derivative of (A2), $dc/dt = e(dc_1/dt) + a(dc_2/dt)$, entails that each of the right-hand terms in (A1) is as well a linear combination of primary and secondary terms, e.g. $F = eF_1 + aF_2$. The basic assumptions of this analysis ($R_1 = E_2 = 0$) lead to $e = E''/E_1''$ and $a = R/R_2$. Therefore *e* and *a* are strictly ratios of emissions and net photochemical production rates, respectively. If *a* is to be a (time independent) constant, the surrogate secondary species must have the same chemical sources and sinks than CH_2O. This requirement is better fulfilled by species like PAN than by O_3. Linear combination of the net advective and entrainment fluxes results in $c^0 = ec_1^0 + ac_2^0$ and $c^\infty = ec_1^\infty + ac_2^\infty$, which implies that the emission (*e*) and net photochemical production (*a*) constants must be also valid upwind and aloft the box. A good spatial homogeneity concerning emission sources implies that measurements must be performed far from major point sources. Finally, the linear combination condition as applied to the deposition rate entails identity of the deposition velocities, $u_{d,1} = u_{d,2} = u_d$ (CH_2O ~0.36 cm s^{-1}). Regarding the deposition rate only, NOx (~0.09 cm s^{-1}) would perform better than CO (~0.02cm s^{-1}) as surrogate of primary CH_2O, as much as O_3 (~0.26 cm s^{-1}) than PAN (~0.10 cm s^{-1}) and H_2O_2 (~0.9 cm s^{-1}) as surrogate of secondary CH_2O. u_d values were taken from von Kuhlmann (2001).

Investigation of the Emission of Monocyclic Aromatic Hydrocarbons from a Wastewater Treatment Plant at Lausanne (Switzerland) by Differential Optical Absorption Spectroscopy (DOAS)

Rodrigo Jiménez, Tiziana Iannone, Hubert van den Bergh and Bertrand Calpini
Air Pollution Laboratory (LPAS)
Swiss Federal Institute of Technology (EPFL)
CH-1015 Lausanne, Switzerland
rodrigo.jimenez@epfl.ch

Dieter Kita
Thermo Environmental Instruments Inc.
Franklin, MA 02038, USA

Abstract

Recent research works show that wastewater treatment plants may significantly contribute to the total emission of volatile organic compounds (VOC) in urban areas. In order to investigate this contribution, a measurement campaign was carried out during September 1999 in the Lausanne area. The concentrations of monocyclic aromatic hydrocarbons (MAH) over a wastewater treatment plant at Lausanne were monitored by differential optical absorption spectroscopy (DOAS) and gas chromatography (GC-FID). A flame ionization detector (FID) was used for monitoring the overall concentration of non-methane hydrocarbons (NMHC). The local meteorological conditions were also measured. The concentrations of benzene, toluene, ethylbenzene, xylenes, 1,2,4-trimethylbenzene and phenol over the wastewater treatment plant as measured by DOAS and GC-FID are compared. In addition, based upon the results of a recent field experiment, the impact of the oxygen (O_2) interference on DOAS measurements of aromatic compounds is addressed. The MAH concentration time series and its relation to that one of NMHC, as well as to the meteorological conditions, are presented. The VOC release and production phenomena involved in the wastewater and sludge treatment processes are analyzed using complementary measurements of aromatic compounds in wastewater and gas processing streams.

Keywords: air pollution, wastewater, sludge, incineration, emission, non-methane hydrocarbons (NMHC), monocyclic aromatic hydrocarbons (MAH), differential optical absorption spectroscopy (DOAS), gas chromatography (GC), flame ionization detector (FID)

1. Introduction

Photochemical pollution is a widespread air quality problem of major concern nowadays. It is caused by the photo-oxidation of volatile organic compounds (VOC) in the atmosphere. Wastewater and solid waste treatment operations have been identified as significant sources of VOC [1-2]. For instance, it is estimated that 6% of the total VOC emitted in the Chicago area comes from its wastewater treatment plants[2].

Monocyclic aromatic hydrocarbons (MAH) are an important fraction of VOC. They account for about 30% (w/w) of all non-methane hydrocarbons (NMHC) in urban air[3] and usually are the second most important VOC fraction emitted by waste treatment operations[1]. In addition, MAH are toxic or even carcinogenic as benzene, and likely precursors of secondary aerosols[3].

This study is the result of a short measurement campaign aimed at investigating the emission of VOC, and particularly of monocyclic aromatic hydrocarbons (MAH), from a wastewater and sludge treatment facility at Lausanne, Switzerland (Vidy STEP). Despite some measurements were made in wastewater and process gas streams, this investigation was focused on fugitive emissions of MAH from sludge treatment operations. Path averaged measurements of MAH obtained by differential optical absorption spectroscopy (DOAS) were instrumental in this purpose.

The spectral interference of oxygen is the main problem for DOAS measurements of MAH [3]. In order to overcome this difficulty, an alternative approach was devised and applied previous to this investigation for obtaining a set of instrument-specific oxygen reference spectra from plain open-air spectra.

DOAS measurements coupled to meteorological measurements indicate that fugitive MAH stratify vertically in the sludge treatment area. Ambient air samples analyzed by gas chromatography with flame ionization detection (GC-FID) show that a horizontal gradient exists as well. Possible sources of fugitive emissions of VOC, particularly of MAH as detected by DOAS, are the volatilization of VOC already contained in sludge during one or several handling operations previous to incineration, and unintended pyrolysis [4] during the sludge incineration process (on site produced VOC source).

At the average wastewater flow rate of Vidy STEP, the maximum volatilization rate of MAH contained in wastewater is estimated in about 500 Kg per day.

Further investigation will be required to quantify and elucidate the fugitive MAH release phenomena.

2. Measurement of Monocyclic Aromatic Hydrocarbons by DOAS

The differential optical absorption spectroscopy (DOAS) technique has been successfully used for the detection of diverse atmospheric trace gases since the late 70s [5]. A comprehensive description of this technique can be found elsewhere [5]. On the other hand, its application for the detection of monocyclic aromatic hydrocarbons (MAH) has not been without problems [6-11], despite the fact that most MAH exhibit relatively sharp absorption bands in the 240-300 nm wavelength region [7,12]. Besides the simultaneous presence several MAH in the air volume observed, the major difficulty for DOAS measurements of MAH is the spectral interference of oxygen [3]. At this wavelength range, oxygen displays a very complex spectral structure due to the overlapping of 4 band systems with extremely narrow (some picometers) absorption transitions and the spectral interference of the O_2-O_2 and O_2-N_2 systems [3]. While a very high spectral resolution would be required to resolve these bands, the spectral resolution of a typical DOAS system is some angstroms. At this resolution, the oxygen bands overlap, leading to an apparent deviation of the Beer-Lambert-Bouger (BLB) law. The overall result is that at low resolution, oxygen spectra become a non-linear function of concentration, optical path and pressure. In these conditions, a different oxygen reference spectrum would be theoretically required for each location and path length. In practice, a suitable set of *instrument-specific* oxygen reference spectra is required instead on a single oxygen absorption cross section, as it is case for any other light-absorbing compound.

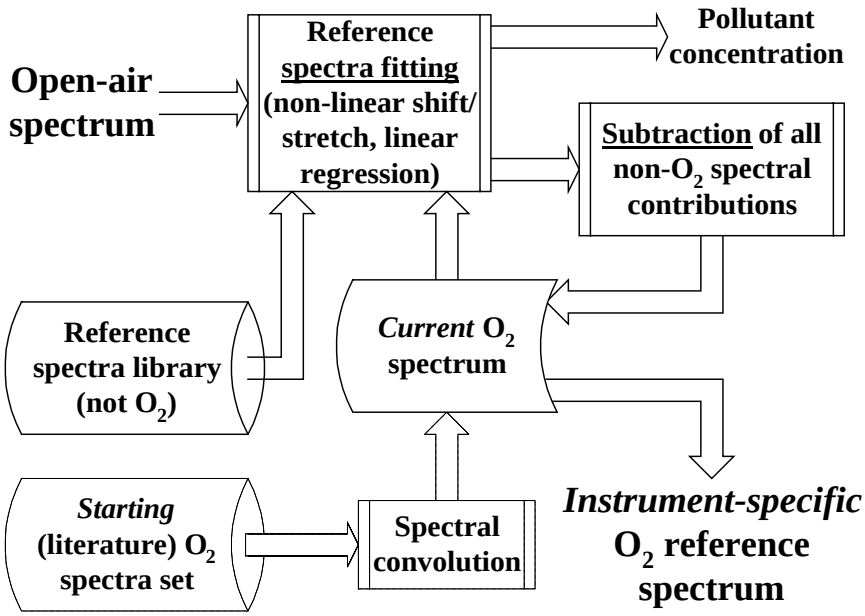

Figure 1. Procedure used for the recovery of instrument-specific oxygen reference spectra from open-air spectra.

In addition, the spectral accuracy and resolution of a DOAS spectrometer must be high enough to allow resolving between the very resembling spectral features of similarly substituted MAH (mono-, di-, tri-substituted), such as those between toluene and ethylbenzene, and among the xylene isomers [7,12].

In order to provide a solution for the oxygen interference problem, we developed and tested an alternative procedure for the recovery of instrument-specific oxygen reference spectra from plain open-air spectra (see Figure 1). This recovery procedure is summarized as follows:

- Open-air spectra in the wavelength region 240-280 nm were recorded at different path lengths from 120 to 1100 m during a long integration time (30 min) in order to assure a high signal to noise ratio. As explained below, the fact the air masses observed were relatively polluted simplified instead of making more difficult the oxygen spectra recovery process.
- A set of oxygen spectra at relatively high resolution (0.15 nm FWHM), obtained in laboratory conditions by Volkamer, Etzkorn, Geyer and Platt [3], was used as *starting* reference spectra for the retrieval of instrument-specific oxygen reference spectra from plain open-air spectra. For this purpose, Volkamer's oxygen spectra were previously convoluted to the spectral resolution of the DOAS instrument used for the field measurements herein reported (DOAS 2000®, Thermo Environmental Instruments Inc.). Figure 2 shows the instrumental function of the DOAS 2000® spectrometer (0.57 nm FWHM) together with a high-resolution oxygen spectrum and the resulting convoluted spectrum.
- The spectral contributions of ozone, sulfur dioxide and a suitable set of MAH (benzene, toluene, ethylbenzene, o-, m-, p-xylene, 1,2,4-trimethylbenzene and phenol) were fitted to and subtracted from each open-air spectrum. Volkamer's spectra were used as dummy wavelength functions in the recovery process; i.e. a best-matching Volkamer's spectrum was found for each open-air spectrum from which an instrument-specific oxygen spectrum was recovered.
- In all cases, the ozone concentrations calculated by the recovery method were in close agreement with field measurements. The calculated concentrations of MAH were as well within the expected concentration range in the measurement location (Grenoble, France). A subset of the recovered oxygen spectra is shown in Figure 3.
- Each new instrument-specific oxygen spectrum was tested as fitting reference for the same open-air spectrum from which it was recovered (second iteration). For every recovered oxygen spectra, the pollutant concentrations retrieved in the second-iteration were in close agreement to those originally obtained when using Volkamer's spectra. This shows that the recovery process converged, thus no additional iterations were carried out.

The process of increasing overlap of the narrower oxygen absorption bands due to the oxygen column density increase is clearly seen in the spectra shown on Figure 3. As explained above, this process is apparent and results of observing extremely sharp absorption transitions at low spectral resolution. The practical consequence is that, while the broader transitions are common among spectra at different oxygen column densities, the narrower transitions seem more difficult to predict. Moreover, since this dependence cannot be explained in simple

terms, in principle a required oxygen spectrum at a given path length could not be calculated from other oxygen reference spectra by any "interpolation" procedure. In despite of this complexity, such an interpolation procedure was developed and applied (see description below).

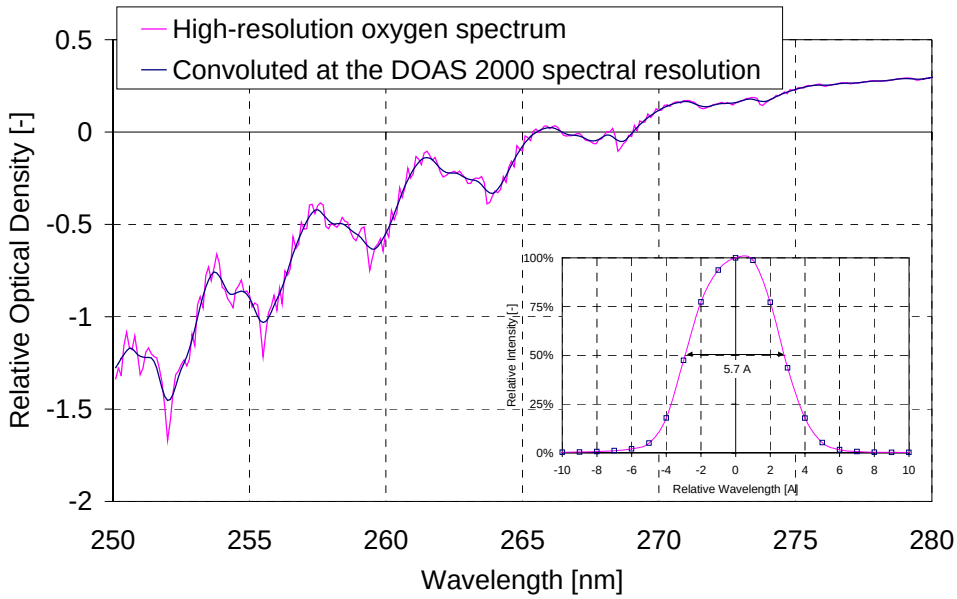

Figure 2. Spectra of oxygen ($1.785 \cdot 10^{24}$ molecules/cm^2 column density) as measured [3] at 0.15 nm FWHM spectral resolution ("high resolution") and convoluted to spectral resolution of DOAS 2000® (0.57 nm FWHM). The instrumental function of DOAS 2000 is shown on the right side.

In addition, it was found that at low spectral resolution, even the broader oxygen transitions do not follow the BLB due to the apparent dependence of the oxygen cross section on the optical path length. This dependence is expressed in the following equation.

Equation 1. Differential BLB law applied to oxygen measured at low spectral resolution (non-linear dependence).

$$D'_{oxygen}\left(\lambda, c_{oxygen}, L\right) = \sigma'_{oxygen}\left(\lambda, c_{oxygen}, L\right) \cdot c_{oxygen} \cdot L$$

where:

λ = wavelength
c = concentration
L = optical path length
σ' = differential absorption cross section
D'= differential optical density

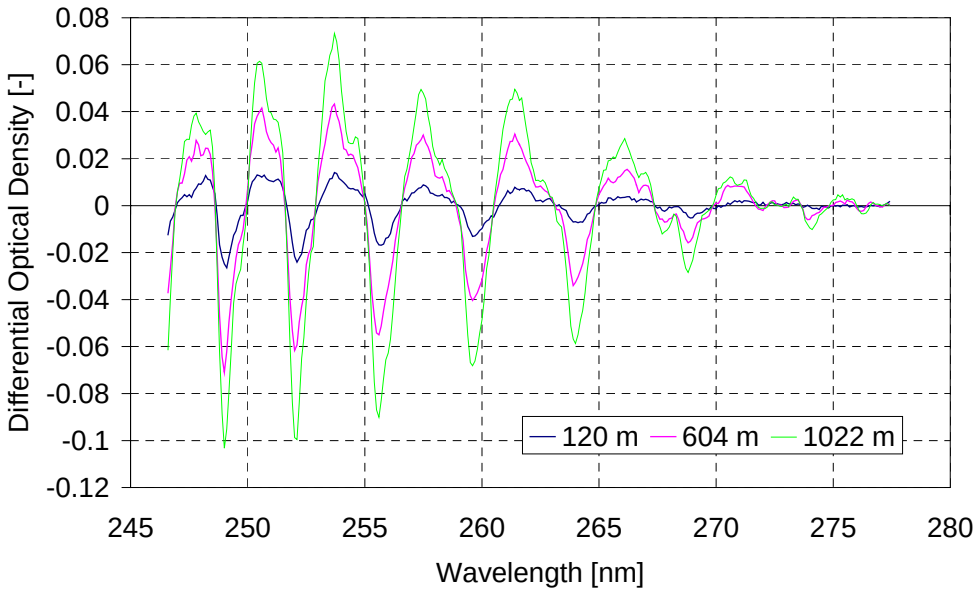

Figure 3. Instrument-specific oxygen reference spectra recovered from plain open-air spectra recorded at Grenoble, France.

Nevertheless, it was found that using an arbitrarily chosen differential oxygen spectrum as "reference" (norm) spectrum, the dependence of the broader oxygen transitions on the optical path length is mathematically described by the equation below.

Equation 2. Dimensionless (non-linear) BLB equation applied for oxygen measured at low spectral resolution.

$$\frac{D'_{oxygen}(\lambda, c_{oxygen}, L)}{D'_{oxygen}(\lambda, c_{oxygen}, L_0)} = \left[\frac{\sigma'_{oxygen}(\lambda, c_{oxygen}, L)}{\sigma'_{oxygen}(\lambda, c_{oxygen}, L_0)}\right] \cdot \left(\frac{L}{L_0}\right) \approx \beta \cdot \left(\frac{L}{L_0}\right)^{\gamma}$$

where:

β, γ = non-linear BLB equation fitting coefficients
L_0 = optical path length of the "reference" (norm) oxygen spectrum

A non-linear regression fitting applied to the recovered instrument-specific oxygen spectra data pairs, (L/L_0, D'/D_0'), gives $\beta \approx 1$ and $\gamma = 0.69$ (see Figure 4). Very similar β and γ coefficients were found for the higher resolution oxygen spectra provided by Volkamer [3].

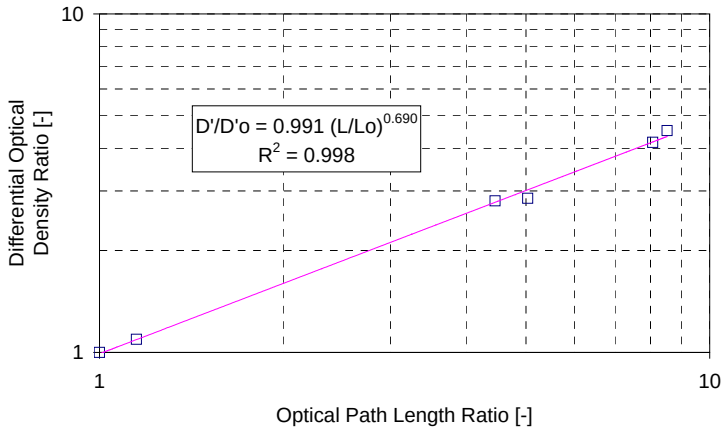

Figure 4. Non-linear BLB correlation applied to the recovered oxygen spectra.

This finding provided the basis for the development of a fairly successful procedure for oxygen reference spectra interpolation. Figure 5 shows an oxygen spectrum at 534 m optical path length (dots) and the one calculated (line) by interpolation using its two "neighbor" spectra (closest shorter and longer path lengths) as orthogonal basis and their weighting coefficients obtained by multiple linear regression forced to zero. The same procedure was used for approximating an oxygen reference spectrum suitable for the optical path length at Vidy STEP (220 m). It was found that the concentration retrieval was better with this interpolated oxygen spectrum than with any other individual oxygen spectrum available in the new oxygen spectra database.

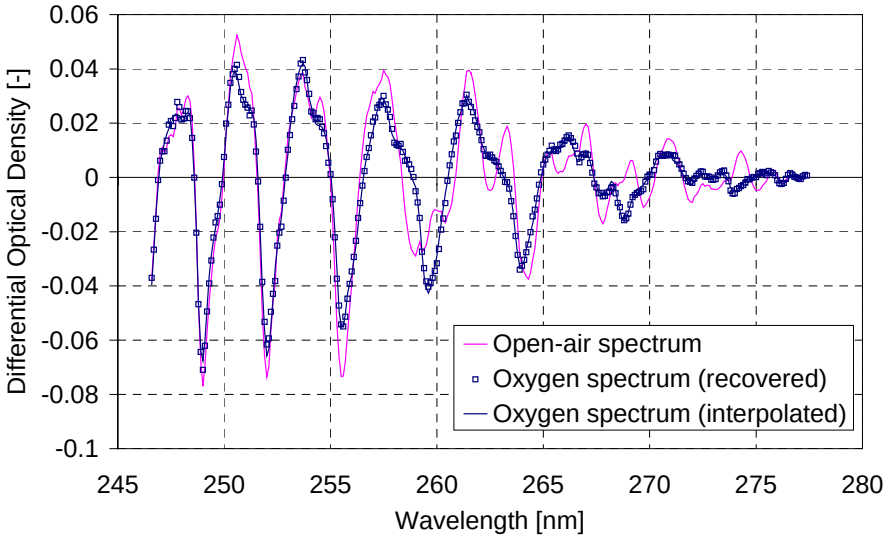

Figure 5. Open-air spectrum (534 m path length) and the oxygen spectrum from it recovered. Interpolated spectrum is shown as well. Note that the oxygen transitions account for a large part of the original spectrum.

3. Emission of Volatile Organic Compounds from a Wastewater and solid waste Treatment Plant at LAusanne, switzerland

Concerned by the impact of photochemical pollution in Switzerland, the Swiss Federal Council issued in 1997 a law (OCOV – 814.018) aimed at reducing within 10 years the VOC emission down to the level of 1960, i.e. a 55% equivalent reduction with respect to the highest annual emission level (324,000 tons in 1984) [13]. This law defines VOC as all organic compounds whose normal boiling point is below 240 °C. OCOV – 814.018 establishes a tax of 3 SFr per Kg of VOC emitted (~ 2 US$/Kg), enforceable to all manufacturing processes involving VOC. This new law does not clearly specifies whether public and private wastewater and solid waste treatment facilities are targeted too [13], despite of recent research work showing that these facilities are potential contributors to the emission and ambient concentration of VOC [1-2].

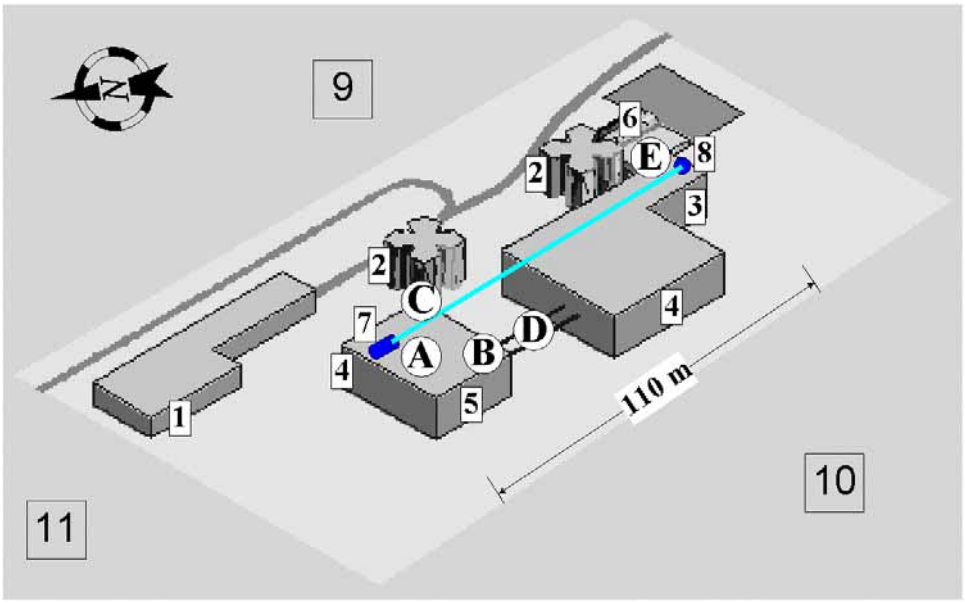

Figure 6. Scale representation of the sludge handling area at Vidy STEP. Key: [1] Screens, grit chambers; [2] Sludge thickeners; [3] Sludge stockage; [4] Sludge dewatering and incineration; [5] Incineration flue gas cleaning; [6] Biological filter for VOC and odor control; [7] DOAS emitter/receiver (coaxial telescope); [8] DOAS retroreflector; [9] 6-lane highway; [10] Geneva lake shoreline t 200 m; [11] Wastewater treatment area; (A) - (E) GC-FID sampling sites; (B) FID sampling site

In order to investigate the VOC emission from such a facility, an exploratory campaign called STEP was carried out in a wastewater treatment plant at Lausanne, Switzerland (Vidy location). The facility (Vidy STEP) is located at 200 m of the Geneva Lake shoreline and adjacent to a 6-lane highway (see Figure 6). Vidy STEP uses a conventional activated sludge process with fine-bubble diffused aeration for treating the wastewater produced by an

equivalent population of 220,000 inhabitants. The facility includes as well process units for the thickening, dewatering (conventional filter presses) and incineration (2 fluidized-bed incinerators) of the sludge produced on site and in neighbor wastewater facilities (57% w/w of the total sludge cake incinerated). Vidy STEP includes as well an incineration flue gas cleaning system (1 cyclone separator and 2 dry electrostatic precipitators for particulate matter removal followed by wet scrubbing with lime and caustic soda solutions) and a biological filtering system for VOC and odor control. A more detailed description of Vidy STEP can be found elsewhere [13].

Table 1 summarizes the analytical instruments used during STEP for the measurement of VOC concentrations in ambient air and wastewater and gas processing streams within the period August 5 - September 10, 1999 (not all measurements performed simultaneously). The FID and GC-FID measurement sites are shown on Figure 6. Additional meteorological data (temperature, pressure, horizontal wind speed and vertical wind speed) from 2 meteorological stations located in the Lausanne area (Chauderon and Plan de Pierre) were provided by SEHL (Lausanne's Environmental Authority).

Technique	**Apparatus**	**Phase / Site**	**Period**	**Comments**
DOAS	DOAS 2000®, Thermo Environmental Instruments Inc.	Ambient air (optical path)	03-10.09	220m optical path length, 15 min integration time
GC-FID	ETA 8521®, DANI 86.10	Ambient air (Sites A to E); Raw incineration flue gas; Biofilter (inlet, outlet)	07-09.09 (ambient air); 23.08 –02.09 (gas processing streams)	Routine calibration tank BTEX mixture (1-3 ppm ± 5%), Scott Specialty Gases
FID	FID 3-100 ®, JUM	Ambient air (Site B)	06-10.09	Calibration tank: Propane (85 ppm ± 2%), SL Gas
SPME-GC-FID	HP 5890 HP 5971-A	Wastewater (inlet, outlet)	02-08.08	

Table 1. Summary of analytical techniques and measurements used and carried out during STEP. DOAS, GC-FID and FID measurement sites are shown on Figure 6. All dates refer to 1999.

Volatilization, whether by free diffusion from stagnant wastewater or forced by aeration (stripping) during the wastewater treatment process, was expected to be an important source of fugitive emissions of MAH. In order to assess this emission area source, MAH contained in wastewater at the inlet (only liquid phase) and outlet of the wastewater treatment process were sampled by solid phase micro-extraction (SPME) and analyzed by gas chromatography with mass spectroscopy (GC-MS) (see Table 2). These measurements confirmed the hypothesis: depending on the efficiency of the volatilization process, up to 500 Kg/day of MAH could be emitted from the activated sludge area.

MAH	**Average Concentration [ppmv]**		**Calculated Maximum Volatilization Rate [Kg/day]**
	Inlet	**Outlet**	
Toluene	1.8	1.5	147.55
Ethylbenzene	0.2	0.0	16.40
Propylbenzene	0.5	0.0	40.75
o-Xylene	0.6	0.5	49.94
m-, p-Xylene	1.0	0.6	81.57
2-Ethyltoluene	0.3	0.0	24.98
1,2-Diethylbenzene	0.0	0.0	0.00
1,4-Diethylbenzene	0.2	0.1	16.30
1,2,4-Trimethylbenzene	1.1	0.2	91.10
1,3,5-Trimethylbenzene	0.8	0.0	65.45
Styrene	0.0	0.0	0.00
Total	**6.5**	**2.9**	**534.04**

Table 2. Inlet and outlet concentrations of MAH in wastewater at Vidy STEP as measured by SPME-GC-MS. Daily SPME samples (3 duplicates) were taken at 10:00-16:00 during the period August 2-8, 1999. Vidy STEP treated 94,600(±18%) m^3/day of wastewater during this period. All average concentrations are within 10% standard deviation.

The DOAS system operated at Vidy STEP is a monostatic commercial system described in detail elsewhere [14]. The light emission and collection side (coaxial telescope) was placed on the roof of one of buildings where sludge is dewatered and incinerated (see Figure 5). The retroreflector was placed on an adjacent building (sludge stockage). Both buildings are located at the East Side of Vidy STEP (sludge handling operations). The measurement path was thus set for monitoring fugitive emissions from the sludge handling operations (thickening, dewatering, incineration and flue gas cleaning). However, the maximum feasible path length was somehow short for the detection of MAH. The resulting optical path length (220 m) limited the detection of MAH at their lowest concentrations. The detection limits are compound-dependent, for instance about 2 ppb for benzene. Nevertheless, the fact the highway (an important MAH linear emission source) is adjacent to the target area would make very difficult to apply the methodology used by Schafer et al [15] for the estimation of area source emissions. This procedure consists in measuring pollutant concentrations downwind (by open-path monitoring when possible) from which area emissions are estimated by inverse modeling.

This investigation focuses on the period of intensive DOAS and GC-FID ambient air concentration measurements (September 3-10, 1999). During this period, Vidy STEP treated 90,300(±5%) m^3/day of wastewater and incinerated 62.6 tons/day of sludge cake. Concerning meteorology, the weather was in general good with the exception of the 6th September, partially cloudy. See Figure 7A. This period was characterized by relatively stagnant, anticyclonic conditions. Airflow was probably only local and controlled by valley-mountain wind and lake breeze effects. See Figure 7B. The maximum wind speed (~ 2 m/s) is observed at midday, when comparatively cleaner air masses flow from the Geneva Lake to the Lausanne area. In the morning and in the evening certainly much polluted air masses flow at low speed from north to south (inverse direction).

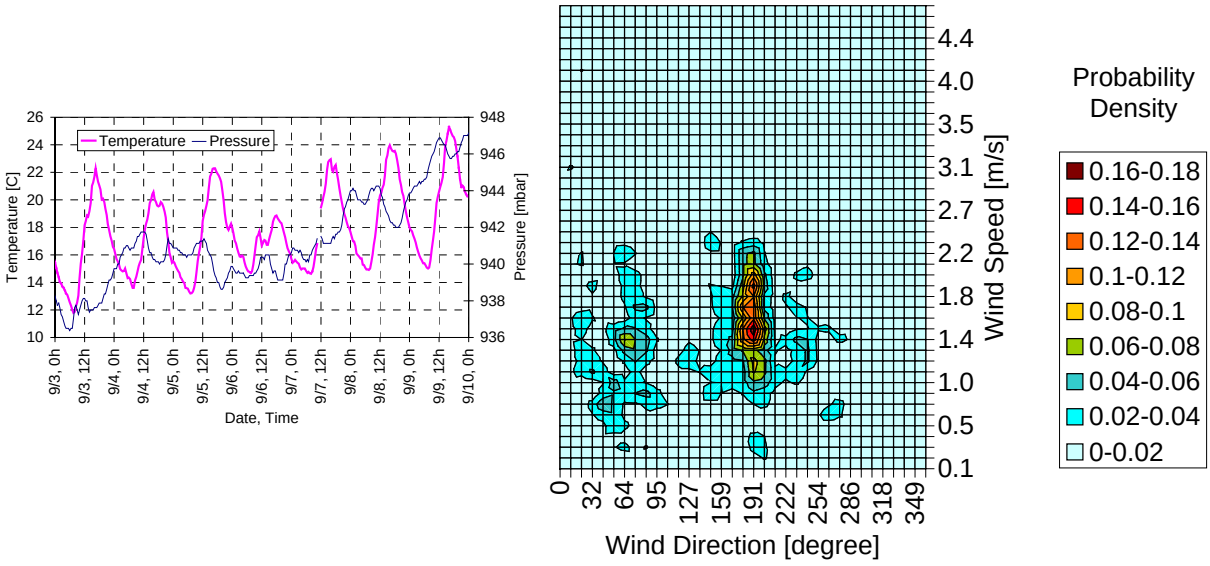

Figure 7. Weather conditions at Lausanne during the STEP campaign DOAS and GC-FID intensive measurement period (September 3-9, 1999). **Up:** Temperature and pressure time series. **Down:** Wind rose.

The ambient air concentrations of MAH as measured by GC-FID are shown on Figure 8. It is clear that a positive concentration gradient exists from site E to site A (refer to Figure 6). Bearing in mind that most the air samples for GC-FID were made early morning or late afternoon, when air was essentially stagnant, it can be concluded that site A is very likely nearby an area where fugitive emissions are stronger. The measured concentrations are probably linked whether to volatilization of MAH formerly contained in sludge at any of its processing stages or to leaking from the flue gas scrubbing process.

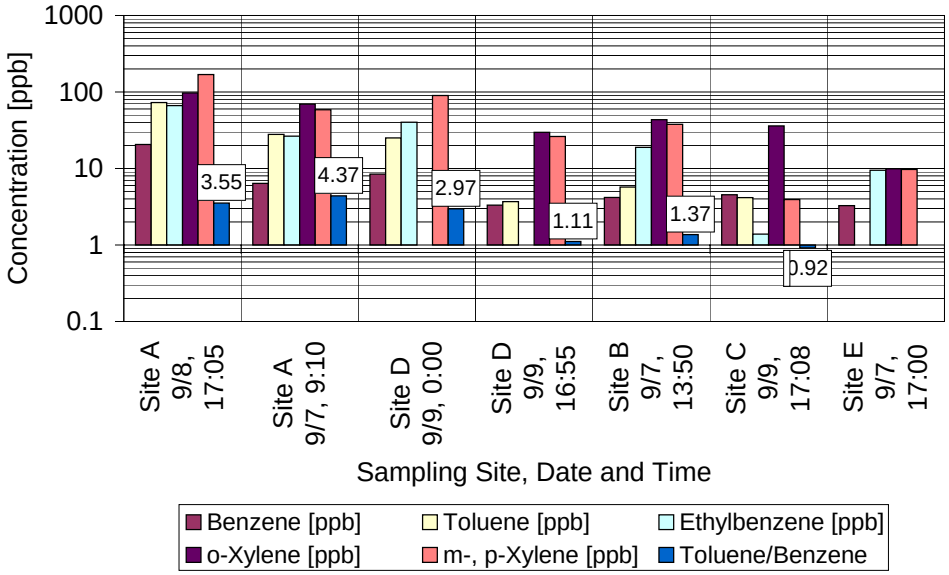

Figure 8. Ambient air concentration of MAH in the sludge handling area as measured by GC-FID. Note that a positive concentration gradient exists between sites A and E.

A close agreement was found between the time trends of MAH (DOAS) and NMHC (FID) measurements (see Figure 9). This correlation leads to conclude that BTEX accounts for approximately a 2% of the carbon of all organic compounds measured at Vidy STEP.

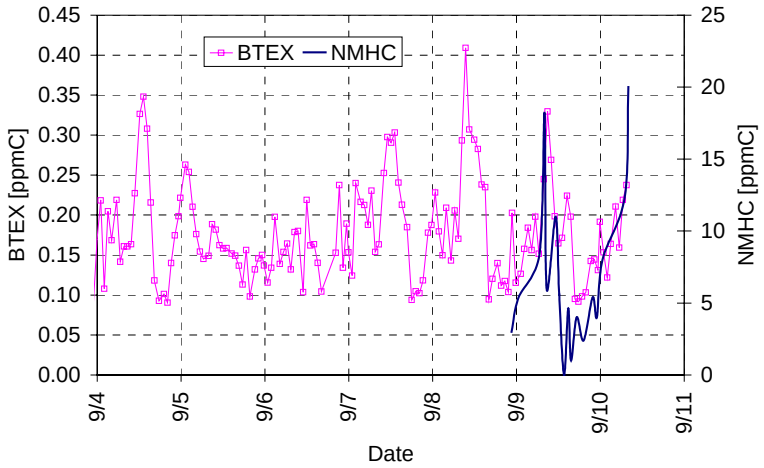

Figure 9. Concentration time series of NMHC as measured by FID and of BTEX as measured by DOAS. Both variables are expressed as carbon (v/v) concentrations. BTEX is the carbon-weighted sum of benzene, toluene, ethylbenzene, o-, m- and p-xylene.

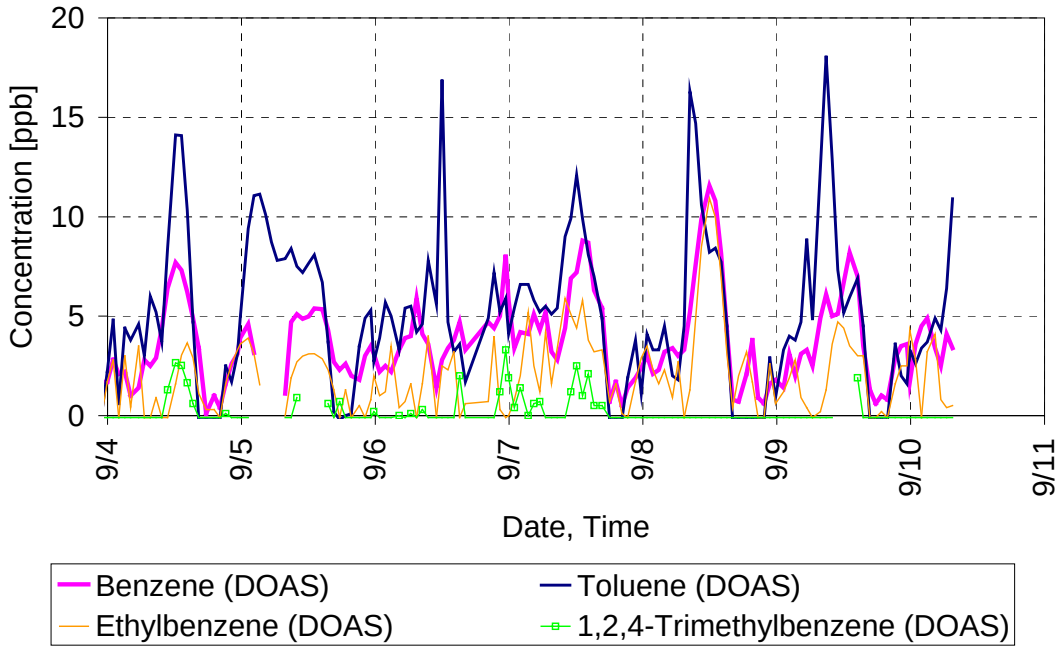

Figure 10. Concentration time series of benzene, toluene, ethylbenzene, and 1,2,4-trimethylbenzene as measured by DOAS.

As shown in Figure 11, DOAS measurements correlate better to GC-FID measurements taken at around midday. This is explained by the fact that the air mass observed is better mixed during that period of the day. The GC-FID measurements corresponding to morning or afternoon samples do not correlate to DOAS measurements not just because of differences in spatial resolution between these techniques [10], but mainly because air is stagnant during these periods of time. Therefore no attempt was made to mathematically correlate the measurements made by these two techniques.

Unexpectedly, peak concentrations of MAH are observed at midday, not during the morning or afternoon as expected if they were related to road traffic and particularly to the linear emission source defined by the adjacent highway. The fact the waste treatment facility is bordered by tall vegetation fences may explain its isolation in term of air mass exchanges. In addition, the ratios of concentration of several MAH to benzene are not in agreement with emission ratios [16] (see table 3). For instance, the average concentration ratio (v/v) of ethylbenzene to benzene is about 0.6, while the expected ratio for emissions from road traffic is around 0.3.

MAH	**Values Normalized to Benzene (v/v)**	
	Ambient air concentrations (DOAS) during STEP	**Emission Factor (Gasoline-powered Road Traffic)** [16]
Toluene	1.27	1.69
Ethylbenzene	0.56	0.25
o-Xylene	0.85	0.34
m-, p-Xylene	1.88	0.77
1,2,4-Trimethylbenzene	0.08	0.29
Phenol	0.08	-

Table 3. Comparison of normalized-to-benzene emission factors [16] and ambient air concentrations of MAH as measured by DOAS at Vidy STEP.

An outstanding correlation was found between the concentration of benzene, toluene, ethylbenzene, o-xylene and 1,2,4-trimethylbenzene as measured by DOAS and the vertical wind speed measured in Chauderon (Lausanne area) (see Figure 11). This leads to conclude that fugitive emissions, accumulated at the ground level of the sludge handling area during a period comprising from late afternoon to early morning, are moved upward by convection during midday. As these polluted air masses rise from the ground level, they cross the DOAS light beam and get detected. No attempt was made to calculate pollutant fluxes, since no local measurements of vertical wind speed were available at the measurement site.

Finally, it is important to mention that very high concentrations of MAH (up to 0.1% v/v of benzene and from 10 to 200 ppm for other MAH) as measured by GC-FID were found in the incineration flue gas stream (previous to gas cleaning operations). It is likely that such elevated quantities of MAH are produced inside the sludge incinerators by unintended pyrolysis [4]. In this case, at least a fraction of the VOC emitted by Vidy STEP would be produced on site.

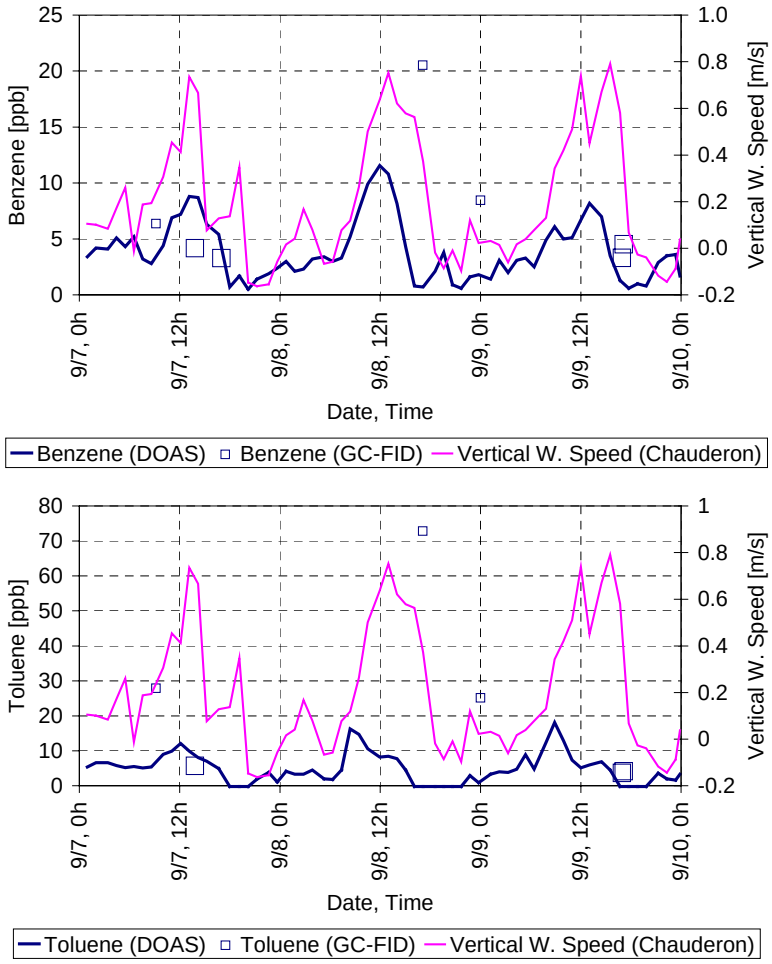

Figure 11. Time series of benzene (up) and toluene (down) as measured by DOAS and vertical wind measured at Chauderon (Lausanne area).

4. Conclusions

A new, alternative approach for the recovery of oxygen spectra from open-air spectra allows obtaining instrument-specific oxygen reference spectra sets. In addition, it was found feasible to interpolate these spectra within a limited range of oxygen column densities in order to improve the quality of the retrieved concentration time series.

DOAS is a very versatile technique for the real-time, simultaneous monitoring of monocyclic aromatic hydrocarbons in regard of its time resolution and detection limits. At the optical path length of this study (220 m), the time trends of m- and p-xylene are not in agreement with those of benzene, toluene, ethylbenzene and 1,2,4-trimethylbenzene. The retrieval of m- and p-xylene is subject of further investigation.

The joint analysis of concentration time series and meteorology would lead to indicate that fugitive emissions of MAH accumulate in stagnant conditions at the ground level and are moved upwards by natural convection around midday.

Despite there is sound evidence that MAH detected by DOAS are emitted inside the sludge handling area perimeter, at this point of the investigation, it is still not possible to apportion the measured concentrations of MAH in ambient air to any particular source of emissions within the sludge handling area. Possible sources of fugitive emissions of VOC are the flue gas scrubbing system and volatilization from sludge.

Concentrations of benzene as high as 0.1% were detected in the incineration flue gas before the gas cleaning operation. Stack measurements are thus required to determine the strength and time variability of this emission point source.

Emission of up to 500 kg/day could be possible if all the MAH contained in wastewater were volatilized. DOAS could be used as well to monitor this volatilization process and its dynamics.

Acknowledgements

We gratefully acknowledge Fadi Kadri and his staff of Vidy STEP, and Antonio Panico and Enga Luye of Belair (Lausanne) for their involvement in the field campaign. We are particularly grateful to Dominick Stadler for setting up, training and advising us in the use of the GC-FID technique for MAH measurements, and to William Baehler and Michel Wanner of SEHL (Lausanne's Environmental Authority) for providing us with valuable meteorological information. We are very grateful as well to Rainer Volkamer and the rest of the DOAS research team at the University of Heidelberg for furnishing us with their oxygen reference spectra set.

References

1. **Leach, J; Blanch, A; Bianchi, A.C.** Volatile Organic Compounds in an Urban Airborne Environment adjacent to a Municipal Incinerator, Waste Collection Centre and Sewage Treatment Plant; *Atmospheric Environment* **1999**, 33, 4309-4325
2. **Van Zandt, S.; Wadden, R.A. and Scheff, P.A.** Estimation of Waste Water Treatment Contributions to Concentrations of Organics in Chicago Air; *A&WMA 89th Annual Meeting and Exhibition*, Nashville, Tennessee, June 23-28, 1996; Paper 96-TA29A.01
3. **Volkamer, R; Etzkorn, T; Geyer, A and Platt, U.** Correction of the Oxygen Interference with UV Spectroscopic (DOAS) Measurements of Monocyclic Aromatic Hydrocarbons in the Atmosphere; *Atmospheric Environment* **1998**, 32, 3731-3747
4. **Elvers, B; Hawkins, S; Russey, W** (Eds.). Ullmann's Encyclopedia of Industrial Chemistry; VCH, Weinheim, Germany, 1995; Volume B8, pp 719-722
5. **Platt, U.;** Differential Optical Absorption Spectroscopy (DOAS); In *Air Monitoring by Spectroscopic Techniques*; Sigrist, M.W.(Ed.); Wiley, New York, 1994; pp 27-84
6. **Allegrini, I. and Febo, A.** Intercomparison between Gas-Chromatography and Long Path UV DOAS Techniques for the Measurement of Benzene and Toluene in Urban

Atmospheres; *Proceedings of Optical Sensing for Environmental and Process Monitoring*, McLean, Virginia, November 7-10, 1994; pp 243-252
7. **Axelsson, H. *et al.*** Measurement of Aromatic Hydrocarbons with the DOAS Technique; *Applied Spectroscopy* **1995**, 49, 1254-1260
8. **Barrefors, G.** Monitoring of Benzene, Toluene and p-Xylene in Urban Air with Differential Optical Absorption Spectroscopy Technique; *The Science of the Total Environment*, **1996**, 189/190, 287-292
9. **Brocco, D. *et al.*** Determination of Aromatic Hydrocarbons in urban Air of Rome; *Atmospheric Environment* **1997**, 31, 557-566
10. **Carter, R.E. *et al.*** A Method of Predicting Point and Path-Averaged Ambient Air VOC Concentrations, Using Meteorological Data; *J. Air Waste Manage. Assoc.* **1993**, 43, 480-488
11. **Lofgren, L.;** Determination of Benzene and Toluene in Urban Air with Differential Optical Absorption Spectroscopy; *Int. J. Environ. Anal. Chem* **1992**, 47, 69-74
12. **Etzkorn, T. *et al.*** Gas-phase absorption cross sections of 24 monocyclic aromatic hydrocarbons in the UV and IR spectral ranges; *Atmospheric Environment* **1999**, 33, 525-540
13. **Iannone, T.** *Etude de Faisabilite pour une Estimation des Composes Organiques Volatiles dans les Stations d'Epuration. Le Cas de la STEP de Vidy*; M.Eng. Thesis, EPFL, Lausanne, Switzerland, September 1999
14. **Schiff, H; Robbins, J.; Nadler, S.D. and Mackay, G.I.** The Sensair – an improved DOAS system. *Proceedings of Optical Sensing for Environmental and Process Monitoring*, McLean, Virginia, November 7-10, 1994;
15. **Schafer, K. *et al***. Emission Source Strengths of Gasoline Filling Processes Determined by Open-Path Spectroscopic Techniques and Inverse Modelling; *Proceeding EUROPTO Conference on Spectroscopic Atmospheric Environmental Monitoring Techniques*, Barcelona, Spain; SPIE Vol. 3493, pp 223-230
16. **Staehelin, J. *et al.*** Emission Factors from Road Traffic from a Tunnel Study (Gubrist Tunnel, Switzerland). Part II: Results of Organic Compounds, SO2, and Speciation of Organic Exhaust Emission; *Atmospheric Environment* **1998**, 32, 999-1009

POSTSCRIPT NOTE / DISCLAIMER

The results of this investigation **suggest** that the wastewater treatment plant studied is a **potentially** significant source of MAH in the Lausanne area. It must be underlined that the measurements here reported represent only a very short period of time at the end of summer 1999. Measured concentrations of MAH in ambient air and process streams **do not necessarily reflect the average operational conditions** of the wastewater treatment plant. It is indeed plausible to think that the measured concentrations in ambient air reflect near-upper limit values as expected from the higher vapor pressures in summer conditions. Moreover, the **maximum** volatilization rate, as calculated on the basis of SPME/GC/MS measurements in wastewater, does not take into account mass transfer limitations to the volatilization process. Actual volatilization rates can be several orders of magnitude lower than the maximum values calculated. **Further investigation is required** to properly quantify the VOC emissions from the wastewater treatment plan and its impact on air quality in the Lausanne air basin.

Chapter 7
Conclusions and perspectives

Two trace gas spectroscopic detection techniques were developed and applied in this research: UV-visible DOAS and mid-IR QCLAS. The first one uses a high-pressure Xe lamp as broadband light source. After absorption along atmospheric paths of some hundred meters, the transmitted beam is analyzed using a grating spectrometer. The light source in the second case is a pulsed, single mode, distributed feedback (DFB) quantum-cascade laser. The tunableness of the laser allows obtaining transmission spectra in the mid-IR using a single channel detector (MCT).

A commercial DOAS system (DOAS 2000, Thermo Electron Air Quality) was used in this research. DOAS 2000 was characterized and tested through a comprehensive set of laboratory and field measurements. Various operational aspects of the system, including thermal management and data processing, were improved in this research. Detection limits were estimated. Air quality data obtained in various field studies were analyzed and interpreted. Further interpretation of the field data was obtained through calculations with photochemical grid models.

Concerning QCLAS, a system was developed and demonstrated for the detection of ozone at ambient pressure. The new ozone detection system was calibrated using simultaneous, co-located DOAS measurements. This research demonstrates the applicability of the differential absorption method in the mid-IR, and shows the potential of quantum-cascade lasers for spectroscopic monitoring using long atmospheric paths.

Conclusions and recommendations for future work are given hereafter on particular aspects of this research.

Differential optical absorption spectroscopy (DOAS)

- The implementation of a vibration-free, Peltier-based thermal management system for DOAS 2000 allowed improving both the temperature control of the spectrometer and the stability of the optical alignment.
- Calculations based on dark noise measurements indicate that the lowest (ever reachable) detectable fractional absorption with DOAS 2000 would be $\sim 10^{-5}$ at a signal-to-noise ratio of 1 and for 1 min integration time.
- A test involving NO_2 absorption in laboratory conditions with an ambient-temperature operated photodiode array (PDA) showed a lower detectable fractional absorption of $8 \cdot 10^{-4}$ (1-sigma) for an integration time of just 3 s. The results and the quality of the spectra obtained with the PDA encourage the implementation of a Peltier-cooled PDA in DOAS 2000. Hamamatsu S5931-1024S built-in Peltier PDA would be a recommended choice for eventual implementation. The PDA should be accompanied with a mode mixer.
- Algorithms developed and implemented in MATLAB in this research should be incorporated in the DOAS 2000 software. Non-linear fitting is currently not available in the DOAS 2000 interpreter software. The routines developed in MATLAB could be in a quite straightforward way translated into C++.

- Theoretical analysis based on the Fourier transform shows that cross sections obtained at wavelength resolutions as low as ~0.2 nm can be "safely" convolved with the DOAS 2000 instrument function (~0.55 nm FWHM) as if they were "highly resolved" without introducing major errors in concentration retrieval.
- Lower detection limits (LDL) derived from analysis of subsequent lamp spectra provide a simple way of estimating the detection capabilities of a given DOAS system. Calculated LDL (3-sigma) from lamp spectra are in agreement with operational detection limits in the field (1-sigma).
- As expected, detection limits were found to decrease with the square root of the integration time, according to lamp spectra analysis, and with the square root of light intensity, according to long-term measurements during DICLA 1999.
- Based on the accumulated experience, it can be stated that the optimal absorption pathlength for DOAS 2000 in its current configuration is ~1 km.
- Intercalibration results show that DOAS 2000 measurements of ozone and nitrogen oxide are in very good agreement with OPSIS measurements. OPSIS is an EPA-approved DOAS system. Five months of intercomparison in Lausanne downtown corroborate the laboratory results, and suggest that part of the discrepancy between the two DOAS systems when operating over different path can be explained by inhomogeneous spatial distribution of pollutants. When sharing essentially identical paths, DOAS 2000 gives ozone concentrations that are ~7% smaller than values obtained by OPSIS, and NO_2 concentrations that are ~5% higher compared to OPSIS. These discrepancies are systematic and can be due to differences between the concentration retrieval algorithms.
- Measurements with the HONO generator show that is advantageous in terms of HONO yield and purity to use sulfuric acid as limiting reactant (continuously added) instead of sodium nitrite. For optimal operation of the generator, the liquid pool should be reduced to the minimum possible volume.
- The estimated detection limit of HONO with DOAS 2000 is ~0.2 ppm·m at a SNR of 2 and for a 30-min integration time

Quantum-cascade laser absorption spectroscopy (QCLAS)

- The differential method was found fully adapted for QCL absorption spectroscopy at ambient pressure. The differential absorption approach should in principle enable sensitive and selective measurements of e.g. ozone in open path conditions.
- Significant improvements in pulse acquisition and wavelength-sweeping rates are required before the QCL-based system can be used for open atmospheric measurements. A fairly large spectral range ($\geq$ 3 cm^{-1}) is in any case required for unambiguous identification of ozone in open-air conditions. It appears feasible to use non-controlled temperature steps for rapid wavelength scanning. Significant improvement in spectral resolution could be achieved using shorter QCL pulses (~20 ns). Noise reduction entails the use of a gated integrator.

- Point and path-integrated measurements of O_3 are usually in good agreement. This is mainly explained by the fact that ozone is a relatively long-lived secondary pollutant. Thus the practical interest in ozone as test compound for detection at ambient pressure with a QCL-based system was the availability of validated techniques for calibration in laboratory and field conditions. Nevertheless, QCL-based spectroscopic systems could be advantageously used for high-frequency (~1 Hz) airborne O_3 measurements using closed-path systems, and for open-path detection in conditions of high aerosol load.
- An interesting perspective for an open path application of the quantum-cascade laser is the detection of nitric acid (HNO_3). As discussed in **Chapter 2** and **Section 6.1**, this compound is of particular interest in the study of photochemical pollution. Nitric acid is in addition a very sensitive compound that can be thermally decomposed and gets easily adsorbed on various surfaces. This is thus a major obstacle for its spectroscopic detection in closed-path systems. Cross sections calculated from HITRAN data show a fairly strong rovibrational band of HNO_3 at 1325 cm^{-1} (7.55 μm). As shown in **Figure 7-1** this band is essentially free of interference from carbon dioxide and water vapor. Moreover, the calculations show that the HNO_3 cross section in this wavelength range is quite insensitive to pressure broadening. This band appear thus to be well suited for open path detection.

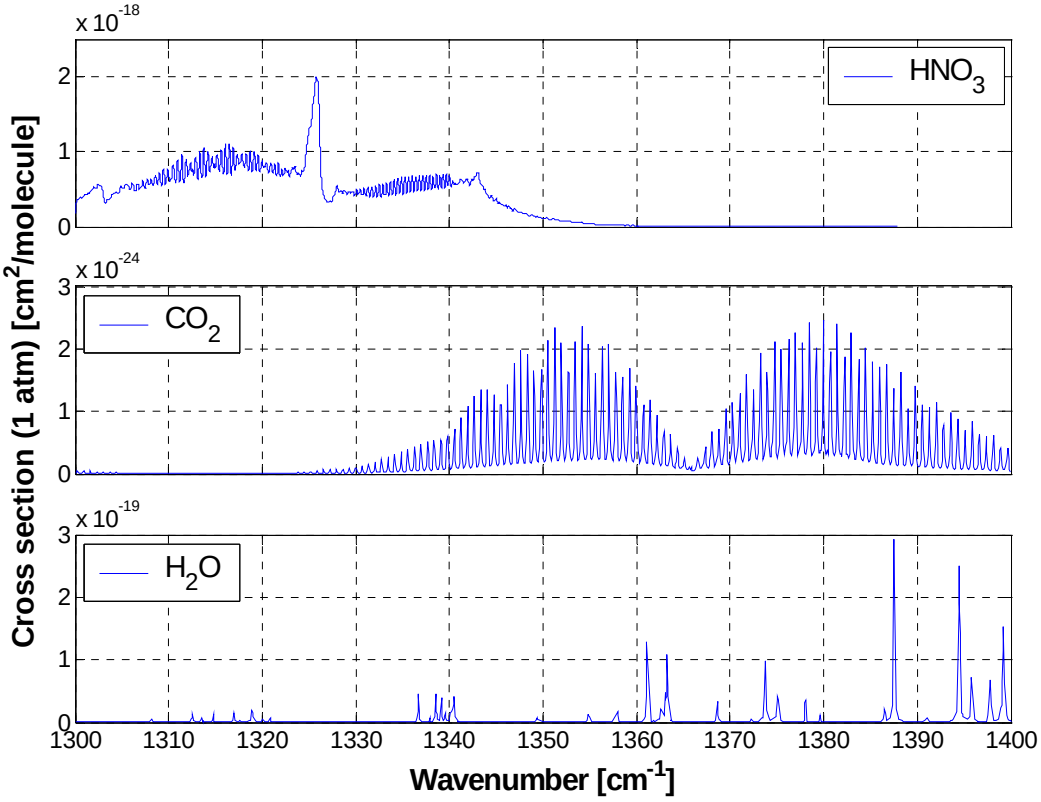

Figure 7-1. Cross section of nitric acid, carbon dioxide and water vapor at atmospheric pressure in the 1300-1400 cm^{-1} spectral region.

Formaldehyde dynamics and photochemical production in Grenoble

- Simultaneous DOAS measurements of CH_2O, O_3 and NO_2 (along with NO from a chemiluminiscence detector) allowed estimating the sources of formaldehyde at a suburban location of Grenoble. Measurements-derived emission and photochemical production rations are in good agreement with literature values, the emission inventory and model calculations. DOAS measurements served at validating the calculations with a photochemical grid, and to some extent, the emission inventory, particularly regarding CH_2O and NOx. This investigation demonstrates also that DOAS is a well-suited technique for model validation purposes.

MAH emission from a wastewater treatment plant

- Monocyclic aromatic hydrocarbons were successfully measured with DOAS within the perimeter of a wastewater/sludge incineration plant. Possible sources of fugitive emissions of VOC are the flue gas scrubbing system and volatilization from sludge.

Annex A
DOAS 2000 Environmental Enclosure
(including Peltier-based thermal management system)

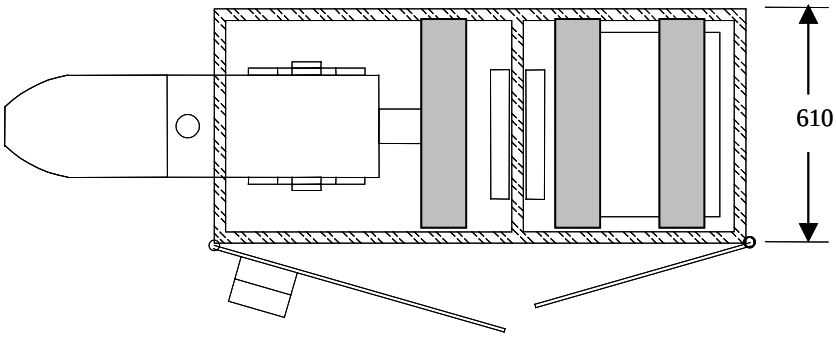

Top View

1. Coaxial telescope
2. Lamp power supply unit
3. Spectrometer
4. Peltier system
5. Fan

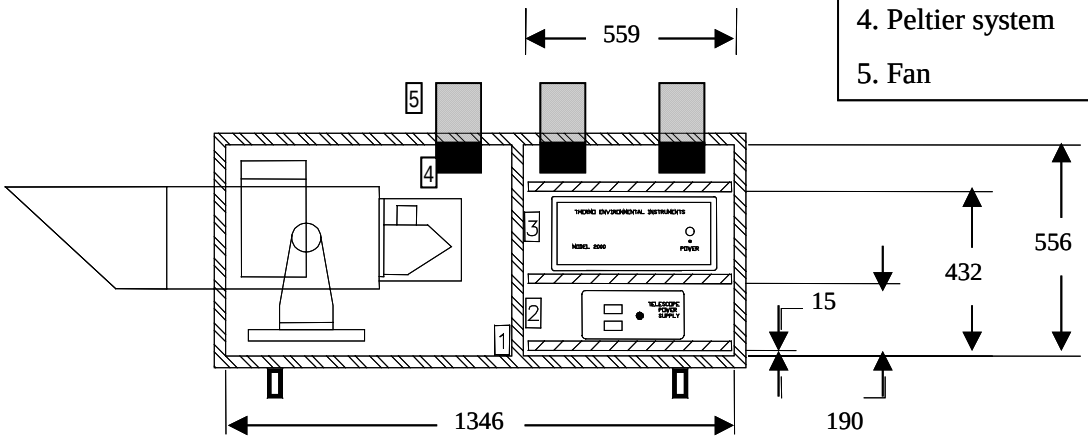

Side View

Annex B

HAMAMATSU

PHOTOMULTIPLIER TUBE
R2368
TRANSMISSION MODE PHOTOCATHODE

Good Spatial Uniformity, Wide Angle of Radiant Input
Multialkali Photocathode
For UV-Visible Spectrophotometers and General Applications

R2386 is a 28mm (1-1/8 Inch) diameter, side-on photomultiplier tube having a transmission mode multialkali photocathode. The transmission mode photocathode offers better spatial uniformity and wider angle of radiation input than conventional side-on tubes which have opaque photocathodes (reflection mode photocathode). Also, this type of photocathodes is independent of polarized light.
The R2368 has a 9-stage dynode which provides high gain and employs an HA Coating for noise reduction and an "Anti-hysteresis design".

Figure 1: Typical Spectral Response

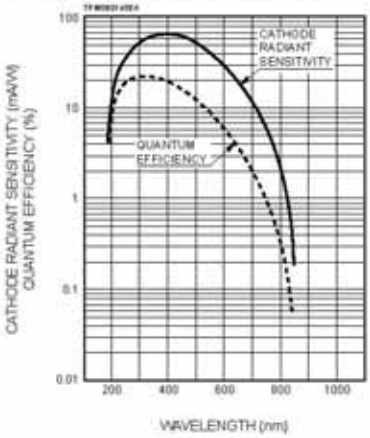

GENERAL

Parameter		Description/Value	Unit
Spectral Response		185 to 850	nm
Wavelength of Maximum Response		420	nm
Photocathode	Material	Multialkali	—
	Useful Area (Minimum)	16 × 18	mm
Window Material		UV glass	—
Dynode	Structure	Circular-cage	—
	Number of Stages	9	—
Base		JEDEC No. B11-88	—
Suitable Socket		E678-11A	—
Suitable Socket Assembly		E717-05	
Direct Interelectrode Capacitance	Anode to Last Dynode	1.2	pF
	Anode to All Other Electrodes	3.4	pF

MAXIMUM RATINGS (Absolute Maximum Values)

Parameter		Value	Unit
Supply Voltage	Anode and Cathode	1250	V
	Anode and Last Dynode	250	V
Average Anode Current (NOTE 1)		0.1	mA
Ambient Temperature		-80 to +50	°C

CHARACTERISTICS (at 25°C)

Parameter	Min.	Typ.	Max.	Unit
Anode Luminous Sensitivity (NOTE 2, 3)	50	200	—	A/lm
Cathode Luminous Sensitivity (NOTE 4)	80	150	—	μA/lm
Cathode Red/White Ratio (NOTE 5)	—	0.15	—	—
Gain (NOTE 2)	—	1.3×10^6	—	—
Anode Dark Current (NOTE 2)	—	5	50	nA
Anode Pulse Rise Time (NOTE 2, 6)	—	1.2	—	ns
Current Hysteresis (NOTE 7)	—	0.1	—	%
Voltage Hysteresis (NOTE 7)	—	1.0	—	%

PHOTOMULTIPLIER TUBE R2368

Figure 2: Typical Spatial Uniformity

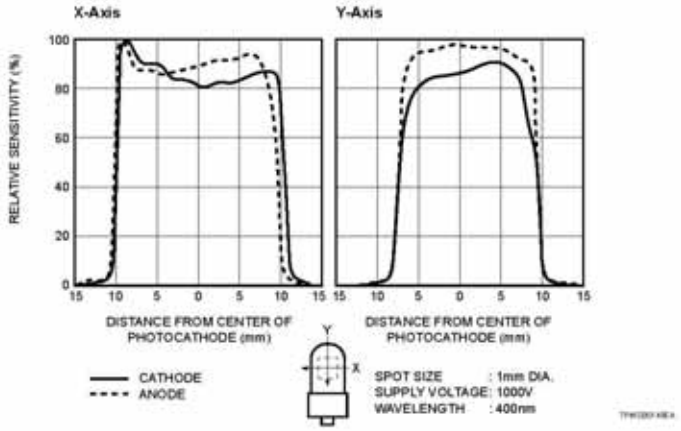

Figure 3: Dimensional Outline and Basing Diagram
(Unit: mm)

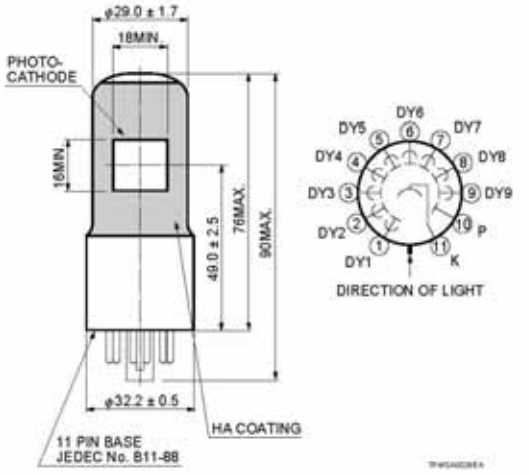

NOTES

1. Averaged over any interval of 30 seconds maximum.
2. Supply voltage of 1000 volts is applied between the cathode and the anode using the voltage distribution ratio shown below.

Electrodes	K	Dy1	Dy2	Dy3	Dy4	Dy5	Dy6	Dy7	Dy8	Dy9	P
Distribution Ratio	1	1	1	1	1	1	1	1	1	1	

K: Cathode, Dy: Dynode, P: Anode

3. The light source is a tungsten filament lamp operated at a distribution temperature of 2856K. The light input is 0.01 microlumen.
4. Under the same conditions as Note 3 except that the light input is 0.01 lumen and 100 volts are applied between the cathode and all other electrodes connected together as an anode.
5. The red/white ratio is the quotient of the cathode current measured using a red filter (Toshiba R-68) interposed between the light source and the tube by the cathode current measured with the filter removed under the same condition as Note 4.
6. The rise time is the time for the output pulse to rise from 10% to 90% of the peak amplitude when the entire photocathode is illuminated by a delta function light pulse.
7. Hysteresis is a temporary instability in anode current after light and voltage are applied.

Warning-Personal Safety Hazards
Electrical Shock — Operating voltage applied to this device presents shock hazard.

HAMAMATSU

HAMAMATSU PHOTONICS K.K., Electron Tube Center
314-5, Shimokanzo, Toyooka-village, Iwata-gun, Shizuoka-ken, 438-0193, Japan, Telephone: (81)539/62-5248, Fax: (81)539/62-2205
U.S.A.: Hamamatsu Corporation: 360 Foothill Road, P. O. Box 6910, Bridgewater, N.J. 08807-0910, U.S.A., Telephone: (1)908-231-0960, Fax: (1)908-231-1218
Germany: Hamamatsu Photonics Deutschland GmbH: Arzbergerstr. 10, D-82211 Herrsching am Ammersee, Germany, Telephone: (49)8152-375-0, Fax: (49)8152-2658
France: Hamamatsu Photonics France S.A.R.L.: 8, Rue du Saule Trapu, Parc du Moulin de Massy, 91882 Massy Cedex, France, Telephone: (33)1 69 53 71 00, Fax: (33)1 69 53 71 10
United Kingdom: Hamamatsu Photonics UK Limited: Lough Point, 2 Gladbeck Way, Windmill Hill, Enfield, Middlesex EN2 7JA, United Kingdom, Telephone: (44)181-367-3560, Fax: (44)181-367-6384
North Europe: Hamamatsu Photonics Norden AB: Färögatan 7, S-164-40 Kista Sweden, Telephone: (46)8-703-29-50, Fax: (46)8-750-58-95
Italy: Hamamatsu Photonics Italia S.R.L.: Via Della Moia, 1/E, 20020 Arese, (Milano), Italy, Telephone: (39)2-935 81 733, Fax: (39)2-935 81 741

TPMS1043E01
JUN. 1998

Annex C
DOAS 2000 Software User Interface
(example shows laboratory HONO spectra)

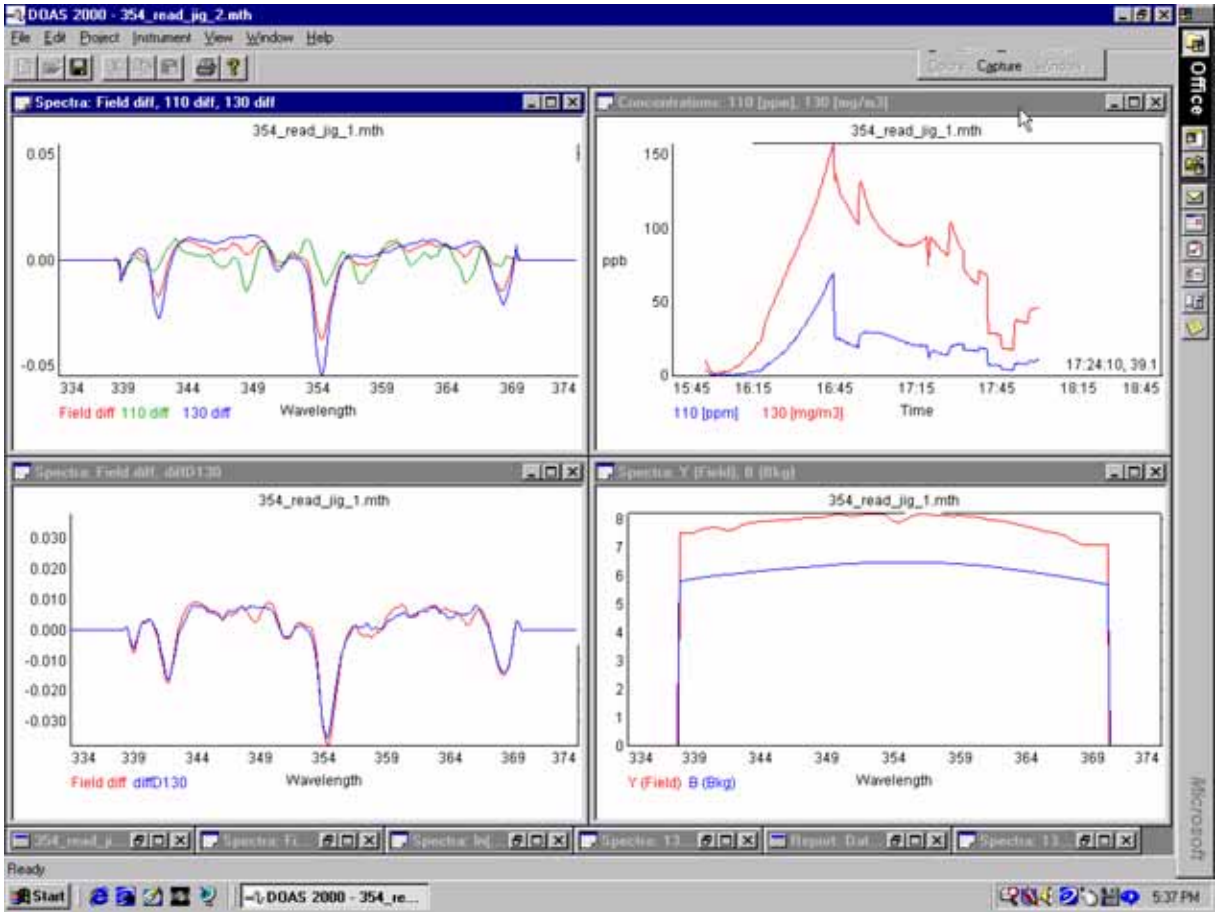

Annex D
Compendium of MATLAB-implemented Routines for Spectra Processing and other Purposes

Differential absorption spectroscopy

I / O	Basic operations	Peak fitting
findFile.m	wvlS.m	findPeakS.m
nameFieldS.m	cwvlS.m	fitPeakS.m
nextFile.m	inzS.m	GaussShape.m
readXS.m	ieffS.m	LorentzShape.m
read2wvlXS.m	inullshortS.m	Humlicek.m
readD2K.m	nullwvlS.m	SALShape.m
readD2Kdir.m	offsetS.m	VoigtShape.m
readSetD2K.m	scalarS.m	**LP/HP filter**
openParam.m	plusS.m	hpfS2.m
writeD2K.m	minusS.m	lpfS2.m
plotS.m	overS.m	diffS2.m
plotSyy.m	lnS.m	sgS2.m
plotXS.m	normS.m	**Convolution**
Format conversion	rmsS.m	convParamXS.m
XS2S.m	sshiftS2.m	convXS1.m
xy2S.m	sshiftS3.m	**Spectra fitting**
	HS2LDL.m	fitLS.m
	HS2rms.m	fit2NLS3.m
	statisticS.m	
	statisticS2NL.m	

Support

I / O	Various
balloon.m	nearest.m
readBC.m	outlier.m
readBCdir.m	recast.m
readIMI.m	wMLR.m
readIMIdir.m	lpftSeries.m
readOPSIS.m	pdf1D.m
readSOLUS.m	pdf2D.m
errorbarxy.m	rose2xy.m
plottSeries.m	xy2rose.m
Unit conversion	Psat.m
ncc2ratio.m	
ratio2ncc.m	
ncc2ugm3.m	
ugm32ratio.m	
txls2ml.m	

Dedicated

HITRAN
readHITRAN.m
HITRAN2XS.m
saveSigma.m
OMA
readOMA.m
readOMAdir.m
QCL
name2tStamp.m
openQCL.m
readQCL2.m
readQCLdir3.m
accum.m

Routines are available upon request to Rodrigo JIMENEZ (rodrigo.jimenez@epfl.ch), and will be soon made available at the EPFL/LPAS – LIDAR Group web site (http://lpas.epfl.ch/lidar).

B

[Y2, Y1, Y0] = **balloon**(name, rows, refAtm, z0, TCal, o3Cal);
Retrieves atmospheric profile data from an EPFL/LPAS tethered balloon data file; detects and filters out outliers, "recast" data (refer to recast.m), and converts data into standard units

C

XS2 = **convParamXS**(XS1, lineshape, P);
Convolves the XS-formatted wavelength/wavenumber-dependent variable XS1 using a wavelength/wavenumber-dependent parameter convolution lineshape

S2 = **convXS1**(XS1, H);
Convolves absorption cross section XS1 using center (strongest) transition line in spectrum H; assumes negligeable peak mixing

C = **cwvlS**(A, B);
C is the spectrum A centered at B.t.wvlc and with wavelength metrics of B as defined by B.t.ic, B.t.a; the wavelength range of C is the largest possible within the range of B; C.t.inull is A.t.inull translated into the wavelength metrics of B

D

[dS, F, nF, p] = **diffS2**(S, nF);
Calculates and subtracts a section-wise fitting polynomial HP-filter (F) from spectrum S(dS = S - F); nF can be whether entered or algorithm-calculated (refer to hpfS2.m for further details)

E

errorbarxy(X, Y, eX, eY);
Creates a XY graph displaying error bars in both coordinate axes, abscissa and ordinate;
X and Y have to be nx1 column vectors, with n = number of data points; eX and eY can be as well nx1 column vectors or nx2 matrices containing [lower upper] error bar data

F

name = **findFile**;
Retrieves a file full name using a directory dialog box

[L, wvlP, FWHM, bBL, S] = **findPeakS**(S0, minSn);
Locates peaks (broaden transition lines/bands) in the spectrum S0

[g, bBL, S, Shat] = **fitPeakS**(S0, lineshape, minSn);
Fits an user-defined lineshape to a spectrum with multiple (broaden) transition lines/bands using non-linear least squares

G

F = **GaussShape**(wvl, wvlP, sigma);

H

XS = **HITRAN2XS**(name, y, P, T);
Line-per-line calculates a molecular species absorption cross section at a given mixing ratio, pressure and temperature using the line transition data in a HITRAN file

[F, nF, p] = **hpfS2**(S, nF);
Calculates a section-wise fitting polynomial HP-filter (F) for spectrum S; an individual polynomial is fitted to each section of the spectrum as defined by the exclusion ranges (refer to nullwvls.m for further details); the degree of the section polynomials can be whether set or automatically calculated according to fitting criteria (lowest degree = 2, minimum coerrelation coefficient = 60%); F inheritates the properties of S

rms, rmsacc, rmsppmm, ppmm, ppmmacc, beppmmacc] = **HS2LDL**(HS, Smean, nF, XSH, ppmm0);
Estimates the lower detection limit (LDL) of a trace gas within a wavelength range using its (convolved) cross section and based on the residual transmittance of sequentially measured light source (lamp) spectra

[rmsD, rmsdD, rmsDacc, rmsdDacc, rmspD, rmspdD, rmspDacc, rmspdDacc] = **HS2rms**(HS, Smean, nP, nF);
Calculates the root-mean-square of the absolute and differential "transmittance" residual (relative noise) of sequentially accumulated spectra referred to the arithmetic mean value calculated with and without polynomial correction

W = **Humlicek**(X, y);
Computes the complex probablity function W(Z) = exp(-Z^2)*erfc(-iZ), with Z = X + iy; the real part of W is identical to the Voigt function K(X,y) = Re(W)

I

ieff = **ieffS**(S);
Determines the effective-for-evaluation data point index vector (ieff) of spectrum S based on the exclusion ranges in S.t.inull; see also inzS.m, nullwvlS.m

S2 = **inullshortS**(S1);
Determines the more compact set expression for the exclusion data points in S1 (S1.t.inull)

S2 = **inzS**(S1);
Determines in S1 and describes in S2.t.inull the zero data point range ("zero mask"); possible zeros within the spectrum "zero mask" range are not taken into account

L

S2 = **lnS**(S1);
Takes the natural logarithm of spectrum S1; the logarithm of zero or negative values is reported as zero

F = **LorentzShape**(wvl, wvlP, alphaL);

S2 = **lpfS2**(S1, f, p);
Applies a Savitzky-Golay (SG) low-pass (LP) filter to spectrum S1

[y, sdy] = **lpftSeries**(t, x, sdx, hwhm);
Applies a Gaussian LP-filter (LPF) to a time series

M

S3 = **minusS**(S1, S2);
Subtracts spectrum S2 from spectrum S1 (S3 = S1 - S2);
S3 t(ag) parameters are determined by pre-defined inheritance rules

tStamp = **name2tStamp**(name, year);
Convert a LabView acquired/formated QCL spectra (temperature-modulated) file name into a numeric time stamp (ML format)
Expected formats:
name: MM_dd_hh_mm
year: yyyy / yy

[path, date, root, index, ext, language] = **nameFieldS**(name);
Retrieves identification fields in a DOAS 2000 spectrum file full name

N

y = **ncc2ratio**(ncc, P, T);
Converts gas-phase concentrations at given pressure(s) and temperature(s) into mixing ratios assuming perfect gas behavior

ugm3 = **ncc2ugm3**(ncc, MW);
Converts a species gas-phase concentrations in molecules/cm3 into ug/m3

ix = **nearest**(y, x, SC);
Looks up x for its values the nearest to y, i.e. those that minimize the residual norm Qj = [y(j)-x(ix(j))]^2 and fulfill the lower- or higher-than-y searching criterium

name2 = **nextFile**(name1);
Finds next existing spectrum file with the same root

[Sn, bSn] = **normS**(S);
Calculates the norm and normalizes the spectrum S (Sn = S / bSn)

S2 = **nullwvlS**(S1, wvlnull);
Adds exclusion data points, corresponding to the wvl/wvn ranges in wvlnull, to spectrum S1; returns input spectrum if wvlnull is not valid

O

S2 = **offsetS**(S1, offset);
Offsets spectrum S1; considers only its effective-for-evaluation data points (refer to ieffS.m for details)

P = **openParam**(fileName);
Retrieves data from a DOAS 2000 "Param" file

[deltaI, E, B, tStamp, tdata, FWHM] = **openQCL**(fileName); Calculates QCL shot properties from time-resolved intensity data Discards header data other than time stamp

[Ymean, Ydev, Y] = **outlier**(X);
Detects and removes outliers based on the Anscombe method; treats X columnwise, i.e. each column is regarded as an independent data set

S3 = **overS**(S1, S2);
Divides element-by-element the spectrum S1 over the spectrum S2 (S3 = S1 / S2); S3 t(ag) parameters are determined by pre-defined inheritance rules, e.g. retains the time stamp of S2, assumed to be the transmission spectrum -> D = ln(I0/I) = lnS(overS(I0, I)) -> D.t.tStamp = I.t.tStamp

P

[XBin, FBin] = **pdf1D**(X);

[XBin, YBin, FBin] = **pdf2D**(X, Y);

plotS(S1, S2, S3, S4, S5, S6, S7, S8, S9);
Displays multiple spectra

plotSyy(S1, S2);
Displays 2 spectra with ordinates in the left (S1) and the right (S2) axes

plottSeries(t, X);
Displays a multiple variable time series

plotXS(XS1, XS2, XS3, XS4, XS5, XS6, XS7, XS8, XS9);
Displays multiple cross sections

S3 = **plusS**(S1, S2);
Adds spectrum S2 to S1 (S3 = S1 + S2); S3 t(ag) parameters are determined by pre-defined inheritance rules

Pj = **Psat**(T, namej);
Calculates a species (pure component) vapor pressure at temperature T

R

ncc = **ratio2ncc**(y, P, T);
Converts gas-phase mixing ratios at given pressure(s) and temperature(s) into concentrations assuming perfect gas behavior

XS = **read2wv**lXS(name);
Retrieves absorption cross section (XS) data from a tab/space delimited ASCII file; header data is discarded; expected header/comment line initial characters: '%' = char(37), '*' = char(42), '/' = char(47), ';' = char(59)

[tBC, BC, S, R, ATN, Q] = **readBC**(name);
Retrieves black carbon (soot) concentration time series (and the optical attenuation raw data) from an BC######.DAT formatted file

[tBC, BC, S, R, ATN, Q] = **readBCdir**(directory);
Retrieves, stacks and "re-casts" sequential black carbon (soot) concentration time series (and the optical attenuation raw data) from BC######.DAT formatted files included in a data directory

S = **readD2K**(name);
Retrieves the spectral data contained in a DOAS 2000-formatted file (.spc, .ref)

HS = **readD2Kdir**(directory);

[MI, H1, H2] = **readHITRAN**(name);
Retrieves spectroscopic data from a .csp-formatted HITRAN output file

[data, tdata, param] = **readIMI**(name);
Retrieves meteorological/point monitor pollutant concentration time series from an "IMMI3 DATACOLL" .IMI formatted file

[data, tdata, param] = **readIMIdir**(directory);
Retrieves, stacks and "re-casts" sequential meteorological/point monitor pollutant concentration time series from "IMMI3 DATACOLL" .IMI formatted files included in a data directory

S = **readOMA**(name);
Reads Hamamatsu NMOS linear image sensor (S3903-1024Q,F - head C4350) data (header + spectrum) as formated by SA1400 s/w

HS = **readOMAdir**(directory);

OPS = **readOPSIS**(name);
Retrieves pollutant concentration time series from an OPSIS .OPS formatted file

data = **readQCL2**(name);
Retrieves data from a LabView acquired/formated QCL (temperature-modulated) spectrum file

[T, UT, DT, TMU, TMD, U, D, tU, tD] = **readQCLdir3**(directory, year, T0, dT);
Retrieves and stacks sequential, LabView acquired/formated (temperature-modulated) QCL spectra files included in a data directory

HS = **readSetD2K**(name0, nS);
Retrieves and stacks sequential DOAS 2000-formatted spectra

[tdata, data] = **readSOLUS**(name);
Retrieves various measured parameter time series from a SOLUS-formatted data file

XS = **readXS**(name);
Retrieves absorption cross section (XS) data from a tab/space delimited ASCII file; header data is discarded; expected header/comment line initial characters: '%' = char(37), '*' = char(42), '/' = char(47), ';' = char(59)

Y = **recast**(X, jX, flag);
Sorts and averages (columnwise) repeated abcissa matrix values

rms = **rmsS**(S);
Calculates the root-mean-square of spectrum S; considers only its effective-for- evaluation data points (refer to ieffS.m for details)

[ux, uy] = **rose2xy**(u, theta, theta0);

S

F = **SALShape**(wvl, wvlP, alphaL, k1);

saveSigma(fileName, P, T, yj, wvn_range, sigma);
Save calculated cross section in a designated .csv file

S = **scalarS**(HS, bHS);
Linearly combines spectra in HS using the linear combination coefficients bHS; (S = HS*bHS = HS(1)*bHS(1) + ... HS(j)*bHS(j) + ...); spectra in HS is assumed to have a common, identical wvl/wvn range; simply co-adds HS if bHS is not entered

F = **sgS2**(S, f, p);
Applies a Savitzky-Golay (SG) low-pass (LP) filter to spectrum S1

B = **sshiftS2**(A, dwvl, m);
Transforms spectrum A into B by performing shifting followed by (1st order) stretching (2 non-linear parameters)

B = **sshiftS3**(A, dwvl, m, wvl0);
Transforms spectrum A into B by performing stretching (1st order) followed by shifting (3 non-linear parameters)

[Smean, Sdev] = **statisticS**(HS, typeMean, typeDev);
Calculates the mean and deviation spectra of an spectra set

[Smean, Sdev, dwvl, m, r2, HS] = **statisticS2NL**(HS0, typeMean, typeDev, nF);
Calculates the mean and deviation spectra of an spectra set after non-linear adjustment of the spectra to the sequential, accumulated spectrum

T

tML = **txls2ml**(tXLS);
Numeric time format: EXCEL -> MATLAB

U

y = **ugm32ratio**(ugm3, MW, P, T);
Converts a species gas-phase concentrations in ug/m3 at (a) given pressure(s) and temperature(s) into mixing ratios assuming perfect gas behavior

V

F = **VoigtShape**(wvl, wvlP, alphaD, alphaL);
Calculates multiple Voigt lineshapes within a wavelength/wavenumber range using Humlicek's approximation for K(X,y) (refer to Humlicek.m for details)

W

[b, SDb, r2, dy, q] = **wMLR**(y, X, w);
Determines the best fitting coefficients (bj, j=1:M) to the linear model y = X*b by weighted least squares multiple linear regression

writeD2K(S, name);
Writes the spectral data contained in an S-formatted spectrum to a DOAS 2000-formatted file

wvl = **wvlS**(S);
Retrieves the wavelength vector (wvl) of spectrum S

X

SX = **XS2S**(XS, S, method);
Tranforms the absorption cross section data structure XS into the spectrum data structure SX; SX inheritates the center wavelength/wavenumber and dispersion parameters of S, thus its wavelength/wavenumber range; SX is calculated by interpolation of XS within the wavelength/wavenumber range intersection of XS and S

[u, theta] = **xy2rose**(ux, uy, theta0);

Sxy = **xy2S**(x, y);
Tranforms the coordinated data pair vectors (x,y) into the S-formatted data structure Sxy;

Annex E
Calibration Cells and Holders

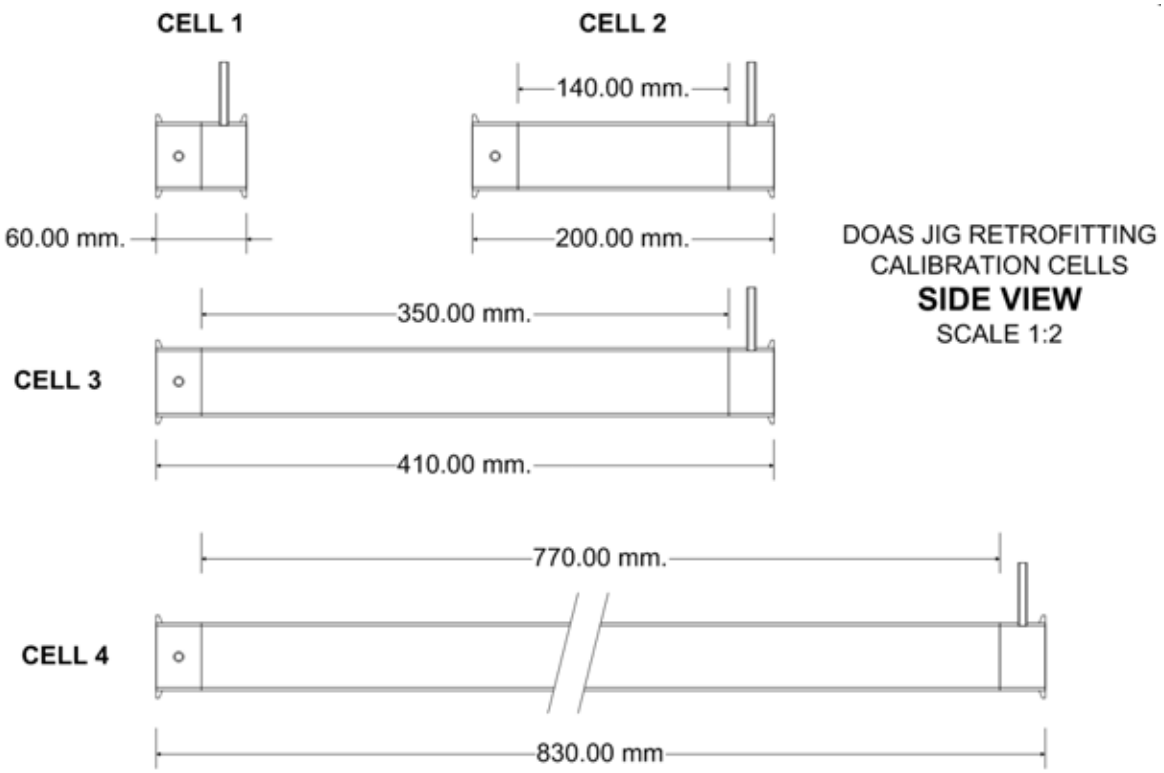

DOAS JIG RETROFITTING
CALIBRATION CELLS
SIDE VIEW
SCALE 1:2

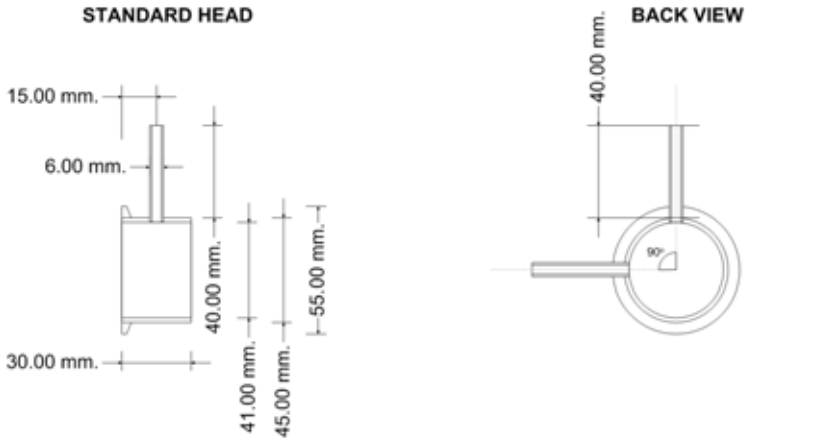

DOAS JIG RETROFITTING
CALIBRATION CELLS
STANDARD HEAD & BACK VIEW
SCALE 1:1

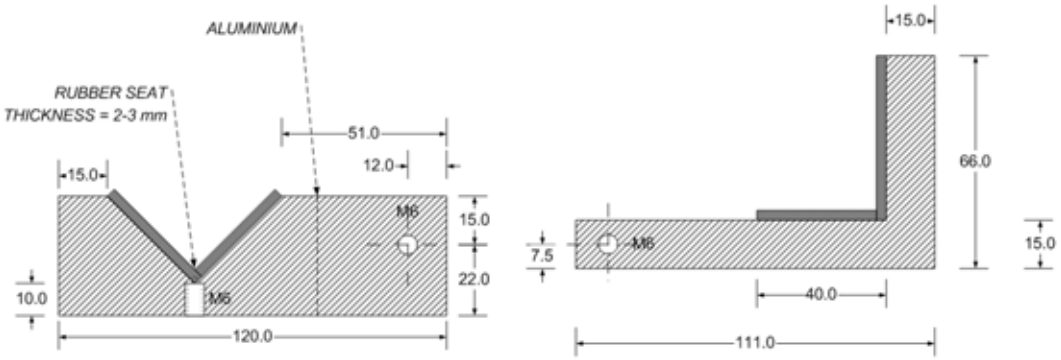

SIDE VIEW

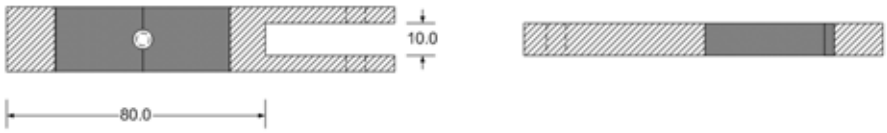

TOP VIEW

DOAS JIG
RETROFITTING
CELL HOLDER
SCALE 1:1

Annex F
Peristaltic Pump Calibration Curve

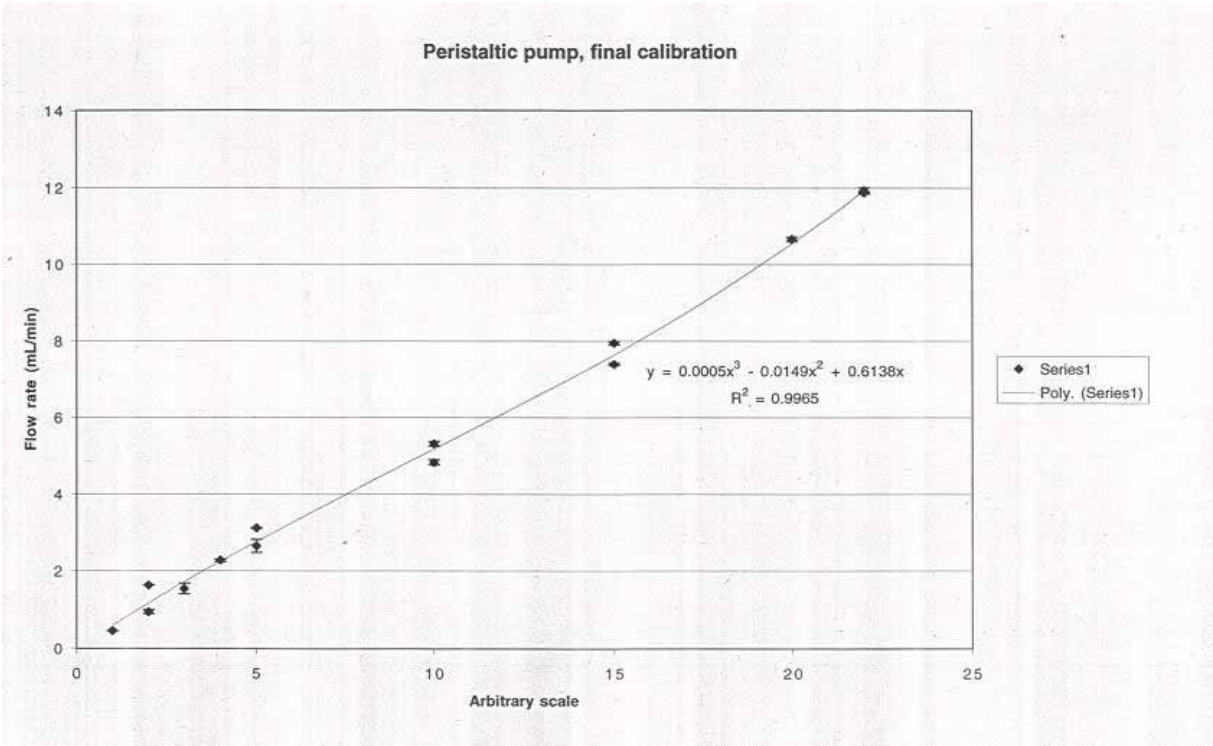

Annex G
Development of a Monocyclic Aromatic Hydrocarbon (MAH) Diluted Gas Mixture Generator

VOC Generator

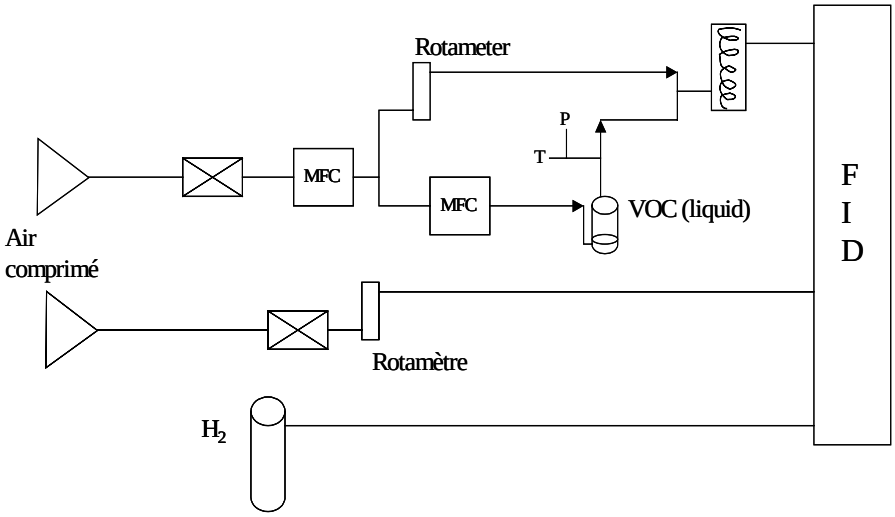

Summary of results

DATES	HC	2σ [ppmC]	C_{mean} [ppmC]	*C_{sat} [ppmC] à 0[°C]	σ/C_{mean}
24.08	p-xylène	4.3	14.4	~ 19	15 %
27.08	toluène	0.7	61.1	~ 65	0.6 %
28.08	toluène	0.98	61.5	~ 66	0.8 %
03.09	toluène	0.7	61.6	~ 63	0.6 %
04.09	toluène	0.9	61	~ 64	0.7 %

*Csat = (Psat/P)*DR

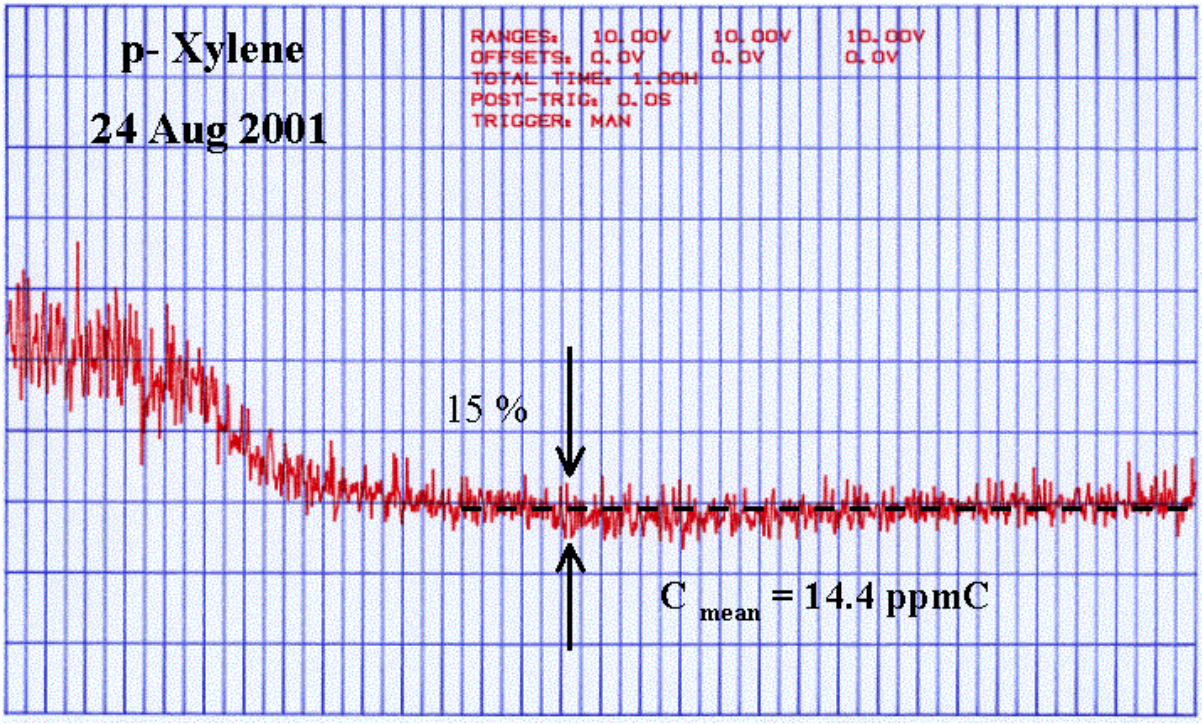
p- Xylene
24 Aug 2001
RANGES: 10.00V 10.00V 10.00V
OFFSETS: 0.0V 0.0V 0.0V
TOTAL TIME: 1.00H
POST-TRIG: 0.0S
TRIGGER: MAN
15 %
C mean = 14.4 ppmC

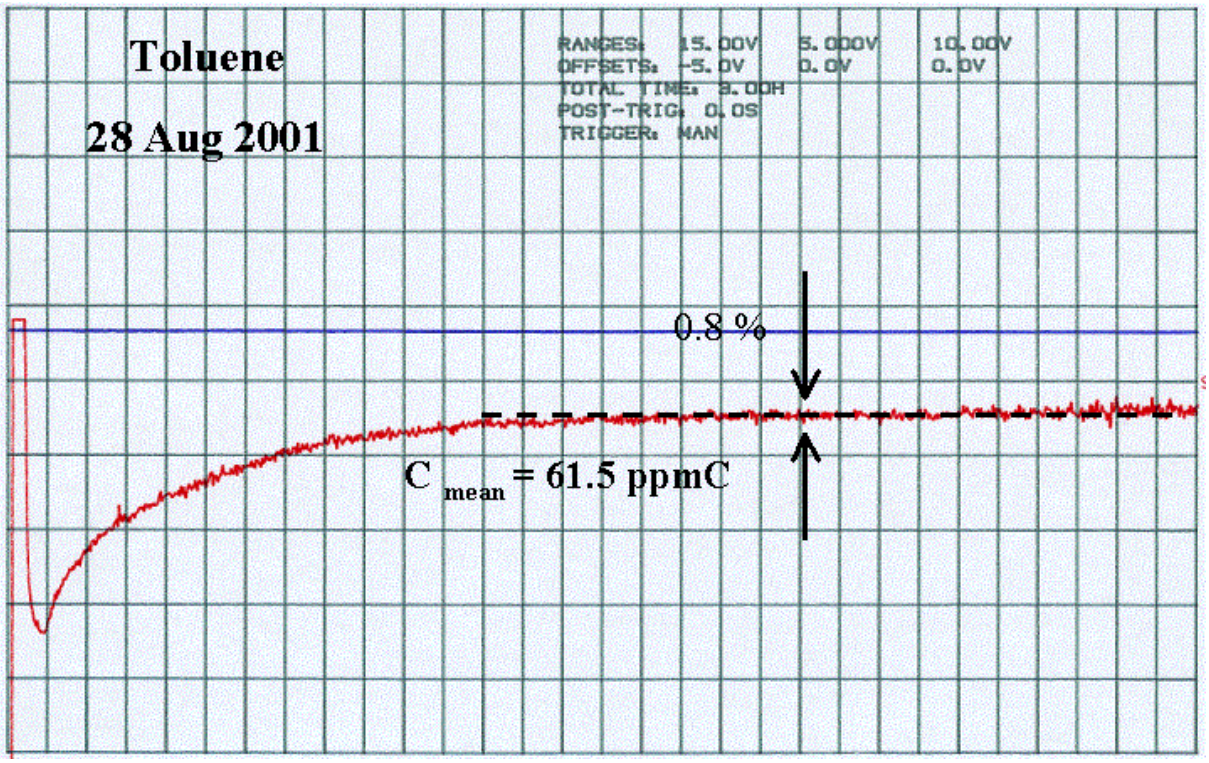
Toluene
28 Aug 2001
RANGES: 15.00V 5.000V 10.00V
OFFSETS: -5.0V 0.0V 0.0V
TOTAL TIME: 8.00H
POST-TRIG: 0.0S
TRIGGER: MAN
0.8 %
C mean = 61.5 ppmC

Annex H
Measurement of Formaldehyde (HCHO) by DOAS: Intercomparison to DNPH Measurements and Interpretation from Eulerian Model Calculations

Rodrigo Jiménez, Alberto Martilli, Ioan Balin, Hubert van den Bergh and Bertrand Calpini
Air Pollution Laboratory (LPAS), Swiss Federal Institute of Technology (EPFL)
CH-1015 Lausanne, Switzerland; rodrigo.jimenez@epfl.ch

Bo R. Larsen
Environment Institute (EI), European Commission Joint Research Center (JRC)
I-21020 Ispra, Italy

Giordano Favaro
Institute of Environmental Protection and Agriculture (IUL); CH-3003 Bern, Switzerland

Dieter Kita
Thermo Environmental Instruments Inc.; Franklin, MA 02038, USA

ABSTRACT

Formaldehyde (HCHO) is a primary and secondary air pollutant. As an intermediate product of hydrocarbon photo-oxidation, it contributes to the formation of photochemical pollution in urban areas. In addition, chronic or acute exposure to HCHO (an anticipated carcinogen) constitutes an important health hazard. Differential optical absorption spectroscopy (DOAS) is one of the best-suited techniques for monitoring formaldehyde. Within the frame of a European Union project, a field measurement campaign (PIPAPO) was carried out from May to June 1998 in the Milan area. During PIPAPO, a large number of air pollutants, including formaldehyde, were monitored at several sites from Milan to the Swiss Alps foothills. Located at Seregno (25 Km north of Milan downtown), EPFL carried out formaldehyde measurements by DOAS and performed intercomparison DNPH samples, which were analyzed at JRC. Despite having different spatial and time resolution, DOAS and DNPH measurements of formaldehyde compare fairly well. The formaldehyde concentration time series retrieved from DOAS were analyzed with respect to the meteorological conditions, particularly regarding heterogeneous removal processes, and the concentration of other air pollutants associated with formaldehyde emission and production. Pollutant dynamics calculations, made with a 3D photochemical grid (Eulerian) model over a wide spatial domain, were compared to the measurements, and provided a basis for the interpretation of the formaldehyde measurements performed during one of PIPAPO's intensive observation periods (IOP).

Keywords: photochemical air pollution, ambient air monitoring, formaldehyde (HCHO), carbon monoxide (CO), ozone (O_3), differential optical absorption spectroscopy (DOAS), DNPH (2,4-dinitrophenylhydrazine) method, photochemical grid model

INTRODUCTION

Formaldehyde (HCHO) is a ubiquitous component of both polluted and clean atmospheres. While its concentration in remote continental locations is typically some hundreds ppt, it can peak more than 100 ppb during severe summer smog episodes at highly polluted urban areas [1].

Roughly speaking, formaldehyde is an unavoidable by-product of hydrocarbon oxidation, whether hydrocarbons are combusted at high-temperature or photochemically oxidized after their release to the atmosphere. Although some industrial and commercial activities release "primary" formaldehyde to the atmosphere, combustion, particularly at mobile sources, is most frequently the main source of "primary" formaldehyde in urban areas. If this is the dominant source, a significant correlation is to be found between the ambient concentration of formaldehyde and other combustion by-products, such as carbon monoxide and NO_X [2-3]. On the other hand, formaldehyde is produced in the atmosphere as an intermediary product of hydrocarbon photo-oxidation. In this case, a correlation must exist to other photochemical pollutants, particularly ozone [3].

Since formaldehyde is a very reactive species and plays an important role in atmospheric chemistry, HCHO measurements are very valuable not just for the initialization but for the validation of atmospheric models, which are normally checked against NO_X and ozone measurements only. In addition, formaldehyde is an air toxic classified as anticipated carcinogen, thus its measurement is important as well from the public health point of view.

Photochemical grid (Eulerian) models are used to determine optimum emission abatement strategies for pollution control. Since formaldehyde is an intermediary compound in the hydrocarbon photo-oxidation, the ability of an atmospheric chemistry model to predict formaldehyde is a good measure of its validity. A close agreement between predicted and measured HCHO concentrations is thus a good indicator of the performance of photochemical grid models.

In this paper we present and compare formaldehyde measurements obtained in spring 1998 in the Milan area by two different techniques, a long-path UV visible absorption spectroscopic system (DOAS) and a sampling technique (DNPH). The DOAS formaldehyde database is subsequently analyzed by statistical means taking into account meteorological conditions and other pollutants measured at the same site. Finally, we present a comparison with concentrations predicted by a photochemical grid model.

INTERCOMPARISON OF FORMALDEHYDE MEASUREMENTS AT SEREGNO (MILAN)

The PIPAPO Field Experiment

The transport of ozone from the Po Valley (Northern Italy) to the Swiss Alps foothills was selected as first case study for LOOP (Limitation of Oxidant Production), an European Union (EUROTRAC-II) research project aimed at understanding the ozone production sensitivity on precursor emissions [4-5]. For this purpose, a field experiment, PIPAPO, was carried out during May-June 1998. PIPAPO involved the participation of some 20 research groups that deployed diverse monitoring apparatuses along a path devised to track Milan's photochemical pollutant plume. During the campaign period, EPFL operated at Seregno, a suburb at 20 Km north of Milan downtown, a set of point monitors (criteria pollutants), a DOAS system, a wind profiler and a ozone DIAL (Differential Absorption LIDAR) system [6] (see Figure 1).

Figure 1. Topography of the Lombardy region (Milan area) and surroundings (Swiss Alps foothills at the North) and sites of measurement during the PIPAPO experiment.

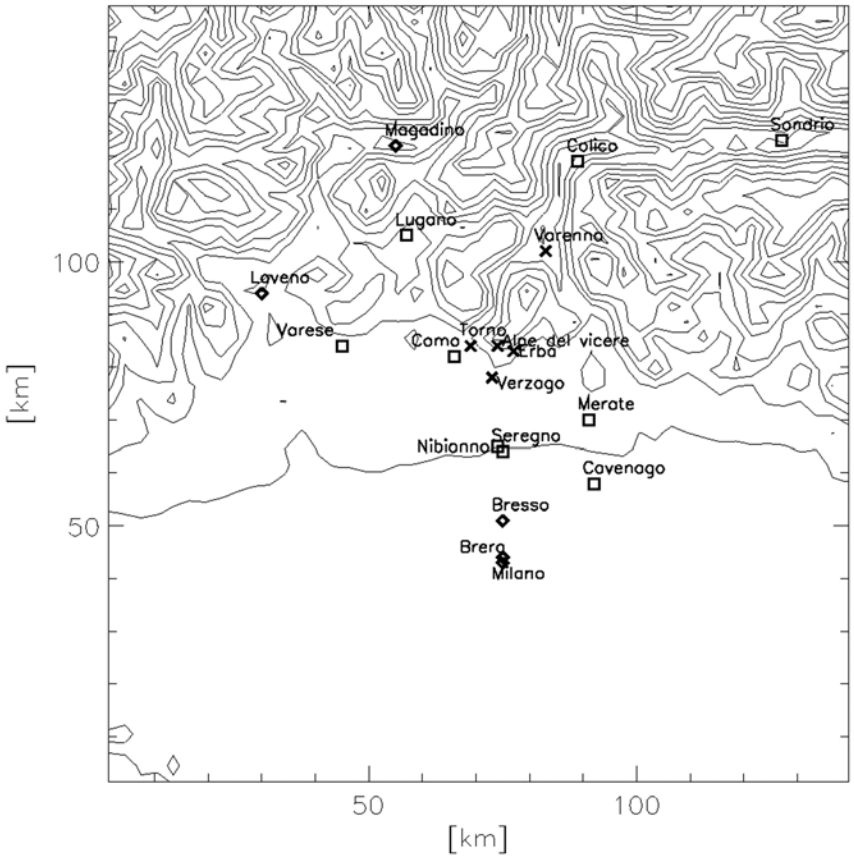

Formaldehyde Measurement Techniques at Seregno

A technical description of the differential optical absorption spectroscopy (DOAS) system installed at Seregno (DOAS 2000®, Thermo Environmental Instruments Inc.) can be found elsewhere [7-9]. The DOAS technique is described in details elsewhere too [10].

DOAS at Seregno measured ozone, BTEX (benzene, toluene, ethylbenzene and xylenes), sulfur dioxide, formaldehyde, nitrogen dioxide and nitrate radical. The system was operated continuously from May 11 to June 10, 1998. Due to the specific site (a technical high school) configuration, the total optical path (425.2 m) was a bit limiting for the monitoring of formaldehyde and some BTEX at their lowest concentrations. This limitation is due to the comparatively smaller contributions of these compounds to light absorption when compared to those of criteria pollutants (ozone, sulfur dioxide and nitrogen dioxide). For retrieving concentrations, open-air spectra were recorded at five different wavelength ranges from 240 to 680 nm. Each open-air spectrum was integrated for 2 minutes, summing up for a measuring cycle (grating cycle) of 10 minutes. Thus, the resulting formaldehyde concentration database, retrieved from open-air spectra at 329-361 nm, has a time resolution of 10 minutes. The quality of the recorded spectra was controlled during the post-processing step. Two spectra rejecting criteria were applied: the first one is based on a previously determined absolute intensity threshold, and the second one on a comparative analysis of differential residual spectra. More details can be found in the PIPAPO formaldehyde measurement quality control and assessment (QC/QA) report [11].

Figure 2. Formaldehyde concentrations time series as measured by DOAS and DNPH at Seregno during the PIPAPO experiment. The solar radiation is included as an indicator of the weather conditions.

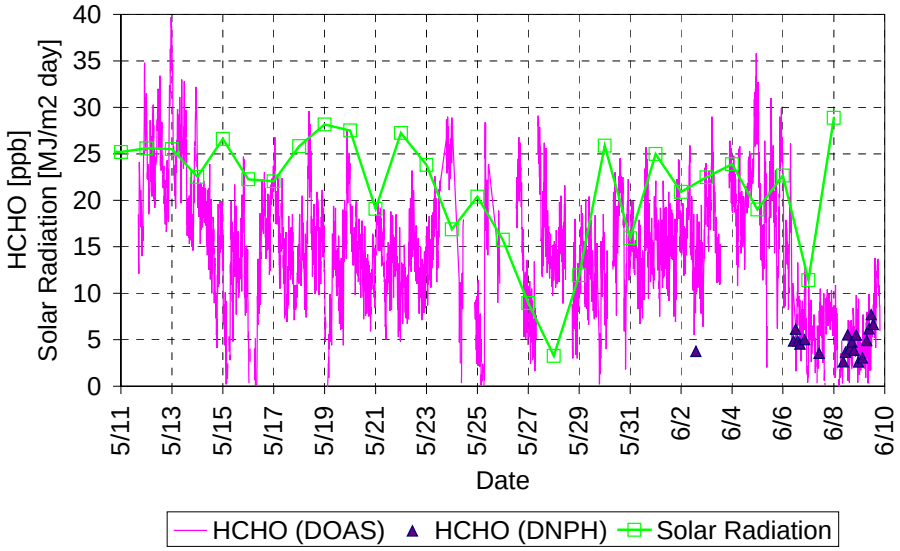

Formaldehyde was measured as well by the DNPH (2,4-dinitrophenylhydrazine) method for quality control and assurance of the DOAS measurements. The DNPH-coated silica gel cartridges (Waters DNPH-Silica Sep-Pak®, Millipore Corp.) and a calibrated, programmable sampling pump were provided by the European Commission Joint Research Center (JRC - Ispra, Italy). The cartridges were analyzed at JRC using the standard HPLC method. Twenty DNPH samples (91-235 min at 1 L/min) were taken during the period June 2-9, 1998. In order to avoid the interference of ozone on this method [12] a homemade ozone scrubber was placed before the cartridges. This potassium iodine (KI) ozone scrubber was tested on site, being its ozone removal efficiency higher than 99% at ozone concentrations above 100 ppb. DNPH samples were taken far from any physical obstacle at 4.6 m above the ground level, same elevation of DOAS. In addition, 2 fresh DNPH cartridges (1 per lot) were kept for background (blank) concentration determination. All DNPH cartridges were protected from sunlight and stored in a refrigerator. The cartridges were eluted and analyzed by HPLC shortly after sampling (within 2 weeks). The analysis method used is the European standard method according to the EMEP (Cooperative program for Monitoring and Evaluation of Long-range Transmission of Air Pollutants in Europe) guidelines. The QC/QA procedures include frequent inter-laboratory comparison exercises. More details can be found in the QC/QC report [11].

Intercomparison Analysis and Discussion

Figure 2 shows the formaldehyde concentration time series as measured by DOAS and DNPH at Seregno during PIPAPO. Solar radiation is included in the plot as well. Its relation to formaldehyde is addressed below. It is observed that during the short intercomparison period (June 2-9, 1998), the two concentrations time series followed very similar trends. This time trend similarity is observed over a relatively low concentration span: 10 ppb compared to 40 ppb over the whole campaign period.

In order to make comparable concentrations obtained at different time resolutions, the 10-minute DOAS values were grouped and averaged to match the DNPH sampling periods. This last one was typically 2 hours, thus each DOAS arithmetic mean containing about 12 individual measurements (see Figure 3). The resulting correlation between DOAS and DNPH measurements of formaldehyde is expressed as follows:

Equation 1. Correlation (linear regression) between formaldehyde measurements by DOAS and DNPH (June 2-9, 1998). Concentrations are in ppb and correlation coefficients are reported with 1 standard deviation.

$$\mathrm{HCHO(DOAS)} = 0.78(\pm 0.54)\cdot \mathrm{HCHO(DNPH)} + 1.96(\pm 2.61)$$

Statistically speaking, the measurements are poorly correlated (r = 0.32). In the case DNPH measurements were accepted as correct, DOAS measurements would be considered as underestimating the concentration of formaldehyde. But beyond the purely statistical description, the following observations must be made:

- DOAS measurements correlate better to DNPH measurements above 4 ppb. The estimated DOAS lower detection limit (LDL) for formaldehyde at the setup conditions of Seregno is 3.75 ppb. This value is 50% lower than the LDL (rms - root mean square) calculated from intrinsic noise measurements. This confirms Stutz's statement [13] on the ability of the DOAS technique to measure concentrations below the concentration equivalent to 1 standard deviation of the differential (absorption) noise.
- From the 6th June, the integration time for open-air spectra for formaldehyde retrieval was doubled, from 2 to 4 min. This change is very likely linked to the fact that the highest discrepancy is seen at the fist sample, averaged from 2-min data.
- Correlation gets better from the sample No. 10. Further investigation is required to determine whether the signal stability underwent any variation from that date.

Figure 3. Formaldehyde measurements by DOAS and DNPH at Seregno during the intercomparison period (June 2-9, 1998).

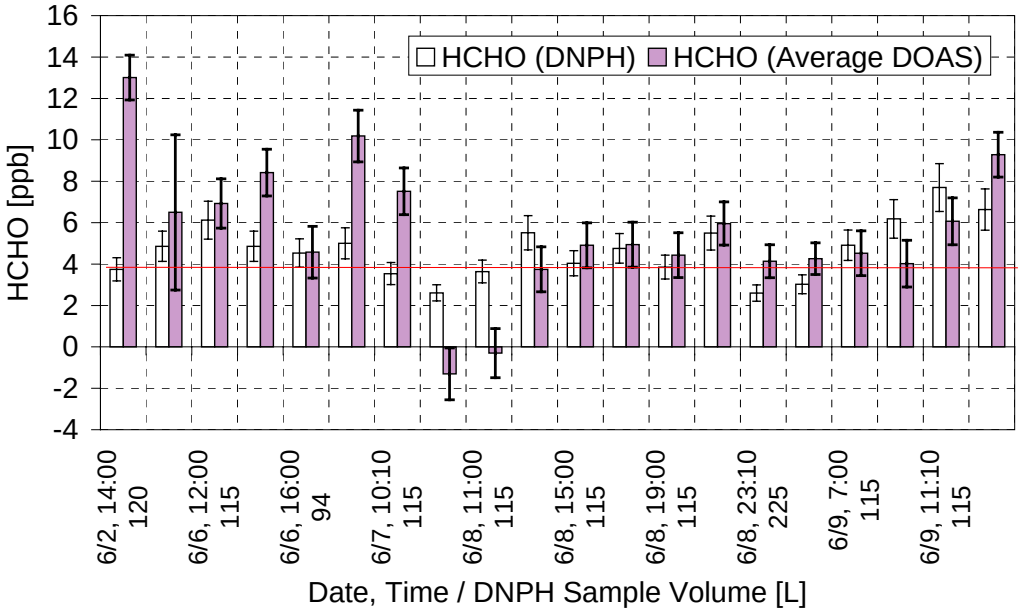

A similar intercomparison, carried out at East Hartford (Connecticut) during summer 1994 [14], got very different results. In that case, no similarity was found between the time trends of formaldehyde as by DOAS and DNPH. Moreover, the daily pattern displayed by DOAS measurements in that study was the one expected at urban sites near to emission sources, while that one from DNPH measurements suggests that at least a fraction of the formaldehyde measured was photochemically produced. Indeed, the expected situation was the opposite, given the differences in spatial representativeness between the measurement techniques.

FORMALDEHYDE AT SEREGNO (MILAN): PRIMARY OR SECONDARY POLLUTANT?

Methodology

The Milan metropolitan area is one the largest urban and industrial regions of Europe. Since both, pollutant emission and solar radiation are high on this area, it is questionable whether formaldehyde at Milan is mainly emitted or photochemically produced. This issue was tackled by statistical means. A daily basis was selected for this analysis instead of an "instantaneous" one. Most of the phenomena (meteorology and emissions) that determine the formaldehyde concentration have roughly repetitive daily pattern. In addition, formaldehyde has a relatively short lifetime in the atmosphere: 2- 4 hours due to photolysis and 3 hours to 1.5 days due to its reaction with OH [15]. On the other hand, formaldehyde produced by hydrocarbon photo-oxidation may have an accumulative effect over several days only. Reaction with NO_3 its generally of minor importance (mean lifetime from 2 to 80 days) [15]. The daily peak concentration of formaldehyde was the variable selected for analysis. It is reasonable to think that this parameter correlates better to three sets of determining variables: emission, photochemical production and meteorology. Emissions are believed to be well represented by the daily peak concentration of carbon monoxide. The capacity of the atmosphere for oxidizing hydrocarbons is certainly well represented by the daily peak concentration of ozone. Meteorological conditions are characterized by the daily averaged (total daily collected) solar radiation. Roughly speaking, this variable determines the height of the mixing layer and the humidity.

Analysis of Results and Discussion

The weather conditions during PIPAPO were in general good, particularly during two anticyclonic periods from May 11 to May 19 (first Intensive Observation Period – IOP-1) and from May 29 to June 4 (IOP-2) (see Figure 2). Some showers and storms were experienced as well (see Figures 2 and 4A). As seen on Figure 4A and 4B, peak formaldehyde and ozone concentrations are in some correlation to solar radiation. The formaldehyde (daily peak concentration) trends during the periods May 11-15 and June 2-6 are better correlated to the ozone trend during those periods. It can be concluded that strong changes in formaldehyde were generally well correlated to strong changes in ozone (see Figure 4B).

The one-independent-variable correlations of formaldehyde to carbon monoxide and ozone are shown on Figure 5. HCHO and CO are not very significantly correlated: $r = 0.46$. This correlation coefficient is considered low according to Riggs' classification [3]. The resulting formaldehyde background concentration from this correlation is 0.77 ppb. This would be the peak concentration of formaldehyde in absence of emissions. The coefficient of correlation is slightly better for HCHO to O_3: $r = 0.54$ (moderate according to Riggs' classification), which would indicate that formaldehyde was mainly of secondary origin during PIPAPO. This correlation allows estimating the ozone background concentration: 30.6 ppb (daily peak). The correlation becomes more significant ($r = 0.59$) when carbon monoxide, ozone, and solar radiation are simultaneously included. The calculated linear "response curve" is as follows:

Figure 4. Time series of formaldehyde (daily peak) in comparison to (**A**) solar radiation (daily average) and (**B**) ozone (daily peak). **C**. HCHO concentration (daily average) change in comparison to particulate matter (<10 mm) concentration (previous day).

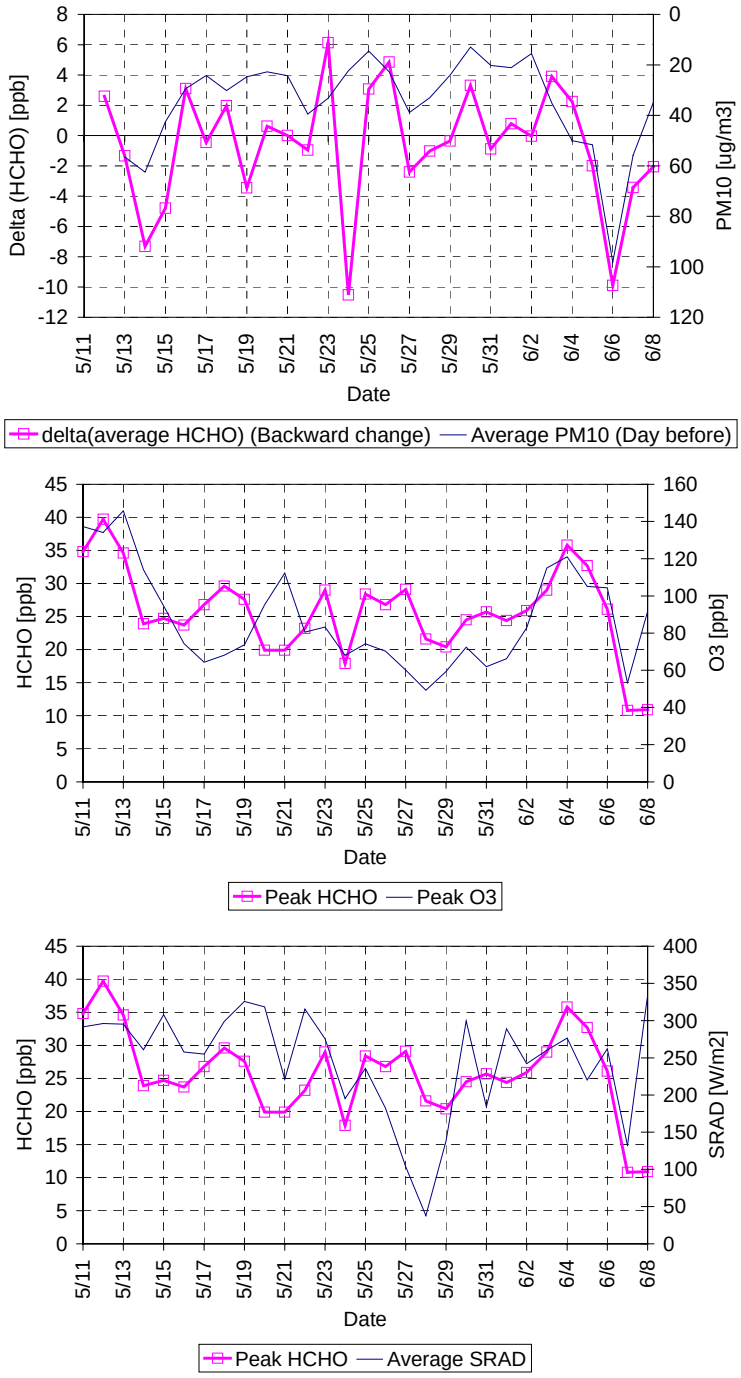

Equation 2. Correlation (multiple linear regression) of formaldehyde to ozone, carbon monoxide and solar radiation measured at Seregno (Milan area) during the period May 11-June 8, 1998. Coefficients are reported with 1 standard deviation.

$$HCHO = 0.11(\pm 0.05)\cdot O_3 + 1.50(\pm 1.14)\cdot CO - 8.25(\pm 17.35)\cdot 10^{-3}\cdot SRAD$$

where:

HCHO = daily peak concentration [ppb] of formaldehyde
O_3 = daily peak concentration [ppb] of ozone
CO = daily peak concentration [ppm] of carbon monoxide
SRAD = daily averaged solar radiation [W/m^2]

The slopes of all above-mentioned correlations are very similar to those found by Anderson [2] and Riggs [3]. The multiple linear correlation indicates that 1.5 molecules of "primary" formaldehyde are emitted per each 1,000 molecules of carbon monoxide emitted. Regarding the photochemical production, the regression indicates that 11 molecules of formaldehyde are produced in the atmosphere each 100 molecules of ozone produced.

Figure 5. One-independent variable correlations of formaldehyde (daily peak) to carbon monoxide (daily peak) and to ozone (daily peak).

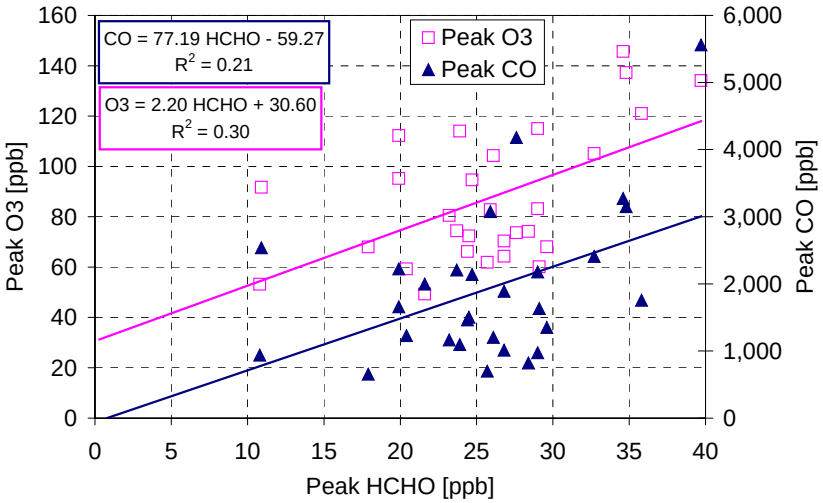

A calculation based again on the multiple linear regression coefficients suggests that the contribution of "emissions" in the build-up of ambient concentrations of HCHO is less important than that one related to photochemical processes. Thus, it may be concluded that formaldehyde during PIPAPO was mainly of secondary origin.

Regarding a different process, a remarkable concurrent decrease in HCHO concentrations and increase in particulate matter concentrations was observed on the 6th June (see Figure 4C). This finding may indicate a heterogeneous removal process of formaldehyde.

INTERPRETATION OF PRELIMINARY CALCULATIONS FROM A PHOTOCHEMICAL GRID MODEL

Model Description and Application

The photochemical grid model used for this study is a modification of the California / Carnegie Institute of Technology (CIT) grid model [16], which uses the TVM model (Topographic Vorticity Model) [17-18] for mesoscale meteorological calculation and the LCC chemical reaction mechanism [19]. TVM uses finite difference techniques to solve simultaneously a thermal energy, a specific humidity, a turbulent kinetic energy budget equation and two vorticity equations. The chemical gas-phase system includes 44 gas-phase species (35 transported, 9 considered in steady state) coupled via 106 reactions. The photolysis rate constants were prepared with the STAR (System for Transfer of Atmospheric Radiation) [20] sub-module.

The inner horizontal domain (see Figure 1) consists of 47 x 50 grid points with a resolution of 3 x 3 Km, centered in Milan and covering the Lombardy region and the southern part of Canton Ticino (Switzerland). A terrain-following coordinate system with 24 levels is used in the vertical coordinate. Grid spacing increases from 25 m at the surface to 1,000 m at the top of the domain (8,550 m). Eight different land-use classes are employed in the calculation.

The emission inventory was provided by Regione Lombardia (Italy) and METEOTEST (Switzerland). Volatile organic compounds (VOC) have been grouped in the 32 classes required by the Regional Acid Deposition Model (RADM) scheme.

The simulation starts at 21:00 (local summertime - LST) on the 12th May 1998, with horizontally homogeneous initial conditions based on the vertical sounding of Linate Airport. On this day, the geostrophic (free troposphere) wind flows to the northwest at a speed of 2-2.5 m/s. The geostrophic wind, atmospheric stability and boundary conditions are fixed constant during the simulation period (exception provided for the temperature profile). Concerning the atmosphere composition, the initial conditions for 13th May were set as the final conditions after a 1-day simulation started from background values and including emission, chemistry, diffusion and advection dynamics. The boundary conditions (1 hour time resolution) were obtained from a previous simulation with the EURAD model, which uses the RADM2 chemical mechanism. The chemical calculations start at midnight after 3 hours of initialization of the dynamics and last for 24 hours.

Analysis of Results and Discussion

As shown on Figure 6A, the implemented model is able to reproduce the ozone increase at Seregno during the simulated day. The calculated ozone peak concentration is in fairly good agreement with the one measured but the calculated peak appears 3 hours later than the measured one. In fact, the simulated ozone plume is lagged 2-3 hours from measurements over the whole domain. Probably more relevant to this study is the fact that the model is completely unable to reproduce the early peak of ozone at 3:00-4:00, and underestimates the ozone concentration from

19:00 and on. This finds an explanation on the fact that the NO_X concentrations during these periods of the day are certainly overestimated (figure not shown). Therefore, the extent of the titration of ozone by nitric oxide is overestimated as well. A deeper analysis of the simulation calculations suggests that the model overestimation of the early morning NO_X concentrations at Seregno is mainly due to the passage of a simulated, north-directed plume containing very high concentrations of primary pollutants. This plume is clearly seen in the simulation results but not in the measurements. Moreover, the NO_X emissions at Seregno's grid cell are only one quarter of those in the adjacent cell at the south.

Figure 6. Measured and simulated (A) ozone and (B) formaldehyde concentrations at Seregno on the 13th May 1998. Note the perfect agreement between DOAS and point monitor measurements of zone.

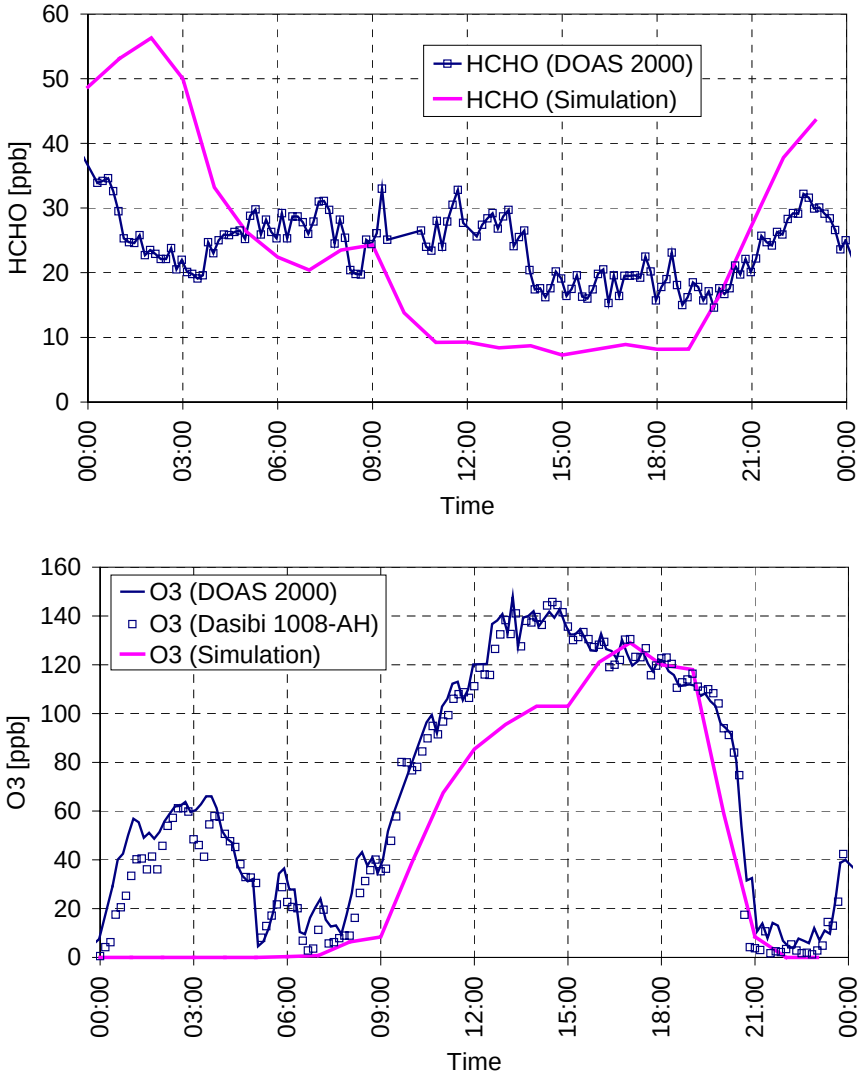

Figure 7. 2D Plots of ozone and formaldehyde concentrations as calculated at ground level over the PIPAPO simulation domain for the 13th May 1998. **A**. O_3 at 10:00. **B**. HCHO at 10:00. **C**. O_3 at 16:00. **D**. HCHO at 16:00.

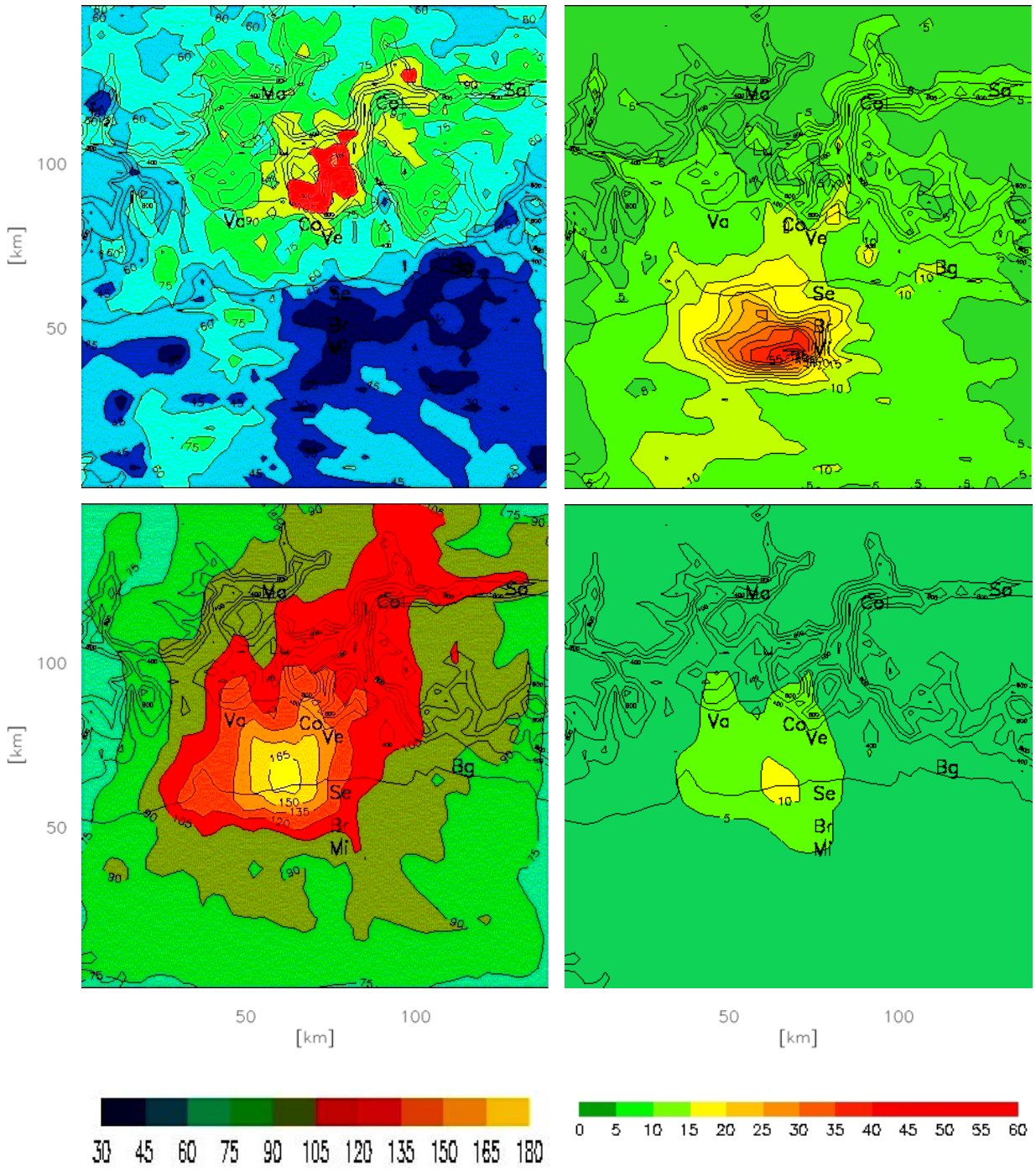

The measured and simulated formaldehyde concentration time series are shown on Figure 6B. The fact the model overestimates HCHO at early morning (0:00 – 7:00) and night (from 19:00) is as well very likely linked to the passage of a primary pollutant plume as analyzed above. Indeed, an extremely significant correlation (r = 0.99) was found between simulated formaldehyde and simulated carbon monoxide. In addition, this regression reports a ratio of 29.5 ppb HCHO/ppm CO, which is about twice the experimental ratio found for the 13th May (13 ppb HCHO/ppm CO), i.e. the model overestimates the "primary" formaldehyde and underestimates the "secondary" one. Nevertheless, it must be remarked that the HCHO concentration "valley-shaped" pattern measured at 14:00-20:00, and probably due to the mixing layer expansion, is calculated by the model at 10:00-20:00. Moreover, the measured "valley base" concentration is around 17 ppb, whereas the simulated one is almost constant at around 8 ppb.

Therefore, it is very likely that the simulation model treats formaldehyde as a primary pollutant only. The simulation results are thus relevant to the dynamics of formaldehyde emission and dispersion. Figure 7 shows the 2-D plots of the simulated ozone and formaldehyde concentrations over the domain at 10:00 and 16:00 on the 13th May 1998. Figures 7A shows that ozone concentrations at 10:00 are very low due to titration with nitric oxide. At this hour, the simulated concentrations of primary pollutants are high, which is observed as well for (calculated) formaldehyde on Figure 7B. At 16:00 (see Figures 7C and 7D) the primary pollutant emissions are lower and the mixing layer gets completely developed. This leads to the development of the ozone plume along the Po Valley and to the dilution of the (calculated) formaldehyde emissions. Moreover, the (calculated) formaldehyde plume peak concentration moves southerly from 10:00 to 16:00, a period when HCHO emissions are comparatively lower. This peak shift phenomenon resembles a puff dispersion process, i.e. advection and dispersion of the "puff" generated by the early morning emissions.

CONCLUSIONS

Formaldehyde as measured by DOAS and DNPH during the PIPAPO experiment are in fairly good agreement, despite of the relatively short length of the DOAS optical path and the fact the concentrations measured during the intercomparison period were close to the lower detection limit of DOAS.

In order to investigate whether formaldehyde was primary or secondary during the PIPAPO experiment, daily peak concentrations of HCHO were correlated to solar radiation and daily peak concentration of ozone and carbon monoxide. The ratios found are in good agreement with literature data and provide evidence for photochemical production as the main source of formaldehyde at Seregno (Milan area) during the PIPAPO experiment. In addition, an episode of concurrent increase of particulate matter and decrease of formaldehyde point to heterogeneous removal processes for formaldehyde.

The comparison of experimental measurements with simulation calculations indicates that the meteorological module, the chemical mechanism and the emission inventory used in this work for simulating the first IOP of PIPAPO have to be revisited.

ACKNOWLEDGEMENTS

We gratefully acknowledge all members of the EPFL experimental team (LIDAR Group) for their involvement during the PIPAPO experiment, and Alain Clappier and Frank Kirchner of EPFL (Numerical Modeling Group) for valuable discussions. This research work was supported by the Swiss Commission for Technology and Innovation (CTI) (contract 3260.1), BUWAL (contract 810.98.VIII) and the OFES STAAARTE office (contract 97.03.13).

REFERENCES

1. Lowe, D.C; Scmidt, U; Ehhalt; *The Tropospheric Distribution of Formaldehyde*; Ph.D. Thesis, Köln University, 1982
2. Anderson, G. et al; Sources and Sinks of Formaldehyde and Acetaldehyde: An Analysis of Denver's Ambient Concentration Data; *Atmospheric Environment* **1996**, 30, 2113-2123
3. Riggs, S.D; Anderson, L.G and Lanning, J.A.; A Comparison of Source Contributions to Carbonyl Concentrations in Denver, Colorado and Outlying Areas; *A&WMA 90th Annual Meeting & Exhibition*, Toronto, June 8-13, 1997
4. LOOP – Limitation of Oxidant Production Home Page; http://www1.psi.ch/~loop (accessed March 2000)
5. Calpini, B et al; Photo-oxidant Formation in the Milan Metropolitan Area. *Proceedings of EUROTRAC Symposium '98*, Garmisch-Partenkirchen (Germany), March 23-27, 1998; Volume 2, pp 875-880
6. Quaglia, Ph. et al; Planetary Boundary Layer Ozone fluxes from Combined Airborne, Ground Based LIDARs and Wind Profilers Measurements; *European J. Analytical Chem. (Analusis)* **1999**, 27, 305-310
7. Chanda, A. et al; Optical Remote Sensing Measurements Using a UV DOAS system; *Proceedings of A&WMA 90th Annual Meeting & Exhibition*, Toronto, June 8-13, 1997; Paper 97-RP115.02
8. Schiff, H.I. et al; Ambient Air Measurements and Practical Detection Limits Determinations with an Improved DOAS System; *Proceedings of A&WMA 89th Annual Meeting & Exhibition*, Nashville, June 23-28, 1996; Paper 96-TP26B.04
9. Schiff, H; Robbins, J.; Nadler, S.D. and Mackay, G.I. The Sensair – an Improved DOAS system; *Proceedings of Optical Sensing for Environmental and Process Monitoring*, McLean (Virginia), November 7-10, 1994
10. Platt, U.; Differential Optical Absorption Spectroscopy (DOAS); In *Air Monitoring by Spectroscopic Techniques*; Sigrist, M.W., Ed.; Wiley, New York, 1994; pp 27-84
11. Jiménez, R., Ed.; Formaldehyde (HCHO) Measurements; In *The PIPAPO Experiment: QA/QC*; http://www1.psi.ch/~loop/pipapo/qaqc_f.html (accessed March 2000)

12. Arnts, R.R and Tejada, S.B.; 2,4-Dinitrophenylhydrazine-Coated Silica Gel Cartridge Method for Determination of Formaldehyde in Air: Identification of an Ozone Interference; *Environ. Sci. Technol.* **1989**, 23, 1428-1430
13. Stutz, J. and Platt, U.; Numerical Analysis and Estimation of the Statistical Error of Differential Optical Absorption Spectroscopy Measurements with Least-Squares Methods; *Applied Optics* **1996**, 35, 6041-6053
14. Hartman, R.M.; Use of an OPSIS Open Path Monitor for Ambient Aldehyde Monitoring. *Proceedings of Optical Sensing for Environmental and Process Monitoring*, McLean (Virginia), November 7-10, 1994; pp 194-205
15. Finlayson-Pitts, B.J; Pitts, J.N.; *Atmospheric Chemistry: Fundamentals and Experimental Techniques*; Wiley, New York, 1986
16. Harley, R et al; Photochemical Modeling of the Southern California Air Quality Study; *Environm. Sci. Technol.* **1993**, 27, 378-388
17. Schayes, G.; Thunis, P; and Bornstein, B.D; Development of the Topographic Vorticity Mode Mesoscale (TVM) Model: Part I – Formulation; *J. Appl. Meteor.* **1996**, 35, 1815 - 1823
18. Bornstein, B.D; Thunis, P; Grossi, P. and Schayes, G.; Development of the Topographic Vorticity Mode Mesoscale (TVM) Model: Part II – Evaluation; *J. Appl. Meteor.* **1996**, 35, 1824-1834
19. Lurmann, F.; Carter, W.P. and Coyner, L.A.; A Surrogate Species Chemical Reaction Mechanism for Urban-Scale Air Quality Simulation Models - I: Adaptation of the Mechanism; EPA Report 600/3-87/014-A, 1987
20. Ruggaber, A.; Modelling Radiation Quantities and Photolysis Frequencies in the Troposphere; *J. Atmos. Chem.* **1994**, 18, 171-210

Annex I
Sogamoso Air Quality Management System
CAVASO 2002

The Valley of Sogamoso (5º 42´ N, 72º 55´ W) is a complex-topography, high-altitude (~2500 m above the sea level - ASL) Andean valley embedded in the Colombian Eastern Mountain Range. See **Figure I-1**. Air quality in the Sogamoso valley is affected, among other, by emissions from a large number (> 600) of highly polluting small-scale industries (brick and quicklime manufacturing). See **Figure I-2**.

Aiming at finding solutions to this socially-complex air quality problem, EPFL/LPAS and a consortium of Colombian institutions (UNIBOYACA, CORPOBOYACA, Municipality of Sogamoso, UNIANDES) accomplished during 1999-2003 the project *Establishment of a demonstrative air quality management system (AQMS) in the Valley of Sogamoso, Colombia*. The Sogamoso AQMS project was funded by ICSC-World Laboratory (Lausanne, Switzerland – Project LAND-14) and the partaking institutions. Further details can be found elsewhere (van den Bergh, 1999).

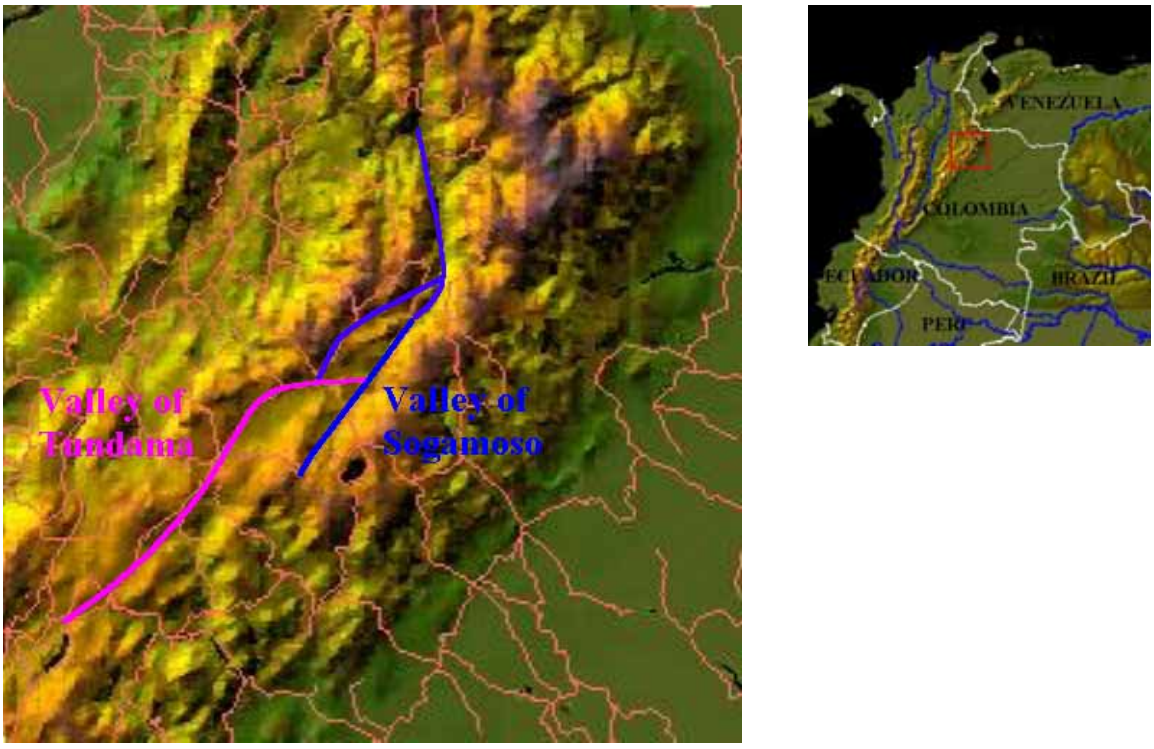

Figure I-1. Left: Valley of Sogamoso and surroundings (256×256 km map). **Right:** Colombia and neighboring countries (2048×2048 km map). This map shows also the domain of the project. The Colombian Eastern Mountain Range extends from the Colombian border with Ecuador to the border with Venezuela.

The Sogamoso AQMS involved training (11 Colombian engineers) and knowledge dissemination on air pollution measurement and simulation (3 scientific conferences/seminars), the establishment of an adapted air quality monitoring network (RMCAS), intensive field measurements (CAVASO 2002), the application of an appropriate simulation model, and scientific support to decision-makers and other partaking institutions.

The Sogamoso Air Quality Monitoring Network (RMCAS – 4 fixed monitoring stations) was equipped in a large part with instrumentation donated by various Swiss environmental authorities. A significant fraction of the civil works were funded by the local industry. As a result, RMCAS is probably the less expensive network of its kind ever achieved in a developing country.(Jiménez, 2003; Jiménez, 2002)[1]. See **Figure I-3**.

Figure I-2. Air pollutant emission sources in the Sogamoso Valley.

Figure I-3. Sogamoso Air Quality Monitoring Network (RMCAS). Fixed monitoring stations and complementary measurement sites during CAVASO 2002 are indicated in dark and light color (blue and red), respectively.

[1] Reports and other documents are available in the EPFL/LPAS web site (Hhttp://lpas.epfl.ch/lidar.htmlH).

An intensive measurement campaign (CAVASO 2002) was conducted during January-February 2002 as part of the Sogamoso AQMS project. CAVASO 2002 involved point measurements of criteria pollutants (PM_{10}, SO_2, CO, NOx, O_3) at the 4 network stations, and complementary gas-phase measurements using differential optical absorption spectroscopy (DOAS) systems at two sites. Atmospheric profiling (pressure, temperature, relative humidity, ozone) was obtained using a tethered balloon developed at EPFL/LPAS. Additional air quality measurements included carbonyl analysis by DNPH/HPLC at 3 sites (Marquez, 2003), and elemental analysis of PM_{10} samples using atomic absorption (Ulloa, 2003).

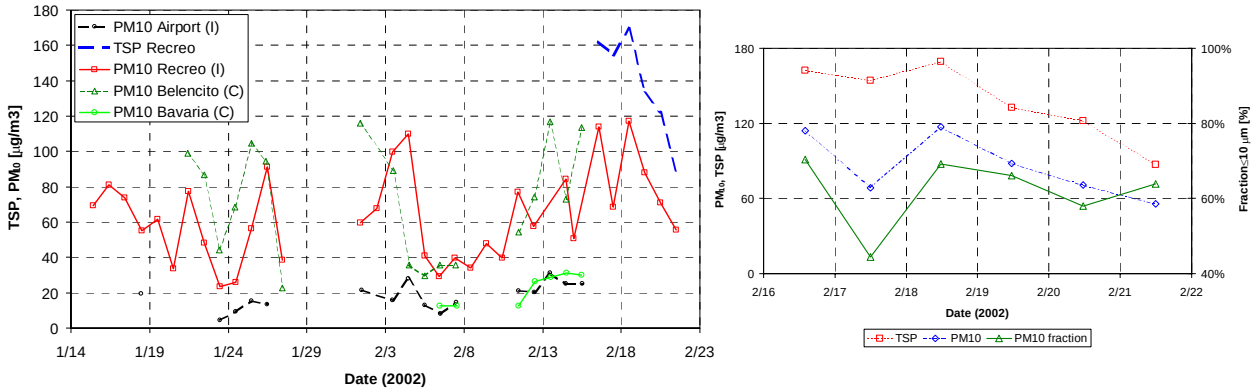

Figure I-4. Left: Particulate matter (PM_{10} and TSP) concentrations (24-h average) measured at various Sogamoso Valley locations during CAVASO 2002. **Right:** Fraction of aerosol below 10 µm at the Recreo site (Sogamoso urban area).

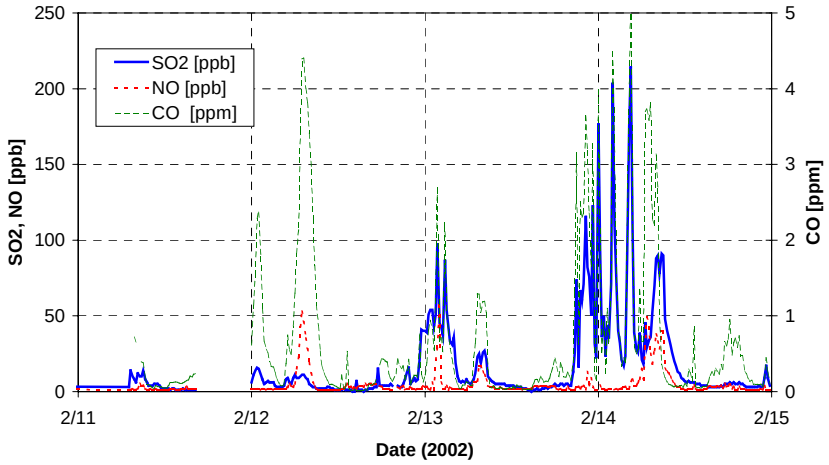

Figure I-5. Concentration time series of SO_2, CO, and NO at the Recreo site during the Intensive Observation Period of CAVASO 2002. Measurements were performed with standard point monitors.

Measurements carried out during CAVASO 2002, especially of PM_{10} concentration, revealed elevated primary pollutant levels in the Sogamoso Valley (see **Figure I-4**). Episodic concentrations of primary pollutants observed at nighttime in the urban area of Sogamoso (Recreo site) appear to be due to downslope (katabatic) advection of emissions from brick kilns located in the valley foothills. This hypothesis is supported by the strong correlation observed between the concentrations of SO_2 and CO during this period of the day (see **Figure I-5**).

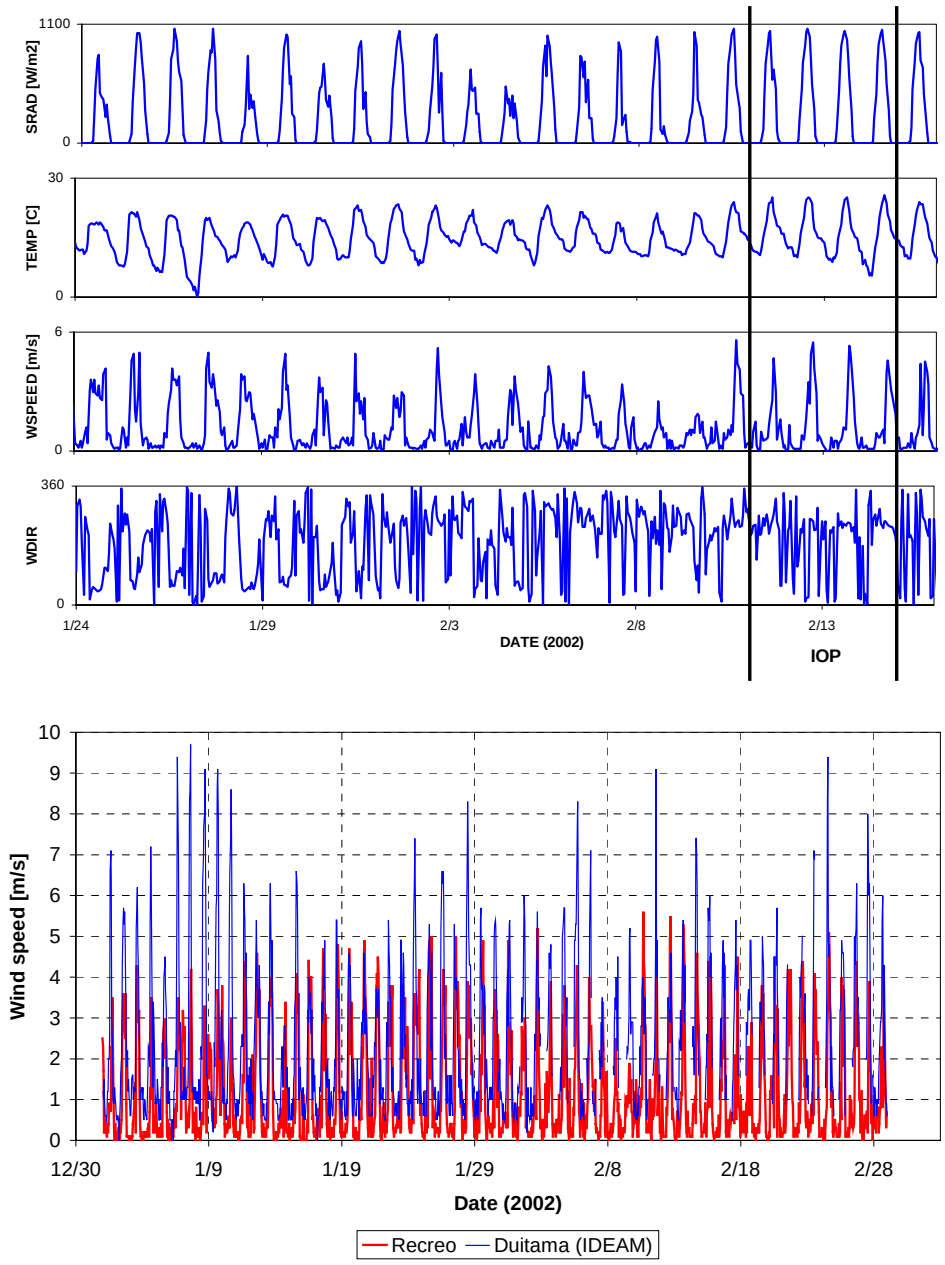

Figure I-6. Meteorological time series during CAVASO 2002. **Above:** Global radiation (direct + scattered), temperature, and wind speed and direction at the Recreo site. **Below:** Wind speed at the Recreo and Duitama sites during January-February 2002.

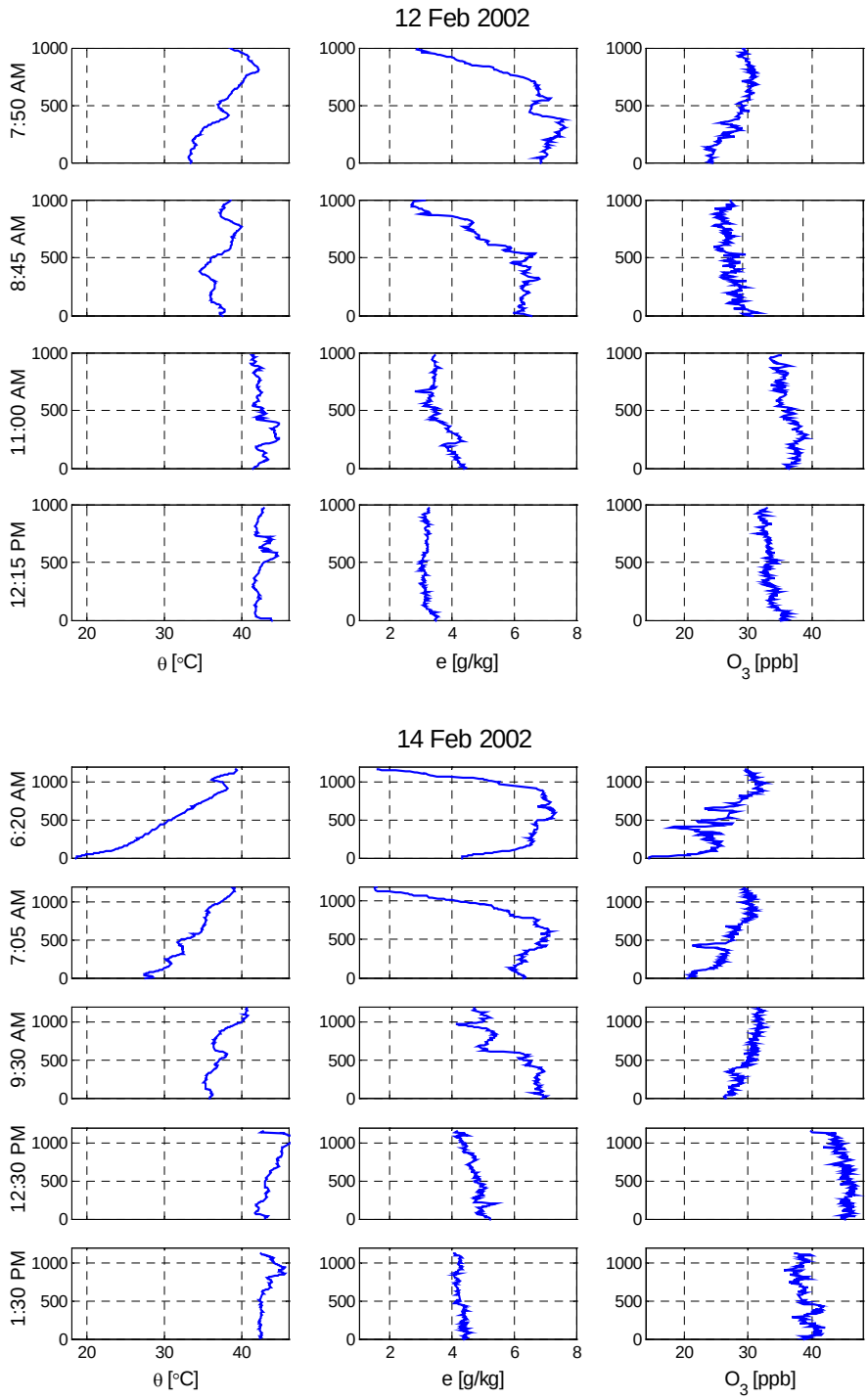

Figure I-7. Sequential vertical profiles of potential temperature, specific humidity and ozone mixing ratio measured with a tethered balloon in the Sogamoso Airport on 12th and 14th February 2002. Altitudes are in meters above the ground level (AGL). Strong surface and altitude winds (> 3 m/s) impeded further profiling of the atmosphere from midday on.

The Sogamoso Valley is a high-altitude valley located in the tropical Andes, which entails high solar radiation levels, particularly during the dry season (typically December through February). The combination of high irradiation levels with the complex topography induce a complex but periodic wind circulation pattern dominated by anabatic-katabatic, valley-mountain winds. The time series indicate that this thermal regime prevails over the synoptic conditions during most of the year. This is demonstrated by the similarity between the diurnal wind speed patterns at two distant locations within the valley (Sogamoso and Duitama). See **Figure I-6**. Higher wind speeds (up to ~10 m/s) are nevertheless observed at Duitama (west side of the valley) due to channeling effects.

Particularly in conditions very clear sky, radiative cooling at nighttime leads to low temperatures at sunrise and consequently to strong diurnal variations of temperature and humidity. Nighttime radiative cooling also induces temperature inversion and stratification of the atmosphere, as measured with a tethered balloon (see **Figure I-7**).

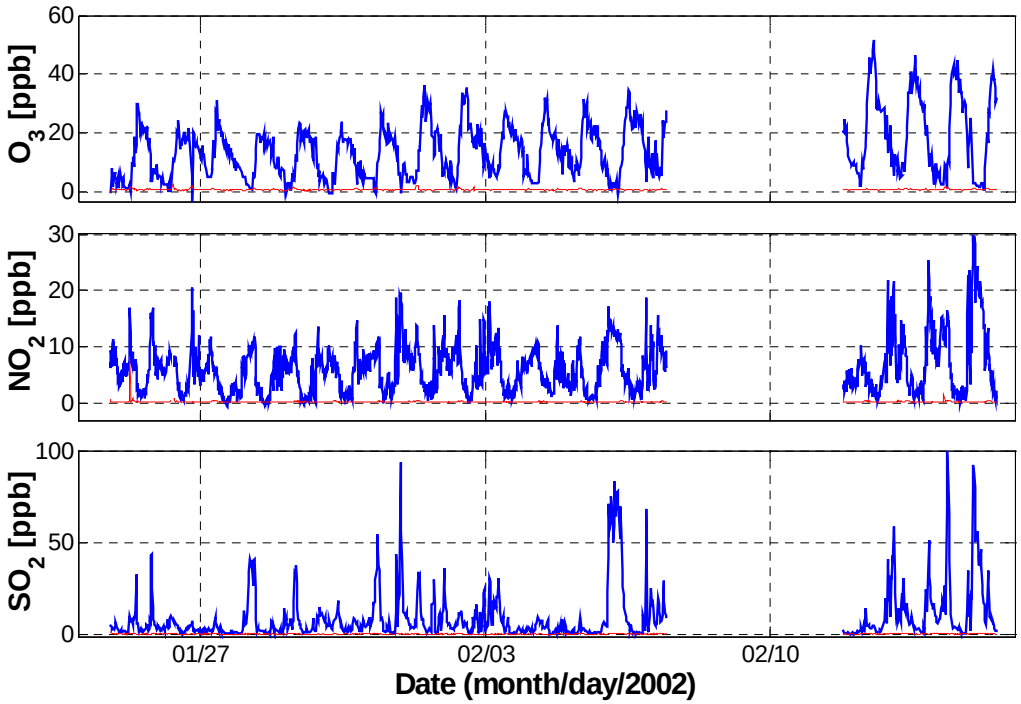

Figure I-8. Ozone, nitrogen dioxide, and sulfur dioxide mixing ratio as measured with a monostatic DOAS system (DOAS 2000) at the Duitama site during CAVASO 2002. Operational detection limits (1-sigma) are shown in light color (red). Note the increase of O_3 and NO_2 during the clear sky conditions of the last period of the campaign.

Tethered balloon measurements also revealed an unexpected behavior of the ozone concentration in the Sogamoso Valley. Balloon measurements indicate an O_3 background mixing ratio of ~30 ppb. Particularly in conditions of high irradiation and consequently of strong convection, the concentration of ozone overpasses the background level before

midday, which suggest local photochemical production. The production rates observed are relatively high (up to 6 ppb/h) for a semi-rural region. Elevated background concentrations of hydroxyl radical over the tropical Andes, as predicted by global models, could explain these relatively high photo-oxidation rates. Then shortly after midday, the concentration of ozone decreases abruptly reaching quasi-constant levels (during ~1 h) that are close to the background concentration. Calculations with a meteorological grid model indicate that this phenomenon is due to advection to the Sogamoso Valley of clean, comparatively drier air masses from the Colombian Eastern Savanna (~200 m ASL). The Sogamoso Valley is separated by a ~30 km wide, ~800 m high topographic barrier from the lowland Savanna. This implies that anabatic advection would be very strong in this part of the Andes. The model shows also the convergence of the strong anabatic winds from the Eastern Savanna with local mountain-valley winds. The calculation indicate that at around midday Savanna winds prevail over mountain-valley winds leading to a rapid ventilation of the valley.

This conclusion, derived from balloon measurements and simulation results, are also corroborated by point measurements of ozone at 4 sites and with DOAS at 2 sites. Analysis of the odd oxygen ($[O_X] \approx [O_3] + [NO_2]$) time series indicates that dry deposition is the predominant O_3 sink at nighttime. As expected, the maximum O_3 production (~20 ppb) is observed over the most densely urbanized area in the region. Evidenced deviation from the photo-stationary state provides evidence that the excess ozone is produced locally by photo-oxidation of hydrocarbons.

DOAS measurements at Duitama (see **Figure I-8**), taken at about 50 m above the street level (DOAS sensing beam), revealed also elevated nighttime concentrations of SO_2 and fairly high levels of NOx. This is also an unexpected result as the Duitama area has no small-scale kilns. Pollutant levels in this area appear to be associated to heavy road traffic at nighttime.

References

Jiménez, R., V. Simeonov, B. Calpini and H. van den Bergh. Project LAND-14 - 2001-2002 Progress report. EPFL/LPAS, Lausanne, 2002

Jiménez, R., A. Clappier, V. Simeonov, H. van den Bergh, B. Calpini, J. Diaz, A. Cortazar, J. Cetina, A. Rodriguez, E. Espindola, W. Gutierrez, J.M. Cordovez and D. Echeverry. Project LAND-14 - Progress report 2002-2003 and 3-year term final report. EPFL-UNIBOYACA-COROPOBOYACA-Municipality of Sogamoso-UNIANDES, Lausanne, 2003

Marquez, W. and W. Palencia. Determination of ambient air carbonyls in the Sogamoso Valley using the DNPH/HPLC technique (in Spanish). Diploma Work, UNIBOYACA-EPFL, Tunja (Colombia), 2003

Ulloa, M. and N. Daza. Characterization of particulate matter bounded heavy metals in the Sogamoso Valley (in Spanish). Diploma Work, UNIBOYACA-EPFL, Tunja (Colombia), 2003

van den Bergh, H., B. Calpini, R. Jiménez, P. Leyva, N. Sanchez, C.M. Paez, B. Caicedo, E. Giraldo, E. Behrentz and A. Rodriguez. Establishment of a demonstrative air quality management system in the Valley of Sogamoso, Colombia - A project proposal to ICSC-World Laboratory. EPFL-IDEAM-UNIANDES-CORPOBOYACA, Lausanne, 1999

Annex J
DOAS Campaigns
Compendium of Pollutant Concentration Time Series

PIPAPO 1999
(Seregno – Milan area, Italy)

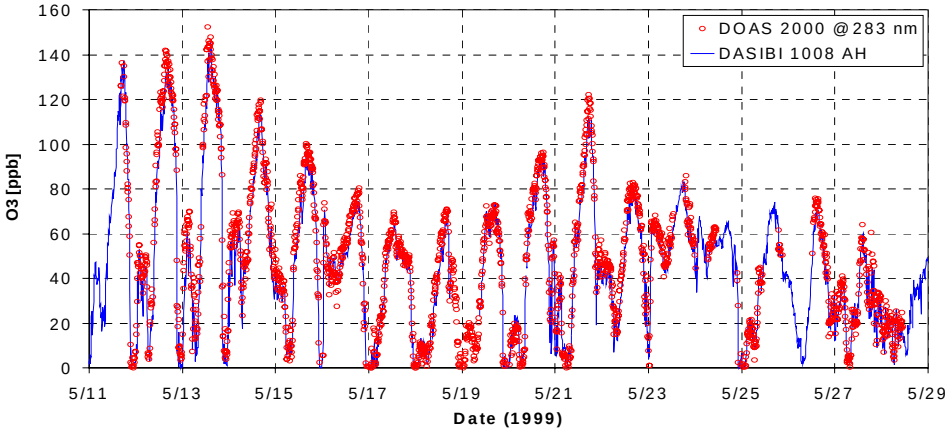

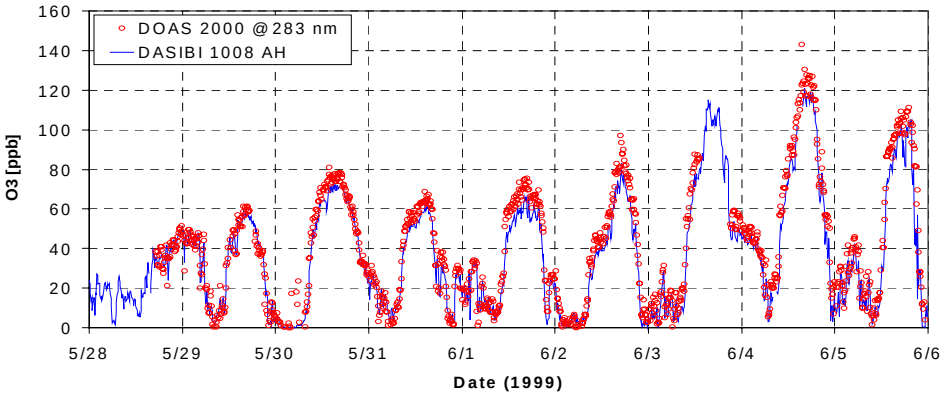

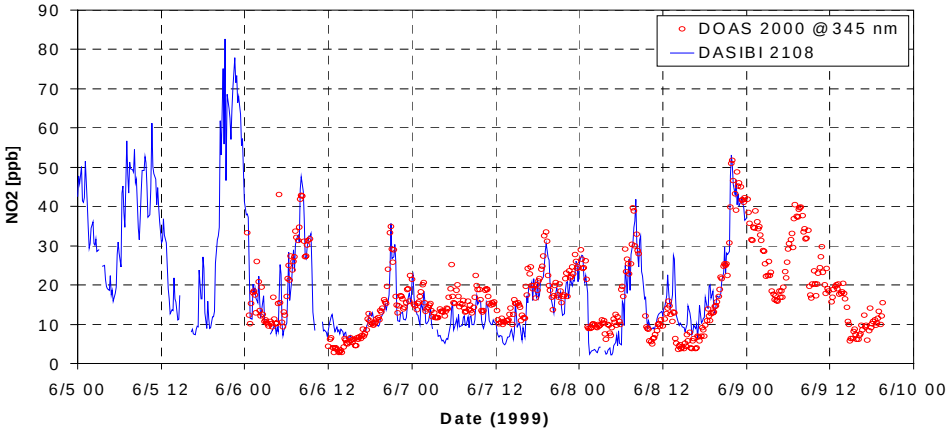

ESCOMPTE 2001
(Saint Chamas – Marseilles area, France)

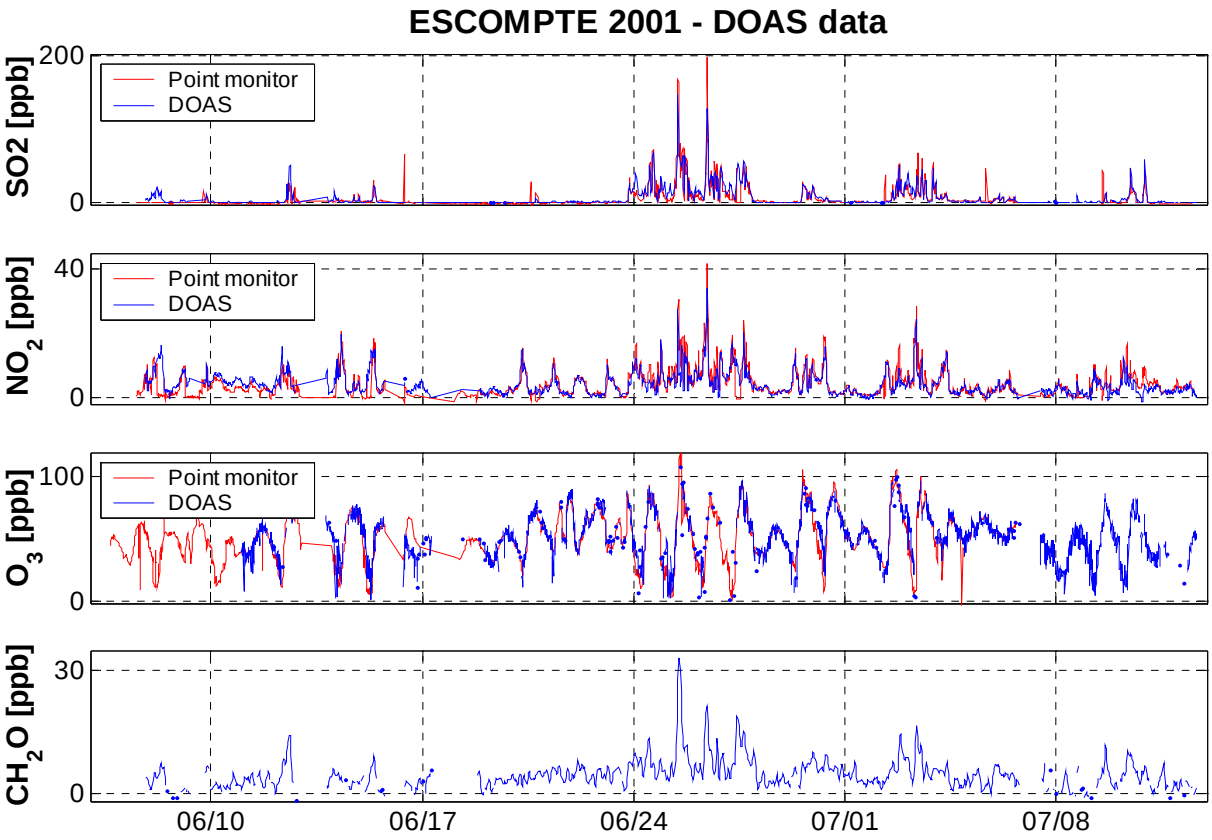

ASPA 2003
(Strasbourg area, France)

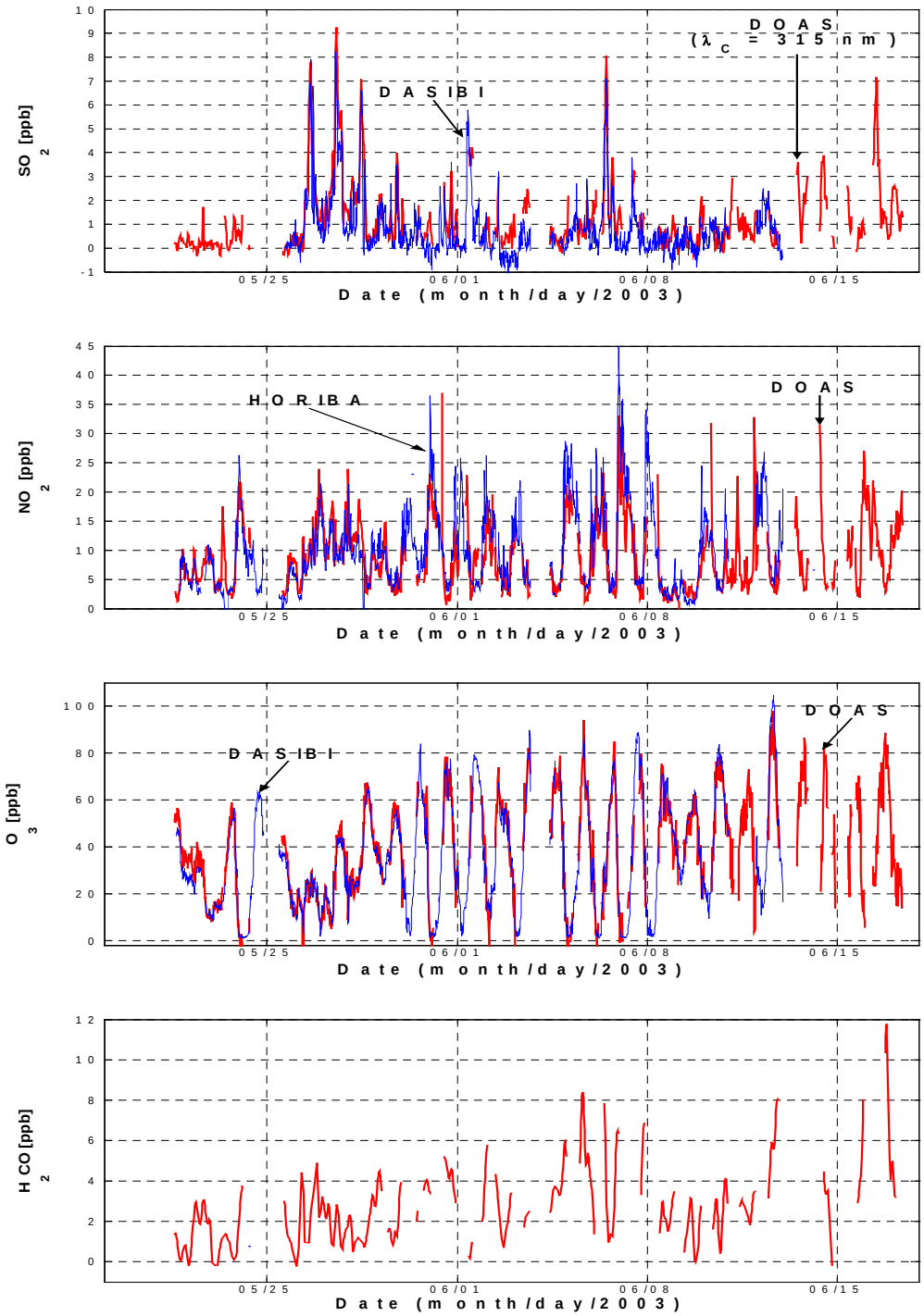

Annex K
Picture Gallery

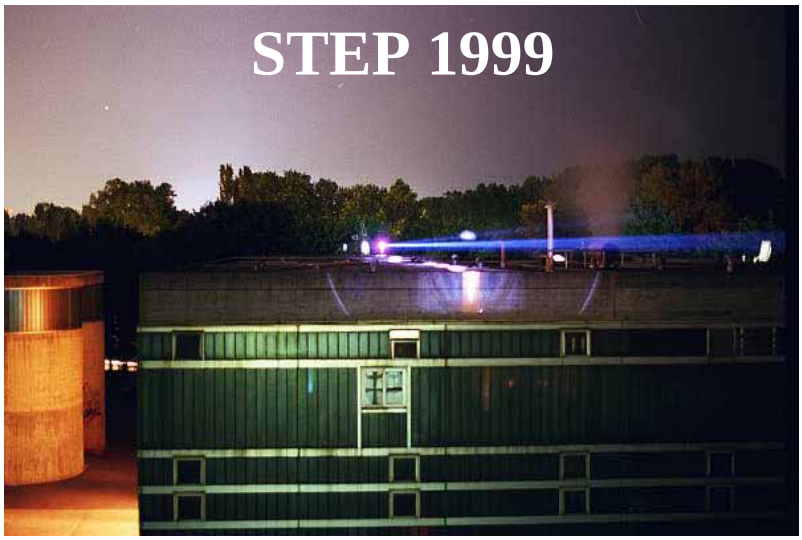

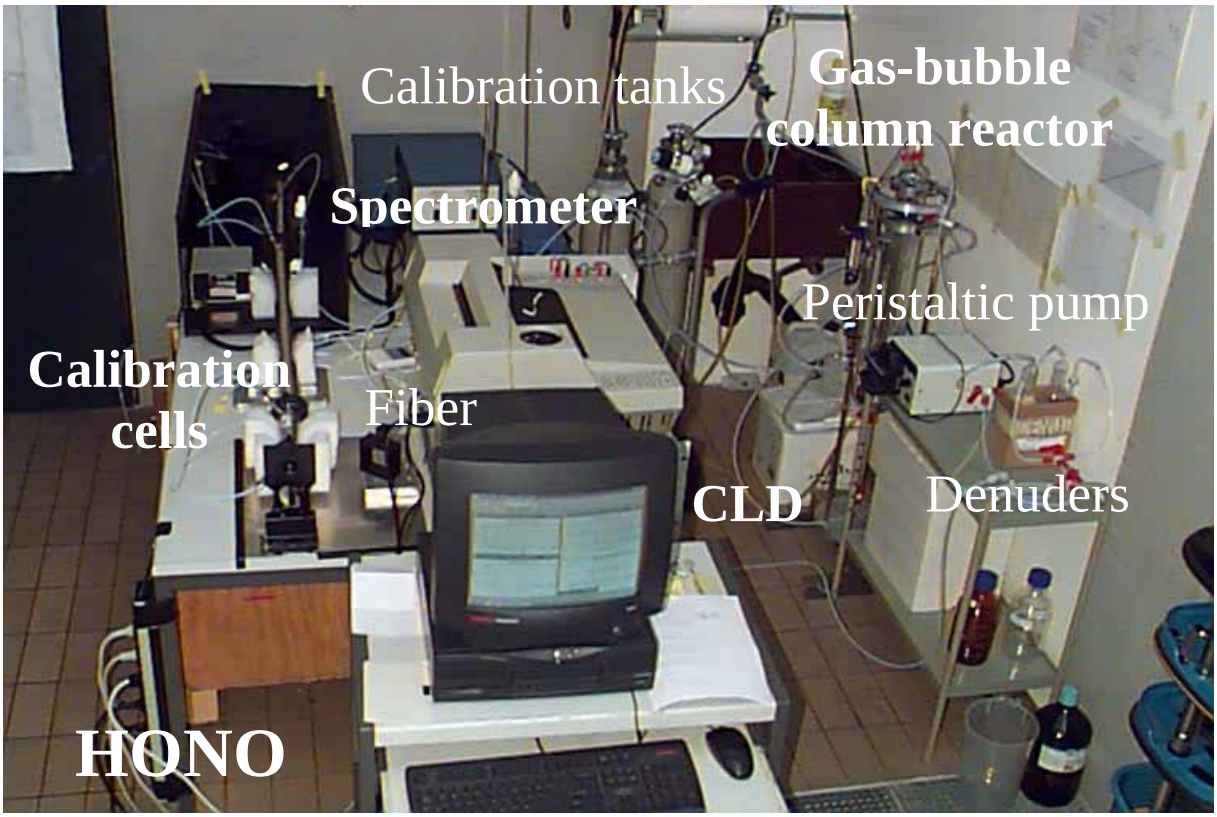
Calibration tanks
Gas-bubble column reactor
Spectrometer
Peristaltic pump
Calibration cells
Fiber
CLD
Denuders
HONO

RODRIGO JIMÉNEZ-PIZARRO

4, Maladière; CH-1022 Chavannes, Switzerland
Mobile: +41-76-457-4252; Office: +41-21-693-3189
Fax: +41-21-693-5145; E-mail: rodrigo.jimenez@epfl.ch

EDUCATION

Ph.D. in Atmospheric Sciences 2004
Swiss Federal Institute of Technology (EPFL), Lausanne
Thesis: *Development and application of UV-visible and mid-IR differential absorption spectroscopy techniques for pollutant trace gas monitoring*

Diploma in Chemical Engineering (B.Sc.$^{+}$) 1997
University of Valle, Cali (Colombia)
Diploma work: *Design and simulation of a miniplant for H_2S gas-solid removal processes*

Pollution Chemistry and Control 1994
National Open University (UNED – Madrid, Spain)

PROFESSIONAL EXPERIENCE

Swiss Federal Institute of Technology (EPFL), Lausanne Since 03/1997
Air Pollution Laboratory (LPAS)
Research and Teaching Assistant

- ***Instrument development***
  - Undertook the development of a trace-gas detection system based on mid-IR *quantum-cascade lasers*; set up the experiments, accomplished spectral analysis (FTIR, CO_2 absorption), and investigated the detection of ozone in laboratory conditions
  - Responsible for a joint R&D project aimed at characterizing, validating and improving a new open-path air pollutant monitoring system (*Differential Optical Absorption Spectroscopy* - DOAS 2000, Thermo Electron Air Quality Inc.); for this purpose developed optical and calibration benches; characterized the light source (high pressure Xe arc lamp) spectral variability and the light detection system (PMT) spectral response; tested detection with a MOS linear image sensor; developed diluted gas mixture generators (HONO, BTEX); experimentally determined lower detection limits; developed a Peltier-based thermal management system for outdoor conditions; conceived and implemented non-linear spectral fitting algorithms for trace gas concentration retrieval
- ***Field campaigns***
  - Actively participated and carried out DOAS measurements in 16 campaigns (14 in Europe, 2 in Colombia); 4 major European field campaigns (PIPAPO 1998, GRENOPHOT 1999, ESCOMPTE 2001, ASPA 2003); devised and carried out 2 campaigns in Colombia (involving 2 DOAS systems, atmospheric profiling with a homemade tethered balloon, aerosol elemental analysis, and DNPH/HPLC carbonyl measurements); accomplished 2 DOAS intercomparison campaigns and 4 campaigns for student training

- Based on field measurements and grid model calculations, investigated the dynamics of photochemical pollution in a narrow valley in central Switzerland (Obwald), the Milan metropolitan area, the Grenoble region (France), and the Sogamoso Valley (Colombia); investigated the emission of aromatic hydrocarbons in a wastewater treatment plant
- Devised and accomplished a field campaign to characterize *the pollutant plume from a road tunnel portal* in central Switzerland (including horizontal profiles of HCHO with DNPH/HPLC)

➢ ***Teaching & training***

- Advised the research work of 2 graduate and 6 undergraduate students
- Developed an experiment for student training (ozone titration kinetics)
- Trained 7 Colombian engineers on air pollution monitoring and data analysis

➢ ***Project development & management***

- Conceived, prepared and managed the project *Demonstrative Air Quality Management System for the Sogamoso Valley, Colombia* (funded by ICSC-World Laboratory ~120 kUSD); designed and managed the construction of a *4-station monitoring network*, co-organized 2 scientific conferences in Bogotá
- In cooperation with Colombian partners, devised and prepared the *Bogotá Air Quality Model* project (funded by the Colombian Government ~250 kUSD)

Condipetrol Ltda., Cali (Colombia) 12/1995 - 12/1996
Consulting & engineering on fuel transport and storage 09/1994 - 07/1995
Project Engineer

➢ ***Engineering & construction***

- Designed systems for *wastewater treatment*, counterfire water storage, and a *computer-controlled flow commuter* for a propane plant
- Prepared, gauged and put in operation 4 propane storage tanks (516 m^3)

➢ ***Consulting***

- Prepared the economic appraisal of the *Panamá-Colón pipeline*
- Managed the *Colombian southwest propane market study*

ESTCO Energy Inc., Ottawa (Canada) 08-11/1995
R&D on electricity storage and conversion
Visiting Engineer

- Developed an algorithm for matching *specialty batteries* used e.g. for satellite power
- Analyzed the energy use efficiency of an electric vehicle fleet

Lloreda Grasas S.A., Yumbo (Colombia) 06-09/1994
Edible fats & oils production
R&D Engineer

- Carried out 2 research projects and obtained approval for implementation:
  - Improvement of color in deodorized cottonseed oil
  - Reduction of processing time in fish oil hydrogenation

University of Valle, Cali (Colombia) 01-05/1993
Research & Teaching Assistant 01/1989 - 07/1990

- Co-developed the executive module of a *sequential-modular chemical process simulator*
- Teaching assistant for *chemical thermodynamics* (multicomp. phase and chem. equilibria)

LANGUAGE & SOFTWARE SKILLS

- **Languages:** Spanish (mother tongue), English (fluent), French (fluent), German (6 month learning), Italian (oral comprehension)
- **Computer languages:** Basic, FORTRAN, Pascal, MATLAB
- **Software:** DOS, Windows, QPro, MS Office, FrameMaker, Visio, LabView, HITRAN

VOLUNTARY WORK, AWARDS & HOBBIES

- ***Association of Colombian Researchers in Switzerland (ACIS)****, since 1997*
- Contributed to a *Science Policy* project submitted to the Colombian Government
- Elected Vice-President for the period 1998-1999
- ***Awards & honors***
- *Project reviewer*, Science & Technology Promotion Agency of Argentina, 2001
- *Research & teaching assistant award*, EPFL/DGR, 2000
- Spanish-American Assn. for Graduate Education (AIESAD) *Scholarship,* 1993.
- ***Hobbies & interests***
- Dance (salsa and Latin rhythms)
- Reading (historical novel, history, archeology)

PUBLICATION LIST

- ***PEER-REVIEWED PUBLICATIONS***

- **Jiménez, R.**, O. Couach, F. Kirchner, I. Balin, S. Perego, B. Calpini and H. van den Bergh (2003). Formaldehyde dynamics and photochemical production regime in the Grenoble region, France. *Atmospheric Environment*, submitted
- Couach, O., F. Kirchner, **R. Jiménez**, I. Balin, S. Perego and H. van den Bergh. A development of ozone abatement strategies for the Grenoble area using modeling and indicators. *Atmospheric Environment* 38: 1425-1436, 2004
- **Jiménez, R.**, M. Taslakov, V. Simeonov, B. Calpini, F. Jeanneret, D. Hofstetter, M. Beck, J. Faist and H. van den Bergh (2004). Ozone detection by differential absorption spectroscopy at ambient pressure with a 9.6 μm pulsed quantum-cascade laser. *Applied Physics B* 78: 249-256, 2004
- Couach, O., I. Balin, **R. Jiménez**, P. Ristori, S. Perego, F. Kirchner, V. Simeonov, B. Calpini and H. van den Bergh (2003). An investigation of ozone and planetary boundary layer dynamics over the complex topography of Grenoble combining measurements and modeling. *Atmospheric Chemistry and Physics* 3: 549–562
- Couach, O., I. Balin, **R. Jiménez**, S. Perego, F. Kirchner, P. Ristori, V. Simeonov, P. Quaglia, V. Vestri, A. Clappier, B. Calpini and H. van den Bergh (2002). Study of a photochemical episode over the Grenoble area using a mesoscale model and intensive measurements. *Pollution Atmospherique* (174): 277-295
- **Jiménez, R.**, T. Iannone, H. van den Bergh, B. Calpini and D. Kita (2000). Investigation of the emission of monocyclic aromatic hydrocarbons from a wastewater treatment plant at Lausanne (Switzerland) by DOAS. *A&WMA 93rd Annual Conf. & Exhib.*, Salt Lake City (USA), June 18-22: Paper 830

- **Jiménez, R.**, A. Martilli, I. Balin, H. van den Bergh, B. Calpini, B.R. Larsen, G. Favaro and D. Kita (2000). Measurement of formaldehyde (HCHO) by DOAS: Intercomparison to DNPH measurements and interpretation from Eulerian model calculations. *A&WMA 93rd Annual Conf. & Exhib.*, Salt Lake City (USA), June 18-22: Paper 829
- **Jiménez, R.**, H. van den Bergh and B. Calpini (1999). Evidence of primary air pollutant reduction and photochemical pollution enhancement after opening a road tunnel to the public. *Analusis* 27 (4): 313-318
- Quaglia, P., G. Larchevêque, **R. Jiménez**, B. Lazzarotto, V. Simeonov, G. Ancellet, H. van den Bergh and B. Calpini (1999). Planetary boundary layer ozone fluxes from combined airborne, ground-based LIDARs and wind profiler measurements. *Analusis* 27 (4): 305-310

➢ ***CONFERENCE PROCEEDINGS***

- Couach, O., F. Kirchner, **R. Jiménez**, I. Balin, S. Perego, A. Clappier and H. van den Bergh (2002). Grenoble Region: Test and application of different indicators in order to develop ozone abatement strategies. EUROTRAC-2 Symp. 2002, Garmisch-Partenkirchen (Germany), March 11-15
- Calpini, B., I. Balin, O. Couach, **R. Jiménez**, P. Ristori, P. Quaglia, H. van den Bergh and V. Simeonov (2002). Air pollution study over Grenoble-France in summer 1999: LIDAR measurements and model predictions. 21st ILRC, Quebec, July 8-12
- Couach, O., **R. Jiménez**, I. Balin, P. Quaglia, F. Kirchner, S. Perego, A. Clappier and H. van den Bergh (2001). Mesoscale photochemical modeling of GRENOPHOT 1999 data: Studying the air pollution over Grenoble's complex topography area. JRC/IES, 8th Europ. Symp. Phys.-Chem. Behavior Atmos. Pollutants, Torino (Italy), Sept. 17-20: Paper UP45
- **Jiménez, R.**, H. van den Bergh and B. Calpini (2000). DOAS as an analytical tool for effective air pollution management. 3rd Spec. Conf. Environ. Progress Petroleum & Petrochem. Industries, Bahrain, May 1-3: Paper 6
- Quaglia, P., **R. Jiménez**, V. Simeonov, G. Larchevêque, B. Lazzarotto, I. Balin, C. Besson and B. Calpini (1999). The EPFL contribution to the PIPAPO experiment. Regione Lombardia - Universitá degli Studi di Milano, Photochemical Oxidants and Aerosols in Lombardy Region, Milan, Jun 21-22: 45-50

➢ ***POSTER PRESENTATIONS***

- **Jiménez, R.**, M. Taslakov, V. Simeonov, B. Calpini and H. van den Bergh (2003). Open-path spectroscopic detection of trace gases with quantum-cascade lasers: Potential and challenges. Swiss Chemical Society, Fall Meeting, Oct. 9 - Abstract in *Chimia* 57 (7/8): 394
- **Jiménez, R.**, V. Simeonov, O. Couach, H. van den Bergh and B. Calpini (2001). Development and application of UV-visible and mid-infrared differential absorption spectroscopy techniques at the Swiss Federal Institute of Technology - Lausanne (EPFL). IUP – University of Heidelberg, DOAS Workshop 2001, Heidelberg, Sept. 13-14
- **Jiménez, R.**, H. van den Bergh and B. Calpini (2001). DOAS - A versatile, state-of-the-art technique for ambient air monitoring. AGS Annual Meeting 2001, Lausanne, Jan. 14-17

- ***REPORTS***

- Calpini, B., A. Clappier, **R. Jiménez**, G. Larchevêque, A. Martilli, F. Pasi, P. Quaglia, V. Simeonov and H. van den Bergh (1998). Photo-oxidant formation in the Milan metropolitan area. EUROTRAC-2 Symp. 1998, Garmisch-Partenkirchen (Germany), Mar 23-27
- **Jiménez, R.** (1999). Quality assessment of the formaldehyde measurements carried out within the PIPAPO experiment (EUROTRAC-2). http://loop.web.psi.ch
- Calpini, B., S. Perego, **R. Jiménez**, G. Larchevêque and H. van den Bergh (1998). Air quality in the Canton Obwald. Final report (in German). EPFL/LPAS, Lausanne
- **Jiménez, R.**, C. Dubois, F. Jeanneret, G. Larchevêque, B. Lazzarotto, V. Simeonov and B. Calpini (1997). Assessment of air quality in the Canton of Obwald. Field measurement campaign 1997 - Preliminary experimental report. EPFL/LPAS, Lausanne

- ***THESIS & DIPLOMA WORKS ADVISED***
- **Ulloa, M. and N. Daza** (2003). *Characterization of particulate matter bounded heavy metals in the Sogamoso Valley* (in Spanish). Diploma Work (Sanitary and Environmental Engineering), UNIBOYACA-EPFL, Tunja (Colombia)
- **Marquez, W. and W. Palencia** (2003). *Determination of ambient air carbonyls in the Sogamoso Valley using the DNPH/HPLC technique* (in Spanish). Diploma Work (Sanitary and Environ. Eng.), UNIBOYACA-EPFL, Tunja
- **Jaramillo, F.** (2001). Emiss*ion and fate of particulate matter generated by the small-scale brick and quicklime industry in the Valle of Sogamoso, Colombia: Properties and measuring techniques* (in Spanish). Diploma Work (Civil and Environmental Engineering), EPFL-University of Andes, Lausanne
- **Székely, L.** (2000). *Contribution to the development of a calibration system for the measurement of nitrous acid (HONO) by differential optical absorption spectroscopy (DOAS)*. Diploma work (Environmental Engineering), EPFL-University of Veszprém, Lausanne
- **Iannone, T.** (1999). *Preliminary estimation of the emission of volatile organic compounds from a wastewater treatment plan (Vidy, Lausanne* - in French). M.Eng. Thesis, EPFL, Lausanne
- **Balin, I.** (1998). *Differential optical absorption spectroscopy (DOAS) for air pollution measurements*. M.Sc. Thesis, EPFL, Lausanne